Universidade Federal do Rio Grande – FURG

Instituto de Oceanografia

Programa de Pós-Graduação em Oceanologia

PROCESSOS CONTROLADORES DAS TROCAS DE CO_2 ENTRE O OCEANO E A ATMOSFERA NO OESTE DA PENÍNSULA ANTÁRTICA E DO ATLÂNTICO TROPICAL

THIAGO MONTEIRO DA SILVA

Tese apresentada ao Programa de Pós-Graduação em Oceanologia, como parte dos requisitos para a obtenção do Título de Doutor.

Orientador: *Prof. Dr.* Rodrigo Kerr
Universidade Federal do Rio Grande (FURG), Brasil

Coorientadora: *Profa. Dra.* Sian Henley
The University of Edinburgh, UK

Rio Grande, RS, Brasil

Abril de 2023

PROCESSOS CONTROLADORES DAS TROCAS DE CO_2 ENTRE O OCEANO E A ATMOSFERA NO OESTE DA PENÍNSULA ANTÁRTICA E DO ATLÂNTICO TROPICAL

Tese apresentada ao Programa de Pós-Graduação em Oceanologia, como parte dos requisitos para a obtenção do Título de Doutor

por

THIAGO MONTEIRO DA SILVA

Rio Grande, RS, Brasil

Abril de 2023

Ficha Catalográfica

S586p Silva, Thiago Monteiro da.
Processos controladores das trocas de CO2 entre o Oceano e a atmosfera no oeste da Península Antártica e do Atlântico Tropical / Thiago Monteiro da Silva. – 2023.
236 f.

Tese (doutorado) – Universidade Federal do Rio Grande – FURG, Programa de Pós-Graduação em Oceanologia, Rio Grande/RS, 2023.
Orientador: Dr. Rodrigo Kerr.
Coorientador: Dra. Sian Henley.

1. Oceano Austral 2. Pluma do rio Amazonas 3. Biogeoquímica 4. Ciclo do carbono I. Kerr, Rodrigo II. Henley, Sian III. Título.

CDU 551.46

Catalogação na Fonte: Bibliotecário José Paulo dos Santos CRB 10/2344

UNIVERSIDADE FEDERAL DO RIO GRANDE - FURG
IO – INSTITUTO DE OCEANOGRAFIA
PROGRAMA DE PÓS-GRADUAÇÃ0 EM OCEANOLOGIA
E-mail: ccpofqg@furg.br – home-page: www.ppgo.furg.br

ATA ESPECIAL DE DEFESA DE TESE DE DOUTORADO – 01/2023

Às 08h do dia 24 de abril do ano de dois mil e vinte e três , Sala 1 Ceocean-IO/FURG e por videoconferência, reuniu-se a Comissão Examinadora da Tese de **DOUTORADO** intitulada **" Processos controladores das trocas de CO_2 entre o oceano e a atmosfera no oeste da Península Antártica e do Atlântico Tropical"**, do **Acad. Thiago Monteiro da Silva** . A Comissão Examinadora foi composta pelos seguintes membros: Prof. Dr. Rodrigo Kerr Duarte Pereira – Orientador – (IO/FURG), Profa. Dra. Sian Henley - (University of Edinburgh-Escócia), Profa. Dra. Leticia Cotrim da Cunha – (UERJ), Profa. Dra. Eunice da Costa Machado – (IO/FURG), Prof. Dr. Carlos Rafael Borges Mendes – (IO/FURG) e Prof. Dr. Mauricio Magalhães Mata – (IO/FURG). Dando início à reunião, a Coordenadora do Programa de Pós-Graduação em Oceanologia-PPGO, Profa. Dra. Grasiela Lopes Leães Pinho, agradeceu a presença de todos e fez a apresentação da Comissão Examinadora. Logo após esclareceu que o Candidato teria um tempo de 45 a 60 min para explanação do tema, e cada membro da Comissão Examinadora, um tempo máximo de 30 min para perguntas. A seguir, passou à palavra ao Candidato que apresentou o tema e respondeu às perguntas formuladas. Após ampla explanação, a Comissão Examinadora reuniu-se em reservado para discussão do conceito a ser atribuído ao Candidato. Foi estabelecido que as sugestões de todos os membros da Comissão Examinadora, que seguem em pareceres em anexo, foram aceitas pelo Orientador/Candidato para incorporação na versão final da Tese. Finalmente, a Comissão Examinadora considerou o candidato APROVADO, por unanimidade. Nada mais havendo a tratar, foi lavrada a presente ATA que após lida e aprovada, será assinada pela Comissão Examinadora, pelo Candidato e pela Coordenadora do Programa de Pós-Graduação em Oceanologia.

Documento assinado digitalmente
gov.br RODRIGO KERR DUARTE PEREIRA
Data: 25/04/2023 14:44:00-0300
Verifique em https://validar.iti.gov.br

Prof. Dr. Rodrigo Kerr Duarte Pereira

Documento assinado digitalmente
gov.br LETICIA COTRIM DA CUNHA
Data: 26/04/2023 11:49:20-0300
Verifique em https://validar.iti.gov.br

Profa. Dra. Sian Henley

Profa. Dra. Letícia Cotrim da Cunha

Profa. Dra. Eunice da Costa Machado

Prof. Dr. Mauricio M. Mata

Prof. Dr. Carlos Rafael Borges Mendes

Acad. Thiago Monteiro da Silva

Profa. Dra. Grasiela Lopes Leães Pinho
Coordenadora PPGO

Documento assinado digitalmente
gov.br GRASIELA LOPES LEAES PINHO
Data: 25/04/2023 14:14:53-0300
Verifique em https://validar.iti.gov.br

À minha mãe, Valdenice Monteiro, que me inspira coragem e resiliência.
À memória de minha avó Laura Monteiro, mulher que dedicou até o seu último suspiro para manter viva a esperança de rever a mim e minha mãe, e que me inspira determinação.
À minha tia Terezinha, o anjo que a vida pôs em meu caminho e a quem atribuo todo meu conhecimento e intelecto.
Às minhas tias Zenilda Monteiro e Rejane Marruaz, por todo apoio ao longo desta jornada.
A Matheus Batista, que me ensinou o mais singelo e profundo significado do amor.

Dedico.

“A ciência será sempre uma busca, jamais uma descoberta.”

Karl Popper

Índice

Agradecimentos

Uma das poucas certezas que eu tenho na vida é que chegar até aqui não foi um mérito somente meu, mas de muitas pessoas que estiveram e estão ao meu lado durante toda essa jornada.

À minha família, que tem me apoiado nessa jornada de me tornar cientista. Especialmente minha mãe, meu pai, minha avó, meus irmãos, tia Nena, Rejane, Alexia, Rebecca e Patrícia... Por estarem sempre perto, apesar da distância.

A Matheus, por todo amor, toda a paciência, por ter sido minha luz nos momentos difíceis e ter me proporcionado os momentos mais felizes da minha vida.

Ao meu orientador, professor Rodrigo Kerr, pela fantástica orientação, por ter me inspirado durante todo esse tempo, pela confiança e por ter me proporcionado oportunidades que mudaram a minha vida.

À minha banca de acompanhamento: Professora Eunice Machado e Professores Mauricio Mata e Rafael Mendes, pelas valiosas considerações nos seminários e nas nossas reuniões, mas, principalmente, por serem cientistas que me inspiram e por quem tenho enorme admiração.

À professora Sian Henley, pela orientação, por ter me proporcionado um período maravilhoso em Edimburgo, pela paciência e pela enorme satisfação de ter conhecido uma pessoa tão incrível.

A Nathasha, que sempre me incentiva e aguentou minha empolgação quando se tratava de ciência, por ter sido uma conselheira e companhia nesses tempos longe da família e por ter me apresentado Olívia, por quem eu morro de amor.

A D. Nenzinha, uma das pessoas mais maravilhosas que conheci na vida, que me acolheu em um dos momentos mais difíceis da minha vida e por quem eu serei eternamente grato.

À minha tia Terezinha, a mulher que mudou o rumo da minha vida, pelo aprendizado, pelas noites em claro, por todas as súplicas às escolas para que me aceitassem como aluno sem nenhum documento. Por ter me ensinado a ler, escrever, fazer contas, capinar, plantar, colher, cozinhar, costurar. Por ter me dado esperanças. Por ter me dado amor.

Às minhas tias Adriana, Claudinha e Lú, mulheres incríveis pelas quais tenho profunda admiração e me inspiraram durante toda a minha infância e adolescência.

Aos meus tios Júlio, Ricardo e Alexandre, pelo acolhimento e incentivo.

Aos meus queridos primos Igor, Paulinha, Anderson, Adriele, Amanda, Andreza e Matheus, por terem me proporcionado uma infância maravilhosa.

A Nelma, Josivaldo e Josinelma, por terem me acolhido, me incentivado e acreditado em mim.

Às professoras Luiza Nakayama e Suzana Bittencourt pelo apoio e incentivo durante o início da minha paixão pela ciência.

A todo pessoal do Laboratório de Estudos dos Oceanos e Clima e ao CARBON Team, pelos incentivos, pelas sugestões, pelas profundas discussões sobre os mais diversos assuntos.

Lista de Figuras da Tese

Lista de Tabelas da Tese

Lista de Acrônimos e Abreviações

A

ACC – Corrente Circumpolar Antártica (*Antarctic Circumpolar Current*)

ARP – Pluma do rio Amazonas (*Amazon River Plume*)

A_T/TA – Alcalinidade Total (*Total Alkalinity*)

C

CDW – Água Profunda Circumpolar (*Circumpolar Deep Water*)

CO_2 – Dióxido de carbono

CRM – Material de Referência Certificado (*Certified Reference Material*)

C_T/DIC – Carbono Inorgânico Dissolvido (*Dissolved Inorganic Carbono*)

CTD – Condutividade-Temperatura-Profundidade (Conductivity-Temperature-Depth)

D

DIN – Nitrogênio Inorgânico Dissolvido (*Dissolved Inorganic Nitrogen*)

DIVA – Análise Variacional de Interpolação de Dados (*Data-Interpolating Variational Analysis*)

DSW – Água Dense de Plataforma (*Dense Shelf Water*)

E

ENSO – El Niño Oscilação Sul (*El Niño Southern Oscillation*)

F

FCO_2 – fluxo de CO_2 entre o oceano e atmosfera

G

GLODAP – Projeto Global de Análise de Dados Oceânicos (*Global Ocean Data Analysis Project*)

GOAL – Grupo de Oceanografia de Altas Latitudes

H

$HgCl_2$ – Cloreto de Mercúrio

HSO_4^- – Sulfato de Hidrogênio

HSSW – Água de Plataforma de Alta Salinidade (*High Salinity Shelf Water*)

I

ITCZ – Zona de Convergência Intertropical (*Intertropical Convergence Zone*)

L

LIAR – Regressão de Alcalinidade Interpolada Localmente (*Locally Interpolated Alkalinity Regression*)

LSSW – Água de Plataforma de Baixa Salinidade (*Low Salinity Shelf Water*)

M

mCDW – Água Profunda Circumpolar modificada (*modified CDW*)

N

NAP – porção norte da Península Antártica

nA_T/nTA – Alcalinidade Total normalizada

NBC – Corrente Norte do Brasil (North Brazil Current)

nC_T/nDIC – Carbono Inorgânico Dissolvido normalizado

NEC – Corrente Norte Equatorial (*North Equatorial Current*)

NECC – Contracorrente Norte Equatorial (*North Equatorial Countercurrent*)

O

OCADS – *Ocean Carbon and Acidification Data System*

P

P^{ar} – Pressão Atmosférica

P_{H_2O} – Pressão de vapor de água

***p*CO_2** – pressão parcial do CO_2

***p*CO_2^{mar}/ *p*CO_2^{sw}** – pressão parcial do CO_2 na superfície do mar

***p*CO_2^{ar}/ *p*CO_2^{air}** – pressão parcial do CO_2 na atmosfera

R

RMSE – Erro Quadrático Médio (*Root Mean Square Error*)

S

SAM – Modo Anual Sul (*Southern Annular Mode*)

SOCAT – Atlas para CO_2 na Superfície do Oceano (*Surface Ocean CO_2 Atlas*)

SSS – Salinidade Superficial do Mar (*Sea Surface Salinity)*

SST – Temperatura Superficial do Mar (*Sea Surface Temperature)*

W

WAP – Oeste da Península Antártica (*western Antarctic Peninsula*)

WTA – Oceano Atlântico Tropical oeste (*western Tropical Atlantic Ocean)*

X

xCO_2 – Fração molar de CO_2

Z

Ω_{Ar} – Estado de saturação da aragonita

Ω_{Ca} – Estado de saturação da calcit

Resumo

O ciclo do carbono é fundamental para a regulação do clima na Terra e o fluxo de dióxido de carbono (CO_2) entre o oceano e atmosfera (FCO_2) é essencial para esse ciclo. Os oceanos têm desempenhado um importante papel em absorver o excesso de CO_2 atmosférico devido às atividades humanas, principalmente através do crescimento do fitoplâncton em regiões com altas concentrações de nutrientes. Logo, conhecer a variabilidade espacial e temporal do FCO_2 nessas regiões é fundamental para compreendermos os processos que o controlam e desacoplarmos as alterações naturais dos impactos devido às mudanças climáticas. Portanto, os processos oceanográficos e biogeoquímicos que controlam as concentrações de nutrientes e o FCO_2 foram investigados em duas importantes regiões altamente dinâmicas e sob forte influência do aporte de água doce: o norte da Península Antártica (NAP) e o oceano Atlântico Tropical oeste (WTA). Para isso, robustas séries temporais foram analisadas para entender a variabilidade dos nutrientes no NAP (1996-2019) e do FCO_2 no NAP (2002-2017) e no WTA (1993-2019). Foi descoberta uma alta variabilidade espacial e interanual nas concentrações dos nutrientes ao longo do NAP, devido principalmente à intensa mistura entre massas de água de distintas origens. Essa mistura é controlada majoritariamente pelos modos de variabilidade climática atuantes no oceano Austral. Além disso, o estreito de Gerlache, no sul do NAP, é uma região altamente favorável ao crescimento do fitoplâncton e, portanto, à intensa absorção de CO_2 durante o verão. Na verdade, essa região libera CO_2 para a atmosfera de abril a novembro (8 ± 2 mmol m^{-2} dia^{-1}), devido à influência de águas antigas, ricas em carbono remineralizado. No entanto, em apenas quatro meses (dezembro-março) a absorção de CO_2 pelo fitoplâncton é tão intensa (-10 ± 3 mmol m^{-2} dia^{-1}) que quase compensa todo CO_2 liberado. A atividade fitoplanctônica também exerce um papel crucial na absorção de CO_2 no WTA (-1.6 ± 1.0 mmol m^{-2} dia^{-1}), principalmente na pluma do rio Amazonas (-5 ± 3 mmol m^{-2} dia^{-1}), que é responsáveis por mais de 85% dessa absorção. Além disso, as diferentes características biogeoquímicas das águas transportadas pelas correntes superficiais e a influência da pluma do rio Amazonas proporcionam uma alta variabilidade espacial do FCO_2 no WTA. Essas informações revelam a importância das regiões estudadas nesse trabalho para o ciclo do carbono e que elas são muito mais sensíveis às alterações climáticas do que se pensava.

Palavras-chave: Oceano Austral, Pluma do rio Amazonas, Biogeoquímica, Ciclo do carbono.

Abstract

The carbon cycle is crucial for regulating the Earth's climate and the sea-air carbon dioxide (CO_2) flux (FCO_2) is essential for this cycle. Oceans have played an important role in absorbing excess atmospheric CO_2 due to human activities, mainly through phytoplankton growth in regions with high concentrations of nutrients. Therefore, knowing the spatial and temporal variability of FCO_2 in those regions is essential to understand the processes controlling it and to decouple natural variations from the impacts due to climate change. Hence, the oceanographic and biogeochemical processes that control nutrient concentrations and FCO_2 were investigated in two important highly dynamic regions and under strong influence of freshwater input: the northern Antarctic Peninsula (NAP) and the western Tropical Atlantic Ocean (WTA). For this, robust time series were analysed to understand the variability of nutrients in NAP (1996-2019) and FCO_2 in NAP (2002-2017) and WTA (1993-2019). A high spatial and interannual variability was found in nutrient concentrations along the NAP, mainly due to the intense mixing between water masses from different origins. This mixture is mainly driven by the modes of climate variability operating in the Southern Ocean. Furthermore, the Gerlache Strait, in the south of the NAP, is a highly favourable region for the phytoplankton growth and, therefore, for the intense CO_2 uptake during the summer. Actually, this region releases CO_2 into the atmosphere from April to November (8 ± 2 mmol m^{-2} day^{-1}), due to the influence of relatively old waters, rich in remineralised carbon. However, in only four months (December-March) the CO_2 uptake by phytoplankton growth is so intense (-10 ± 3 mmol m^{-2} day^{-1}) that it almost counteracts all the CO_2 released. Phytoplanktonic activity also plays a crucial role in CO_2 uptake in the WTA (-1.6 ± 1.0 mmol m^{-2} day^{-1}), mainly in the Amazon River plume (-5 ± 3 mmol m^{-2} day^{-1}), which is responsible for more than 85% of this CO_2 uptake by WTA. Moreover, the different biogeochemical characteristics of the waters transported by surface currents and the influence of the Amazon River plume provide a high spatial variability of FCO_2 over the WTA. This information reveals the importance of the regions studied in this work for the carbon cycle and that they are much more sensitive to climate change than previously thought.

Key words: Southern Ocean, Amazon River Plume, Biogeochemistry, Carbon Cycle.

Prefácio

O fluxo de dióxido de carbono (CO_2) entre o oceano e a atmosfera (FCO_2) é um processo chave no ciclo do carbono, que é um componente fundamental para o controle do clima da Terra. No período pré-industrial, a concentração de CO_2 na superfície dos oceanos e na atmosfera estiveram em equilíbrio, de modo que o FCO_2 era neutro em escalas decenais. No entanto, diversas atividades humanas como o intensivo uso de combustíveis fósseis, o uso irregular de terras e o desflorestamento têm aumentado a concentração do CO_2 na atmosfera – parcela antropogênica do carbono. Como consequência, os oceanos têm absorvido esse excesso de CO_2, minimizando os impactos do aumento da temperatura superficial da Terra devido ao aumento de CO_2 na atmosfera.

Contudo, o excesso de CO_2 absorvido pela superfície do mar tem causado outras consequências nos oceanos, tal como a acidificação oceânica, que impacta diretamente o crescimento de organismos fundamentais para a teia trófica marinha. A absorção de CO_2 pelos oceanos é impulsionada essencialmente pela diferença da pressão parcial do CO_2 entre a atmosfera

(pCO_2^{ar}) e a superfície do mar (pCO_2^{mar}), a qual apresenta uma considerável variabilidade espacial e temporal. Portanto, é fundamental conhecer os processos que controlam a pCO_2^{mar} e, consequentemente, a absorção de CO_2 pelos oceanos, para identificarmos suas variações naturais e os impactos que os ecossistemas estão sofrendo.

Um dos principais processos que controla a pCO_2^{mar} é a atividade biológica, porque o fitoplâncton consome CO_2 durante a fotossíntese enquanto o CO_2 é liberado durante a respiração. No entanto, na maior parte dos oceanos a fotossíntese é limitada pela quantidade de nutrientes. Logo, em algumas regiões, onde há altas concentrações de nutrientes, a atividade fitoplanctônica é intensificada, reduzindo a pCO_2^{mar} e favorecendo a absorção de CO_2. Por exemplo, isso acontece no estreito de Gerlache, uma região costeira da Antártica, e na pluma do rio Amazonas, que são regiões onde há forte absorção de CO_2 da atmosfera para o oceano.

O estreito de Gerlache é uma bacia relativamente pequena, localizada no norte da Península Antártica (NAP), uma região com altas concentrações de nutrientes. Apesar de sua área relativamente pequena, o estreito de Gerlache absorve desproporcionalmente mais CO_2 do que outras regiões costeiras da Antártica com áreas maiores. A pluma do rio Amazonas (ARP) é uma feição oceanográfica na porção oeste do oceano Atlântico Tropical (WTA), formada a partir do intenso aporte de água doce do rio Amazonas. Além de água doce, o rio Amazonas aporta altas concentrações de nutrientes, por isso a ARP é considerada uma região com absorção de CO_2 de importância global. Contudo, apesar da clara importância para a absorção de CO_2, muitos processos

biogeoquímicos que atuam simultaneamente no controle da pCO_2^{mar} e do FCO_2 ainda são pouco compreendidos nessas regiões.

O FCO_2 também é controlado pela solubilidade desse gás na água do mar, sendo influenciada diretamente pela temperatura e pela salinidade da água. Durante o verão, o aporte de água doce pelo degelo continental diminui a salinidade na superfície do mar, mas ainda não está claro qual o impacto desse processo sobre o FCO_2 no estreito de Gerlache. Além disso, a maioria dos estudos realizados nas zonas costeiras da Antártica são restritos ao verão, então pouco se sabe sobre a variabilidade sazonal do FCO_2 e dos processos envolvidos nessa variabilidade. Alguns estudos já indicaram a fotossíntese como a principal responsável pela intensa absorção de CO_2 no estreito de Gerlache. Contudo, ainda não está claro porque essa região é particularmente importante para o crescimento do fitoplâncton, pois é esperado que toda o NAP tenha altas concentrações de nutrientes. Apesar de se esperar esse enriquecimento em nutrientes, poucos estudos investigaram a variabilidade espacial e temporal dos nutrientes ao longo do NAP. Portanto, entender quais processos controlam a dinâmica dos nutrientes nessa região ainda é uma questão em aberto.

Já no WTA, sob a influência da ARP, há uma enorme divergência nas estimativas do FCO_2 e na magnitude da absorção de CO_2 pela ARP. Embora vários estudos sugiram que a fotossíntese seja o principal controlador da absorção de CO_2, pouco é discutido sobre o papel da diluição e da solubilidade, já que o rio Amazonas é responsável pela maior descarrega fluvial do mundo. Portanto, este trabalho visa preencher as lacunas do conhecimento levantadas aqui sobre os processos oceanográficos e biogeoquímicos responsáveis pela variabilidade espacial e temporal do FCO_2 e/ou dos nutrientes em duas

importantes regiões oceânicas: as zonas costeiras do NAP e o WTA. A partir desse conhecimento, poderemos ampliar nossa compreensão sobre o ciclo do carbono, entender melhor o comportamento natural dos ambientes estudados, identificar potenciais alterações e propor alternativas de uso sustentável.

A estrutura desta tese segue o modelo de artigos científicos proposto pelo Programa de Pós-Graduação em Oceanologia (PPGO). Após o prefácio, será apresentada a hipótese a ser testada por esta tese. No Capítulo I temos uma Introdução ao tema abordado, seguida pelos objetivos do estudo. No Capítulo II serão apresentados os métodos utilizados para atingir os resultados esperados. Os resultados deste trabalho, por sua vez, serão apresentados na língua inglesa e na forma de artigos científicos nos Capítulos III, IV e V. O Capítulo III traz o primeiro estudo, que aborda a variabilidade espacial e interanual dos macronutrientes na porção norte da península Antártica e porque o estreito de Gerlache é particularmente importante para o crescimento do fitoplâncton e para a absorção de CO_2. No Capítulo IV, é apresentado o segundo estudo, que mostra quais os processos responsáveis pela variabilidade sazonal e interanual do FCO_2 no estreito de Gerlache. No Capítulo V temos o terceiro estudo, sobre os processos controladores da variabilidade espacial e temporal do FCO_2 no oceano Atlântico Tropical oeste e qual o papel da pluma do rio Amazonas na absorção de CO_2. Em anexo, encontram-se os materiais suplementares dos artigos apresentados nos Capítulos III, IV e V. No capítulo VI, temos uma síntese das principais discussões e conclusões sobre esses resultados. Finalmente, no Capítulo VII encontram-se descritas todas as referências bibliográficas utilizadas nesta tese.

Hipótese

Em geral, há uma alta variabilidade nas trocas de CO_2 entre o oceano e atmosfera, muitas vezes resultando em estudos com conclusões divergentes em relação ao comportamento do oceano como fonte ou sumidouro de CO_2 em determinados mares e oceanos. Mesmo quando a maioria dos estudos aponta para um único comportamento, há ainda uma alta variabilidade na magnitude das trocas de CO_2, embora os processos que controlam essa variabilidade ainda sejam pouco compreendidos. Nesse contexto, a hipótese testada nesta tese foi que:

"A alta produtividade primária proporcionada pelas altas concentrações de nutrientes é o principal controlador da absorção de CO_2 no norte da Península Antártica e no oeste do oceano Atlântico Tropical."

Capítulo I: Introdução

Os oceanos e a atmosfera são reservatórios de diversos compostos químicos, como o CO_2, que é um importante gás para o efeito estufa. O FCO_2 é essencial para o balanço do ciclo global do carbono e para o equilíbrio do clima na Terra. O FCO_2 ocorre primordialmente por difusão, devido à diferença da pressão parcial do CO_2 entre a superfície do mar e a atmosfera [Millero 2013]. Como a pCO_2^{ar} é relativamente estável comparada à pCO_2^{mar}, a variabilidade espacial e temporal do FCO_2 responde, majoritariamente, às alterações de pCO_2^{mar} [Sarmiento & Gruber 2006]. Por isso, algumas regiões oceânicas podem atuar como fonte de CO_2 para atmosfera (i.e., liberar CO_2 para a atmosfera), enquanto outras podem atuar como sumidouro de CO_2 atmosférico (i.e., absorver CO_2 da atmosfera).

Devido ao progressivo aumento da pCO_2^{ar} pelas atividades humanas desde o início da revolução industrial, os oceanos têm absorvido cerca de 25% desse excesso de CO_2 na atmosfera [Friedlingstein *et al*. 2020], contribuindo como um amortecedor do aquecimento antropogênico do planeta. O CO_2 reage

com a água do mar, quando é dissolvido no oceano, e depois se dissocia em um conjunto de compostos químicos denominado carbono inorgânico dissolvido [Williams & Follows 2011; Sarmiento & Gruber 2006]. Uma das principais consequências da intensa absorção de CO_2 pelos oceanos é a alteração na química da água do mar [Millero 2007, 2013], causando o processo de acidificação oceânica [Orr *et al*. 2005; Doney *et al*. 2009; Lauvset *et al*. 2020]. Esta reduz as concentrações do íon carbonato [Millero 2007; Lauvset *et al*. 2020], que é essencial para a síntese de estruturas corporais de diversos organismos marinhos que são fundamentais para o equilíbrio da teia trófica nos oceanos [Doney *et al*. 2020].

A combinação de diversos processos químicos, físicos e biológicos contribui para uma região oceânica se comportar como fonte ou sumidouro de CO_2. O aquecimento das águas superficiais, o transporte de águas subsuperficiais e profundas, ricas em carbono inorgânico dissolvido, para a superfície e a atividade heterotrófica podem levar ao aumento da pCO_2^{mar} e consequente liberação de CO_2 para a atmosfera [Takahashi *et al*. 2014; Roobaert *et al*. 2019]. Por outro lado, o aumento da solubilidade em baixas temperaturas e/ou salinidade [Williams & Follows 2011; Millero 2013], a formação de águas profundas [Takahashi *et al*. 2014; Roobaert *et al*. 2019] e a intensa produtividade primária, por meio da fotossíntese [Takahashi *et al*. 2014; Brown *et al*. 2019; Louchard *et al*. 2021], podem levar à diminuição da pCO_2^{mar} e consequente absorção de CO_2 atmosférico.

A fotossíntese tem sido reportada como um dos principais processos responsáveis pela absorção de CO_2 dissolvido na água do mar [Takahashi *et al*. 2014], principalmente em regiões costeiras [Roobaert *et al*. 2019]. Em diversas

regiões costeiras, o crescimento do fitoplâncton é intensificado devido ao aporte continental de nutrientes, por meio de rios e estuários [Stukel *et al*. 2014; Dai *et al*. 2023]. Além disso, o aporte de água doce reduz a salinidade superficial e aumenta a estabilidade da camada superior do oceano, contribuindo para o crescimento do fitoplâncton, que é um forte indicador de alta produtividade primária [Stukel *et al*. 2014; Louchard *et al*. 2021]. Simultaneamente, o aumento da solubilidade causado pela redução da salinidade também pode contribuir para absorção de CO_2 [Cooley *et al*. 2007; Takahashi *et al*. 2014; Roobaert *et al*. 2019], levando essas regiões a se comportarem como fortes sumidouros de CO_2 atmosférico.

As regiões de altas latitudes também são importantes sumidouros de CO_2 atmosférico, principalmente devido às baixas temperaturas e salinidade, durante o período de degelo [Takahashi *et al*. 2014; Roobaert *et al*. 2019]. Porém, o oceano Austral, que circunda a Antártica, tem um papel ainda mais relevante nesse contexto, já que ele é responsável por cerca de 40% da absorção de CO_2 antropogênico do planeta, apesar de cobrir menos de 20% da área oceânica global [Landschützer *et al*. 2015; Henley *et al*. 2020]. Além disso, as regiões costeiras ao redor da Antártica também são particularmente relevantes, porque em geral elas absorvem desproporcionalmente mais CO_2 do que as regiões de oceano aberto [Monteiro *et al*. 2020a; Dejong & Dunbar 2017].

A maior parte dessa absorção ocorre durante o verão austral e é impulsionada pela fotossíntese [Hauck *et al*. 2015; Brown *et al*. 2019; Henley *et al*. 2020], devido às altas concentrações de nutrientes [Hauck *et al*. 2015; Henley *et al*. 2020]. Na verdade, o oceano Austral é uma das regiões oceânicas com maiores concentrações de nutrientes [Pollard *et al*. 2006; Henley *et al*. 2020] e

muitas vezes considerada uma fonte importante de nutrientes para o oceano global [Murphy *et al*. 2021]. Apesar disso, as concentrações de clorofila *a*, as quais podem ser usadas como indicador de biomassa fitoplanctônica e, poranto de produtividade primária, são consideradas baixas no oceano Austral [de Baar *et al*. 1995; Henley *et al*. 2020; Murphy *et al*. 2021]. Isso ocorre porque, embora haja altas concentrações de macronutriente, essa região é relativamente pobre em ferro, um micronutriente fundamental para o fitoplâncton realizar a fotossíntese [de Baar *et al*. 1995; Henley *et al*. 2020].

Entretanto, o NAP é uma região da Antártica onde a concentração de ferro parece não ser um fator limitante para a fotossíntese [Ardelan *et al*. 2010; Henley *et al*. 2019]. Além de ter fontes locais de ferro, principalmente de origem continental [De Jong *et al*. 2012; Sherrell *et al*. 2018], alguns grupos de fitoplâncton, como as diatomáceas, podem compensar a ausência de ferro por silicato [Pondaven *et al*. 2000; Smith *et al*. 2000], um macronutrientes com altas concentrações ao redor do NAP [Henley *et al*. 2019]. Embora alguns estudos tenham feito registros instantâneos das concentrações de macronutrientes em alguns ambientes do NAP [Mendes *et al*. 2018; Höfer *et al*. 2019; Costa *et al*. 2020; Mascioni *et al*. 2021], pouco se sabe sobre como esses nutrientes variam temporal e espacialmente ao longo do NAP. Além disso, não está claro quais processos estão envolvidos nessa variabilidade e porque algumas regiões do NAP são mais produtivas e absorvem mais CO_2 do que outras.

Uma dessas regiões é o estreito de Gerlache, uma bacia relativamente rasa (~1000 m), localizada ao sul do NAP (Fig. I-2) e caracterizada por uma abundante biomassa fitoplanctônica [Mendes *et al*. 2018; Costa *et al*. 2020], que sustenta uma alta diversidade ao longo da teia trófica [Dalla Rosa *et al*. 2008;

Nowacek *et al*. 2011; Mendes *et al*. 2018]. Além disso, o estreito de Gerlache é considerado uma região chave para absorção de CO_2 atmosférico porque durante o verão essa região absorve CO_2 em magnitudes maiores do que regiões com áreas mais extensas ao redor da Antártica [Monteiro *et al*. 2020a]. Apesar de alguns estudos associarem essa forte absorção de CO_2 principalmente à fotossíntese [Brown *et al*. 2019; Monteiro *et al*. 2020a; Costa *et al*. 2020], não está claro o que torna o estreito de Gerlache uma região particularmente importante para a fotossíntese.

Uma das explicações em comum nos estudos é a alta concentração de macronutrientes e o aporte local de ferro [Henley *et al*. 2019; Costa *et al*. 2020], embora essas condições sejam geralmente presentes ao longo de todo o NAP [Henley *et al*. 2019]. Além disso, a maioria dos estudos que investigaram o FCO_2 em regiões costeiras da Antártica foram conduzidos no verão [Álvarez *et al*. 2002; Kerr *et al*. 2018; Brown *et al*. 2019; Monteiro *et al*. 2020a]. Portanto, pouco se sabe sobre a variabilidade sazonal e interanual do FCO_2 nessas regiões. Destaca-se, ainda, o pouco conhecimento sobre o papel da solubilidade na absorção de CO_2, visto que o estreito de Gerlache é fortemente influenciado pelo aporte de água doce. Este ocorre devido ao aporte do degelo de plataformas de gelo continental [Cook *et al*. 2016; Silva *et al*. 2020; Meredith *et al*. 2022] e/ou de águas do derretimento local e alóctone de gelo marinho [Parra *et al*. 2020; Su *et al*. 2022], durante o verão austral.

Outra importante região oceânica caracterizada por intenso aporte de água doce e altas concentrações de nutrientes é o WTA, sob influência do rio Amazonas. O rio Amazonas é responsável pela maior descarga fluvial do mundo (120000 $m^3\ s^{-1}$) [Dai & Trenberth 2002; Coles *et al*. 2013], aportando para o

oceano Atlântico Tropical a mesma quantidade de água doce que os próximos oito maiores rios do mundo juntos [Coles *et al*. 2013]. Esse grande volume de água doce forma a ARP, que é muito dinâmica e se estende por uma significativa área no WTA [Hellweger & Gordon 2002; Coles *et al*. 2013; Korosov *et al*. 2015]. Além de água doce, o rio Amazonas é responsável por transportar altas concentrações de nutrientes para essa região [Del Vecchio & Subramaniam 2004; Gomes *et al*. 2018], proporcionando um ambiente altamente favorável para o crescimento do fitoplâncton, intensificando a produtividade primária [Gomes *et al*. 2018; Louchard *et al*. 2021].

Contudo, o rio Amazonas também transporta altas concentrações de material particulado em suspensão, aumentando a turbidez das águas oceânicas adjacentes [Gouveia *et al*. 2019; Louchard *et al*. 2021], o que pode dificultar o processo de fotossíntese [Gouveia *et al*. 2019]. Além disso, a remineralização da matéria orgânica lixiviada ao longo da bacia de drenagem aumenta as concentrações de carbono inorgânico dissolvido [Abril *et al*. 2014; Araujo *et al*. 2017], contribuindo para o aumento da pCO_2^{mar}. Apesar desses processos atenuarem a absorção de CO_2 atmosférico [Abril *et al*. 2014; Araujo *et al*. 2017; Louchard *et al*. 2021], diversos estudos apontam a ARP como um sumidouro de CO_2 de importância global [Cooley *et al*. 2007; Ibánhez *et al*. 2015, 2016; Lefèvre *et al*. 2010]. No entanto, há uma enorme divergência entre os estudos em relação à magnitude dessa absorção [Louchard *et al*. 2021; Mu *et al*. 2021] e ao comportamento líquido do FCO_2 no WTA sob influência da ARP.

Algumas estimativas do FCO_2 indicam que o WTA se comporta como uma fonte líquida de CO_2 para a atmosfera [e.g., Cooley *et al*. 2007; Louchard *et al*. 2021; Valerio *et al*. 2021]. Outros estudos indicam um comportamento de

sumidouro líquido de CO_2 atmosférico, principalmente devido à alta produtividade primária alimentada pela alta disponibilidade de nutrientes fornecida pelas águas do rio Amazonas [e.g., Ibánhez *et al*. 2015; Ibánhez *et al*. 2016; Körtzinger, 2003; Lefèvre *et al*. 2010; Mu *et al*. 2021]. Mesmo quando essas estimativas indicam um mesmo comportamento, isto é, o FCO_2 na mesma direção, a magnitude desses fluxos pode variar consideravelmente entre as estimativas. Por exemplo, estimativas de FCO_2 com base em dados de satélite mostraram uma liberação anual média de CO_2 de 4,6 mmol m^{-2} dia^{-1} [Valerio *et al*. 2021], enquanto modelos biogeoquímicos indicaram uma fonte de CO_2 uma ordem de magnitude menor (0,5 mmol m^{-2} dia^{-1}) [Louchard *et al*. 2021] em uma vasta área do WTA.

Tanto o NAP quanto o WTA são regiões oceânicas caracterizadas por intenso aporte de água doce (Fig. I-1a) e por altas concentrações de nutrientes (Fig. I-1b), que sustentam uma alta produtividade primária, geralmente associada a altas concentrações de clorofila a (Fig. I-1c). Essas condições tornam essas regiões altamente favoráveis à absorção de CO_2, caracterizada por baixas pCO_2^{mar} (Fig. I-1d), impulsionada tanto pela fotossíntese quanto pelo aumento da solubilidade desse gás. No entanto, outros processos biogeoquímicos ocorrendo simultaneamente adicionam complexidade ao entendimento do FCO_2 nessas regiões e identificar a magnitude desses processos ainda é um desafio.

Por exemplo, apesar das altas concentrações de nutrientes esperadas no NAP, a variabilidade espacial e temporal nessas concentrações ainda é desconhecida, assim como os processos que a controla. Da mesma forma, ainda não se sabe qual o comportamento sazonal do FCO_2 no estreito de Gerlache,

apesar de sua importância para a absorção de CO_2 no NAP, durante o verão austral. Já se sabe bem que as altas concentrações de nutrientes promovidas pela ARP no WTA impulsiona a produtividade primária, através da fotossíntese. É consenso entre os estudos que essas condições favorecem a absorção de CO_2 atmosférico sob o domínio da ARP. No entanto, o impacto da diluição e da solubilidade, promovidas pelo aporte de água doce do rio, sobre o FCO_2 ainda é pouco compreendido.

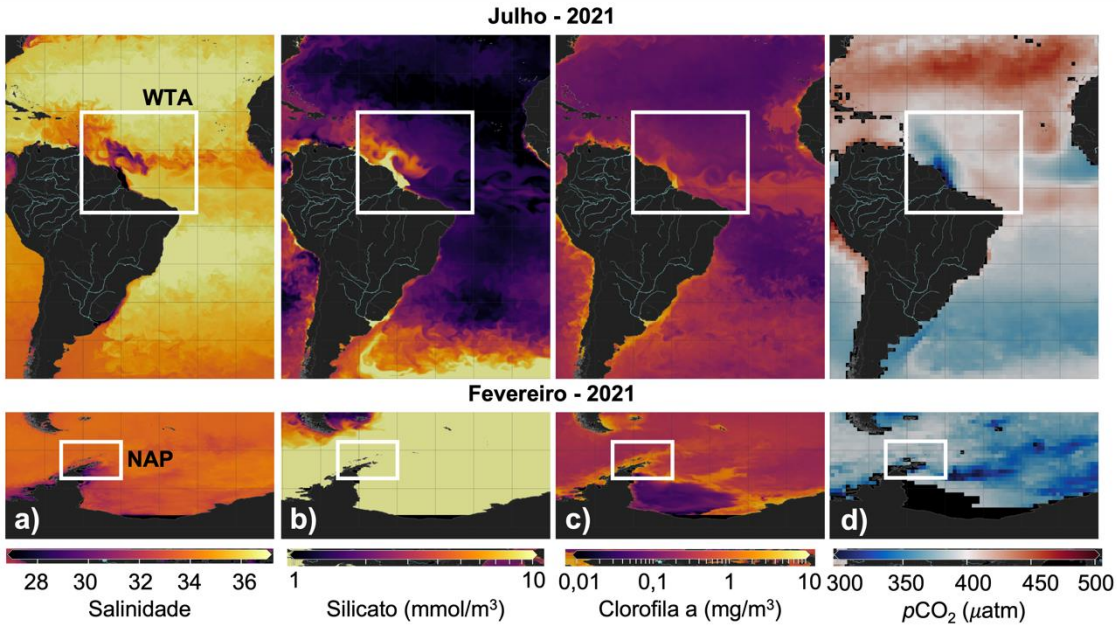

Figura I-1: Distribuição espacial de propriedades biogeoquímicas na superfície do mar no oceano Atlântico, destacando as regiões do norte da Península Antártica (NAP) e do Atlântico Tropical oeste (WTA). As propriedades são: a) salinidade, b) silicato, c) clorofila a e d) pressão parcial do CO_2 (pCO_2). Todas as imagens foram obtidas do repositório de dados do *Copernicus Marine Service* (https://data.marine.copernicus.eu/products), para julho de 2021 no WTA e para fevereiro de 2021 para o NAP.

Nesse sentido, o objetivo desse trabalho foi responder às lacunas de conhecimento apontadas ao longo desse capítulo relacionadas principalmente (i) aos processos envolvidos na variabilidade espacial e temporal dos macronutrientes ao longo do NAP, (ii) à sazonalidade do FCO_2 no estreito de Gerlache e (iii) à importância da ARP para a absorção de CO_2 e quais processos estão envolvidos nessa absorção.

1. 1 Objetivos

1.1.1 Geral

Investigar os processos oceanográficos e biogeoquímicos controladores da variabilidade dos macronutrientes e do FCO_2 no norte da Península Antártica e do FCO_2 no oeste do oceano Atlântico Tropical.

1.1.2 Objetivos específicos

(i) Investigar os processos envolvidos na variabilidade espacial e temporal dos macronutrientes ao longo do NAP e como eles tornam o estreito de Gerlache uma região chave para a absorção de CO_2.

(ii) Determinar a variabilidade sazonal do FCO_2 no estreito de Gerlache e identificar quais processos controlam o balanço entre absorção e liberação de CO_2 na região.

(iii) Verificar por que há divergências na magnitude do FCO_2 no WTA.

(iv) Investigar a magnitude da importância da ARP para a absorção de CO_2 e quais processos estão envolvidos nessa absorção.

1. 2 Características oceanográficas do NAP

O NAP é uma região chave para entender as mudanças biogeoquímicas no oceano Austral porque é uma das regiões da Antártica onde se tem observado mudanças rápidas no sistema acoplado entre a atmosfera, o oceano e a criosfera [e.g., Kerr *et al*. 2018a; Henley *et al*. 2019]. Estudos das últimas duas décadas relataram mudanças nos padrões de vento [Dinniman *et al*. 2012], na cobertura de gelo marinho e continental [Shepherd *et al*. 2018], na atividade biológica [Seyboth *et al*. 2016; Mendes *et al*. 2018] e no sistema carbonato marinho [Kerr

et al. 2018a; Orselli *et al*. 2022a; Santos-Andrade *et al*. 2023]. Além disso, o NAP é uma das regiões da Antártica mais influenciadas pela Corrente Circumpolar Antártica (ACC), que transporta a Água Profunda Circumpolar (CDW).

A CDW é uma massa de água relativamente antiga, proveniente da Água Profunda do Atlântico Norte [e.g., Ferreira & Kerr 2017], por isso ela é pobre em oxigênio dissolvido e rica em carbono e macronutrientes remineralizados [Prézelin *et al*. 2000, 2004; Dinniman *et al*. 2012; Hauri *et al*. 2015]. Como o NAP é muito exposto à influência da ACC, ele é constantemente influenciado por intrusões de CDW [García *et al*. 2002; Barlett *et al*. 2018; Wang *et al*. 2022], alterando a dinâmica biogeoquímica nesta região [Meredith *et al*. 2017; Henley *et al*. 2019; Orselli *et al*. 2020; Santos-Andrade *et al*. 2023]. A CDW é uma massa de água relativamente quente (> 1°C), que intrude nas camadas intermediárias ao longo do NAP [Prézelin *et al*. 2000; Couto *et al*. 2017; Venables *et al*. 2017]. As propriedades físicas da CDW mudam à medida que ela se mistura com águas mais frias e menos salinas, formando a CDW modificada (mCDW) na plataforma e no domínio costeiro [Couto *et al*. 2017; Venables *et al*. 2017].

A região costeira do NAP abrange os estreitos de Gerlache e de Bransfield e a plataforma continental do noroeste do mar de Weddell (Fig. I-2). Ao sul do NAP, o estreito de Gerlache (Fig. I-2b) é uma região relativamente rasa (profundidade ~1000 m), com altas concentrações de gelo marinho [Parra *et al*. 2020; Su *et al*. 2022] e fortemente impactada por água de delego das geleiras continentais [Cook *et al*. 2016; Silva *et al*. 2020; Meredith *et al*. 2022]. Apesar de cobrir uma área pequena, o estreito de Gerlache absorve mais CO_2 no verão do que regiões com áreas mais extensas, como o estreito de Bransfield [Monteiro *et al*. 2020a). Essa forte absorção de CO_2 é impulsionada principalmente pela

alta produtividade primária [Monteiro *et al*. 2020a; Costa *et al*. 2020], que sustenta uma teia trófica diversificada e produtiva [Dalla Rosa *et al*. 2008; Nowacek *et al*. 2011; Mendes *et al*. 2018]. De fato, intensas florações de diatomáceas [Costa *et al*. 2020] e alta densidade de krill [Nowacek *et al*. 2011], pinguins [Pitman & Durban 2010] e de baleias [Secchi *et al*. 2011] são registradas no estreito de Gerlache.

Ao norte, o estreito de Bransfield é uma região com circulação oceânica ciclônica, rápida e dinâmica [Zhou *et al*. 2006; Dotto *et al*. 2016; Sangrà *et al*. 2017; van Caspel *et al*. 2018] e compreende as bacias oeste, central e leste, separadas por soleiras relativamente rasas (Fig. I-2b). A bacia oeste é a mais rasa (~1000 m), seguida pelas bacias central (~2000 m) e leste (~2200 m). A circulação superficial no NAP (Fig. I-2a) é caracterizada por águas locais e mCDW, provenientes principalmente do mar de Bellingshausen [Zhou *et al*. 2002, 2006; Sangrà *et al*. 2017]. Essas águas superficiais são advectadas do estreito de Gerlache para a bacia leste do estreito de Bransfield por um jato baroclínico de mesoescala relativamente intenso, conhecido como Corrente de Bransfield [Zhou *et al*. 2002, 2006; Savidge & Amft 2009]. Essa corrente flui na direção sudoeste-nordeste ao longo da quebra da plataforma das ilhas Shetland do Sul [Sangrà *et al*. 2017]. A temperatura das águas oriundas da Corrente de Bransfield é relativamente alta (~1,25 ºC) e altamente produtivas [Mendes *et al*. 2018; Costa *et al*. 2020, 2021], podendo transportar biomassa fitoplanctônica e organismos zooplanctônicos ao longo do NAP [Ferreira *et al*. 2020].

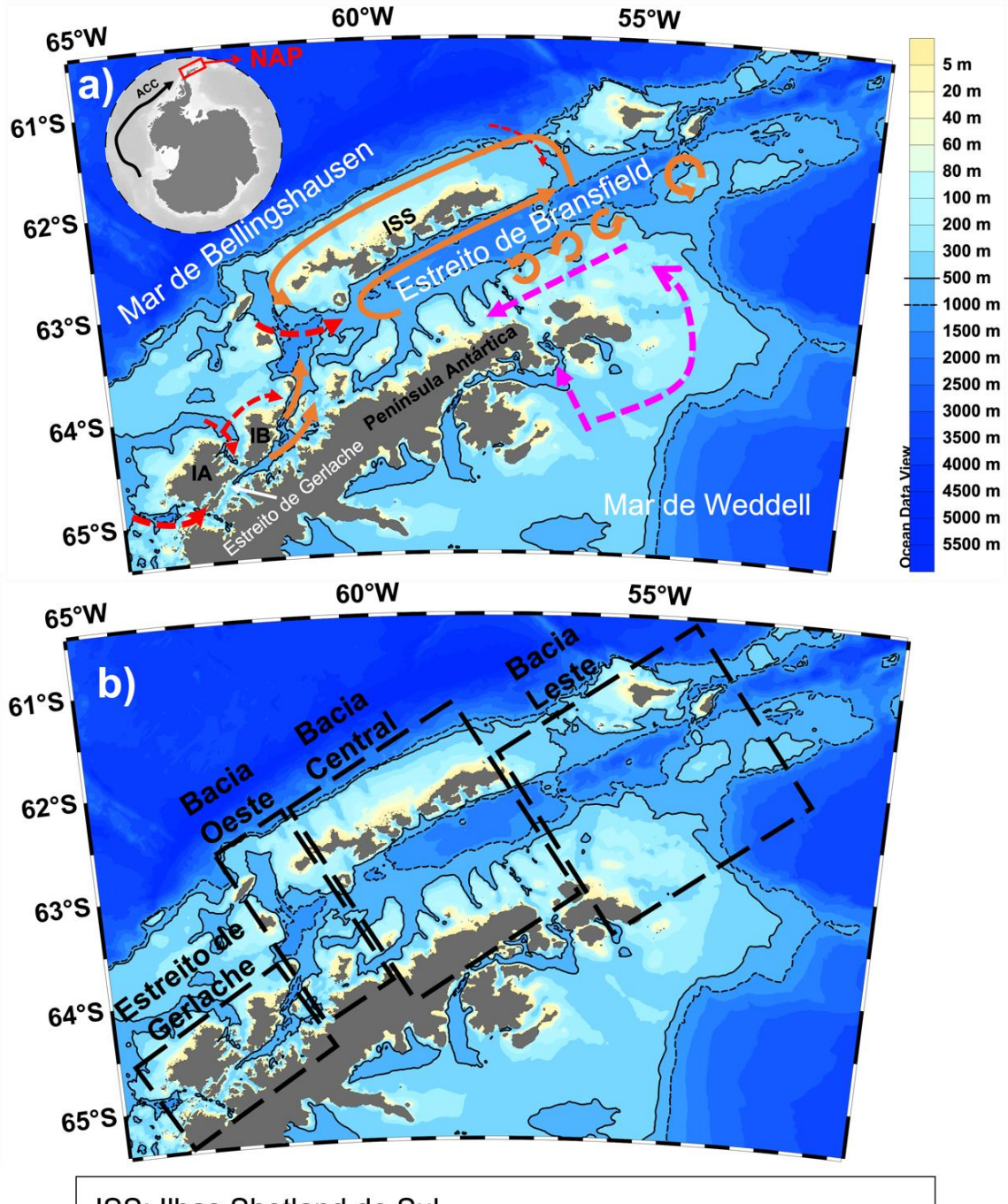

Figura I-2: Região norte da Península Antártica (NAP) e o (a) padrão de circulação oceânica na área de estudo. A circulação superficial, as regiões de estruturas de mesoescala, bem como os locais de intrusões da Água Profunda Circumpolar (CDW) e de advecção de Água Densa de Plataforma (DSW) foram baseadas em estudos anteriores [i.e., Wang *et al*. 2022; Dotto *et al*. 2016; Moffat & Meredith, 2018; Niiler *et al*. 1991; Sangrà *et al*. 2011, 2017; Savidge & Amft, 2009; Thompson *et al*. 2009; Zhou *et al*. 2002, 2006]. Subregiões que compõem o NAP, incluindo (b) o estreito de Gerlache e as bacias oeste, central e leste (do estreito de Bransfield.

A bacia oeste do estreito de Bransfield é fortemente influenciada por intrusões de mCDW em níveis intermediários [Barlett *et al*. 2018; Wang *et al*. 2022], enquanto a região profunda das bacias central e leste são preenchidas pela Água Densa de Plataforma (DSW) do mar de Weddell [Dotto *et al*. 2016; Damini *et al*. 2022; Wang *et al*. 2022]. A DSW refere-se às variedades da Água de Plataforma (i.e., Água de Plataforma de Alta Salinidade e Água de Plataforma de Baixa Salinidade) [Damini *et al*. 2022; Wang *et al*. 2022]. Essas águas são provenientes da plataforma continental do noroeste do mar de Weddell [van Caspel *et al*. 2018; Wang *et al*. 2022], na porção leste da Península Antártica (Fig. I-2). Ao contrário da mCDW, a DSW foi recentemente ventilada sob o domínio de plataforma, portanto é uma água rica em oxigênio dissolvido e com temperatura é relativamente baixa (< -1 ºC) [Dotto *et al*. 2016; Damini *et al*. 2022; Wang *et al*. 2022].

A DSW é advectada para o NAP e retida em sua forma mais pura principalmente na bacia central do estreito de Bransfield, onde há intensa mistura com a mCDW em níveis intermediários e superiores, alterando suas propriedades físicas [Dotto *et al*. 2016; Damini *et al*. 2022; Wang *et al*. 2022] e biogeoquímicas [Santos-Andrade *et al*. 2023]. Enquanto a mCDW é transportada em camadas intermediárias a partir do sul do NAP (i.e., do estreito de Gerlache e da bacia oeste do estreito de Bransfield), a DSW é advectada em camadas mais profundas a partir do norte do NAP (i.e., da bacia leste do estreito de Bransfield) [Moffat & Meredith 2018; Wang *et al*. 2022].

A variabilidade interanual das intrusões de mCDW e da advecção de DSW ao longo do NAP é modulada por modos de variabilidade climática, como o Modo Anular Sul (SAM) e o El Niño-Oscilação Sul (ENSO) [Barlett *et al*. 2018;

Damini *et al*. 2022; Wang *et al*. 2022]. Durante SAM positivo e/ou ENSO negativo, a intrusão de mCDW é intensificada, enfraquecendo a propagação de DSW ao longo do NAP. Por outro lado, durante SAM negativo e/ou ENSO positivo, a advecção de DSW é intensificada, podendo alcançar o estreito de Gerlache [Wang *et al*. 2022]. De fato, a DSW no estreito de Gerlache já foi identificada por meio de sinais termohalinos [Parra *et al*. 2020; Wang *et al*. 2022] e de concentrações de carbono antropogênico [Kerr *et al*. 2018b; Lencina-Avila *et al*. 2018].

Além disso, os ambientes ao longo do NAP são influenciados por processos oceanográficos de mesoescala que adicionam complexidade ao entendimento da biogeoquímica nesta região. O efeito da topografia rasa facilita a ressurgência de mCDW no estreito de Gerlache e na bacia oeste do estreito de Bransfield [Venables *et al*. 2017; Parra *et al*. 2020], mas pouco se sabe sobre sua influência nas concentrações de macronutrientes, que sustenta a produção primária, intensificando a absorção de CO_2 [Henley *et al*. 2019]. O efeito da topografia e da circulação oceânica também leva à formação de vórtices de mesoescala na bacia leste do estreito de Bransfield [Thompson & Heywood 2009; Wang *et al*. 2022; Damini *et al*. 2023], embora esses processos sejam frequentemente negligenciados em estudos biogeoquímicos devido à sua complexidade [Jones *et al*. 2015; Damini *et al*. 2023].

1. 3 Características oceanográficas do WTA

A dinâmica superficial no WTA é caracterizada por um sistema complexo de correntes oceânicas (Fig. I-3). A Corrente Norte Equatorial (NEC) flui para oeste no hemisfério norte, transportando águas relativamente frias do oceano

Atlântico Norte para o Atlântico Tropical oeste (Fig. I-3c) [Johns *et al*. 2021]. Por outro lado, a Corrente Norte do Brasil (NBC) flui para noroeste ao longo da costa brasileira [Rodrigues *et al*. 2007; Silva *et al*. 2009; Stramma *et al*. 1995], transportando águas com maiores temperatura e salinidade (Figs. I-3b,c) do Atlântico Equatorial para o hemisfério norte [Johns *et al*. 1998, 2021; Salisbury *et al*. 2011]. As águas da NBC atingem a foz do rio Amazonas em aproximadamente 5°N, onde ocorre intensa mistura entre as águas oceânicas e fluviais. Ao norte da foz do rio Amazonas, a NBC retroflete sazonalmente (Fig. I-3a), transportando águas tanto da NBC quanto da ARP para leste no oceano Atlântico Tropical, formando a Contracorrente Norte Equatorial (NECC) [Fonseca *et al*. 2004; Garzoli *et al*. 2004].

As águas da NECC atingem a porção mais a leste do WTA em setembro-outubro [Araujo *et al*. 2017; Lefèvre *et al*. 2020], quando sua velocidade é máxima [Richardson & Reverdin 1987], enquanto não há sinais claros da formação da NECC nos primeiros meses do ano [Johns *et al*. 2021]. Além disso, a retroflexão da NBC pode levar à formação de vórtices anticiclônicos (Fig. I-3a), que transportam águas com propriedades da NBC para o noroeste do oceano Atlântico Tropical [e.g., Aroucha *et al*. 2020; Didden & Schott 1993]. Essas águas advectadas por vórtices também carregam propriedades oriundas do oceano Atlântico Sul, que é influenciado por fontes do oceano Índico [Azar *et al*. 2021; Orselli *et al*. 2019a; Orselli *et al*. 2019b], destacando importantes transportes interoceânicos e inter-hemisféricos.

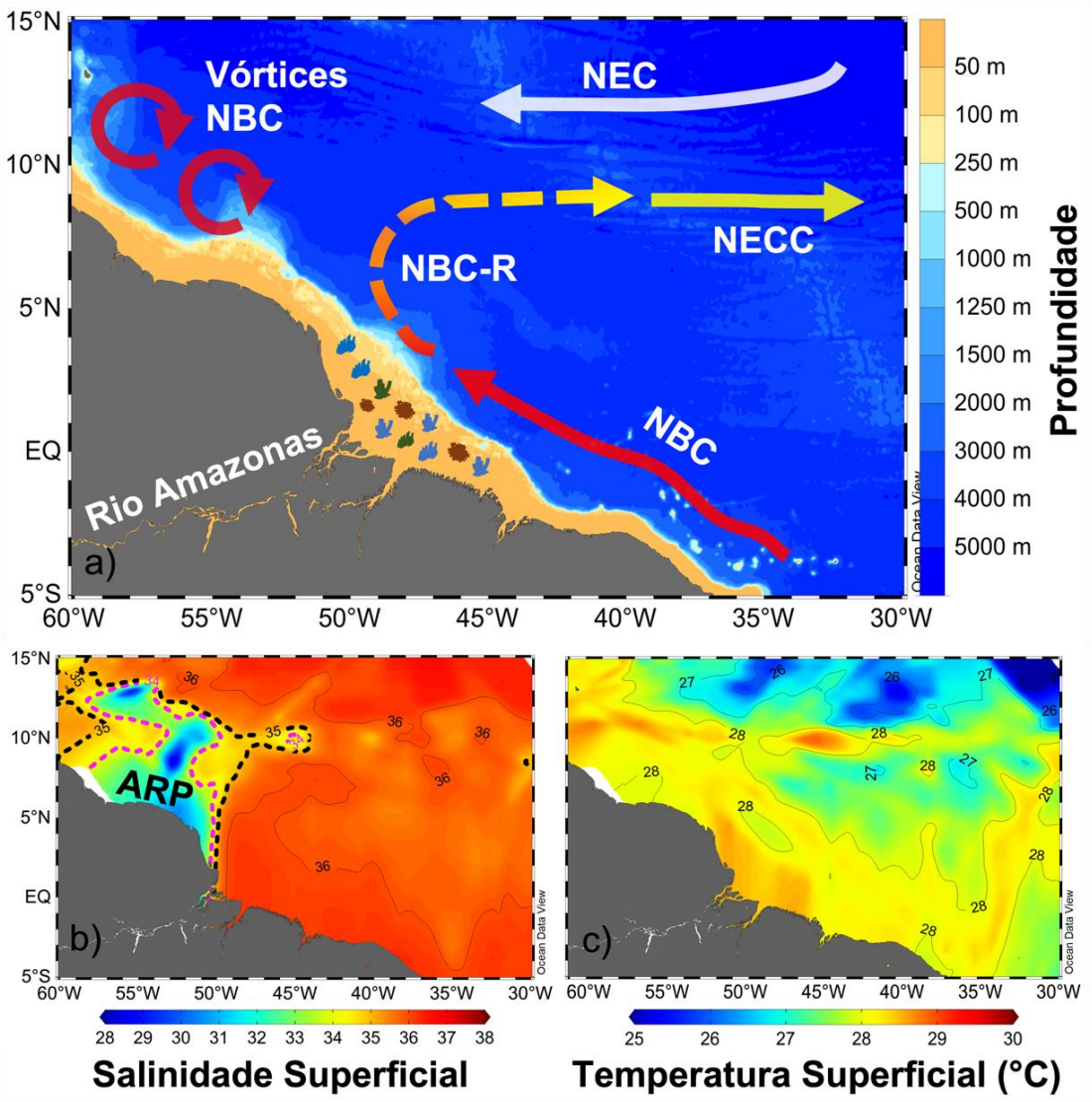

Figure I-3: a) Oceano Atlântico Tropical oeste e as principais correntes superficiais, que caracterizam a dinâmica oceânica nesta região (ver Johns *et al*. [2021] e referências nele contidas): Corrente Norte Equatorial (NEC), Corrente Norte do Brasil (NBC) e Contracorrente Norte Equatorial (NECC), que se origina da retroflexão da NBC (NBC-R), originando também os vórtices da NBC. Os símbolos sobre a foz do rio Amazonas (a) representam o extenso sistema de recifes de corais nesta região. (b) Climatologia anual da salinidade superficial para o período 1993-2019, com isolinhas de salinidade 35 (linha preta tracejada) e 34 (linha rosa tracejada), representando a pluma do rio Amazonas (ARP). (c) Climatologia anual da temperatura superficial para o mesmo período na região.

Além de seu complexo sistema de correntes oceânicas superficiais, o WTA é fortemente influenciado pelo aporte de água doce do rio Amazonas (Fig. V-S1a), que descarrega cerca de 6,6 x 10^3 km^3 de água fluvial para o Atlântico Tropical anualmente [Korosov *et al*. 2015; Salisbury *et al*. 2011]. À medida em que deságua no oceano, o rio Amazonas desenvolve a ARP, que pode se estender por 10^6 km^2 e atingir profundidades de até 30-35 m, cobrindo uma vasta

porção do WTA e atingindo até 30°W e 15°N [Coles *et al*. 2013]. A descarga máxima na foz do rio Amazonas ocorre em março [Liang *et al*. 2020] e há um atraso de cerca de 3 meses até que essas águas se espalhem pelo WTA [e.g., Coles *et al*. 2013; Hellweger & Gordon 2002; Korosov *et al*. 2015].

Embora as águas fluviais reduzam a zona eufótica nesta região, devido às altas concentrações de sedimentos em suspensão, existe um extenso sistema de recifes de corais em torno de 0° e 49°W (Fig. I-3a), que quase se limita à foz do rio Amazonas [Moura *et al*. 2016]. As propriedades das águas da ARP influenciam a solubilidade do CO_2 [Cooley *et al*. 2007] e aumentam a produção primária, proporcionando a subsaturação do CO_2 na superfície do mar [Ibánhez *et al*. 2015; Körtzinger, 2003; Louchard *et al*. 2021]. Assim, as águas da ARP atuam como um sumidouro de CO_2 atmosférico de relevância global [Cooley *et al*. 2007; Ibánhez *et al*. 2015, 2016; Lefèvre *et al*. 2010].

A intensa precipitação (Fig. V-S1b) impulsionada pela posição da zona de convergência intertropical (ITCZ, do inglês *intertropical convergence zone*) também influencia a dinâmica oceânica no WTA. A ITCZ varia sazonalmente, atingindo sua posição mais ao norte (próximo a 10°N) de junho a agosto e mais ao sul (próximo a 4°S) de março a maio [Fonseca *et al*. 2004; Utida *et al*. 2019], contribuindo para a regulação sazonal da salinidade da superfície do mar. Além disso, essa região é influenciada pelo ENSO, que intensifica os períodos seco e chuvoso [Marengo & Espinoza 2016], e pelo aquecimento anômalo do oceano Atlântico [Tyaquiçã *et al*. 2017]. Esses eventos podem ocorrer simultaneamente, com uma variedade de respostas nas propriedades físicas e químicas da superfície do mar [Kucharski *et al*. 2016], adicionando ainda mais complexidade aos ciclos biogeoquímicos no WTA.

Capítulo II: Dados e Métodos

Neste trabalho foram utilizados dados hidrográficos e biogeoquímicos previamente coletados e parcialmente processados de diferentes bancos de dados, que serão detalhados ao logo deste capítulo. Os principais bancos de dados utilizados foram o Atlas para CO_2 na Superfície do Oceano (SOCAT, do inglês *Surface Ocean CO_2 Atlas*), o Projeto Global de Análise de Dados Oceânicos (GLODAP, do inglês *Global Ocean Data Analysis Project*) e o Grupo de Oceanografia de Altas Latitudes (GOAL). Uma série temporal de 1996 a 2019 foi construída para o estudo da variabilidade dos macronutrientes, cuja maior parte (~90%) foi proveniente do banco de dados do GOAL (Fig. II-1b) e complementada por dados do GLODAP. Séries temporais, com os dados do SOCAT, foram construídas para os estudos de FCO_2 no estreito de Gerlache, no NAP (2002-2017, Fig. II-1b), e no WTA (1993-2019, Fig. II-1a).

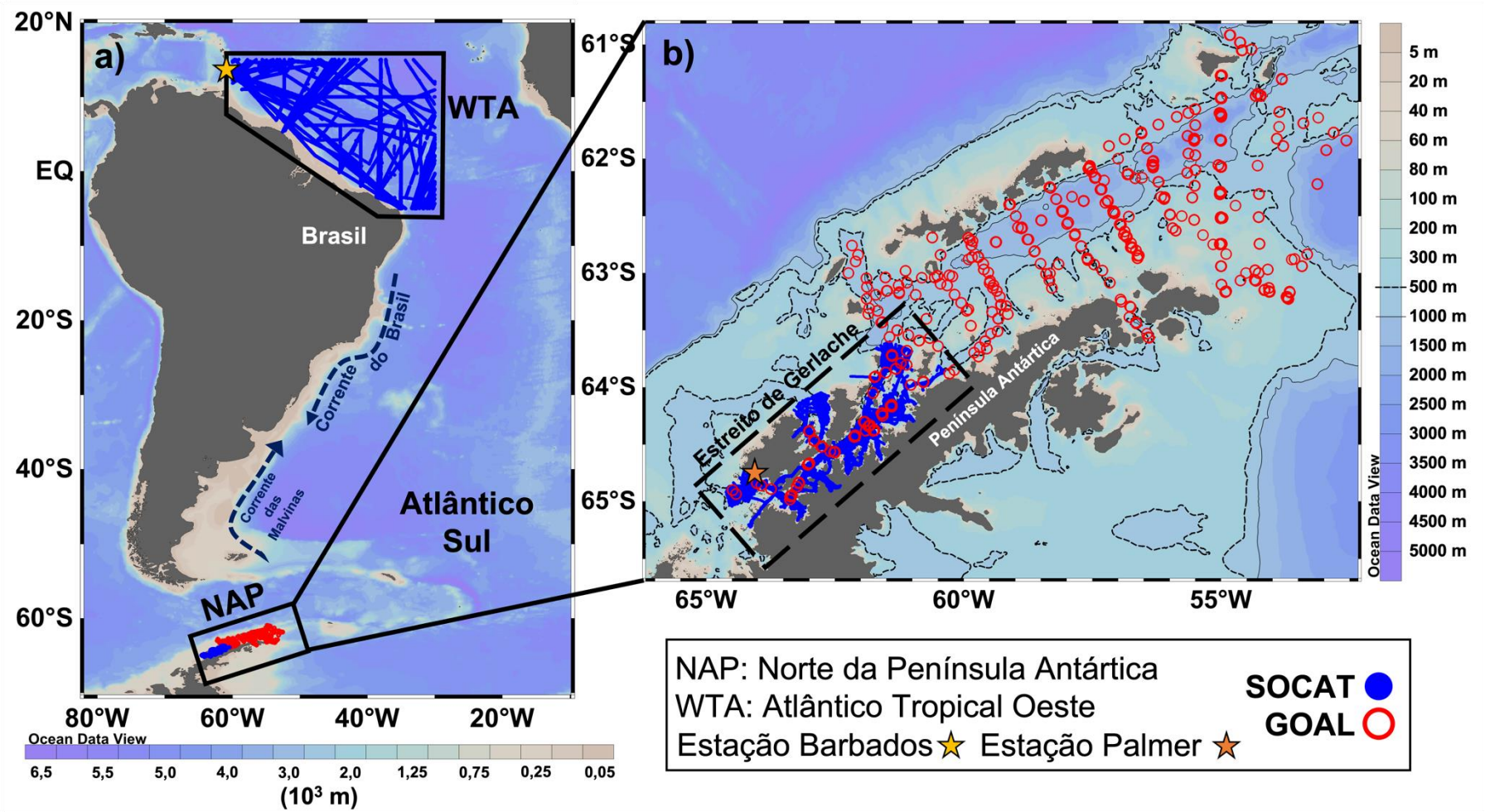

Figura II-1: Cobertura espacial dos dados do SOCAT e do GOAL no oceano Atlântico Tropical oeste (WTA) e ao longo do norte da Península Antártica (NAP). Os dados sobre o WTA são compostos por uma série temporal de 1993 a 2019, incluindo os períodos seco (outubro-março) e chuvoso (abril-setembro) da região. Os dados do SOCAT no estreito de Gerlache são compostos por uma série temporal de 2002 a 2017, incluindo o verão (janeiro a março), o outono (abril a junho), o inverno (julho a setembro) e a primavera austral, enquanto os dados do GOAL ao longo do NAP são compostos por uma série temporal de 1996 a 2019 durante o verão austral. As estrelas em amarelo (a) e laranja (b) indicam a localização das estações atmosféricas de Barbados e de Palmer, respectivamente.

2. 1 Banco de dados

2. 1. 1 *Surface Ocean CO_2 Atlas (SOCAT)*

Os dados superficiais (até 5 m de profundidade) de temperatura (SST), salinidade (SSS) e pCO_2^{mar} foram obtidos do banco de dados SOCAT. O SOCAT é um compilado de dados da fugacidade do CO_2 na superfície do mar para o oceano global e mares costeiros, com um rigoroso controle de qualidade e atualizações regulares [Bakker *et al*. 2016]. Foram usados dados de fugacidade do CO_2 com incertezas < 2 µatm e < 5 µatm. A fugacidade do CO_2 extraída do SOCAT é medida diretamente através de um sistema de equilíbrio entre o oceano e a atmosfera e analisadores de infravermelho para a quantificação do CO_2 [Bakker *et al*. 2016]. Os dados de fugacidade do CO_2 foram convertidos para pCO_2^{mar} por meio das equações amplamente conhecidas de Weiss [1974].

2. 1. 2 *Global Ocean Data Analysis Project (GLODAP)*

Além disso, foram utilizados dados superficiais de alcalinidade total (A_T ou TA) e carbono inorgânico dissolvido (C_T ou DIC) do GLODAP para a validação das estimativas de A_T no WTA e no estreito de Gerlache. O GLODAP inclui medições de perfis verticais de diferentes variáveis hidrográficas e biogeoquímicas, com ênfase no carbono inorgânico da água do mar [Olsen *et al*. 2020]. Assim como o SOCAT, o GLODAP tem um rigoroso controle de qualidade dos dados e disponibiliza apenas dados considerados de boa qualidade, de acordo com seus critérios de qualidade, incluindo especialmente avaliações sistemáticas de viés. Foram utilizados os dados de SST, SSS e A_T com precisões de ± 0,002 °C, ± 0,003 e ± 4,0 µmol kg^{-1}, respectivamente. Além disso, foram utilizados dados hidrográficos e de macronutrientes do GLODAP para

complementar a série temporal desses parâmetros o longo da coluna de água no NAP. Detalhes sobre a amostragem e análise dos dados de macronutrientes obtidos do GLODAP podem ser acessados na plataforma do *Ocean Carbon and Acidification Data System* (OCADS) em www.ncei.noaa.gov/access/ocean-carbon-acidification-data-system-portal/.

2. 1. 3 *Grupo de Oceanografia de Altas Latitudes (GOAL)*

Os dados de A_T no estreito de Gerlache disponíveis no GLODAP eram restritos apenas ao verão austral de 1995/1996. Por isso também foram utilizados dados de SST, SSS e A_T do GOAL, coletados entre 2015 e 2019 para a validação das estimativas de A_T nesta região. O GOAL mede dados hidrográficos (temperatura, salinidade e oxigênio dissolvido) e coleta amostras de água do mar para análise biogeoquímica (macronutrientes, A_T e C_T). Para isso, é utilizado um sistema CTD/Rosette, equipado com sensores e 24 garrafas Niskin de 5 e/ou 12 L. Os sensores são duplicados e a diferença entre eles é usada para avaliar a precisão da temperatura e da salinidade, que são em torno de ± 0,002°C e ± 0,003, respectivamente. O sensor de oxigênio é pós-calibrado com base em medições de oxigênio dissolvido realizadas a bordo através da titulação pelo método de Winkler.

2. 1. 3. 1 *Medições de A_T e C_T*

As amostras de água do mar para análise de A_T e C_T foram coletadas em frascos de borosilicato de 250 mL ou 500 mL. Elas foram imediatamente preservadas com 50 µL ou 100 µL de cloreto de mercúrio ($HgCl_2$) supersaturado e armazenadas a 4°C para posterior análise em laboratório, seguindo os

protocolos descritos em por Dickson *et al*. [2007]. No laboratório, a A_T e o C_T foram medidos simultaneamente por titulação potenciométrica em uma cela fechada a uma temperatura controlada de 25 ± 0,1 °C [Dickson *et al*. 2007]. O controle de qualidade foi realizado regularmente através da análise de material de referência certificado (CRM, do inglês *Certified Reference Material*) adquirido do *Scripps Institution of Oceanography* [Dickson *et al*. 2003]. A precisão analítica das medições de A_T e C_T foi estimada diariamente a partir da análise duplicada de uma mesma amostra ao longo das análises das amostras e variou em torno de ± 4 µmol kg^{-1} e de ± 5 µmol kg^{-1}, respectivamente.

2. 1. 3. 2 *Medições de macronutrientes*

As amostras discretas de água do mar ao longo da coluna de água para medições de macronutrientes inorgânicos dissolvidos foram coletadas em frascos de polipropileno e filtradas através de filtros de membrana de acetato de celulose (0,45 µm). Os macronutrientes inorgânicos dissolvidos analisados foram: nitrogênio inorgânico dissolvido (DIN: nitrato, nitrito e amônio), fosfato e ácido silícico (silicato). As análises foram realizadas a bordo, imediatamente após a coleta, entre 2008-2011 e 2013-2015. Nos demais anos de amostragem (2003-2005 e 2016-2019) as amostras foram congeladas imediatamente a -20 °C até a análise em laboratório. Em ambos os casos, as análises seguiram os métodos de determinação espectrofotométrica descritos por Aminot & Chaussepied [1983] com uma precisão em torno de ± 5% para todos os macronutrientes analisados. O ortofosfato foi medido por reação com molibdato de amônio, com leituras de absorção em 885 nm. As medições de ácido silícico, na forma de Si reativo, foram corrigidas para a interferência do sal marinho. Os

máximos limites de detecção foram 0,11 µmol kg^{-1} para DIN, 0,10 µmol kg^{-1} para fosfato e 0,50 µmol kg^{-1} para ácido silícico.

2. 2 Estimativas de A_T nas regiões de estudo

Uma vez que o SOCAT dispõe apenas de dados de SST, SSS e pCO_2^{mar}, a A_T foi estimada a partir da SSS no estreito de Gerlache e da combinação da SSS com a SST no WTA. A forte relação entre a A_T e a salinidade é bem estabelecida, especialmente em ambientes com variações significativas de SSS [Lee *et al*. 2006; Carter *et al*. 2018], como as regiões de estudo. A alta variabilidade de SSS é causada pelo aporte de água doce, que no estreito de Gerlache é resultado do degelo continental e de gelo marinho no verão, enquanto no WTA é resultado do aporte de água doce pelo rio Amazonas.

Alguns testes com estimativas de A_T globais [Lee *et al*. 2006; Carter *et al*. 2018] e regionais [Hauri *et al*. 2015; Monteiro *et al*. 2020] foram feitos para o estreito de Gerlache. A estimativa que apresentou menor erro quadrático médio (RMSE, do inglês *root mean square error*) foi uma correlação polinomial de primeira ordem entre a A_T e a SSS com base nos dados locais. Assim, os dados de A_T e de SSS do GOAL e do GLODAP foram utilizados para estimar A_T a partir da SSS através da Eq. II-1 (r^2 = 0,98; RMSE = 4,4; n = 140; $p < 0,05$).

$$A_T = 36,72 \times SSS + 1052 \qquad \text{II-1}$$

A Equação II-1 foi desenvolvida usando a caixa de ferramentas de ajuste de curvas do MATLAB, com o modo residual mínimo absoluto e ajuste polinomial de primeira ordem. Para esta análise, todos os dados foram considerados importantes, o que minimizou os resíduos. Esta abordagem geralmente é

utilizada quando as séries de dados têm poucos valores não configuráveis [Patil & Rao 1994].

No WTA a A_T foi estimada com base na abordagem de regressão de alcalinidade interpolada localmente (LIAR, do inglês *locally interpolated alkalinity regression*) de Carter *et al*. [2018], usando a SSS e a SST como variáveis de entrada. A LIAR é um conjunto de regressões lineares capazes de estimar a A_T a partir de diferentes conjuntos de parâmetros de entrada, considerando a profundidade e as coordenadas das medições. Espera-se que a incerteza global nas estimativas de A_T usando SSS e SST como variáveis de entrada seja de 4,4 µmol kg^{-1} [Carter *et al*. 2018]. Os resultados obtidos a partir da LIAR foram comparados com os dados de A_T *in situ* do GLODAP e o RMSE foi de 6,5 µmol kg^{-1} (r^2 = 0,99; n = 453; p < 0,0001).

2. 3 Estimativas dos demais parâmetros do sistema carbonato

Apenas dois parâmetros do sistema carbonato são necessários para estimar todos os outros através das equações de equilíbrio do sistema carbonato marinho [Millero, 2007]. Então, o C_T, o pH e o estado de saturação da calcita (Ω_{Ca}) e da aragonita (Ω_{Ar}) foram determinados usando o programa CO2Sys v2.1 [Pierrot & Wallace 2006], com base nas entradas de pressão, SST, SSS, pCO_2^{mar} e A_T. O programa calcula os parâmetros do sistema carbonato pela relação termodinâmica de equilíbrio entre as espécies carbonáticas, utilizando as constantes de dissociação do carbonato. Existem diferentes constantes de dissociação que são mais ou menos adequadas para diferentes regiões, dependendo principalmente das variações de temperatura e de salinidade.

As constantes de sulfato por Dickson [1990] e de borato por Uppström [1974] foram utilizadas em ambas as regiões. Devido a um bom resultado em regiões de altas latitudes [e.g. Wanninkhof *et al*. 1999; Laika *et al*. 2009; Kerr *et al*. 2017; Monteiro *et al*. 2020a], as constantes K1 e K2 propostas por Goyet & Poisson [1989] foram utilizadas para o estreito de Gerlache. Como não há um consenso sobre quais são as melhores constantes K1 e K2 para o WTA, foi feito um teste de sensibilidade entre as principais constantes usadas em estudos anteriores. Foram analisadas as constantes K1 e K2 de Millero *et al*. [2006], Millero [2010], Lueker *et al*. [2000] e Mehrbach *et al*. [1973] reajustado por Dickson & Millero [1987], geralmente recomendado para as faixas de SSS e SST da região, e as de Cai & Wang [1998] para baixas salinidades.

A maior inconsistência para o C_T entre as constantes testadas foi de 4,64 µmol kg^{-1} entre Millero *et al*. [2006] e Cai & Wang [1998], enquanto a menor inconsistência foi de -0,13 µmol kg^{-1} entre Lueker *et al*. [2000] e Mehrbach *et al*. [1973] reformado por Dickson & Millero [1987]. Ambas as inconsistências são menores que o erro de ± 6,5 µmol kg^{-1} associado à estimativa de A_T pela aproximação da LIAR. Por isso, optou-se por usar as constantes K1 e K2 de Millero *et al*. [2006], porque elas têm sido amplamente utilizadas em estudos costeiros no WTA [Araujo *et al*. 2018; Bonou *et al*. 2016] e no oceano Atlântico Sul [Liutti *et al*. 2021].

2. 4 Cálculo do FCO_2

O FCO_2 (em mmol m^{-2} dia^{-1}) foi calculado por meio da Eq. II-2:

$$FCO_2 = K_t \times K_s \times (1 - gelo) \times \left(pCO_2^{mar} - pCO_2^{ar}\right), \qquad \text{II-2}$$

onde K_t é a velocidade de transferência do gás, em função da velocidade do vento (m s^{-1}) [Wanninkhof, 2014]; K_s é o coeficiente de solubilidade do CO_2, em função da SST e da SSS [Weiss, 1974]; gelo é um coeficiente adimensional (entre 0 e 1) correspondente à fração da interface ar-mar coberta por gelo marinho; e pCO_2^{mar} e pCO_2^{ar} são as pressões parciais do CO_2 na superfície do mar e na atmosfera, respectivamente.

A pCO_2^{ar} foi calculada a partir das médias mensais da fração molar de CO_2 na atmosfera (xCO_2^{ar}) e da pressão atmosférica (P^{ar}) através da Eq. II-3. A P^{ar} foi corrigida para a o efeito da pressão de vapor de água (P_{H_2O}), estimada em função da SST e da SSS através da Eq. II-4 de Weiss & Price [1980]:

$$pCO_2^{ar} = xCO_2^{ar} \times \left[\left(P^{ar} - \frac{1,5}{101,325}\right) - P_{H_2O}\right] \qquad \text{II-3}$$

$$P_{H_2O} = e^{\left[24,4543 - \left(\frac{6745,09}{SST + 273,15}\right) - 4,8489 \times \ln\left(\frac{SST + 273,15}{100}\right) - 0,000544 \times SSS\right]} \qquad \text{II-4}$$

Para o estreito de Gerlache, foram utilizadas médias mensais de xCO_2^{ar}, P^{ar} e velocidade do vento da estação de Palmer, localizada ao sul do estreito (Fig. II-1b) e que mede continuamente essas variáveis ao longo do ano [Dlugokencky *et al*. 2015]. A cobertura de gelo marinho foi obtida a partir da média mensal dos produtos de satélite diários de Reynolds *et al*. [2007], com resolução espacial de 0,25°, cobrindo toda a extensão do estreito de Gerlache (Fig. IV-S9e-h).

Para o WTA, foram utilizadas médias mensais de xCO_2^{ar} da estação de Barbados (Fig. II-1a), localizada a 13,16°N - 59,43°W [Dlugokencky *et al*. 2021] e a P^{ar} foi obtida do SOCAT. A velocidade do vento utilizada para esta região foram as médias mensais a 10 m da reanálise atmosférica ERA5 (Fig. V-S1d)

com uma resolução espacial de 0,25° [Hersbach*et al*. 2020]. Para isso, as coordenadas e o mês de amostragem da pCO_2^{mar} do SOCAT foram combinadas com os dados da análise ERA5 para garantir que a velocidade do vento cobrisse a mesma região e o mesmo período.

2. 5 Cálculo dos controladores da pCO_2^{mar}

Os controladores da pCO_2^{mar} foram calculados com base na decomposição da pCO_2^{mar} nos principais parâmetros que a influenciam. Este método consiste em converter as alterações nos parâmetros analisados em unidades de pCO_2^{mar} (i.e., µatm). Isso é possível porque a proporção da alteração na pCO_2^{mar} em função das mudanças em determinados parâmetros já é bem conhecida. Por exemplo, a pCO_2^{mar} tem uma dependência logarítmica com a SST, de modo que um aquecimento de 1°C aumenta a pCO_2^{mar} em aproximadamente 13 µatm [Sarmiento & Gruber, 2006]. Dessa forma, as alterações na pCO_2^{mar} foram decompostas nas alterações de C_T, A_T, SST e SSS a partir da decomposição descrita na Eq. II-5, seguindo Lenton *et al*. [2012].

$$\Delta pCO_2^{mar} = \frac{\partial pCO_2^{mar}}{\partial C_T}\Delta C_T + \frac{\partial pCO_2^{mar}}{\partial A_T}\Delta A_T + \frac{\partial pCO_2^{mar}}{\partial SST}\Delta SST + \frac{\partial pCO_2^{mar}}{\partial SSS}\Delta SSS \qquad \text{II-5}$$

A decomposição expressa na Eq. II-5 significa que uma determinada alteração de pCO_2^{mar} (ΔpCO_2^{mar}) ocorreu em função da combinação das alterações nos Δparâmetros (ΔC_T, ΔA_T, ΔSST, ΔSSS). No estreito de Gerlache, a ΔpCO_2^{mar} e as Δparâmetros foram consideradas como as diferenças nos valores dos parâmetros entre a estação do ano e suas respectivas médias nas estações anteriores. No WTA, a ΔpCO_2^{mar} e as Δparâmetros foram consideradas

como a diferença dos valores médios entre o período chuvoso (abril a setembro) e seco (outubro a março).

As derivadas parciais foram calculadas usando as Eqs. II-6 a II-9, que são detalhadas em Sarmiento & Gruber [2006]. Essas equações têm sido amplamente utilizadas em diferentes regiões oceânicas para avaliar os controlares da pCO_2^{mar} [Lenton *et al*. 2012; Takahashi *et al*. 2014; Brown *et al*. 2019; Monteiro *et al*. 2020; Liutti *et al*. 2021]. Os fatores de Revelle e de Alcalinidade são definidos como a sensibilidade da pCO_2^{mar} às mudanças em C_T e A_T, respectivamente [Sarmiento & Gruber 2006]. Os valores médios dos fatores de Revelle e de Alcalinidade utilizados foram, respectivamente, 14 e –13 no estreito de Gerlache e 9,1 e –8,5 no WTA.

$$\frac{\partial pCO_2^{mar}}{\partial C_T} = \frac{pCO_2^{mar}}{C_T} \times \text{Fator de Revelle} \qquad \text{II-6}$$

$$\frac{\partial pCO_2^{mar}}{\partial A_T} = \frac{pCO_2^{mar}}{A_T} \times \text{Fator de Alcalinidade} \qquad \text{II-7}$$

$$\frac{\partial pCO_2^{mar}}{\partial SSS} \approx pCO_2^{mar} \times 0{,}026\ (\pm\ 0{,}002) \qquad \text{II-8}$$

$$\frac{\partial pCO_2^{mar}}{\partial SST} \Delta SST \approx 2 \times pCO_2^{mar} \times \left(e^{0{,}0423 \times \frac{\Delta SST}{2}} - 1 \right) \qquad \text{II-9}$$

Para avaliar o efeito da SST na série temporal de pCO_2^{mar} no WTA, a sua componente térmica foi removida através da normalização da pCO_2^{mar} pela SST média anual, por meio da Eq. II-10, seguindo a abordagem de Takahashi *et al*. [2002]:

$$pCO_{2\ \text{não-termal}}^{mar} = pCO_{2\ \text{obs}}^{mar} \times e^{0{,}0423 \times (SST_{\text{média}} - SST_{\text{obs}})}, \qquad \text{II-10}$$

onde $pCO_{2\ obs}^{mar}$ e SST_{obs} são a pCO_2^{mar} e a SST *in situ*, respectivamente, e $SST_{média}$ é a SST média para todo o período de estudo em cada sub-região (i.e., NBC-NECC: 27,65°C, NEC: 26,89°C, ARP: 28,29 ºC).

A dispersão de A_T e C_T e a razão entre esses parâmetros pode ser usada para identificar os processos físicos e biogeoquímicos que os influenciam, porque cada processo altera A_T e C_T a uma certa razão [Zeebe & Wolf-Gladrow 2001]. As razões A_T:C_T para os processos identificados são as seguintes: 2:1 para calcificação/dissolução, 6:5 para diluição/evaporação, 0,85:1 para formação/derretimento de gelo marinho, –0,14:1 para fotossíntese/respiração, enquanto apenas C_T é alterado nos processos de liberação/absorção de CO_2.

2. 6 Perfis médios de propriedades hidrográficas e macronutrientes na NAP

Cerca de 97% dos dados de DIN foram compostos por nitrato, seguido por 2% de amônio e 1% de nitrito. As concentrações médias de nitrito foram de 0.21 ± 0.24 µmol kg^{-1} e de amônio foram de 0.54 ± 0.59 µmol kg^{-1}. Portanto, em alguns casos (11% de todos os dados), a concentração de nitrato foi considerada como DIN, quando não havia dados de nitrito e/ou amônio disponíveis. As amostras discretas de água do mar foram coletadas em intervalos irregulares de profundidade desde a superfície (5 m) até o fundo (aproximadamente 15 m do fundo).

Então, foram calculadas médias dos parâmetros para cada região ao longo do NAP em intervalos regulares de profundidade da superfície até o fundo (i.e., 0, 25, 50, 75, 100, 250, 500, 750, 1000, 1250, 1500, 1750, 2000 m) para obter um perfil médio de verão para cada ano (Figs. III-S1 a III-S4). Todos os

dados hidrográficos e de macronutrientes estão disponíveis livremente em https://doi.org/10.5281/zenodo.7384423 [Monteiro *et al*., 2022].

2. 7 Redução sazonal dos macronutrientes no NAP

A redução sazonal dos macronutrientes (∆nutrientes) nos perfis médios para cada ano foi estimada como a diferença entre a concentração de macronutrientes integrada entre 50 e 100 m e a concentração integrada entre 0 e 50 m (Eq. II-11). Portanto, foi assumido que as concentrações dos macronutrientes entre 50 e 100 m no verão eram representativas das concentrações dos macronutrientes entre 0 e 50 m no inverno antecedente.

$$\Delta[\mathrm{nutrientes}]_{\text{inverno-verão}} = \int_{50\ \mathrm{m}}^{100\ \mathrm{m}} [\mathrm{nutrientes}]\mathrm{dz} - \int_{0\ \mathrm{m}}^{50\ \mathrm{m}} [\mathrm{nutrientes}]\mathrm{dz} \qquad \text{II-11}$$

Usando essa mesma abordagem, também foi estimada a redução sazonal dos macronutrientes nos perfis médios para cada ano nos dados da estação americana de Palmer [Ducklow *et al*. 2019], onde Kim *et al*. [2016] mediram a redução sazonal dos macronutrientes a partir de dados *in situ* coletados no inverno e no verão subsequente.

As estimativas de redução sazonal dos macronutrientes foram muito similares aos resultados obtidos por Kim *et al*. [2016] com medidas *in situ*, o que atesta a robustez do método adotado baseado apenas em dados de verão. Os autores mediram uma redução sazonal entre 1993 e 2013 de 415 ± 110 mmol m^{-2}, 23 ± 10 mmol m^{-2} e 985 ± 386 mmol m^{-2} para DIN, fosfato e ácido silícico, respectivamente. Para o mesmo período, foram estimadas reduções sazonais de 411 ± 191 mmol m^{-2}, 25 ± 9 mmol m^{-2} e 950 ± 269 mmol m^{-2} para DIN, fosfato e ácido silícico, respectivamente.

2. 8 Composição de perfis médios dos macronutrientes em relação aos modos de variabilidade climática

Para avaliar a influência dos modos de variabilidade climática SAM e ENSO nas concentrações dos macronutrientes, foram separados os perfis médios de verão entre anos de SAM ou ENSO positivo e negativo e calculada a diferença entre eles. O índice SAM foi obtido no site do *British Antarctic Survey* (http://www.nerc-bas.ac.uk/icd/gjma/sam.html), que se baseia nas diferenças das médias zonais mensais normalizadas da pressão ao nível do mar entre 40°S e 65°S [Marshall, 2003]. O índice ENSO foi obtido do repositório *Climate Prediction Center* (http://www.cpc.ncep.noaa.gov), sendo definido como a média consecutiva de três meses de anomalias da temperatura da superfície do mar do conjunto de dados ERSST.v4 na região Niño 3,4 (5°N – 5°S, 120°W – 170°W) [Vera & Osman 2018; La *et al*. 2019].

Embora o tempo de resposta das propriedades físicas e biogeoquímicas às variações de SAM e ENSO ao longo do NAP ainda não esteja bem compreendido, estima-se que ele varie de 4 a 6 meses para SAM e de 6 a 9 meses para ENSO [Kim *et al*. 2016; Dotto *et al*. 2016; Meredith *et al*. 2008; Barllet *et al*. 2018]. Assim, foi utilizado um atraso de 4 meses a partir do mês de amostragem para o índice SAM e de 6 meses para o índice ENSO.

A incerteza propagada no cálculo da diferença entre as médias foi calculada através da seguinte equação: $\sigma_z=\sqrt{(\sigma_{\bar{x}})^2 + (\sigma_{\bar{y}})^2}$, onde "$\sigma_{\bar{x}}$" e "$\sigma_{\bar{y}}$" são os erros padrão de cada média. Para avaliar a diferença estatística dos perfis médios entre SAM e ENSO positivos e negativos, foi feito teste t de *Student* para perfis com distribuição normal. Para perfis com distribuição não normal, foi

utilizado o teste não paramétrico de Mann-Whitney-Wilcoxon. Para testar se a distribuição era normal, foi utilizado o teste estatístico Shapiro-Wilk.

2. 9 Distribuições espaciais de propriedades

Todos os mapas de distribuição espacial das propriedades mostradas nos estudos foram interpolados para fornecer uma visualização de fácil compreensão dos resultados. Assim, as médias e todos os cálculos realizados nos estudos foram baseados apenas nos dados observados ou reconstruídos e não nos dados interpolados. Duas metodologias de interpolação foram utilizadas, dependendo da distribuição e da cobertura espacial dos dados. Uma delas foi a análise variacional de interpolação de dados (DIVA) [Troupin *et al*. 2012] e a outra foi uma grade de médias ponderadas [Schlitzer, 2018]. Em ambas as metodologias, foram utilizados valores de escala de comprimento entre 15 e 20 ‰ para os eixos X e Y para garantir uma melhor preservação da estrutura e da suavidade dos dados.

Capítulo III: Dinâmica dos macronutrientes no NAP

Neste estudo foi investigado quais processos controlam a variabilidade espacial e interanual dos macronutrientes na coluna de água durante o verão austral ao longo do NAP. Como o NAP é composta por sub-regiões com características distintas em relação à hidrografia e às massas de água, as análises foram focadas no estreito de Gerlache, e nas bacias oeste, central e leste do estreito de Bransfield. Assim, foi possível identificar como os diferentes processos físicos e biogeoquímicos atuam em cada sub-região especificamente e como eles influenciam a dinâmica dos macronutrientes no NAP como um todo. Além disso, devido à robusta série temporal composta majoritariamente por dados inéditos do GOAL, foi possível relacionar a variabilidade interanual dos macronutrientes com os modos de variabilidade climática predominantes na no oceano Austral. Este estudo foi submetido e está sendo avaliado no periódico *Limnology and Oceanography*.

Spatiotemporal variability of dissolved inorganic macronutrients along the northern Antarctic Peninsula

Thiago Monteiro, Sian Henley, Ricardo César Gonçalves Pollery, Carlos Rafael Borges Mendes, Mauricio Mata, Virginia Maria Tavano, Carlos Alberto Eiras Garcia, Rodrigo Kerr

3. 1 Introduction

The Southern Ocean plays a critical role in regulating the global climate [e.g., Henley *et al*. 2020]. Although Southern Ocean surface waters cover less than 20% of the global ocean, they account for 40-50% of the total oceanic uptake of anthropogenic carbon from the atmosphere [Khatiwala *et al*. 2009; Landschützer, *et al*. 2015]. Part of the carbon uptake in the Southern Ocean is driven by photosynthesis during the summer, which is fuelled by high concentrations of macronutrients, supporting ecosystem functioning and carbon storage [Henley *et al*. 2020]. Nevertheless, the Southern Ocean is one of the regions that experiences pronounced changes in biogeochemical properties, altering the functioning of the entire ecosystem [Henley *et al*. 2020 and references therein]. A key region for understanding biogeochemical changes in the Southern Ocean is the NAP, which has experienced rapid changes in the coupled atmosphere-ocean-cryosphere system [e.g., Kerr *et al*. 2018a; Henley *et al*. 2019]. For example, investigations over the last two decades have reported changes in wind patterns [Dinniman *et al*. 2012], land and sea ice cover [Shepherd *et al*. 2018], biological activity [Seyboth *et al*. 2016; Mendes *et al*. 2018] and the carbonate system [Kerr *et al*. 2018a; Monteiro *et al*. 2020; Orselli *et al*. 2022].

The micronutrient iron is an important fuel for photosynthesis and known to be limiting for primary production in vast areas of the Southern Ocean [de Baar *et al*. 1995; Henley *et al*. 2020]. However, the regions around the NAP were

shown to have sufficient iron supply to sustain high levels of phytoplankton production and biomass [Ardelan *et al*. 2010]. Moreover, the NAP is an important region of the Southern Ocean because it is one of the regions most impacted by the ACC, which carries the CDW. CDW is a relatively old water mass sourced from North Atlantic Deep Water [e.g., Ferreira & Kerr 2017], so it is low in dissolved oxygen and rich in remineralised carbon and macronutrients [Prézelin *et al*. 2000, 2004; Dinniman *et al*. 2012; Hauri *et al*. 2015]. Since the NAP is one of the Antarctic coastal regions most exposed to the ACC, it is constantly influenced by CDW intrusions [García *et al*. 2002; Barlett *et al*. 2018; Wang *et al*. 2022], altering the biogeochemical dynamics in this region [Meredith *et al*. 2017; Henley *et al*. 2019; Orselli *et al*. 2020). The CDW is a relatively warm water mass (>1 °C) that intrudes into the intermediate layers along the NAP [Prézelin *et al*. 2000; Couto *et al*. 2017; Venables *et al*. 2017]. The physical properties of CDW change as it is mixed with cooler and less saline waters, forming the mCDW in the shelf and coastal domain [Couto *et al*. 2017; Venables *et al*. 2017].

The NAP coastal region encompasses the Gerlache and Bransfield Straits, and the northwestern Weddell Sea continental shelf (Fig. III-1). At the southernmost part of the NAP, the Gerlache Strait is a relatively shallow region (depth ~ 800 m), with high concentrations of sea ice [Monteiro *et al*. 2020b; Parra *et al*. 2020; Su *et al*. 2022] and strongly impacted by meltwater from continental glaciers [Cook *et al*. 2016; Silva *et al*. 2020; Meredith *et al*. 2022]. Despite covering a small area, Gerlache Strait acts as a stronger summer CO_2 sink than regions with wider areas, such as Bransfield Strait [Monteiro *et al*. 2020a]. This strong CO_2 sink behaviour is driven mainly by high primary productivity [Monteiro *et al*. 2020b; Costa *et al*. 2020], which sustains a diverse and productive food

web [Dalla Rosa *et al*. 2008; Nowacek *et al*. 2011; Mendes *et al*. 2018]. Indeed, intense blooms of diatoms [Costa *et al*. 2020] and high densities of krill [Nowacek *et al*. 2011], penguins [Pitman & Durban 2010] and whales [Secchi *et al*. 2011] are recorded in Gerlache Strait. Towards the north, the Bransfield Strait is a region with rapid and dynamic ocean circulation [Zhou *et al*. 2006; Dotto *et al*. 2016; Sangrà *et al*. 2017; van Caspel *et al*. 2018; Damini *et al*. 2022] and comprises the western, central, and eastern basins, separated by relatively shallow sills (Fig. III-b). The western basin is the shallowest (~1000 m), followed by the central (~ 2000 m) and eastern (~ 2500 m) basins.

The NAP surface circulation (Fig. III-a) is characterised by local surface water and the mCDW, mainly coming from the Bellingshausen Sea [Zhou *et al*. 2002, 2006; Sangrà *et al*. 2017]. These surface waters are advected from the Gerlache Strait to the eastern basin of Bransfield Strait by a relatively intense mesoscale baroclinic jet known as the Bransfield Current [Zhou *et al*. 2002, 2006; Savidge & Amft 2009]. This current flows in a southwest-northeast direction along the shelf break of the South Shetland Islands [Sangrà *et al*. 2017]. The waters advected by the Bransfield Current are relatively warm (~1.25ºC) and highly productive [Mendes *et al*. 2018; Costa *et al*. 2020, 2021], being able to transport phytoplanktonic biomass and zooplanktonic organisms along the NAP [Ferreira *et al*. 2020]. The western basin of Bransfield Strait is strongly influenced by mCDW intrusions at intermediate levels [Barlett *et al*. 2018; Wang *et al*. 2022], while the central and eastern deep basins are fuelled by DSW from the Weddell Sea [Dotto *et al*. 2016; Damini *et al*. 2022; Wang *et al*. 2022]. DSW refers to distinct shelf water varieties (i.e., High Salinity Shelf Water and Low Salinity Shelf Water) [Damini *et al*. 2022; Wang *et al*. 2022] sourced in the northwestern

continental shelves of the Weddell Sea [van Caspel *et al*. 2018; Wang *et al*. 2022], east of the Antarctic Peninsula (Fig. III-1). Unlike mCDW, DSW is recently ventilated under the shelf domain, therefore it is cold (< –1 ºC) and rich in dissolved oxygen [Dotto *et al*. 2016; Damini *et al*. 2022; Wang *et al*. 2022].

The DSW is advected into the NAP and retained in its most pure form mainly in the central basin of Bransfield Strait, where there is intense mixing with the mCDW at intermediate and upper levels, changing its physical and biogeochemical properties [Dotto *et al*. 2016; Damini *et al*. 2022; Wang *et al*. 2022]. Hence, while mCDW is transported from the south (i.e., Gerlache Strait, western basin of Bransfield Strait) at intermediate layers along the NAP, the DSW is advected in deeper layers from the north (i.e., eastern basin of Bransfield Strait) [Moffat & Meredith 2018; Wang *et al*. 2022]. On interannual timescales, the strength of mCDW intrusion and DSW advection along the NAP is driven by regional modes of climate variability, such as the SAM and the ENSO [Barlett *et al*. 2018; Damini *et al*. 2022; Wang *et al*. 2022]. During positive SAM and/or negative ENSO, mCDW intrusion is intensified, weakening the spreading of DSW along the NAP. Conversely, when SAM is negative and/or ENSO is positive, DSW advection is strengthened and can reach the Gerlache Strait [Wang *et al*. 2022]. Indeed, the DSW in the Gerlache Strait has already been identified through thermohaline signals [Parra *et al*. 2020; Wang *et al*. 2022] and anthropogenic carbon concentrations [Kerr *et al*. 2018b; Lencina-Avila *et al*. 2018].

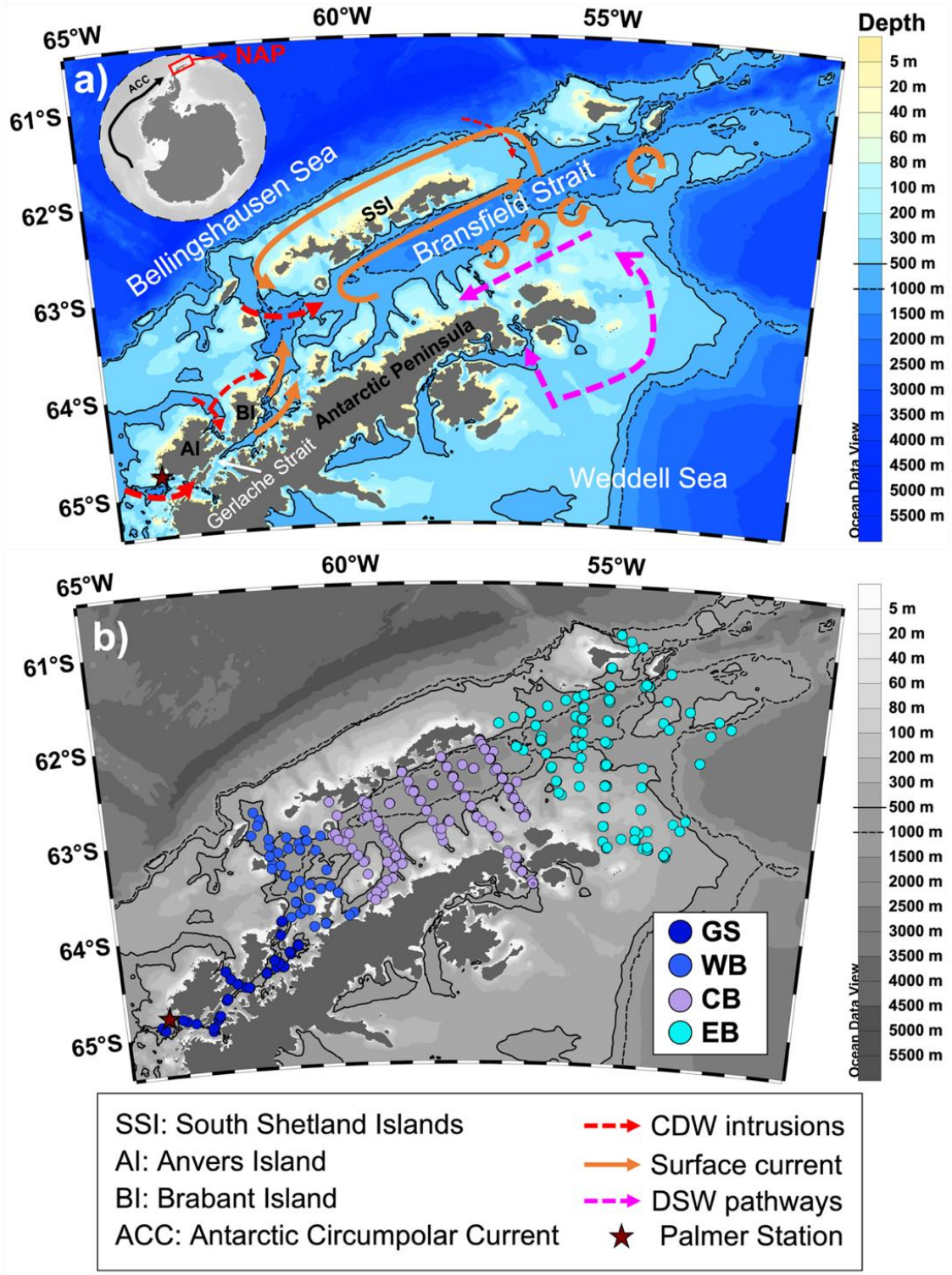

Figure II-1: The northern Antarctic Peninsula (NAP) region and (a) ocean circulation pattern in the study area. The surface circulation (orange arrows), regions of mesoscale structures, as well as Circumpolar Deep Water (CDW) and Dense Shelf Water (DSW) pathways were based on previous studies [e.g., Wang *et al*. 2022; Dotto *et al*. 2016; Moffat & Meredith 2018; Niiler *et al*. 1991; Sangrà *et al*. 2011, 2017; Savidge & Amft 2009; Thompson *et al*. 2009; Zhou *et al*. 2002, 2006]. The brown star in (a) and (b) depicts the U.S. Palmer Station location (64.8°S, 64.1°W), from which we extracted dissolved oxygen [Waite 2022] used in Fig. III-9 and macronutrients data [Ducklow *et al*. 2019] to validate the seasonal drawdown approach described in the methods. (b) Distribution of hydrographic stations where macronutrients were sampled and used in this study, including: Gerlache Strait (GS; purple dots), western (WB, red dots), central (CB, green dots), and eastern (EB, yellow dots) basins of the Bransfield Strait.

Furthermore, the environments along the NAP are influenced by mesoscale oceanographic processes that add complexity to the understanding of biogeochemistry in this region. The effect of shallow topography facilitates the upwelling of mCDW in Gerlache Strait and the western basin of Bransfield Strait [Venables *et al*. 2017; Parra *et al*. 2020], but little is known about its influence on macronutrient concentrations, which fuel primary production and enhance CO_2 uptake [Henley *et al*. 2019]. The effect of topography and ocean circulation also leads to the formation of mesoscale eddies and increased eddy-fuelled productivity in the eastern basin of Bransfield Strait [Thompson & Heywood 2009; Wang *et al*. 2022, Damini *et al*. 2023], although these processes are often neglected in biogeochemical studies due to their complexity [Jones *et al*. 2015; Damini *et al*. 2023]. Understanding temporal variability patterns of macronutrients is also a challenge along the NAP, because the response time to SAM and ENSO variability modes is not well elucidated [Meredith *et al*. 2008; Barlett *et al*. 2018; Wang *et al*. 2022] and the mesoscale processes themselves may also play an important role in this variability [Meredith *et al*. 2017; Kerr *et al*. 2018a; Henley *et al*. 2019]. For example, intense diatom blooms enhance CO_2 uptake [Brown *et al*. 2019; Costa *et al*. 2020] and can lead to nutrient depletion in the upper ocean and increase further local remineralisation of carbon and macronutrients below the mixed layer [Henley *et al*. 2017, 2018]. In addition, melting sea and glacial ice regulates summer water column stability [Höfer *et al*. 2019; Wang *et al*. 2020], driving phytoplankton blooms [Kim *et al*. 2016; Brown *et al*. 2019; Costa *et al*. 2020], CO_2 uptake [Brown *et al*. 2019; Costa *et al*. 2020; Monteiro *et al*. 2020b), and nutrient depletion and replenishment in the upper ocean [Henley *et al*. 2017, 2018].

The importance of nutrients to fuel the primary production that underpins the food chain has been emphasised in some studies throughout the NAP [Mendes *et al*. 2018; Höfer *et al*. 2019; Costa *et al*. 2020; Mascioni *et al*. 2021], as well as the impact of mesoscale processes on nutrient supply [Wang *et al*. 2020; Forsch *et al*. 2021; Meredith *et al*. 2022]. Furthermore, some studies have provided important information on the processes that regulate macronutrient concentrations south of the NAP, i.e., on the continental shelf of the Western Antarctic Peninsula (WAP) [Henley *et al*. 2019 and references therein], although little is known about these processes and their interannual variability in the NAP. Even less is known about the processes that regulate the spatial and temporal variability of macronutrients along the NAP and how the high complexity of this region is reflected in macronutrient concentrations. Therefore, we explored a dataset comprising 24 years of sampling to understand the processes involved in the spatial and temporal variability of macronutrients during the austral summer along the NAP.

3. 2 Material and Methods

3. 2. 1 The hydrographic and macronutrient datasets

We compiled a time series spanning the period from 1996 to 2019 (Figs. III-S1 to III-S4) of the seawater hydrographic variables conservative temperature (^{o}C), absolute salinity (g kg^{-1}) and dissolved oxygen (µmol kg^{-1}), and the macronutrients nitrate, nitrite, ammonium, phosphate, and silicic acid (µmol kg^{-1}). The study area covered the NAP regions including the Gerlache Strait, which separates the Anvers and Brabant Islands from the Antarctic Peninsula, and the Bransfield Strait, between the South Shetland Islands and the Peninsula (Fig. III-

1a). To better understand the different processes influencing the variability of macronutrient concentrations, the sampling stations were split into four sub-regions: the Gerlache Strait and the western, central, and eastern basins of Bransfield Strait (Fig. III-1b). Most data (~90%) were obtained from the GOAL [Mata *et al*. 2018; Dotto *et al*. 2021] from austral summer field campaigns (January-March). In some years (1996, 2005, 2006, 2010, 2011) we used hydrographic and macronutrient data from GLODAP 2020 [Olsen *et al*. 2020] along the NAP and exceptionally for 1996 we used data available from December 1995 to February 1996 (the FRUELA cruises) [García *et al*. 2022; Álvarez *et al*. 2002]. Details on the sampling and analysis of macronutrient data obtained from GLODAP dataset can be accessed on the OCADS platform (https://www.ncei.noaa.gov/access/ocean-carbon-acidification-data-system-portal/).

3. 2. 2 Sampling and macronutrient analyses from GOAL dataset

For the GOAL dataset, hydrographic data profiles were measured, and discrete seawater samples were collected using a combined Sea-Bird CTD/Carousel 911 + system® equipped with oxygen sensors and 24 12 L Niskin bottles. Seawater samples were filtered through cellulose acetate membrane filters (0.45 µm) for determination of dissolved inorganic macronutrient concentrations (i.e., DIN, phosphate and silicic acid). Prior to 2015, the analyses were carried out on board immediately after collection and from 2015 onwards the samples were frozen immediately at −20°C until laboratory analysis. In both cases the analyses followed the spectrophotometric determination methods described by Aminot & Chaussepied [1983] with an accuracy around ± 5% for all

analysed macronutrients. Orthophosphate was measured by reaction with ammonium molybdate, with absorption readings at 885 nm. Silicic acid measurements, in the form of reactive Si, were corrected for sea salt interference. Detection limits were 0.11 μmol kg^{-1} for DIN, 0.10 μmol kg^{-1} for phosphate and 0.50 μmol kg^{-1} for silicic acid.

3. 2. 3 Summer average profiles of hydrographic properties and macronutrients

About 97% of the DIN data were composed of nitrate, followed by ammonium (2%) and nitrite (1%). Therefore, in some cases (11% of all data), we considered DIN as the nitrate concentration, when no nitrite and/or ammonium data were available. Discrete seawater samples were collected at irregular depth intervals from surface (5 m) to deep waters (at approximately 15 m from the bottom). We averaged the parameters for each region at regular depth intervals from the surface to the bottom (i.e., 0, 25, 50, 75, 100, 250, 500, 750, 1000, 1250, 1500, 1750, 2000 m) to obtain an averaged summer profile for each year (Figs. III-S1 to III-S4). All hydrographic and macronutrients data are freely available at https://doi.org/10.5281/zenodo.7384423 [Monteiro *et al*. 2022].

3. 2. 4 Seasonal macronutrient drawdown

We estimated seasonal macronutrient drawdown on the averaged profiles for each year (grey profiles in Fig. III-5) as the difference between the depth-integrated nutrient concentration between 50 and 100 m and the depth-integrated concentration between 0 and 50 meters. Therefore, we assumed that summer macronutrient concentrations between 50 and 100 m were representative of macronutrient concentrations between 0 and 50 m in the previous winter. Using

this method, we also estimated the seasonal macronutrient drawdown on the averaged profiles for each year in the Palmer Station LTER data (Fig. III-1) [Ducklow *et al*. 2019], where Kim *et al*. [2016] measured seasonal macronutrient drawdown from in situ data collected in winter and the following summer. Our estimates of seasonal macronutrient drawdown agree with the results obtained by Kim *et al*. [2016], which attests to the robustness of our adopted method based on summer data alone. They measured a seasonal drawdown from 1993 to 2013 of 415 ± 110 mmol m^{-2}, 23 ± 10 mmol m^{-2}, and 985 ± 386 mmol m^{-2} for DIN, phosphate, and silicic acid, respectively. For the same period, we estimated a seasonal drawdown of 411 ± 191 mmol m^{-2}, 25 ± 9 mmol m^{-2}, and 950 ± 269 mmol m^{-2} for DIN, phosphate, and silicic acid, respectively.

3. 2. 5 Composite macronutrient profiles by climate modes

To assess the influence of the SAM and ENSO modes of climate variability on the concentrations of macronutrients, we separated the austral summer profiles between years of positive and negative SAM or ENSO and calculated the difference between them. SAM index was obtained from the British Antarctic Survey website (http://www.nerc-bas.ac.uk/icd/gjma/sam.html), which is based on the differences between normalised monthly zonal means of sea-level pressure observations at 40°S and 65°S [Marshall 2003]. ENSO index was obtained from the Climate Prediction Centre (http://www.cpc.ncep.noaa.gov), which is defined as the consecutive three-month average of sea surface temperature anomalies from the ERSST.v4 dataset in the Niño 3.4 region (5°N – 5°S, 120°W – 170°W) [Vera & Osman 2018; La *et al*. 2019]. Although the response time of physical and biogeochemical properties to variations in SAM

and ENSO along the NAP is not well understood, it has been estimated to range from 4 to 6 months for SAM and 6 to 9 months for ENSO [e.g., Kim *et al*. 2016; Dotto *et al*. 2016; Meredith *et al*. 2008; Barllet *et al*. 2018]. Here, we used a lag of 4 months from the sampling month for the SAM index and of 6 months for the ENSO index (Tab. III-1).

Table III-1: Sign of the SAM and ENSO indices in the respective sampling years along the NAP. The SAM and ENSO indices refer to 4 and 6 months prior to the sampling month, respectively.

Year	Sampling month	SAM	ENSO
1996	January	+	-
2003	January	-	+
2004	January	+	+
2005	January	-	+
2006	March	+	-
2008	February	-	-
2009	February	+	-
2010	March	+	+
2011	March	+	-
2013	February	-	+
2014	February	-	-
2015	February	+	+
2016	February	-	+
2017	February	+	-
2018	February	+	-
2019	January	+	+

We calculated the uncertainty propagated in calculating the difference between the averages through the following equation: $\sigma_z = \sqrt{(\sigma_{\bar{x}})^2 + (\sigma_{\bar{y}})^2}$, where "$\sigma_{\bar{x}}$" and "$\sigma_{\bar{y}}$" are the standard errors of each average. To assess the statistical difference between the average positive and negative SAM or ENSO profiles, we used Student's t-tests for normally distributed profiles. For profiles with non-normal distribution, we used the non-parametric Mann-Whitney-

Wilcoxon test. To test the normal distribution, we used the Shapiro-Wilk statistical test.

3. 3 Results

3. 3. 1 Spatial distribution of hydrographic properties and macronutrients

In general, the surface temperature was higher than 0ºC along the NAP (Fig. III-2a). However, along the Bransfield Strait we observed a front between waters colder than 0ºC towards the Antarctic Peninsula and waters warmer than 0ºC towards the South Shetland Islands (Fig. III-S5). Through the water column, the temperature was higher than 0ºC at Gerlache Strait, decreasing (< 0ºC) along the Bransfield Strait (Fig. III-2a). Temperatures higher than 0ºC were observed at the southern end of Gerlache Strait and western basin of Bransfield Strait from the surface to the deep layer (Fig. III-S5). Temperatures lower than –1ºC were observed in the central basin of Bransfield Strait below 500 m and a slight temperature rise was observed at the eastern end of Bransfield Strait below 500m. Salinity was lower above 50 m (34.28 ± 0.18 g kg^{-1}) along the NAP (Fig. III-2b), and even lower in Gerlache Strait (34.09 ± 0.25 g kg^{-1}) (Fig. III-S5). Below 200 m the salinity was relatively homogeneous in the central basin of Bransfield Strait (34.70 ± 0.04 g kg^{-1}), while there was an increase in salinity in the western basin of Bransfield Strait (34.72 ± 0.02 g kg^{-1}) and in the Gerlache Strait (34.79 ± 0.05 g kg^{-1}) (Fig. III-2b). Dissolved oxygen concentrations were lowest (< 225 µmol kg^{-1}) below the surface in the Gerlache Strait and western basin of Bransfield Strait, and highest (> 275 µmol kg^{-1}) in the central basin of Bransfield Strait, mainly below 1000 m (Fig. III-2c). The highest concentrations of DIN (> 35.00 µmol kg^{-1}) were observed in the transition between the central and eastern

basins of Bransfield Strait below 500 m (Fig. III-2d). Although the DIN concentrations did not have as clear a west-east pattern as the other macronutrients, in general a slight increase in DIN concentration was observed in the central basin of Bransfield Strait. Average DIN concentration through the water column was 29.67 ± 3.09 μmol kg^{-1} in the Gerlache Strait and 28.23 ± 2.84 μmol kg^{-1}, 30.39 ± 2.49 μmol kg^{-1}, and 29.42 ± 2.08 μmol kg^{-1} in the western, central, and eastern basins of Bransfield Strait, respectively.

Both phosphate (Fig. III-2e) and silicic acid (Fig. III-2f) concentrations were higher in the Gerlache Strait and western basin of Bransfield Strait than the rest of the NAP below the subsurface (50 m) down to 750 m. Average silicic acid concentration through the water column was 80.67 ± 8.99 μmol kg^{-1} in the Gerlache Strait and 74.71 ± 6.02 μmol kg^{-1}, 60.93 ± 4.72 μmol kg^{-1}, and 62.38 ± 7.87 μmol kg^{-1} in the western, central, and eastern basins of Bransfield Strait, respectively. Average phosphate concentration through the water column was 1.88 ± 0.26 μmol kg^{-1} in the Gerlache Strait and 2.00 ± 0.19 μmol kg^{-1}, 1.86 ± 0.20 μmol kg^{-1}, and 1.88 ± 0.17 μmol kg^{-1} in the western, central, and eastern basins of Bransfield Strait, respectively. We also observed high phosphate concentrations in both central (2.00 ± 0.21 μmol kg^{-1}) and eastern (1.99 ± 0.15 μmol kg^{-1}) basins of Bransfield Strait below 1000 m (Fig. III-2e). In some profiles in central and eastern basins of Bransfield Strait there were concentrations of phosphate (1.75 μmol kg^{-1}) and silicic acid (55.00 μmol kg^{-1}) in the deep layer as low as in the surface layer (Fig. III-2e,f). The lowest concentrations of silicic acid were recorded in the central basin of Bransfield Strait, from the surface to the deep layer (Fig. III-S5).

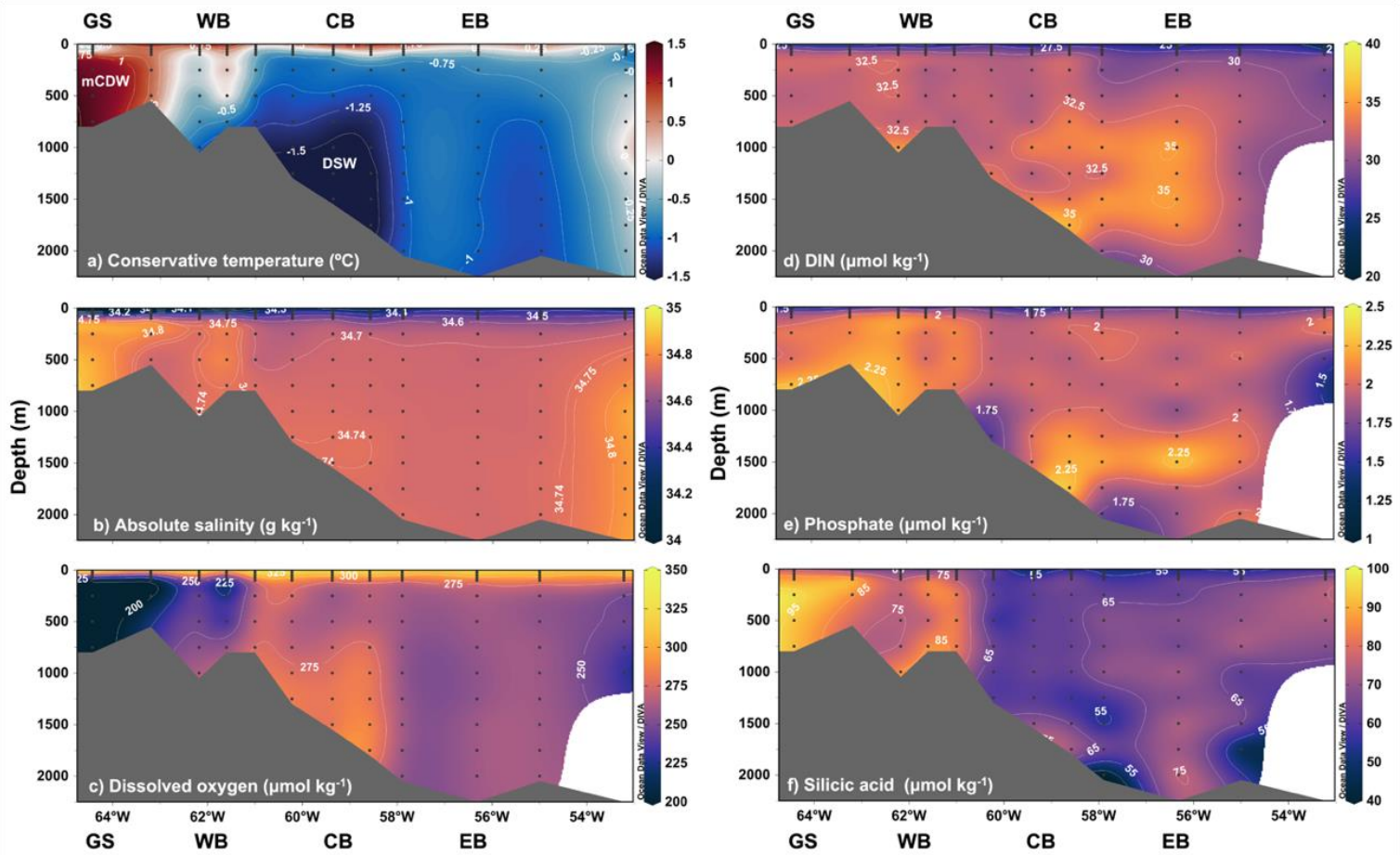

Figure III-2: Zonal sections of water column distributions of (a) conservative temperature, (b) absolute salinity, (c) dissolved oxygen, (d) dissolved inorganic nitrogen (DIN), (e) phosphate, and (f) silicic acid during austral summer (Jan-Mar) along the northern Antarctic Peninsula (NAP). Each profile composing the section are averaged profiles at each degree of longitude, considering the entire dataset (from 1996 to 2019). The zonal section comprises the regions from the south to north of the NAP: Gerlache Strait (GS), and the western (WB), central (CB) and eastern (EB) basins of Bransfield Strait. At the western end of the NAP (GS) there are intense intrusions of modified Circumpolar Deep Water (mCDW) whereas in the CB there are intense intrusions of Dense Shelf Water (DSW) from the Weddell Sea. Grey dots are sampling depths.

The lowest temperatures (< –1ºC) below 500 m were associated with a greater influence of DSW while the highest temperatures (> 0ºC) were associated with a greater influence of mCDW in intermediate layers (Fig. III-3a). Lower dissolved oxygen concentrations (< 225 µmol kg^{-1}) were evident in warmer waters associated with the mCDW in contrast to the more oxygenated (> 275 µmol kg^{-1}) waters associated with DSW (Fig. III-3b).

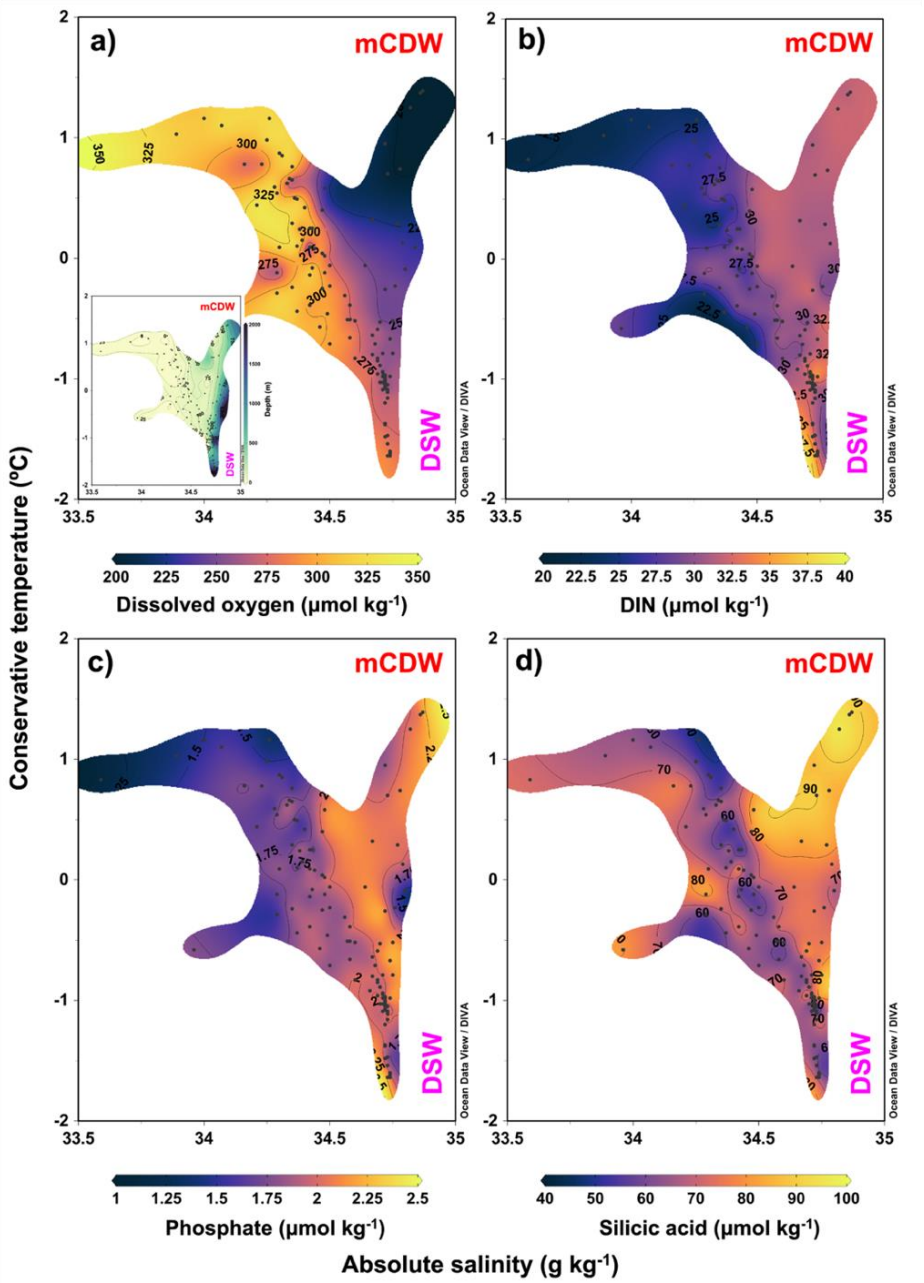

Figure III-3: Conservative temperature-absolute salinity (Θ-S_A) diagram vs properties during austral summer (Jan-Mar) along the northern Antarctic Peninsula. Θ-S_A vs (a) dissolved oxygen, (b) dissolved inorganic nitrogen (DIN), (c) phosphate, (d) silicic acid, and depth on the inset (a). In each Θ-S_A diagram the influence of mixing of modified Circumpolar Deep Water (mCDW) and Dense Shelf Water (DSW) is shown.

In general, the highest concentrations of phosphate (> 2 µmol kg^{-1}) and silicic acid (> 80 µmol kg^{-1}) were associated with greater influence of mCDW (Fig. III-3c-e) in intermediate and deep layers (Fig. III-3a), although high concentrations of DIN (> 30 µmol kg^{-1}) and phosphate (> 2 µmol kg^{-1}) were observed under the influence of DSW (Fig. III-3c-d). The lowest silicic acid concentrations below 500 m were observed under the influence of DSW, with concentrations (< 60 µmol kg^{-1}) as low as in the surface layer. However, silicic acid concentrations were also relatively high in the surface layer, reaching values > 70 µmol kg^{-1} (Fig. III-3c).

3. 3. 2 Interannual variability of hydrographic properties and macronutrients

The highest interannual variability in temperature was observed in the western basin of Bransfield Strait (Fig. III-4d), also associated with the highest variability of both salinity (Fig. III-4e) and dissolved oxygen, mainly in the depth interval 250-500m (Fig. III-4f) in the same area. Dissolved oxygen concentrations also showed interannual variability in the central (Fig. III-4i) and eastern (Fig. III-4l) basins of Bransfield Strait, albeit to a lesser degree and more homogeneously with depth. In the western basin of Bransfield Strait, there was an increase of more than 1°C between 250 m and 500 m with a subsequent decrease in the deep layer (Fig. III-4d) in 2008, when the highest salinities (Fig. III-4e) and the lowest concentrations of dissolved oxygen (Fig. III-4f) were also observed. Conversely, in the western and eastern basins of Bransfield Strait the temperature was anomalously lower than –1°C below 500 m in 2016, when the highest concentrations of dissolved oxygen (> 270 µmol kg^{-1}) below 250 m in the western basin of Bransfield Strait was also observed (Fig. III-4f).

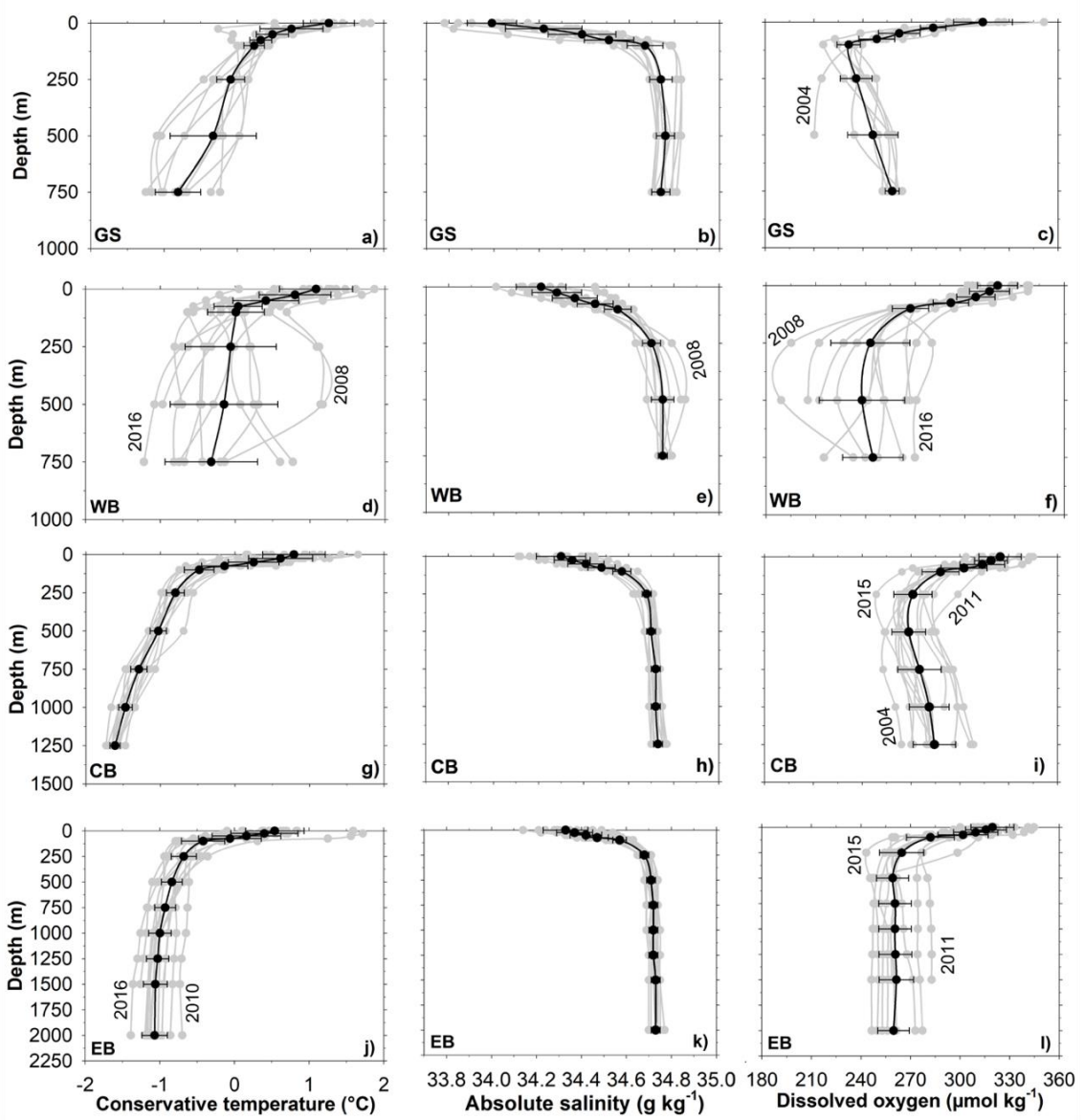

Figure III-4: Summer (Jan-Mar) average profiles of hydrographic properties for each year from 1996 to 2019 along the northern Antarctic Peninsula, comprising the regions: (a-c) Gerlache Strait (GS), (d-f) western (WB), (g-i) central (CB), and (j-l) eastern (EB) basins of Bransfield Strait. Profiles for each year are presented in grey lines and the black lines are the averaged profiles over the period for each property and region. The horizontal black bars are the standard deviations for each depth. Years showing anomalous behaviour (i.e., outside the standard deviation) are highlighted.

Gerlache Strait showed the second highest interannual variability in temperature and salinity among the regions examined here (Fig. III-4b,c). Even in the eastern basin of Bransfield Strait, with less temperature variability, there were variations of up to 1ºC among the years, but more homogeneously with depth (Fig. III-4j) than in the western basin of Bransfield Strait and Gerlache Strait. Other anomalous behaviours were recorded, such as the lowest

concentration of dissolved oxygen in 2004 in Gerlache Strait (Fig. III-4c) and central basin of Bransfield Strait (Fig. III-4i), and in 2015 in the central (Fig. III-4i) and eastern (Fig. III-4l) basins of Bransfield Strait at 250 m. On the other hand, the highest anomalous concentrations of dissolved oxygen in central (Fig. III-4i) and eastern (Fig. III-4l) basins of Bransfield Strait were recorded in 2011.

There was high interannual variability in the summer average profiles of all macronutrients along the NAP (Fig. III-5). The highest interannual variability was observed in silicic acid, with concentrations varying by up to a factor of three (~ 40-120 µmol kg^{-1}) through the water column (third column in Fig. III-5). In most profiles, the concentration of silicic acid increased from surface waters to ~100-200 m and then became more homogeneous with depth. DIN (first column in Fig. III-5) and phosphate (second column in Fig. III-5) concentrations were lower at the surface and consistently higher below 100 m. On average, silicic acid concentrations were highest in the western basin of Bransfield Strait (Fig. III-5f) and in Gerlache Strait, where the highest concentrations occurred in 2016 and 2017 (Fig. III-5c). The highest silicic acid concentrations were observed in 2017 and the lowest in 2014 along the entire NAP. However, silicic acid in 2017 were even higher, and throughout the entire water column, in the central and eastern basins of Bransfield Strait (Fig. III-5i,l) than in the western basin of Bransfield Strait and the Gerlache Strait (Fig. III-5c,f), where this increase was more pronounced below 100 m. In the central basin of Bransfield Strait there was higher interannual variability and concentrations of DIN, which were higher in 2011 and 2018 (Fig. III-5g), while across the entire NAP they were higher in 2015 and lower in 2016. High interannual variability was also observed in phosphate concentrations of up to two-fold (~1-3 µmol kg^{-1}) throughout the NAP (second

column in Fig. III-5). The highest concentrations of phosphate were measured in 2003 in the Gerlache Strait (Fig. III-5b), 2010 in the western basin of Bransfield Strait (Fig. III-5e), and 2011 in the central basin of Bransfield Strait (Fig. III-5h), and the lowest in 2008 in the eastern basin of Bransfield Strait (Fig. III-5k) and 2014 in both Gerlache Strait (Fig. III-5b) and the western basin of Bransfield Strait (Fig. III-5e).

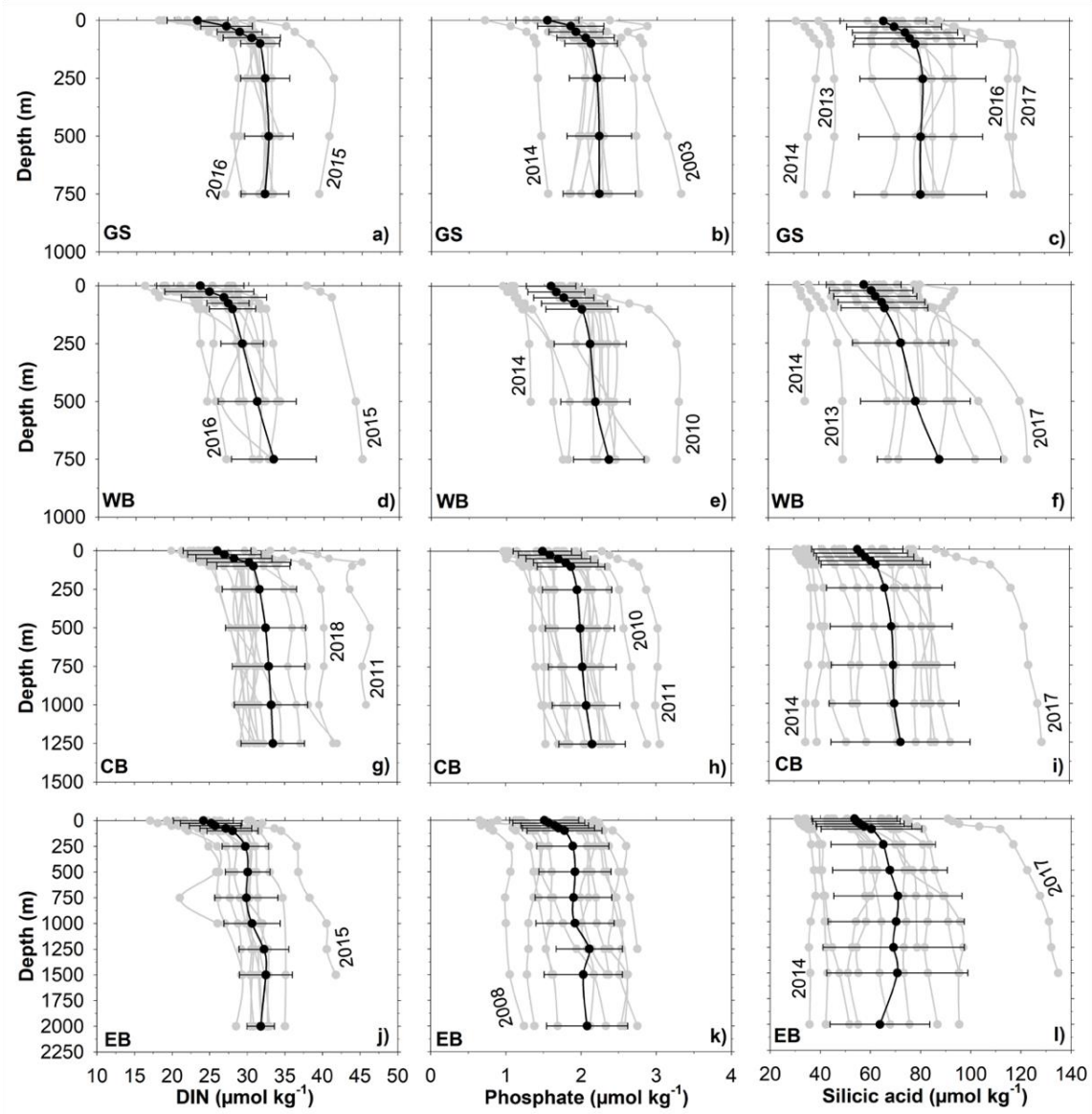

Figure III-5: Summer (Jan-Mar) averaged profiles of macronutrients for each year from 1996 to 2019 along the northern Antarctic Peninsula, comprising the regions: (a-c) Gerlache Strait (GS), and the (d-f) western (WB), (g-i) central (CB) and (j-l) eastern (EB) basins of Bransfield Strait. Profiles for each year are presented in grey lines and the black lines are the averaged profiles over the period for each property and region. The horizontal black bars are the standard deviations for each depth. Years showing anomalous behaviour (i.e., outside the standard deviation) are highlighted.

We compared the average profiles of macronutrients along the NAP during periods of positive and negative SAM or ENSO (Fig. III-6). In years of positive SAM there was an increase (red line profiles on positive values in Fig. III-6) in the concentrations of DIN (first column in Fig. III-6), phosphate (second column in Fig. III-6), and silicic acid (third column in Fig. III-6) through the water column along the NAP. Such an increase was more pronounced in silicic acid concentrations, mainly in the central (Fig. III-6i) and eastern (Fig. III-6l) basins of Bransfield Strait, particularly below 250 m. Although phosphate and DIN concentrations increased in all regions during positive SAM, phosphate increase was not significant in the central basin of Bransfield Strait (Fig. III-6h). Furthermore, there was greater uncertainty in the phosphate increase in the Gerlache Strait (Fig. III-6b), where the DIN increase (Fig. III-6a) was also not significant.

Compared to SAM, there was a smaller difference in macronutrient concentrations between the years of positive and negative ENSO (blue line profiles in Fig. III-6). Yet, higher differences were observed in the central (Fig. III-6g-i) and eastern (Fig. III-6j-l) basins of Bransfield Strait, where macronutrient concentrations were lower during positive ENSO. Silicic acid concentrations were lower during positive ENSO in all regions, but the differences were not significant. On the other hand, there was a significant decrease in DIN in the central (Fig. III-6g) and eastern (Fig. III-6j) basins of Bransfield Strait, while DIN increased in the western basin (Fig. III-6d). In addition, there was a significant increase in phosphate during years of positive ENSO in the Gerlache Strait (Fig. III-6b) and the western basin of Bransfield Strait (Fig. III-6e), while in the eastern basin phosphate concentrations decreased (Fig. III-6k).

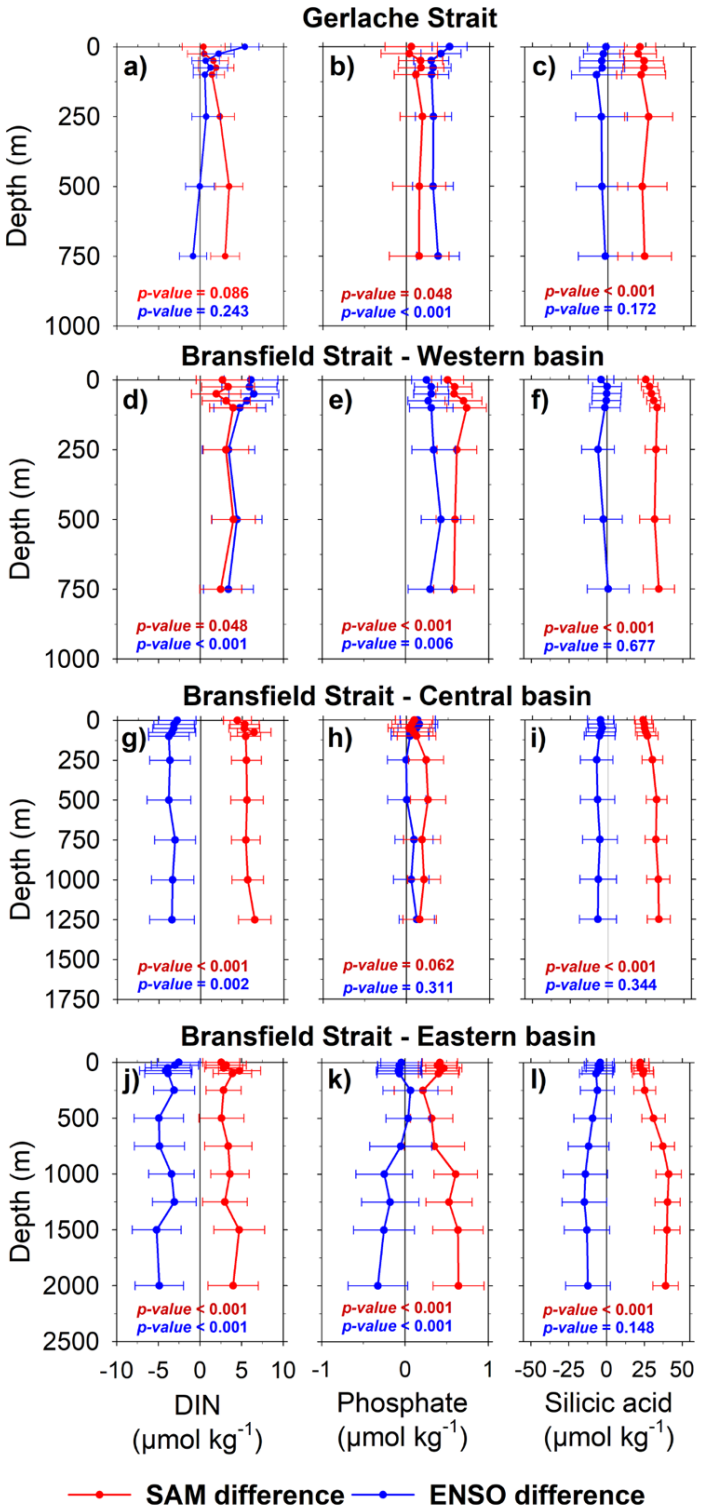

Figure III-6: Influence of Southern Annular Mode (SAM) and El Niño-Southern Oscillation (ENSO) modes of climate variability on the average profiles of macronutrients along the northern Antarctic Peninsula, comprising the regions: (a-c) Gerlache Strait, and the (d-f) western, (g-i) central and (j-l) eastern basins of Bransfield Strait. In red the difference in average profiles between positive and negative SAM is shown, while in blue the same is shown for ENSO. Positive values indicate an increase in macronutrients during positive SAM and ENSO years, while negative values indicate a decrease in macronutrients during positive SAM and ENSO years and vice versa. The horizontal bars are the propagated uncertainties in calculating the difference between the averages for each depth and the p-values refer to the statistical tests to assess the significance of the difference between the average profiles.

3. 3. 3 Uptake stoichiometry and seasonal drawdown of macronutrients

The full-depth average DIN/phosphate ratio across the NAP environments ranged from 11.8 ± 0.9 (r^2 = 0.965; p < 0.001) to 14.2 ± 0.7 (r^2 = 0.978; p < 0.001), observed in the western and eastern basins of Bransfield Strait (Fig. III-7a), respectively. From 2013 to 2019, when data are available for all NAP environments, the lowest DIN/phosphate ratios (< 11) were observed in 2016 along the Bransfield Strait (Table S2), while in the Gerlache Strait the lower DIN/phosphate ratio (9.40 ± 0.87; r^2=0.95; p<0.001; n=8) was recorded in 2019. DIN/phosphate ratios higher than 20 were observed in the western basin of Bransfield Strait in 2018 and in the eastern basin in 2017 and 2019.

The average silicic acid/DIN ratio ranged from 1.7 ± 0.1 (r^2 = 0.974; p < 0.001) in Gerlache Strait to 3.1 ± 0.3 (r^2 = 0.956; p < 0.001) in the western basin of Bransfield Strait (Fig. III-7b). From 2013 to 2019 the lowest silicic acid/DIN ratio (< 1.2) was recorded in 2014 along the entire NAP and the highest ratios (> 3.8) were recorded in 2015 and 2017 along Bransfield Strait. A silicic acid/DIN ratio of 5.5 ± 0.5 was recorded in 2009 in the central basin of Bransfield Strait, two-fold the average for the entire period in that region (2.2 ± 0.2).

The seasonal drawdown in all macronutrients is characterised by a decreasing pattern from south (Gerlache Strait) to north (eastern basin of Bransfield Strait) along the NAP (Fig. III-8). High seasonal drawdown of phosphate was observed in 2010 in the western basin of Bransfield Strait, while higher drawdown in silicic acid was observed in 2016 and 2017 in Gerlache Strait.

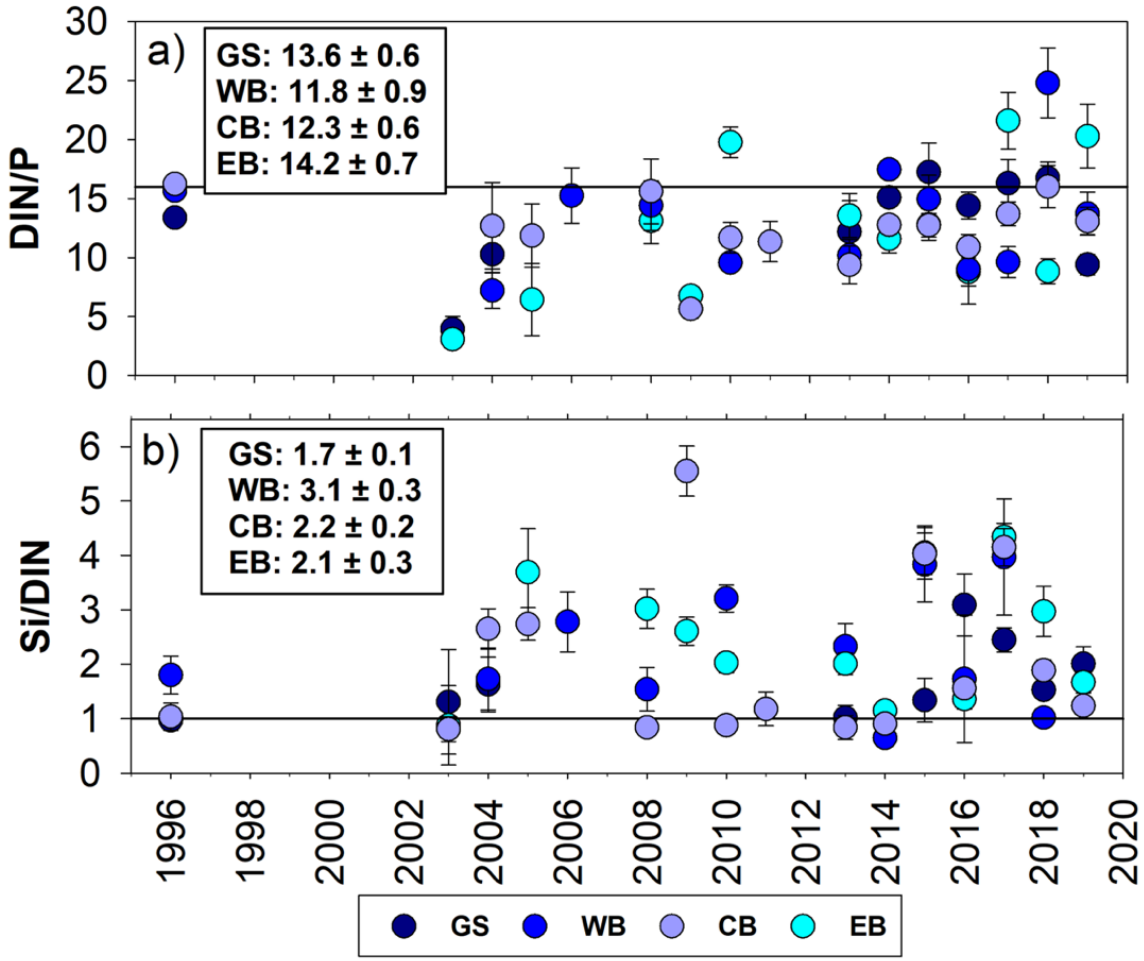

Figure III-7: Time series of macronutrient uptake stoichiometry. (a) Dissolved inorganic nitrogen (DIN)/phosphate (P) and (b) silicic acid (Si)/DIN ratios during austral summer (Jan-Mar) and along the northern Antarctic Peninsula. Colours show the sub-regions studied (GS: Gerlache Strait; WB: Western Bransfield; CB: Central Bransfield; EB: Eastern Bransfield). The vertical bars are the standard error on the slope of the regression DIN versus P, and Si versus DIN. Likewise, the values shown on the inset of each plot are the (a) DIN/P and (b) Si/DIN ratios with the respective standard deviations, considering the average profiles over the period for each region (Fig. III-5). The solid black line marks the ratios (a) DIN/P=16 and (b) Si/DIN=1. Statistics for each year are shown in Table S2.

Seasonal drawdown of silicic acid close to zero was observed in 2015 and 2016 in the western basin of Bransfield Strait, while for phosphate this depletion was found in 2015 in Gerlache Strait. The interannual variability in drawdown of phosphate (Fig. III-8b) and silicic acid (Fig. III-8c) concentration was high in the western basin of Bransfield Strait, while the variability in drawdown of DIN was fairly similar in all sub-regions along the NAP (Fig. III-8a).

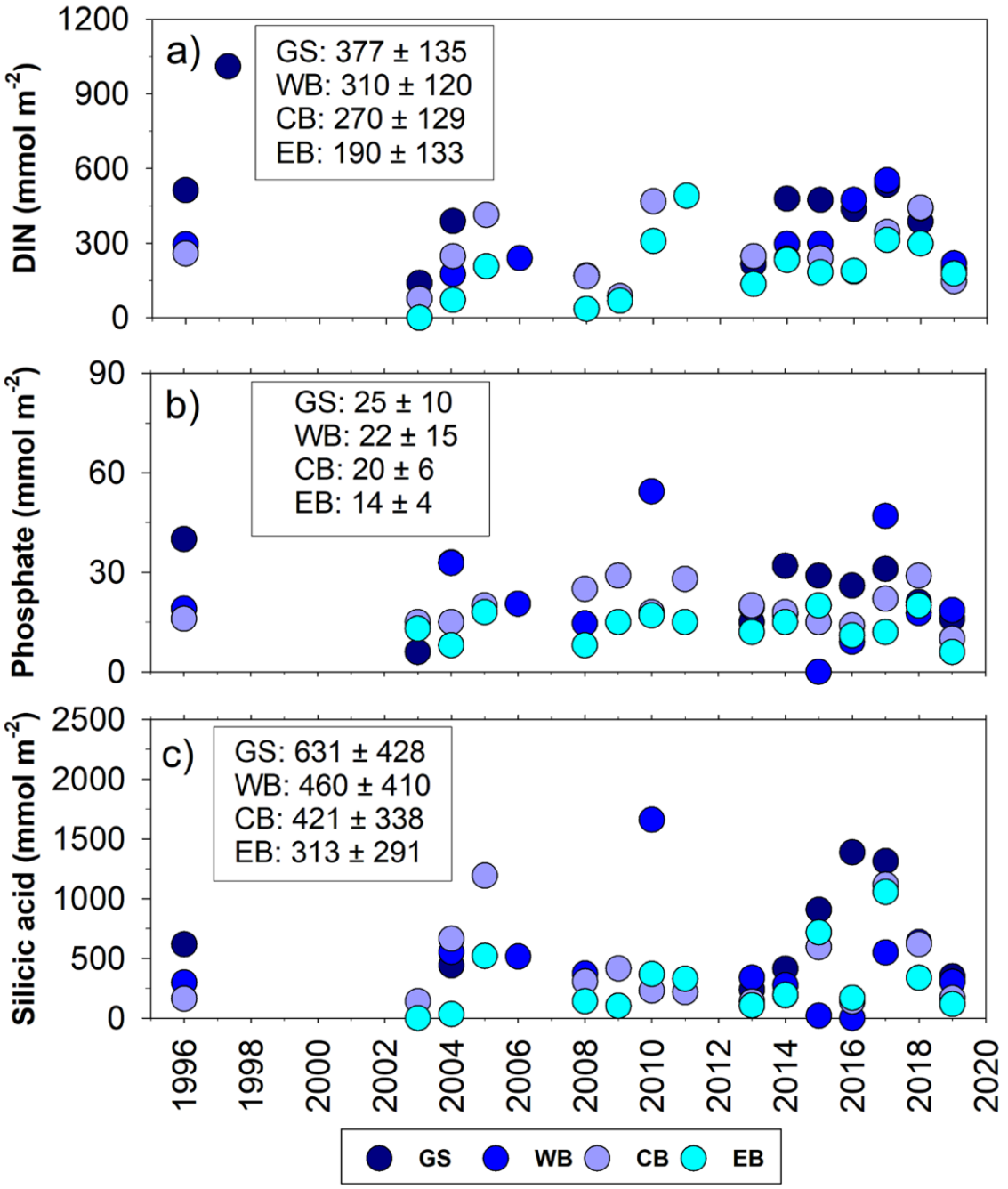

Figure III-8: Time series of seasonal nutrient drawdown. (a) Dissolved inorganic nitrogen (DIN), (b) phosphate and (c) silicic acid, during austral summer (Jan-Mar) along the northern Antarctic Peninsula. Each circle represents the seasonal drawdown of each nutrient in Gerlache Strait (GS) and the western (WB), central (CB), and eastern (EB) basins of Bransfield Strait. The values shown on the inset are the averages for the entire period with the respective standard deviations.

3. 4 Discussion

3. 4. 1 Main sources of macronutrients for the NAP

The main source of macronutrients for the NAP environments is the mCDW intrusions in the coastal and shelf domains [Henley *et al*. 2019], which

carry DIN, phosphate, and silicic acid (Fig. III-2 and 3) as this intermediate water intrudes onto the continental shelf [Prézelin *et al*. 2000; Couto *et al*. 2017; Venables *et al*. 2017]. When mCDW intrudes into the shelf domains (i.e., Gerlache Strait, and western basin of Bransfield Strait), it often upwells by topographic effect [Venables *et al*. 2017; Parra *et al*. 2020], decreasing oxygen at intermediate depths and transporting macronutrients into surface waters. These waters are further advected northward by the Bransfield Current towards the eastern basin of Bransfield Strait, enriching the surface waters of the NAP with high concentrations of macronutrients. Therefore, macronutrient concentrations are mostly not exhausted in the NAP surface waters during summer, even in years with strong phytoplankton blooms (e.g., 2016) Costa *et al*. 2020, 2021]. Although the mCDW is also an important source of macronutrients for the western Antarctic Peninsula (WAP) south of the NAP [Prézelin *et al*. 2000; Klinck *et al*. 2004; Henley *et al*. 2019], surface waters almost exhausted with respect to DIN and phosphate have been recorded in summer over the WAP continental shelf [Henley *et al*. 2017, 2018]. However, along the NAP surface, concentrations of DIN and phosphate were not lower than 15 and 0.5 µmol kg^{-1}, respectively (Fig. III-5 and III-S6a,d). This is likely because both Gerlache Strait and the western basin of Bransfield Strait are regions more exposed to the ACC influence, which probably facilitate more frequent intrusions of mCDW [García *et al*. 2002; Parra *et al*. 2020], favouring higher supply of macronutrients into the surface layer through topographic upwelling and advective mixing. For example, high sea surface concentrations of nitrate (12-24 µmol kg^{-1}) and phosphate (1.0-1.6 µmol kg^{-1}) are observed offshore the WAP [Hauri *et al*. 2015], under strong influence of the ACC that carries CDW. Indeed,

at Palmer Station region, in the southernmost part of the NAP, mCDW is expected to exert a strong and constant influence on macronutrient supply (Fig. III-9) [Prézelin *et al*. 2000; Kim *et al*. 2016]. In both the NAP (Fig. III-5c,f,i,l) and near Palmer Station region (Fig. III-S6g), the surface concentrations of silicic acid are higher than 50 µmol kg^{-1}. This is likely due to the local terrestrial sources of silicic acid in both regions [e.g., Hawkings *et al*. 2017], further supplementing the high silicic acid input from mCDW (see section 4.2 below). Indeed, the surface silicic acid concentration at Palmer Station region (69.0 ± 10.4 µmol kg^{-1}, Fig. III-S6a) is higher than that found along the NAP (third column in Fig. III-5). In both regions, such concentrations are even higher than those found in the northwest Weddell Sea [Hoppema *et al*. 2015], where the direct influence of mCDW is comparatively small.

CDW is sourced from North Atlantic Deep Water [e.g., Ferreira & Kerr 2017], so it has had a long period over which remineralised organic matter has accumulated and hence high concentrations of macronutrients. Along the NAP, this is even more evident in the concentrations of phosphate (Fig. III-2e) and silicic acid, whose concentrations are up to 50% higher under the influence of mCDW in the Gerlache Strait and western basin of Bransfield Strait than in the rest of the NAP (Fig. III-2f). The central basin of Bransfield Strait is strongly influenced by DSW from the Weddell Sea in the deep layers (> 800 m) [Dotto *et al*. 2016; Damini *et al*. 2022; Wang *et al*. 2022], where there are higher concentrations of DIN (Fig. III-2d), phosphate (Fig. III-2e) and dissolved oxygen (Fig. III-2c) associated with lower concentrations of silicic acid (Figs. III-2f and III9). This is a result of the slower rate of opal dissolution, as diatom frustules sink out of the surface layer, compared to the remineralisation of sinking organic

matter [Brown *et al*. 2006] that releases DIN and phosphate [Hoppema *et al*. 2015]. Indeed, phytoplankton blooms recorded in the northwestern Weddell Sea are often composed mostly (> 80%) of diatoms [Mendes *et al*. 2012], associated with low DIN/phosphate uptake ratios (< 14) and high silicic acid/DIN ratios (> 1) [Flynn *et al*. 2021]. Due to the marked depletion of silicic acid during diatom growth, the DSW from the Weddell Sea is relatively low in silicic acid while the concentrations of DIN and phosphate are increased by remineralisation of sinking organic matter as it is advected towards the NAP. This is reinforced by the low DIN/phosphate uptake ratios (< 16, Fig 7a) and high silicic acid/DIN uptake ratios (> 2, Fig 7b) along the NAP, although there is great interannual variability in these ratios. The advection time of shelf waters from the Weddell Sea towards the Bransfield Strait is estimated to be between 1 and 5 months to reach the central basin [van Caspel *et al*. 2018; Damini *et al*. 2022]. This time should not be enough to release high silicic acid concentrations from late spring diatom blooms. Thus, the interannual variability in nutrient concentrations driven by DSW advection is likely due to variability in the advection time of these waters and in the timing and duration of diatom blooms, from early spring to summer. The influence of mCDW and DSW from the Weddell Sea on silicic acid concentrations is most evident when we estimate the contribution of these waters along the NAP from the silicic acid versus dissolved oxygen mixing diagram (Fig. III-9). Below 50 m, the southern end of the NAP (near Palmer Station) is strongly influenced by the silicic acid-rich and dissolved oxygen-poor mCDW. Conversely, the central basin of Bransfield Strait is strongly influenced by the high dissolved oxygen and low silicic acid DSW. This west-east pattern in the fractional contributions of mCDW and DSW to the total mixture is very close to the estimates determined by Damini *et*

al. [2022] in the region. For the deep layers (i.e., > 800 m) of central basin of Bransfield Strait, those authors estimated an averaged contribution of 31 ± 9 % of mCDW and 69 ± 9 % of DSW, while for the eastern basin of Bransfield Strait the averaged contribution to the mixture was 44 ± 8 % for mCDW and 56 ± 8 for DSW. Although the Palmer Station region is made up of almost 100 % mCDW below 50 m (Fig. III-9), silicic acid concentrations are higher than those expected only from mCDW input, revealing that there are important local sources of silicic acid in this region.

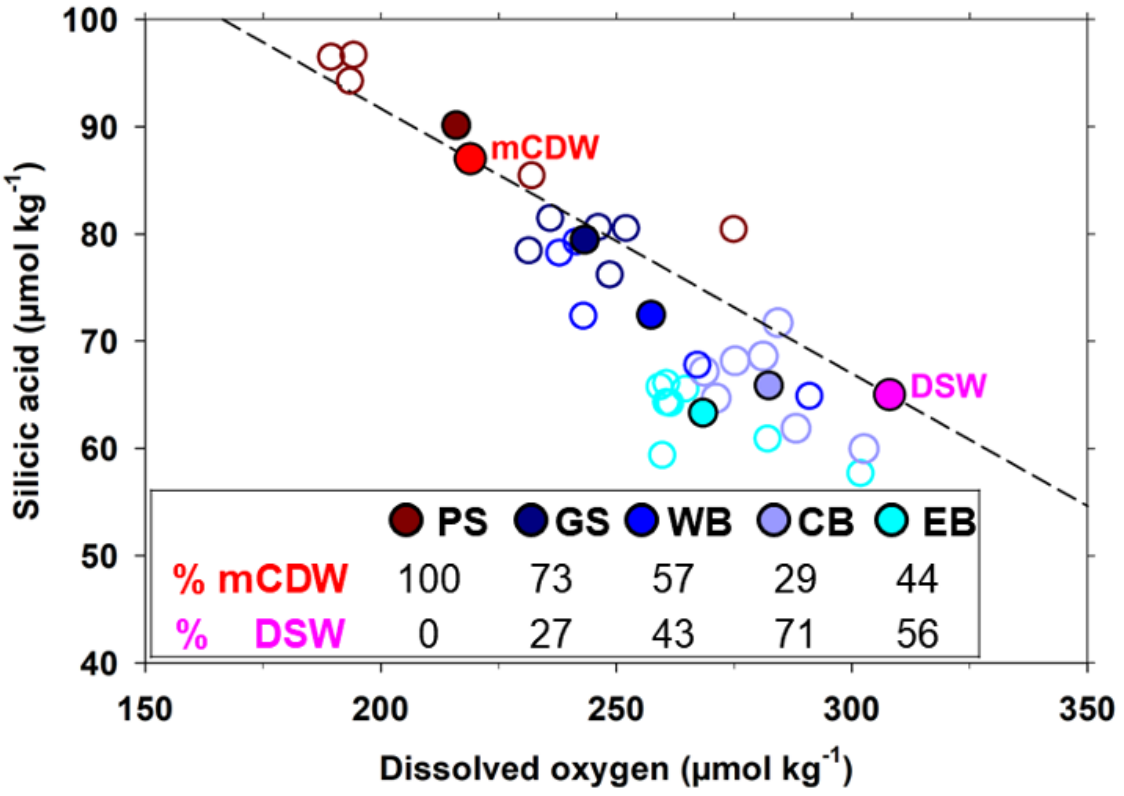

Figure III-9: Influence of the mixture between modified Circumpolar Deep Water (mCDW) and Dense Shelf Water (DSW) from the Weddell Sea on dissolved oxygen and silicic acid below 50 m along the northern Antarctic Peninsula. Open circles represent the average concentrations of dissolved oxygen and silicic acid for each depth interval below 50 m and closed circles indicate the average through the water column below 50 m at Palmer Station (PS), Gerlache Strait (GS) and the western (WB), central (CB) and eastern (EB) basins of Bransfield Strait. The data used here are from the profiles shown in Figs. III-4 and III5. For PS we used dissolved oxygen [Waite 2022] and silicic acid [Ducklow *et al*. 2019] data from the U.S. Palmer Station (Fig.III-1). The dissolved oxygen concentration endmembers were 219 µmol kg^{-1} for mCDW (red closed circle) and 308 µmol kg^{-1} for DSW (blue closed circle), from Damini *et al*. [2022]. The silicic acid concentration endmembers were 87 µmol kg^{-1} [Cape *et al*. 2019] for mCDW and 65 µmol kg^{-1} [Hoppema *et al*. 2015] for DSW.

3. 4. 2 Additional sources of macronutrients for the NAP

In fact, local sources of macronutrients are also important along the NAP. Terrestrial input of iron [De Jong *et al*. 2012; Hatta *et al*. 2013; Annett *et al*. 2017; Sherrell *et al*. 2018] and silicic acid [e.g., Hawkings *et al*. 2017] is well known over the Antarctic continental shelf. However, intense phytoplankton booms in fjords that flow into the NAP [e.g., Mascioni *et al*. 2021; Forsch *et al*. 2021] can inject high concentrations of remineralised DIN and phosphate into downstream regions. Moreover, the abrupt freshwater inflow from fjords increases the upper ocean stability and fertilises the region with iron [Forsch *et al*. 2021], triggering intense phytoplankton blooms downstream. Likewise, such favourable conditions for intense phytoplankton growth, mainly diatoms, are also triggered by glacial [Höfer *et al*. 2019; Wang *et al*. 2020; Meredith *et al*. 2022] and sea ice melting [Mendes *et al*. 2018; Brown *et al*. 2019; Costa *et al*. 2020]. Such high primary productivity sustains a high zooplankton density [e.g., Henley *et al*. 2019; Plum *et al*. 2020], which intensifies the remineralised nutrient stocks [Alcaraz *et al*. 1998; Whitehouse *et al*. 2011; Ratnarajah & Bowie 2016; Plum *et al*. 2020] locally and further advected along the NAP. Furthermore, the eastern basin of Bransfield Strait is an important pathway of icebergs released from the Weddell Sea [Collares *et al*. 2018; Barbat & Mata 2022], which transport iron [Hopwood *et al*. 2017; Laufkötter *et al*. 2018] and likely silicic acid [Höfer *et al*. 2019] from the eastern shelf of the Antarctic Peninsula into the NAP. Hence, there is an increased supply of silicic acid in the eastern basin of Bransfield Strait (Fig. III-2f), where there are also episodic intrusions of silicic acid-enriched mCDW at intermediate levels [Dotto *et al*. 2016; Damini *et al*. 2022). Although widely neglected in biogeochemical studies [Jones *et al*. 2015], mesoscale eddies may

have a relevant impact on nutrient supply along the NAP. Such structures can favour nutrient supply via upwelling of waters enriched with remineralised material [Jones *et al*. 2015; Damini *et al*. 2023] and by intensifying remineralisation by deepening the mixed layer depth within the eddies [Dufois *et al*. 2014]. Moreover, eddies can trap advected water masses [Thompson & Heywood 2009] with high remineralised material content [Dufois *et al*., 2014; Damini *et al*. 2023], such as modified Warm Deep Water (a mixture of CDW with Winter Water in the Weddell Sea) [Hoppema *et al*. 2015].

The high concentration of macronutrients (Fig. III-2) and the supply of iron [Ardelan *et al*. 2010; Annett *et al*. 2017; Sherrell *et al*. 2018] coupled with the increased upper ocean stability driven by sea ice melting and/or glacial freshwater input during the summer supports high productivity along the NAP [Mendes *et al*. 2018; Höfer *et al*. 2019; Costa *et al*. 2020]. We found an average DIN/phosphate uptake ratio (Fig. III-7a) within the expected range for the NAP (~13-21) [Henley *et al*. 2019], supporting the observations that diatoms are the dominant group composing high biomass phytoplankton blooms [Mendes *et al*. 2008; van Leeuwe *et al*. 2020; Costa *et al*. 2020, 2021]. In the Southern Ocean, lower DIN/phosphate ratios (<16) have been observed during diatom blooms, while other smaller phytoplankton groups are associated with a higher (> 16) ratio [Arrigo *et al*. 1999; Henley *et al*. 2019, 2020]. This is particularly true along the NAP, where we observed low DIN/phosphate uptake ratios (< 16, Fig. III-7a) when the phytoplankton composition was dominated by diatoms (Fig. III-S7). For example, a low DIN/phosphate uptake ratio was observed in 2016 along the NAP (Table S2), when an intense phytoplankton bloom was recorded (Costa *et al*., 2020, 2021) and over 90% of it was composed of diatoms (Fig. III-S7).

Conversely, there were high DIN/phosphate ratios (> 20; Fig. III-7a) when phytoplankton composition was dominated by other smaller groups, such as dinoflagellates, haptophytes (*Phaeocystis antarctica*), cryptophytes and green flagellates, in 2017 along the NAP and in 2018 in the western basin of Bransfield Strait (Fig. III-S7). However, we found even lower DIN/phosphate uptake ratios (< 9) in some years (Fig. III-7a), indicating possible additional sources of phosphate in relation to DIN. This may be associated with the release of phosphate accumulated in sea ice [Fripiat *et al*. 2017], although its effect on the water column remains unclear [Henley *et al*. 2019]. Moreover, the high density of krill enriched by diatom blooms [Henley *et al*. 2020] may favour phosphate supply, as krill release phosphate and ammonium through grazing and excretion processes [Tovar-Sanchez *et al*. 2007]. We identified silicic acid/DIN ratios that were within the range previously observed along the WAP and at Palmer Station (1-3) [Henley *et al*. 2019; Kim *et al*. 2016]. Silicic acid/DIN ratios higher than 1 have been associated with diatoms growing under iron-limited conditions [Henley *et al*. 2019, 2020], but the NAP is not expected to experience iron limitation [De Jong *et al*. 2012; Hatta *et al*. 2013; Kim *et al*. 2016; Annett *et al*. 2017; Sherrell *et al*. 2018]. The higher silicic acid/DIN uptake ratios are likely to be a result of high silicic acid concentrations being supplied by mCDW intrusions and local remineralisation/dissolution of diatoms walls. The intense diatom blooms in early spring can lead to a depletion in silicic acid in the upper ocean [Kim *et al*. 2016] and then opal dissolution increases the silicic acid concentration again towards summer. Indeed, we found the highest silicic acid/DIN ratio and the lowest DIN/phosphate ratio in the western basin of Bransfield Strait (Fig. III-7), where

there is a great influence of mCDW intrusions (Fig. III-2) and intense diatom-dominated blooms [Álvarez *et al*. 2002; Costa *et al*. 2020].

3. 4. 3 Drivers of interannual variability of macronutrients

The huge interannual variability in nutrient concentrations along the NAP is driven mainly by the relative strength of mCDW intrusions and the advection of DSW from the Weddell Sea. During positive SAM, westerly winds are intensified southward [Marshall *et al*. 2006; Dinniman *et al*. 2012], strengthening mCDW intrusions along the NAP [Barllet *et al*. 2018; Damini *et al*. 2022; Wang *et al*. 2022] and increasing nutrient concentration. In addition to direct nutrient input, greater vertical mixing leads to an increased supply of organic matter [da Cunha *et al*. 2018; Avelina *et al*. 2020] and a consequent increase in remineralised nutrient concentrations throughout the water column. Overall, the influence of SAM on nutrient concentrations is more evident in the central and eastern basins of Bransfield Strait because these regions are more influenced by DSW from the Weddell Sea than both the western basin of Bransfield Strait and Gerlache Strait [Barllet *et al*. 2018; Damini *et al*. 2022; Wang *et al*. 2022]. In these regions, greater differences between positive/negative SAM are observed in silicic acid concentrations (Fig. III-6) because DSW (mCDW) is depleted (enriched) in silicic acid (Fig. III-9). During positive SAM, DSW advection into Bransfield Strait is weakened, while mCDW intrusion is strengthened [Wang *et al*. 2022], increasing the difference between greater/lesser influence of these distinct water masses. On the other hand, the influence of DSW is smaller in the western basin of Bransfield Strait and the Gerlache Strait [Wang *et al*. 2022], decreasing the silicic acid depletion due to DSW advection. This is supported by the lower influence of

SAM on phosphate and DIN concentrations in Gerlache Strait (Fig. III-6), as the time for organic matter remineralisation is likely shorter than the advection time for DSW to reach this region.

Conversely, during positive ENSO, westerly winds typically migrate northward [Stammerjohn *et al*. 2008] and weaken mCDW intrusions over the NAP [Barllet *et al*. 2018; Damini *et al*. 2022], decreasing nutrient supply. Such conditions strengthen the extent of the DSW advected from the Weddell Sea, reaching the southern end of the NAP (i.e., Gerlache Strait) [Wang *et al*. 2022]. Since DSW is enriched in DIN and phosphate (Fig. III-2d,e) and contains lower concentrations of silicic acid (Fig. III-2f), the interannual variability in silicic acid concentrations is intensified over the NAP. Indeed, we observed a 57% decrease in silicic acid from 2015 (a year of positive SAM) to 2016 (a year of strong positive ENSO) in the central basin of Bransfield Strait, where significant changes were also observed in organic carbon concentrations between these two years (Avelina *et al*., 2020). The influence of ENSO on nutrient concentrations is minor compared to SAM (Fig. III-6) because DSW also contains high concentrations of DIN and phosphate. Moreover, variations in ENSO are expected to exert less influence on circulation along the NAP than variations in SAM [e.g., Wang *et al*. 2022]. This may be associated with uncertainties in the circulation response time to ENSO variations (i.e., 6 to 9 months) [Meredith *et al*. 2008; Barlett *et al*. 2018; Dotto *et al*. 2016] and DSW advection time along the NAP, which are still a challenge to understand. The DSW is estimated to take around 1 to 5 months to reach the central basin of Bransfield Strait [van Caspel *et al*. 2018; Damini *et al*. 2022]. The period of around 5 months is consistent with the estimated time for the drift of medium-sized icebergs from the northwestern Weddell Sea to reach

the central basin of Bransfield Strait [Collares *et al*. 2018]. However, its interannual variability and sensitivity to SAM and ENSO events, as well as the residence time of the waters within Bransfield Strait remain unclear. Nutrient concentrations appear to be more sensitive to ENSO in the eastern basin of Bransfield Strait (Fig. III-6) because this is the main pathway of DSW input into the NAP [van Caspel *et al*. 2018; Wang *et al*. 2022]. Therefore, it is reasonable to conclude that the high interannual variability in nutrient concentrations along the NAP is driven mainly by changes in ocean circulation and water mass mixing caused by strong variability in the SAM. The effect of ENSO variability on silicic acid concentrations via advected DSW is more evident while its effect on DIN and phosphate concentrations is often counteracted because DIN and phosphate are also high in DSW.

In addition, the effects of SAM and ENSO on the biogeochemistry of waters along the NAP can either superimpose or counteract each other, depending on whether the region experiences concomitant periods of positive SAM and positive ENSO or vice versa [e.g., Stammerjohn *et al*. 2008]. Regarding our results, unfortunately, we could not accurately assess these combined effects because we only have a more robust time series in the last decade when the Southern Ocean has been experiencing successive positive SAM [e.g., Keppler *et al*. 2019] and negative ENSO conditions [Santoso *et al*. 2017]. Moreover, extreme events can trigger processes that change the concentration of macronutrients over different time scales. For example, the anomalously high silicic acid concentrations in 2017 (Fig. III-5), mainly noted in the central and eastern basins of Bransfield Strait, may have been a result of massive diatom blooms triggered by the intense positive ENSO during 2016 [e.g., Costa *et al*.

2020, 2021], which were subsequently remineralised. Although they were recorded during the summer of 2016, reaching chlorophyll *a* concentrations > 45 mg m^{-3} with more than 95% composed of diatoms [e.g., Costa *et al*. 2020], these blooms are thought to occur over a wider temporal window, including early austral spring [Gonçalves-Araujo *et al*. 2015; Ferreira *et al*. 2020). Therefore, these anomalously high concentrations of silicic acid in 2017 may be a result of subsequent remineralisation of the intense diatom blooms during 2016. In fact, silica concentrations as high as 110 µmol kg^{-1} have been recorded above 150 m in this region, associated with high diatom biomass in the 1980s [Heywood & Priddle, 1987]. Nevertheless, such an anomalous increase in silicic acid likely was the result of an additional supply besides the remineralisation of diatom blooms, as DIN and phosphate concentrations were not anomalously high. Although it is unclear what the additional sources of silicic acid there were in this year, these could be linked to other extreme events during 2016. Since March 2016, an iceberg with an area of approximately 10% of the Larsen-C Ice Shelf began its calving process until it was calved off the ice shelf in July 2017 [Hogg & Gudmundsson, 2017]. Since continental ice can be an important source of silicic acid to the polar oceans [Hawkings *et al*. 2017], the calving process of this iceberg may have been one of the additional sources of silicic acid for the NAP. Furthermore, a dramatic switch from the strong positive SAM index in September to the strong negative SAM index in November 2016 favoured a 3°C anomalous increase in air temperature over the Weddell Sea [Turner *et al*. 2020]. This rapid change has led to a record reduction in sea ice extent in the Weddell Sea since the satellite era began [Turner *et al*. 2020]. Both the strong positive SAM index and the reduction in sea ice extent may have intensified the influence of modified

Warm Deep Water with high silicic acid concentrations (> 125 µmol kg^{-1}) [Hoppema *et al*. 2015] in the northwestern Weddell Sea. Hence, part of the anomalous increase in silicic acid in 2017 may be associated with this chain of extreme events, as modified Warm Deep Water influences the waters that are advected to the Bransfield Strait [e.g., van Caspel *et al*. 2018; Barlett *et al*. 2018]. We cannot account for the impact of each event on the additional increase in silicic acid. However, this increase is more likely to be associated with events in the Weddell Sea, as the highest concentrations were recorded in the central and eastern basins of Bransfield Strait (Fig. III-5). This suggests that the calving process of the giant iceberg from the Larsen-C Ice Shelf probably had a greater impact on silicic acid concentrations due to input from sediments on the shallow continental shelf.

3. 4. 4 Seasonal macronutrients drawdown

Despite the high concentration of macronutrients that we observed throughout the NAP environments, supporting high primary productivity, Gerlache Strait and the western basin of Bransfield Strait appear to be the most favourable regions for strong phytoplankton growth. Seasonal nutrient drawdown in these regions is nearly double that observed in the rest of the NAP (Fig. III-8). There is a clear south-north decreasing gradient in seasonal nutrient drawdown along the NAP. Even in the Gerlache Strait, where the seasonal drawdown is higher (Fig. III-8), it is lower than that found at the Palmer Station region [Kim *et al*. 2016] and further south along the WAP [Henley *et al*. 2017, 2018]. The relatively lower seasonal drawdown of macronutrients, reaching values close to zero (Fig. III-8) along the NAP, occurs because the surrounding environments

are more exposed regions, prone to be influenced by mCDW intrusions [García *et al*. 2002; Parra *et al*. 2020] and normally show a high degree of mixing in the water column structure. However, as Gerlache Strait and the western basin of Bransfield Strait are shallower, more enclosed areas, and closer to the coast, they are more likely to experience increased upper ocean stability as a result of sea ice melting and glacial freshwater input. Such conditions are favourable to phytoplankton blooms [Costa *et al*. 2020; Ferreira *et al*. 2022] and, therefore, to greater seasonal drawdown of macronutrients. As the summer phytoplankton blooms in these regions are dominated by diatoms [Costa *et al*. 2020, 2021; Ferreira *et al*. 2022], which are known to enhance CO_2 uptake [Brown *et al*. 2019; Costa *et al*. 2020], these regions also act as a strong summer atmospheric CO_2 sink [Monteiro *et al*. 2020a,b]. The dominance of phytoplankton growth either by diatoms or smaller cells was thought to act as an additional control factor over the magnitude of CO_2 uptake in Gerlache Strait [Kerr *et al*. 2018c]. In fact, the highest seasonal drawdown of silicic acid was recorded in Gerlache Strait in 2016 (Fig. III-8c), when there was an intense diatom bloom [Costa *et al*. 2020] and the strongest summer CO_2 uptake since 1999 [Monteiro *et al*. 2020a,b]. The great interannual variability in seasonal nutrient drawdown must also be driven to some extent by winter sea ice cover [Kim *et al*. 2016; Henley *et al*. 2017]. During the negative SAM condition, increased winter sea ice cover enhances the upper ocean stability driving phytoplankton blooms in the following summer [Saba *et al*. 2014], increasing the seasonal nutrient drawdown [Kim *et al*. 2016]. Moreover, diatom blooms can be strengthened by the release of diatom cells residing within the sea ice when there is intense sea ice melting during the summer [Kim *et al*. 2016]. Hence, part of the high interannual variability in nutrient concentration

associated with the SAM and ENSO climate modes along the NAP must be driven by the oscillation in sea ice extent, which is also driven by SAM and ENSO.

3. 5 Conclusions

High concentrations of macronutrients (DIN, phosphate, and silicic acid) were recorded during austral summer in environments along the NAP. The macronutrient concentrations exhibited huge interannual variability, reaching up to three-fold changes in silicic acid and two-fold changes in phosphate concentrations among the annually-averaged profiles for each region. The coupling of mCDW intrusions together with local sources, such as remineralisation of organic matter, terrigenous inputs of silicic acid, mesoscale structures and circulation, and sea ice dynamics, explains the high nutrient concentrations found along the NAP. The great interannual variability is also driven largely by the extent of mCDW intrusions and its mixing with the DSW advected from the Weddell Sea, which can be intensified by local mesoscale processes. The strength of mCDW intrusions, and hence nutrient supply, is often modulated by the SAM, and to a lesser extent by ENSO. However, further studies are still needed to better decouple their influences on changes in the mixture between mCDW and DSW. In addition, we found stoichiometric uptake ratios of DIN/phosphate less than 16 and silicic acid/DIN greater than 1, associated with high phytoplankton biomass, mainly composed of diatoms, which have been associated to strong CO_2 uptake in the coastal and relatively shallow zone of the NAP. Despite the enhanced summer phytoplankton growth, relatively low seasonal nutrient drawdown was found in most sub-regions of the NAP, reaching down to near-zero drawdown for phosphate and silicic acid. This is likely due to

the high supply of macronutrients from different sources, which makes NAP environments highly favourable for growth and development of phytoplankton blooms. This is particularly important as the NAP is one of the most productive regions in the Southern Ocean and where major climate-driven change is being observed. Hence, these findings are critical to improving our understanding of the natural variability of Southern Ocean ecosystems and informing our predictions of how these nutrient inputs may respond to ongoing and expected climate and environmental change.

Acknowledgements

***** Todos os agradecimentos e financiadores serão listadas ao final deste documento.

References

***** As referências serão listadas ao final deste documento, contendo todas as referências utilizadas nesta tese.

APÊNDICE I

Este apêndice contém as seguintes figuras mencionadas no capítulo III: Fig. III-S1; Fig. III-S2; Fig. III-S3; Fig. III-S4; Fig. III-S5; Fig. III-S6; Fig. III-S7 e Fig. III-S8. E a tabela Tab. III-S1.

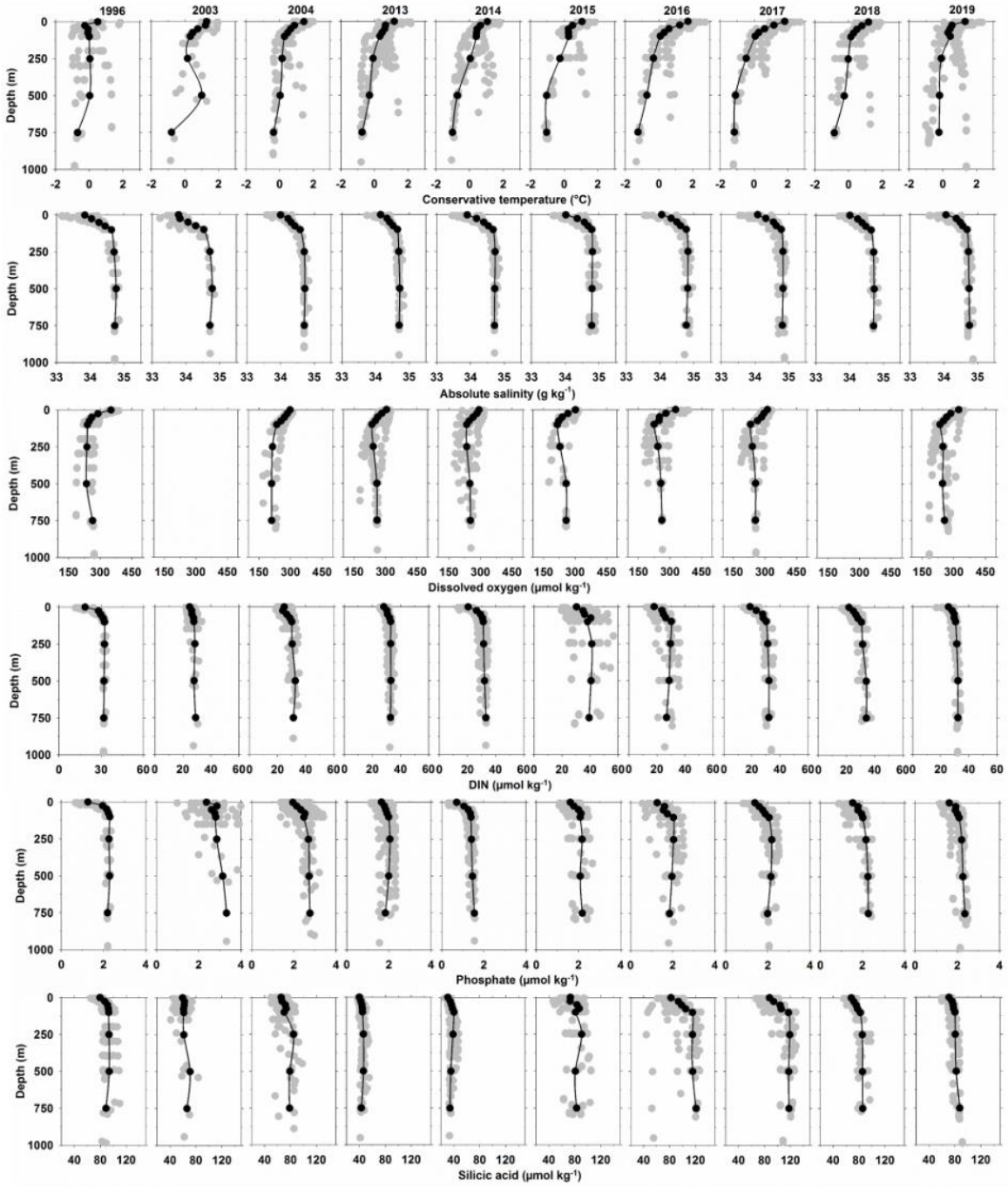

Figure III-S1: The gray dots show the profiles of hydrographic parameters and macronutrients sampled in the austral summer along the Gerlache Strait from 1996 to 2019 and the black dots show the average profiles of each property, used to compose Figs. III-4 and III-5 in the main text.

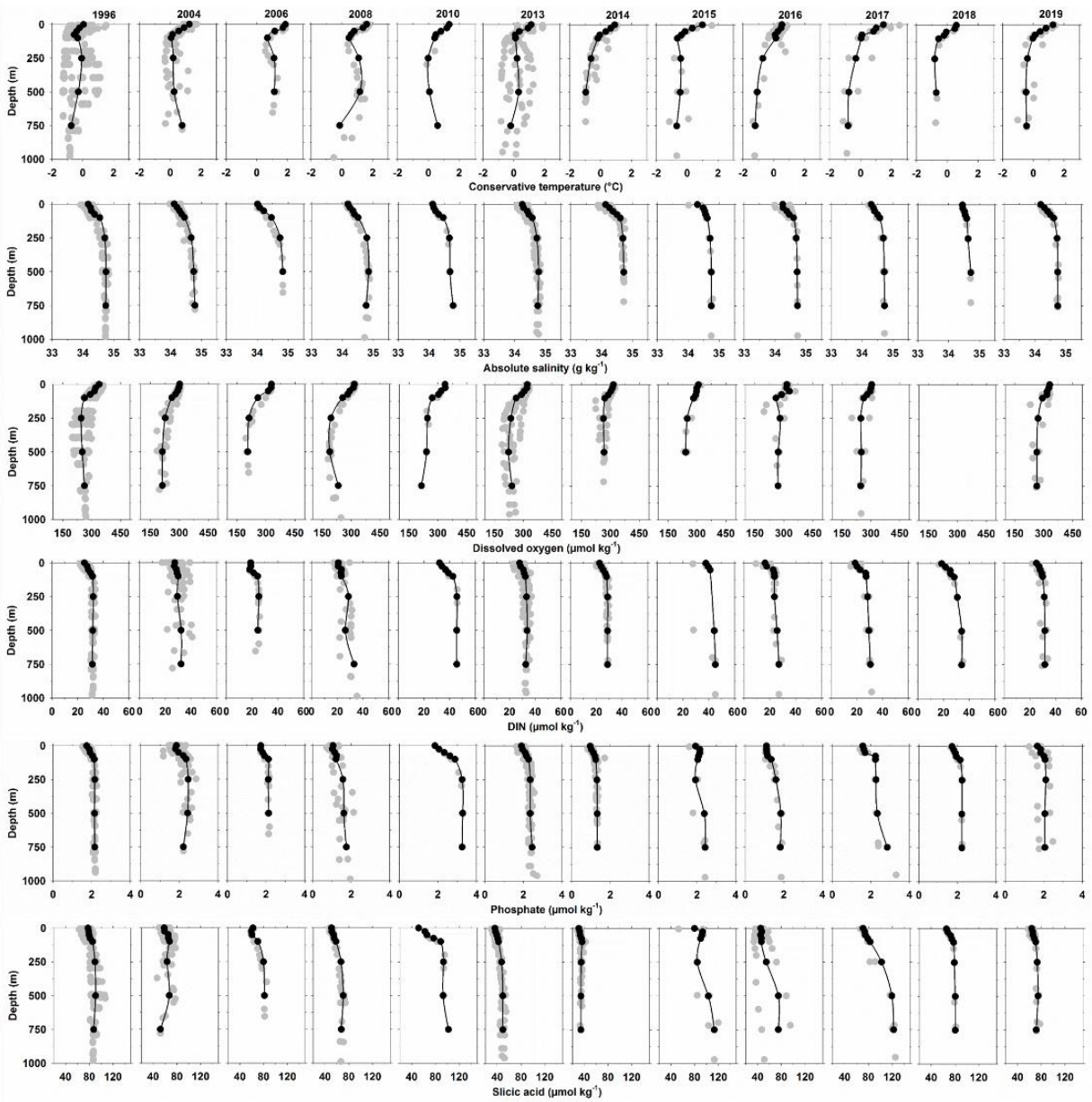

Figure III-S2: The gray dots show the profiles of hydrographic parameters and macronutrients sampled in the austral summer along the western basin of the Bransfield Strait from 1996 to 2019 and the black dots show the average profiles of each property, used to compose Figs. III-4 and III-5 in the main text.

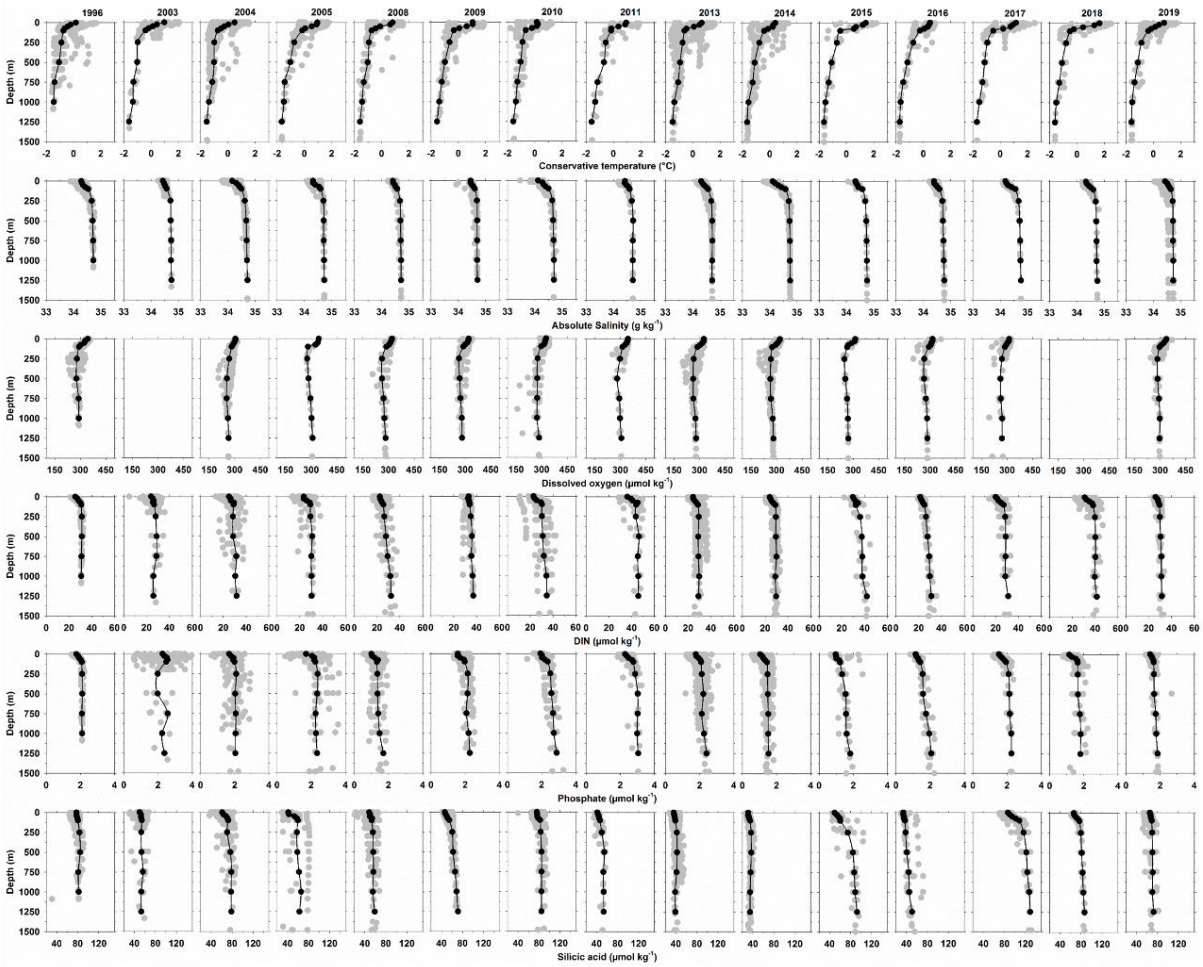

Figure III-S3: The gray dots show the profiles of hydrographic parameters and macronutrients sampled in the austral summer along the central basin of the Bransfield Strait from 1996 to 2019 and the black dots show the average profiles of each property, used to compose Figs. III-4 and III-5 in the main text.

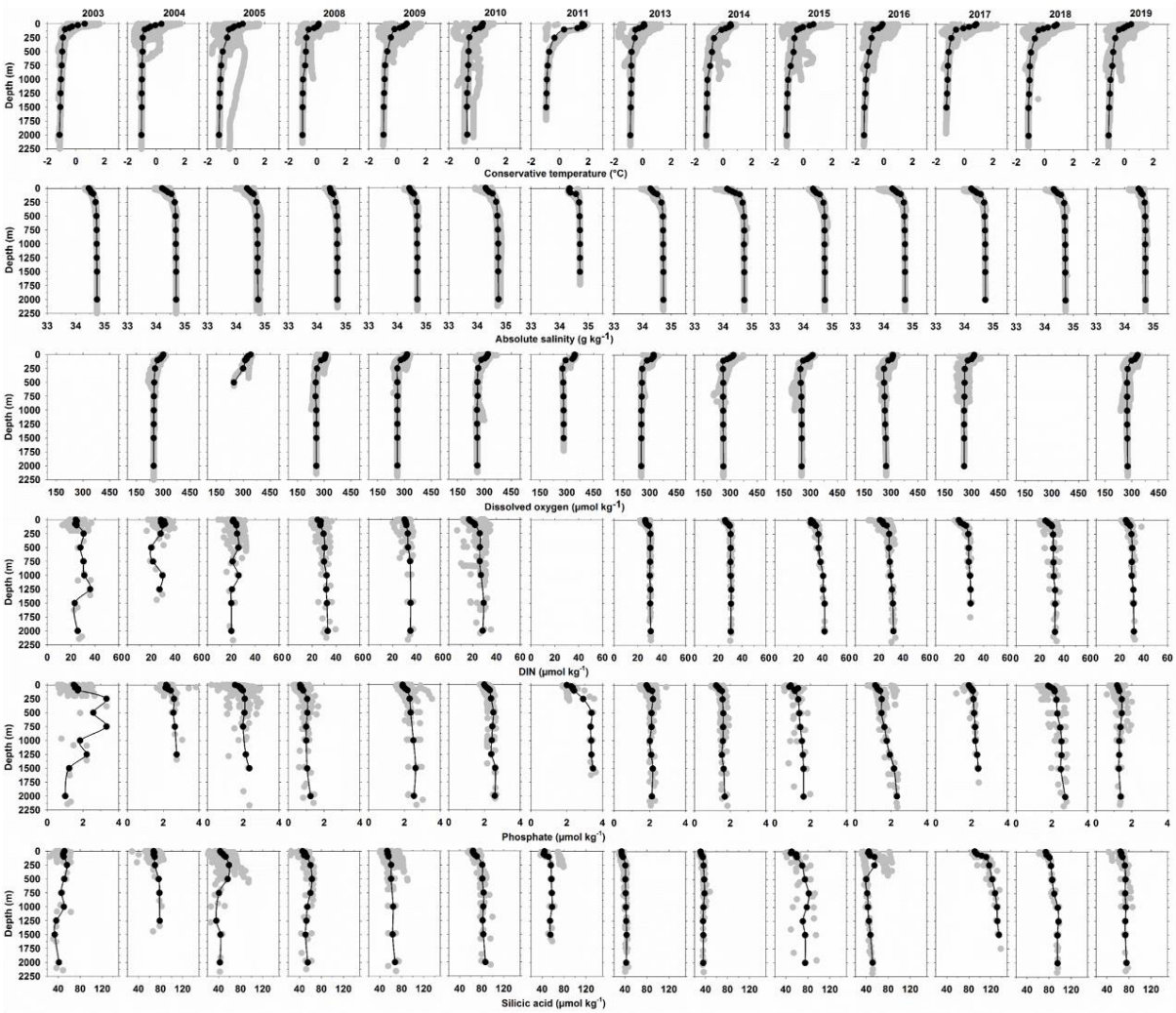

Figure III-S4: The gray dots show the profiles of hydrographic parameters and macronutrients sampled in the austral summer along the eastern basin of the Bransfield Strait from 1996 to 2019 and the black dots show the average profiles of each property, used to compose Figs. III-4 and III-5 in the main text.

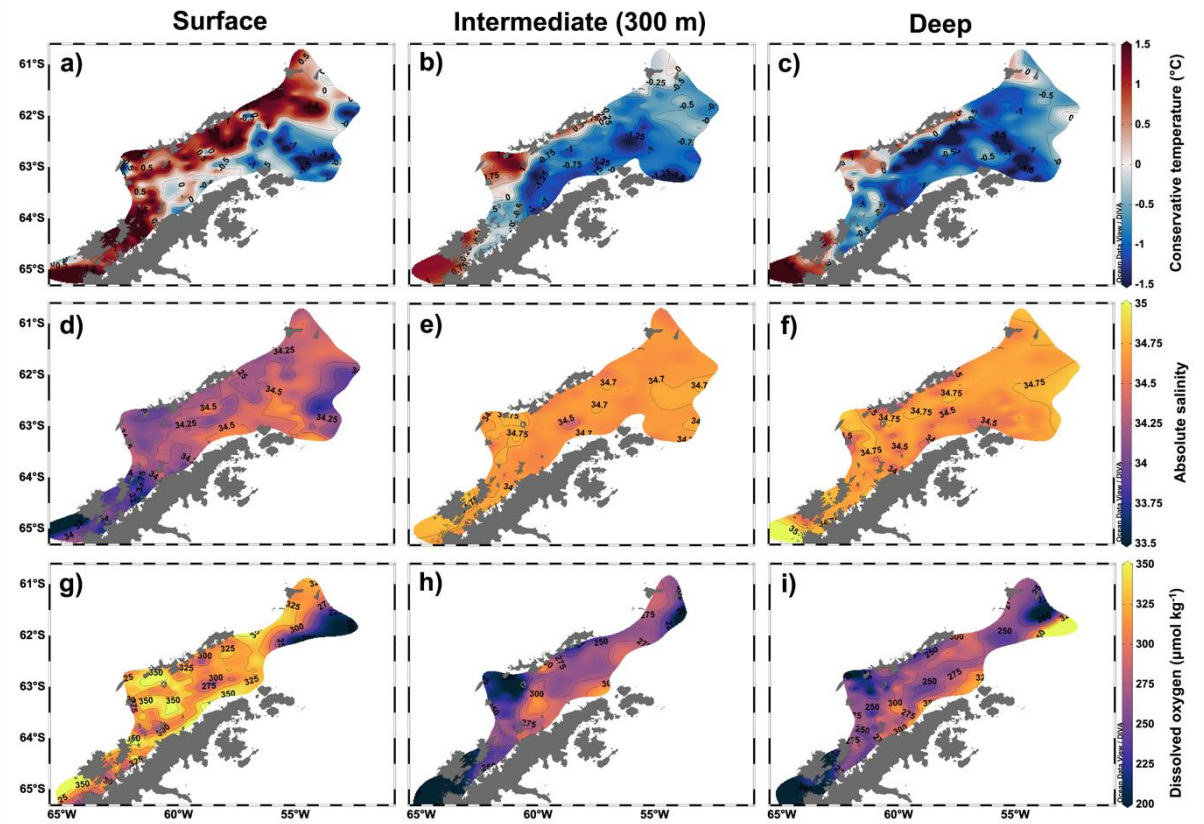

Figure III-S5: Surface (up to 5m), intermediate (at 300m) and deep spatial distribution of (a-c) conservative temperature, (d-f) absolute salinity, and (g-i) dissolved oxygen during austral summer (Jan-Mar) along the northern Antarctic Peninsula from 1996 to 2019.

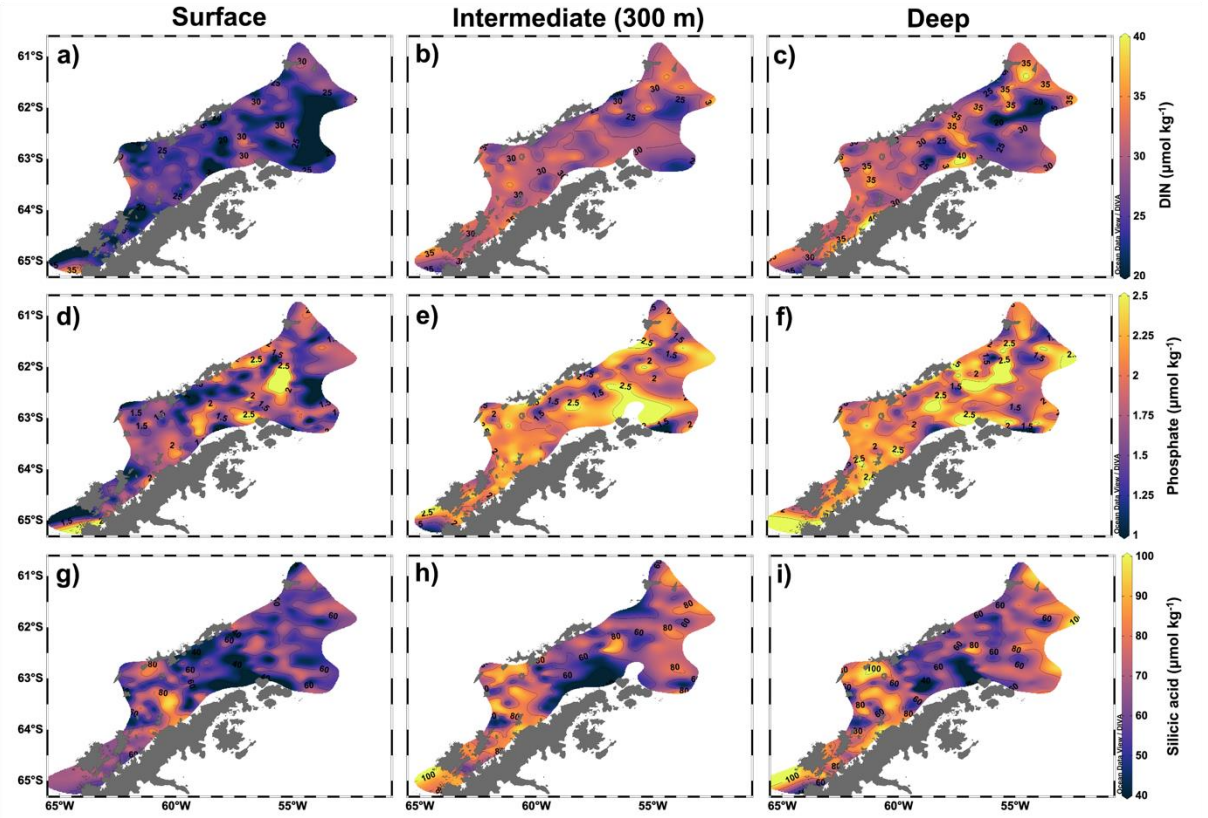

Figure III-S6: Surface (up to 5m), intermediate (at 300m) and deep spatial distribution of (a-c) dissolved inorganic nitrogen (DIN), (d-f) phosphate, and (g-i) silicic acid during austral summer (Jan-Mar) along the northern Antarctic Peninsula from 1996 to 2019.

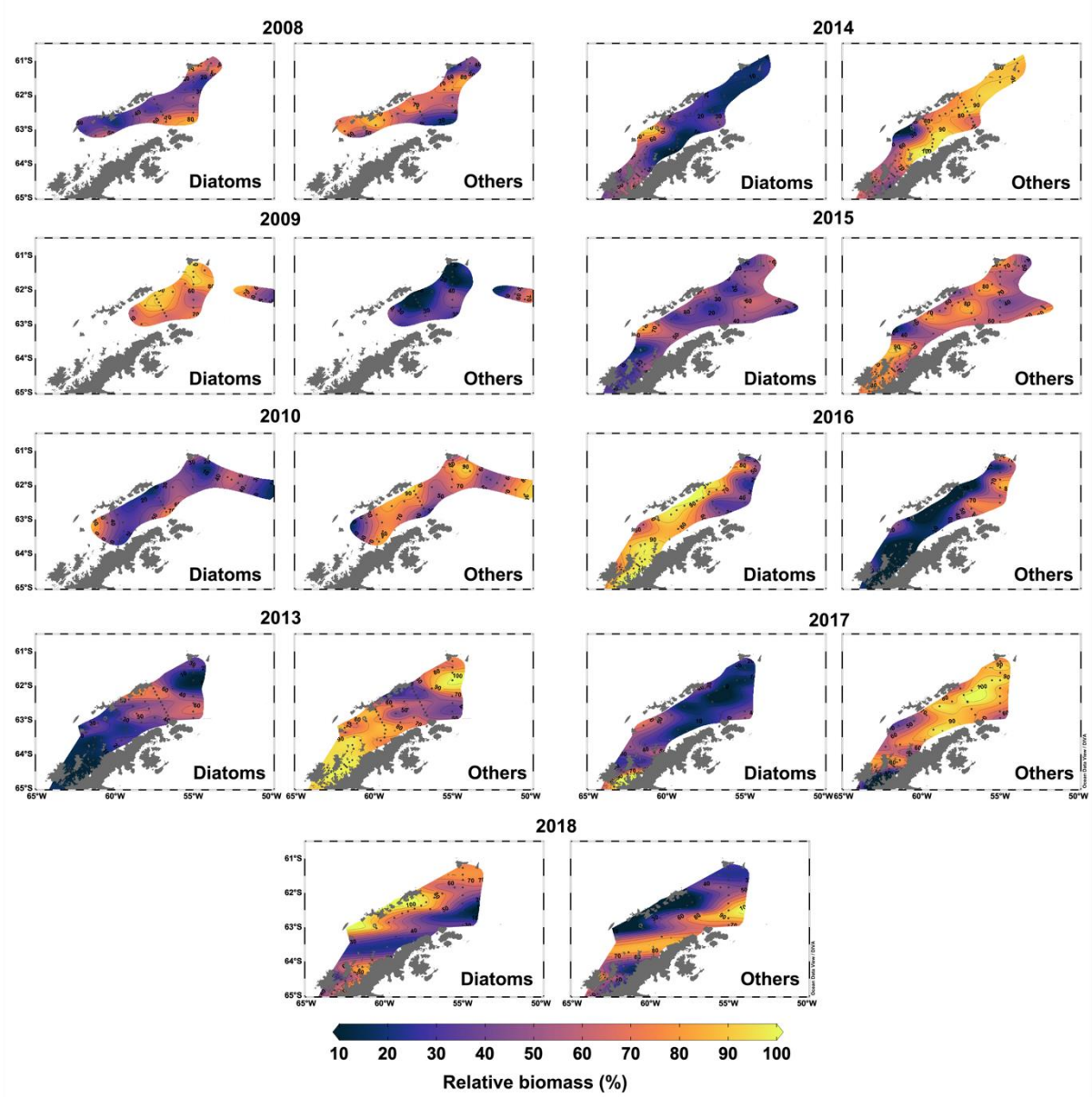

Figure III-S7: Percentage of relative phytoplankton biomass during austral summer along the northern Antarctic Peninsula from 2008 to 2018. Here we separate the phytoplankton composition between diatoms and other smaller groups (Dinoflagellates, Phaeocystis, Cryptophytes, and green flagellates). All analyses of the composition of phytoplankton groups used here are detailed in Costa *et al*. (2020, 2021 and references therein).

Table III-S1: DIN/phosphate and silicic acid/DIN regression statistics for the summer profiles in each year along the northern Antarctic Peninsula. The ratios ± the standard deviations are the slope and root mean square error from the regressions, respectively.

	Year	Gerlache Strait	Western Bransfield	Central Bransfield	Eastern Bransfield
DIN/P statistics	1996	13.38 ± 0.59 (R^2=0.99; p<0.001; n=8)	15.66 ± 0.46 (R^2=0.99; p<0.001; n=8)	16.24 ± 0.40 (R^2=0.99; p<0.001; n=9)	
	2003	3.94 ± 1.07 (R^2=0.69; p=0.010; n=8)			
	2004	10.28 ± 1.59 (R^2=0.88; p<0.001; n=8)	7.21 ± 1.53 (R^2=0.82; p=0.005; n=7)	12.69 ± 3.67 (R^2=0.63; p=0.011; n=9)	
	2005			11.86 ± 2.69 (R^2=0.71; p=0.002; n=10)	6.44 ± 3.07 (R^2=0.42; p<0.081; n=8)
	2006		15.25 ± 2.36 (R^2=0.91; p=0.003; n=6)		
	2008		14.4 ± 2.10 (R^2=0.89; p<0.001; n=8)	15.62 ± 2.74 (R^2=0.80; p<0.001; n=10)	13.12 ± 1.94 (R^2=0.84; p<0.001; n=11)
	2009			5.64 ± 0.79 (R^2=0.86; p<0.001; n=10)	6.76 ± 0.49 (R^2=0.97; p<0.001; n=9)
	2010		9.57 ± 0.23 (R^2=0.99; p<0.001; n=8)	11.68 ± 1.30 (R^2=0.91; p<0.001; n=10)	19.77 ± 1.31 (R^2=0.96; p<0.001; n=11)
	2011			11.35 ± 1.71 (R^2=0.86; p<0.001; n=9)	
	2013	12.19 ± 2.62 (R^2=0.78; p=0.003; n=8)	10.19 ± 1.35 (R^2=0.90; p<0.001; n=8)	9.38 ± 1.59 (R^2=0.81; p<0.001; n=10)	13.57 ± 1.87 (R^2=0.84; p<0.001; n=12)
	2014	15.09 ± 0.41 (R^2=0.99; p<0.001; n=8)	17.46 ± 0.71 (R^2=0.99; p<0.001; n=7)	12.77 ± 0.79 (R^2=0.97; p<0.001; n=10)	11.58 ± 1.19 (R^2=0.90; p<0.001; n=12)
	2015	17.25 ± 2.46 (R^2=0.89; p<0.001; n=8)	14.95 ± 2.02 (R^2=0.95; p=0.005; n=6)	12.74 ± 1.01 (R^2=0.95; p<0.001; n=10)	12.81 ± 1.33 (R^2=0.94; p<0.001; n=8)
	2016	14.41 ± 1.15 (R^2=0.96; p<0.001; n=8)	9.00 ± 2.96 (R^2=0.61; p=0.023; n=8)	10.89 ± 0.71 (R^2=0.97; p<0.001; n=10)	8.78 ± 1.19 (R^2=0.85; p<0.001; n=12)
	2017	16.30 ± 2.02 (R^2=0.92; p<0.001; n=8)	9.62 ± 1.31 (R^2=0.90; p<0.001; n=8)	13.70 ± 1.00 (R^2=0.96; p<0.001; n=10)	21.60 ± 2.41 (R^2=0.90; p<0.001; n=11)
	2018	16.74 ± 1.37 (R^2=0.97; p<0.001; n=7)	24.80 ± 2.96 (R^2=0.93; p<0.001; n=7)	16.01 ± 0.91 (R^2=0.91; p<0.001; n=10)	8.84 ± 1.05 (R^2=0.88; p<0.001; n=12)
	2019	9.40 ± 0.87 (R^2=0.95; p<0.001; n=8)	13.72 ± 1.82 (R^2=0.82; p<0.001; n=7)	13.09 ± 0.94 (R^2=0.94; p<0.001; n=10)	20.29 ± 2.71 (R^2=0.90; p<0.001; n=8)

Continua na próxima página...

	Year	Gerlache Strait	Western Bransfield	Central Bransfield	Eastern Bransfield
Silicic acid/DIN statistics	1996	0.97 ± 0.14	1.8 ± 0.35	1.04 ± 0.25	
		(R^2=0.89; p<0.001; n=8)	(R^2=0.82; p=0.002; n=8)	(R^2=0.71; p=0.004; n=9)	
	2003	1.31 ± 0.96		0.81 ± 0.23	3.07 ± 0.47
		(R^2=0.24; p=0.223; n=8)		(R^2=0.64; p=0.010; n=8)	(R^2=0.84; p<0.001; n=10)
	2004	1.63 ± 0.50	1.73 ± 0.57	2.65 ± 0.37	
		(R^2=0.64; p=0.017; n=8)	(R^2=0.70; p=0.039; n=6)	(R^2=0.87; p<0.001; n=9)	
	2005			2.74 ± 0.30	3.69 ± 0.80
				(R^2=0.91; p<0.001; n=10)	(R^2=0.84; p<0.010; n=8)
	2006		2.78 ± 0.55		
			(R^2=0.86; p=0.007; n=6)		
	2008		1.54 ± 0.40	0.84 ± 0.16	3.02 ± 0.36
			(R^2=0.71; p=0.009; n=8)	(R^2=0.78; p<0.001; n=10)	(R^2=0.92; p<0.001; n=8)
	2009			5.55 ± 0.46	2.61 ± 0.26
				(R^2=0.95; p<0.001; n=10)	(R^2=0.93; p<0.001; n=9)
	2010		3.21 ± 0.25	0.88 ± 0.13	2.03 ± 0.18
			(R^2=0.97; p<0.001; n=8)	(R^2=0.84; p<0.001; n=10)	(R^2=0.93; p<0.001; n=11)
	2011			1.18 ± 0.31	
				(R^2=0.68; p=0.006; n=9)	
	2013	1.02 ± 0.23	2.33 ± 0.42	0.84 ± 0.22	2.01 ± 0.20
		(R^2=0.76; p=0.005; n=8)	(R^2=0.83; p=0.002; n=8)	(R^2=0.64; p=0.006; n=10)	(R^2=0.91; p<0.001; n=12)
	2014	0.65 ± 0.17	0.65 ± 0.17	0.91 ± 0.12	1.15 ± 0.17
		(R^2=0.75; p=0.012; n=7)	(R^2=0.76; p=0.002; n=8)	(R^2=0.88; p<0.001; n=10)	(R^2=0.82; p<0.001; n=12)
	2015	1.34 ± 0.40	3.83 ± 0.68	4.03 ± 0.38	4.05 ± 0.49
		(R^2=0.66; p=0.015; n=8)	(R^2=0.91; p<0.011; n=5)	(R^2=0.93; p<0.001; n=10)	(R^2=0.90; p<0.001; n=12)
	2016	3.09 ± 0.57	1.73 ± 1.17	1.56 ± 0.16	1.36 ± 0.18
		(R^2=0.83; p=0.002; n=8)	(R^2=0.31; p=0.197; n=7)	(R^2=0.92; p<0.001; n=10)	(R^2=0.86; p<0.001; n=12)
	2017	2.45 ± 0.22	3.97 ± 1.07	4.15 ± 0.34	4.34 ± 0.25
		(R^2=0.95; p<0.001; n=8)	(R^2=0.70; p=0.01; n=8)	(R^2=0.95; p<0.001; n=10)	(R^2=0.97; p<0.001; n=11)
	2018	1.53 ± 0.12	1.02 ± 0.11	1.89 ± 0.19	2.97 ± 0.46
		(R^2=0.97; p<0.001; n=7)	(R^2=0.95; p<0.001; n=7)	(R^2=0.92; p<0.001; n=10)	(R^2=0.81; p<0.001; n=12)
	2019	2.01 ± 0.31	1.67 ± 0.20	1.24 ± 0.11	1.67 ± 0.17
		(R^2=0.87; p<0.001; n=8)	(R^2=0.93; p<0.001; n=7)	(R^2=0.95; p<0.001; n=10)	(R^2=0.91; p<0.001; n=12)

Capítulo IV: Variabilidade sazonal e interanual do FCO_2 na NAP

Neste estudo foi investigada a variabilidade sazonal e interanual do FCO_2 no estreito de Gerlache, no NAP, entre 2002 e 2017. Foi identificado que durante oito meses (de abril a novembro) o estreito de Gerlache libera CO_2 para a atmosfera, mas em apenas quatro meses (de dezembro a março) essa região absorve quase a mesma quantidade de CO_2 que é liberada nos outros oitos meses. Como consequência, o FCO_2 médio anual entre 2002 e 2017 foi de $1{,}24 \pm 4{,}33$ mmol m^{-2} dia^{-1}, mostrando que o ciclo do carbono nessa região é muito mais sensível que se imaginava. Além disso, os processos que controlam o ciclo sazonal do FCO_2 foram identificados, sendo a fotossíntese a principal responsável pela intensa absorção de CO_2 durante o verão e a afloração de águas ricas em CO_2, principalmente CDW, como o principal responsável pela liberação de CO_2 nas outras estações do ano. Este estudo foi publicado no periódico *Scientific Reports* (https://doi.org/10.1038/s41598-020-71814-0).

Seasonal variability of net sea-air CO_2 fluxes in a coastal region of the northern Antarctic Peninsula

Thiago Monteiro, Rodrigo Kerr and Eunice Machado

Veja online aqui

4. 1 Introduction

The investigation of Antarctic coastal regions has long been neglected because they are difficult to access [Takahashi *et al*. 2009; Lenton *et al*. 2013; Takahashi *et al*. 2014; Roobaert *et al*. 2019], especially during periods other than the austral summer [Gibson & Trull 1999; Metzl *et al*. 2006; Roden *et al*. 2013; Legge *et al*. 2015]. This occurs because of most of the year (i.e., from April to November), these regions are almost completely or completely covered by sea ice [Cavalieri & Parkinson 2008; Parkinson & Cavalieri 2012]. Such conditions lead to a biased representation of sampling in autumn and winter, which are likely critical periods for changes in seawater carbonate chemistry and FCO_2.

In fact, several studies have been conducted during the austral summer to better understand the FCO_2 [Karl *et al*. 1991; Takahashi *et al*. 1993; Arrigo & Van Dijken 2007; Brown *et al*. 2019; Monteiro *et al*. 2020a; Caetano *et al*. 2020] and carbonate system parameter variability [Nomura *et al*. 2014; Jones *et al*. 2017; Legge *et al*. 2017; Kerr *et al*. 2018a; Kerr *et al*. 2018b; Lencina-Avila *et al*. 2018] in the remote Southern Ocean. It is widely known that the Antarctic coasts behave as a strong CO_2 sink during the summer [Monteiro *et al*. 2020a; Dejong & Dunbar 2017], which has intensified during recent years [Brown *et al*. 2019; Monteiro *et al*. 2020a]. Actually, the intensity of this behaviour is marked by high interannual variability, since the summer FCO_2 in the Gerlache Strait, for example, oscillate between periods of strong CO_2 sink (i.e., < -12 mmol m^{-2} day^{-1}) and sea-air near-equilibrium conditions at inter-annual scales [Monteiro *et al*. 2020]. However,

even when Antarctic coastal regions do not behave as a strong CO_2 sink, they take up CO_2 in the summer [Monteiro *et al*. 2020a], although eventual episodes of CO_2 outgassing can occur [Kerr *et al*. 2018a].

Although some studies have provided important information on the seasonality of the FCO_2 [Roden *et al*. 2013; Legge *et al*. 2015; Legge *et al*. 2017], they are restricted to a few specific years or localised regions, which may bias the modelled long-term trends of these regions. Hence, understanding the annual budget of FCO_2 remains a challenge [Roobaert *et al*. 2019; Henley *et al*. 2019]. This is particularly true for the Gerlache Strait and likely other major embayments around the Antarctic coasts since it remains unclear whether this CO_2 sink behaviour persists throughout the year or is balanced in other seasons. Moreover, little is known about the main drivers of FCO_2 seasonality and their consequences for the sea surface carbonate system.

Therefore, here, we present an annual overview of the FCO_2 and the carbonate system properties in the Gerlache Strait, an ecologically and climatically important area of the NAP. Furthermore, we demonstrate that this region acted as an annual net CO_2 source to the atmosphere from 2002 to 2017, contrasting with previous findings for the western Antarctic Peninsula environments [Roden *et al*. 2013; Legge *et al*. 2015; Legge *et al*. 2017] and other regions around Antarctica [Lenton *et al*. 2006; Bakker *et al*. 2008; Arrigo *et al*. 2008].

4. 2 Oceanographic features of the Gerlache Strait

The Gerlache Strait is a coastal region along the NAP that is being impacted by climate change [Henley *et al*. 2019; Kerr *et al*. 2018c] and is

essential for the health of the Antarctic food web [Nowacek *et al*. 2011; Dalla Rosa *et al*. 2008; Mendes *et al*. 2018]. The strait is a shallow basin that lies between the NAP and the Palmer Archipelago and is connected to the Bellingshausen Sea (to the west) and the Bransfield Strait (to the north) (Fig. IV-1a,b). Although it covers a smaller area (~ 8000 km^2) than other coastal regions around the NAP, the Gerlache Strait is a highly productive coastal zone.

In the Gerlache Strait, records of chlorophyll a (used as an indicator of primary producer biomass) range from ~ 2.0 mg m^{-3} [Mendes *et al*. 2018] to ~ 23 mg m^{-3} [Costa *et al*. 2020] under distinct austral summer conditions. These concentrations have the same or a greater magnitude than those observed in more extensive regions, such as the Bransfield Strait (4.4 ± 3.84 mg m^{-3}) [Costa *et al*. 2020] and the northwestern Weddell Sea (1.38 ± 2.01 mg m^{-3}) [Ito *et al*. 2018]. In addition, the Gerlache Strait has experienced intense diatom blooms reaching > 45 mg m^{-3} of chlorophyll a [Costa *et al*. 2020]. Although higher, this value is consistent with that recorded in the vicinity of Palmer Station, in the southernmost part of the Gerlache Strait, where the maximum chlorophyll a recorded was ~ 30 mg m^{-3} [Kim *et al*. 2018].

The high biological productivity in this region, reflected at different trophic levels [Secchi *et al*. 2011], is mainly due to the complex interplay of its distinct water mass sources, sea ice dynamics, ocean circulation, nutrient-rich meltwater input and protection from severe weather conditions [Prézelin *et al*. 2000; Wadham *et al*. 2019]. Additionally, the rapid effects of climate change [Henley *et al*. 2019; Kerr *et al*. 2018c; Meredith & King 2005], a recent increase in glacial meltwater discharge [Moreau *et al*. 2015], and likely the advection of both organic and anthropogenic carbon around the NAP [Kerr *et al*. 2018b; da Cunha *et al*.

2018; Avelina *et al*. 2020] have influenced the coupled physical-biological processes changing the carbon biogeochemistry across the entire western Antarctic Peninsula shelf region [Kerr *et al*. 2018c; Moreau *et al*. 2015].

Moreover, the Gerlache Strait is affected by irregular intrusions of CDW [e.g., Prézelin *et al*. 2000; Smith *et al*. 1999; García *et al*. 2002; Couto *et al*. 2017] (Fig. IV-1b). CDW is a warm, salty, poorly oxygenated, and carbon- and nutrient-rich water mass flowing eastward with the ACC at intermediate and deep levels around the continent [García *et al*. 2002; Barllet *et al*. 2018; Cape *et al*. 2019]. CDW intrusions along the western shelf of the Antarctic Peninsula are often associated with upwelling, mainly caused by shallow bathymetry [Venables *et al*. 2017] and predominant wind systems [Prézelin *et al*. 2000].

These intrusions are also affected by modes of climate variability that regulate the intensity of winds in the Southern Ocean, such as the ENSO and SAM [Barllet *et al*. 2018; Stammerjohn *et al*. 2008; Dinniman *et al*. 2012]. During the positive phases of the SAM, the westerly winds are intensified, and the frequency and intensity of episodic CDW intrusions increase [Barllet *et al*. 2018]. Conversely, under extreme ENSO, winds are weakened and cooled [Stammerjohn *et al*. 2008], probably reducing CDW intrusions on the western shelf of the Antarctic Peninsula. Under any of these conditions, the physical properties of CDW change when it is mixed with cooler and less saline surface waters, originating the mCDW in the shelf and coastal domain.

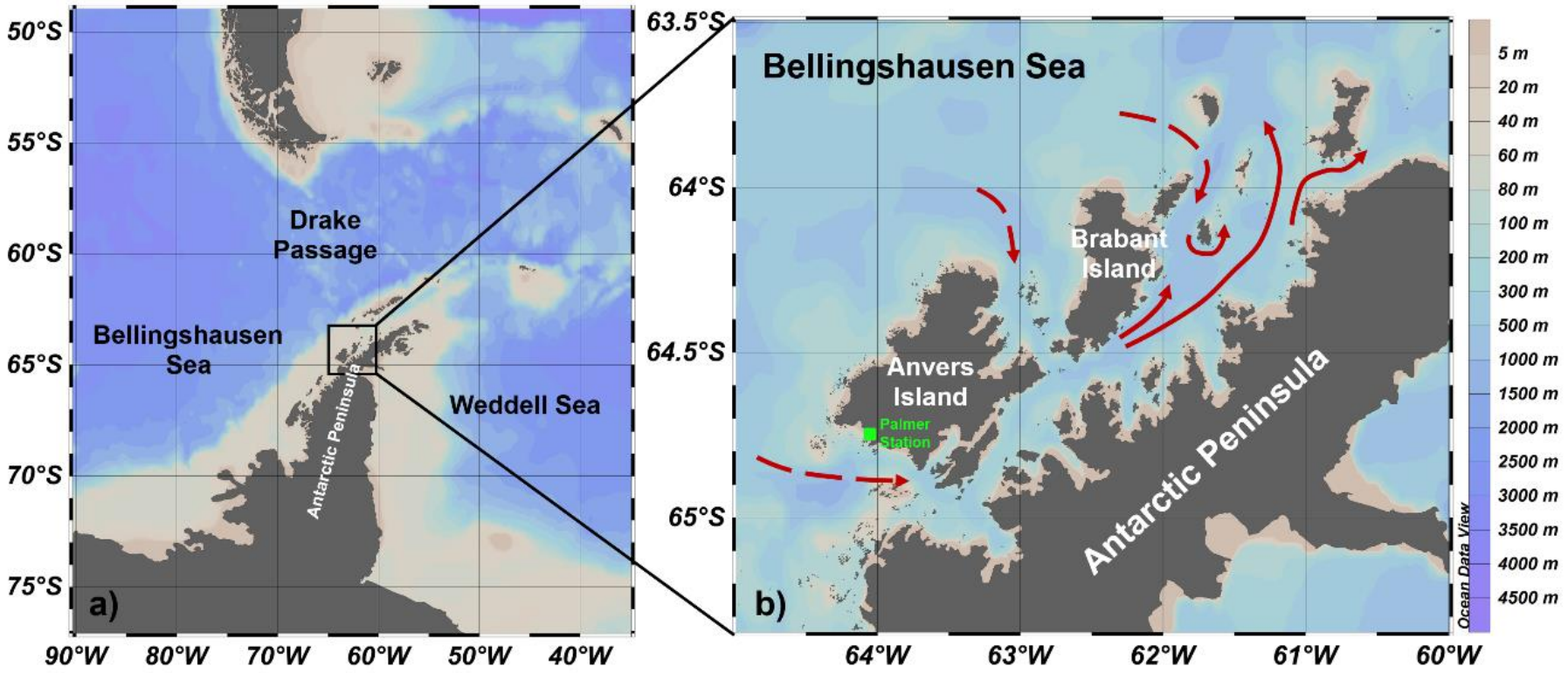

Figure IV-1: Location of the (a) western and northern Antarctic Peninsula and the (b) Gerlache Strait, with a simplified surface circulation pattern (red arrows) that is strongly influenced by the Bellingshausen Sea. The surface circulation in (b) was based on Savidge & Amft [2009]. The dashed red arrows represent the modified Circumpolar Deep Water intrusions into the strait, which were identified by Smith *et al*. [1999], Prézelin *et al*. [2000] and García *et al*. [2002]. The green square depicts the U.S. Palmer Station location (64.8°S, 64.1°W), from which we extracted atmospheric data. The colour shading represents the bottom bathymetry. These maps were generated by using the software Ocean Data View (v. 5.3.0, https://odv.awi.de).

At depths greater than 100 m, the Gerlache Strait is influenced by the mixing of water masses sourced from the Bellingshausen and Weddell seas. In addition to mCDW, the north of the strait is influenced by a modified variety of High Salinity Shelf Water (HSSW), which is cooler and more oxygenated than CDW [Barllet *et al*. 2018; Zhou *et al*. 2002]. HSSW is formed on the northwestern Weddell Sea continental shelf and is advected towards and along the Bransfield Strait by the Antarctic Coastal Current [Zhou *et al*. 2002; Dotto *et al*. 2016]. Signs of its presence at deep levels of the Gerlache Strait are an important aspect of the NAP because HSSW is younger than CDW, and the biogeochemical impact of mixing between the modified varieties of these waters is not yet completely understood [Kerr *et al*. 2018b; Lencina-Avila *et al*. 2018; da Cunha *et al*. 2018]. However, a consequence of HSSW is the intrusion of anthropogenic carbon in deep levels of the strait (Lenton *et al*., 2006; Bakker *et al*., 2008), which can intensify the ocean acidification process in the region.

4. 3 Material and Methods

4. 3. 1 Dataset and carbonate system properties

We used the data available from SOCAT [Bakker *et al*. 2016] to compile a temporal series spanning 2002 to 2017 (Fig. IV-S2) of the SST, SSS and pCO_2^{sw} of the Gerlache Strait. Here, we evaluated the seasonal variability of the FCO_2 and hydrographic and carbonate system parameters. Therefore, the seasons were defined as (1) summer: January to March; (2) autumn: April to June; (3) winter: July to September; and (4) spring: October to December. We analysed the months in which the data covered the majority of the Gerlache Strait in all seasons (Fig. IV-S3).

The pCO_2^{sw} data extracted from SOCAT were directly measured using air–water equilibrators and an infrared analyser for CO_2 quantification [Bakker *et al*. 2016]. However, SOCATv6 provides surface pCO_2^{sw} data with only corresponding SST and SSS values. Hence, we used A_T from the GOAL [Mata *et al*. 2018] and the World Data Centre PANGAEA [Hellmer & Rohardt 2010] to estimate A_T from SSS using Eq. IV-1 ($r^2 = 0.98$, RMSE = 4.4, n = 140).

$$A_T = 36.72 \times SSS + 1052 \qquad \text{IV-1}$$

These data were sampled in the austral summers of 1995/96 (PANGAEA; https://doi.pangaea.de/10.1594/PANGAEA.825645) [Anadón & Estrada 2002] and 2015–2019 (GOAL); [Monteiro *et al*. 2020; Lencina-Avila *et al*. 2018]. Equation 1 was developed using the curve fitting toolbox of MATLAB, with the least absolute residual mode and first-order polynomial adjustment. This option considered all the data important, minimised the residuals, and can be used when data series have few nonconfigurable values [Patil & Rao1994].

Using the estimated A_T and pCO_2^{sw} from SOCATv6, we calculated the C_T, pH, Ω_{Ca} and Ω_{Ar} with CO2SYS version 2.1 [Lewis *et al*. 1998; Pierrot *et al*. 2006]. This program determines these parameters from the thermodynamic equilibrium relation among the carbonate species using carbonate dissociation constants. Because of the good response obtained in high-latitude regions [Brown *et al*. 2019; Monteiro *et al*. 2020a; Kerr *et al*. 2018a; Millero *et al*. 2002; Laika *et al*. 2009], we used the constants K1 and K2 proposed by Goyet & Poisson [1989] and the sulphate and borate constants proposed by Dickson [1990] and Uppström [1974], respectively.

4. 3. 2 Drivers of pCO_2^{sw} changes

The pCO_2^{sw} drivers throughout the seasons were calculated based on the difference between the values of the parameters in each season and their respective averages in previous seasons (ΔpCO_2^{drv}; Table IV-1). Then, the ΔpCO_2^{drv} values were separated into categories representing the contributions of differences in C_T, A_T, SST and SSS. The relative contributions of the drivers changing pCO_2^{sw} were assessed by converting their relative changes into pCO_2^{sw} units (µatm) following Lenton *et al*. [2012] as in Eq. IV-2:

$$\Delta pCO_2^{drv} = \frac{\partial pCO_2^{sw}}{\partial C_T}\Delta C_T + \frac{\partial pCO_2^{sw}}{\partial A_T}\Delta A_T + \frac{\partial pCO_2^{sw}}{\partial SST}\Delta SST + \frac{\partial pCO_2^{sw}}{\partial SSS}\Delta SSS \qquad \text{IV-2}$$

where ΔC_T, ΔA_T, ΔSST and ΔSSS are the differences between the values of the parameters and their respective averages in previous seasons. This analysis was conducted in each year, and the results were averaged to represent an average year.

The partial derivatives were calculated using Eqs. IV-3 to IV-6 (see details in Takahashi *et al*. [2014]). These approximations have been widely used in the Southern Ocean [Lenton *et al*. 2012; Takahashi *et al*. 2014; Brown *et al*. 2019] to evaluate pCO_2^{sw} drivers, both seasonally and spatially. Here, we used the average Revelle and Alkalinity factors of 14 and −13, respectively.

$$\frac{\partial pCO_2^{sw}}{\partial C_T} = \frac{pCO_2^{sw}}{C_T} \times \text{Revelle Factor} \qquad \text{IV-3}$$

$$\frac{\partial pCO_2^{sw}}{\partial A_T} = \frac{pCO_2^{sw}}{A_T} \times \text{Alkalinity Factor} \qquad \text{IV-4}$$

$$\frac{\partial pCO_2^{sw}}{\partial SSS} \approx 0.026 \times pCO_2^{sw} \qquad \text{IV-5}$$

$$\frac{\partial pCO_2^{sw}}{\partial SST}\Delta SST \approx 2 \times pCO_2^{sw} \times \left(e^{0.0423 \times \frac{\Delta SST}{2}} - 1\right) \quad \text{IV-6}$$

Table IV-2: Average differences and standard deviations for the SST (°C), SSS, A_T (µmol kg^{-1}), and C_T (µmol kg^{-1}) involved in pCO_2^{sw} (µatm) changes. The table shows the differences between the values of the parameters in each season and their respective averages in previous seasons (ΔpCO_2^{drv}).

	Summer	Autumn	Winter	Spring
ΔSST	1.47 ± 0.62	–1.86 ± 0.59	–0.80 ± 0.34	0.86 ± 0.88
ΔSSS	–0.33 ± 0.48	0.34 ± 0.25	0.25 ± 0.20	–0.26 ± 0.29
ΔA_T	–12 ± 18	12 ± 9	9 ± 7	–9 ± 11
ΔC_T	–50 ± 52	62 ± 14	25 ± 10	–36 ± 42
ΔpCO_2^{drv}	–69 ± 70	87 ± 24	38 ± 22	–55 ± 70

4. 3. 3 Calculation of FCO_2

We calculated FCO_2 using Eq. IV-7 [Roobaert *et al*. 2019; Deacon 1977]:

$$FCO_2 = K_t \times K_s \times (1 - Ice)\,\Delta pCO_2 \quad \text{IV-7}$$

where ΔpCO_2 is the difference between pCO_2^{sw} and pCO_2^{air}; K_t is the gas transfer velocity, depending on wind speed [Wanninkhof 2014]; K_s is the CO_2 solubility coefficient, as a function of both SST and SSS [Weiss 1974]; and Ice is a dimensionless coefficient corresponding to the fraction of the air–water interface (between 0 and 1) covered by sea ice.

We used monthly averages of pCO_2^{air} and wind speed (m s^{-1}) data from the U.S. Palmer Station, located in the southern part of the Gerlache Strait. The station continuously measures meteorological parameters throughout the year [Dlugokencky *et al*. 2015]. We calculated pCO_2^{air} from the monthly averages of the xCO_2^{air} and atmospheric pressure (both from the Palmer Station), which was corrected by the water vapour pressure estimated from SST and SSS by the widely used equations of Weiss & Price [1980]. Sea ice cover was obtained from

the monthly mean of the 0.25° daily satellite products by Reynolds *et al*. [2007], which cover the entire length of the Gerlache Strait (Fig. IV-S9e-h).

4. 3. 4 Sea ice growth and melt processes

The sea ice growth and sea ice melt processes represented by the theoretical grey arrow in Fig. IV-3 were built based on the end-members of A_T and C_T described in Rysgaard *et al*. [2011] and references therein. For sea ice growth, the authors estimated that the salinity, A_T and C_T values were 33.98, 2361 µmol kg^{-1} and 2219 µmol kg^{-1}, respectively, and for sea ice melt, these values were 6, 864 µmol kg^{-1} and 480 µmol kg^{-1}, respectively. Therefore, we adapted the widely known biogeochemical diagram [e.g., Zeebe 2012; Wanninkhof *et al*. 2015] and included these two processes through the theoretical line in Fig. IV-S1. Therefore, the closer the relationship between nA_T and nC_T is to this theoretical line, the more likely it will be that the sea ice growth/sea ice melt processes are influencing nA_T and nC_T.

4. 3. 5 Normalisation of A_T and C_T by average seasonal SSS

A_T and C_T data were normalised to a seasonal average salinity using a non-zero freshwater end-member according to the Eq. IV-8 by Friis *et al*. [2003]:

$$nA_T = \frac{A_T^{meas} - A_T^{s=0}}{SSS^{meas}} \times SSS^{avg} + A_T^{s=0} \qquad \text{IV-8}$$

where A_T^{meas} is the measured A_T, $A_T^{s=0}$ is the A_T for a non-zero salinity, SSS^{meas} is the measured salinity and SSS^{avg} is the average salinity for each season. The same equation was used to calculate the C_T normalised by salinity. We used

$A_T^{S=0}$ = 864 µmol kg^{-1} and $C_T^{S=0}$ = 480 µmol kg^{-1} from the end-members proposed by Rysgaard *et al*. [2011] and references therein.

4. 3. 6 Estimation of meteoric water

We estimated the meteoric water percentage (MW) using Eq. IV-9, following Rivaro *et al*. [2011], which is widely used in polar regions [e.g., Rivaro *et al*. 2014; Mendes *et al*. 2018], and assuming an average sea-ice salinity of 6 [Ackley *et al*. 1979]:

$$\text{Meteoric Water} = \left(1 - \frac{\text{Salinty}_{\text{surface}} - 6}{\text{Salinity}_{\text{botton}} - 6}\right) \times 100 \qquad \text{IV-9}$$

where $S_{surface}$ and S_{botton} are the salinities at the surface and bottom of the ocean, respectively. Here, we considered an average bottom salinity of 34.50 following Monteiro *et al*. [2020], who estimated it from the GOAL and World Ocean Database 2013 (WOD13) datasets. MW was defined by Meredith *et al*. [2008] as the freshwater contribution without source distinction from precipitation, glacial discharge and iceberg or sea ice melt.

4. 3. 7 Spatial distributions of properties

All spatial distribution maps for the properties in this study were interpolated using Data-Interpolating Variational Analysis (DIVA) gridding [Troupin *et al*. 2012]. We used a length scale value of 15‰ for both the X and Y axes to ensure optimal preservation of data structure and smoothness. The averaging and all other calculations performed in this study were based only on the observed or reconstructed data and not on the interpolated data. Map interpolations were made to provide reader-friendly visualization of the results.

4. 3. 8 Limitations and uncertainties

We estimated the propagated uncertainty from the partial derivatives of all calculated parameters (Tab. IV-2) in relation to each variable involved in the calculation as follows:

$$\sigma_{f(x)} = \sqrt{\left(\frac{\partial f(x)}{\partial \text{variable a}}\right)^2 \sigma_a^2 + \left(\frac{\partial f(x)}{\partial \text{variable b}}\right)^2 \sigma_b^2 + \ldots + \left(\frac{\partial f(x)}{\partial \text{variable z}}\right)^2 \sigma_z^2} \qquad \text{IV-10}$$

where the derived functions $f(x)$ are the calculated parameters (i.e., FCO_2, C_T, Ω and pH) and σ is the uncertainty associated with each variable involved in calculation of the parameter. Because SSS uncertainties are expected to be low enough to be negligible (i.e., < 0.001, according to the GOAL and PANGAEA datasets), they were not considered here. Hence, the propagated uncertainties in C_T, Ω and pH fundamentally represented the errors associated with the estimated A_T (± 4.4 µmol kg^{-1}), SST (± 0.05 °C) and measured pCO_2^{sw}. We used pCO_2^{sw} data from SOCATv6 with uncertainties < 2 µatm (55% of total) and < 5 µatm (45%).

We calculated the propagated uncertainties for all carbonate system properties with the CO_2SYS error tool [Orr *et al*. 2018]. For FCO_2, uncertainty was related to the standard error of the averaged wind speed for each season, the measured pCO_2^{sw} and xCO_2^{air}, and sea ice cover. The analytical error for xCO_2^{air} measurements from the U.S. Palmer Station was estimated to be ± 0.07 µmol/mol for the studied period [Dlugokencky *et al*. 2015]. Sea ice concentrations were computed to a precision of 1% coverage [Reynolds *et al*. 2007; Grumbine 1996].

Tab IV-2: Average and standard deviation of the uncertainties propagated in the calculations of the carbonate system properties and FCO_2 flux for each season. The units of uncertainty are the same as the units of the evaluated parameters: FCO_2 (mmol m^{-2} d^{-1}), C_T (µmol kg^{-1}), pH (total scale) and Ω (unitless). Standard deviations ~ 0 are smaller than the limit of significant digits in the averages.

	pCO_2^{sw} uncertainty	Summer	Autumn	Winter	Spring
FCO_2		1.96 ± 0.64	2.65 ± 0.83	3.46 ± 1.18	2.34 ± 0.76
C_T		5.58 ± 0.57	5.00 ± 0.10	4.84 ± 0.05	5.13 ± 0.46
Ω_{Ca}	< 2 µatm	0.15 ± 0.03	0.12 ± 0.01	0.11 ± 0.003	0.12 ± 0.03
Ω_{Ar}	(55% of all	0.10 ± 0.02	0.07 ± ~ 0	0.07 ± ~ 0	0.08 ± 0.02
pH	data)	0.0076 ± 0.0003	0.0075 ± 0.0003	0.0075 ± ~ 0	0.0075 ± 0.0002
FCO_2		4.15 ± 0.73	6.53 ± 2.10	8.29 ± 3.04	5.44 ± 1.80
C_T		6.11 ± 1.16	5.22 ± 0.13	5.02 ± 0.07	5.45 ± 0.83
Ω_{Ca}	< 5 µatm	0.16 ± 0.04	0.12 ± 0.01	0.11 ± 0.003	0.13 ± 0.03
Ω_{Ar}	(45% of all	0.10 ± 0.02	0.07 ± ~ 0	0.07 ± ~ 0	0.08 ± 0.02
pH	data)	0.0097 ± 0.0015	0.0087 ± ~ 0	0.0086 ± 0.0001	0.0090 ± 0.0010

Finally, we used a first-order polynomial relationship between A_T and SSS to estimate A_T and calculate the other parameters of the carbonate system based on summertime data. We assumed this relationship for all seasons because the summer was the only period with available A_T data for the study region. However, the summer is characterised by greater A_T variability than other seasons, implying that the ranges of A_T and SSS may represent the annual range (i.e., A_T: 2200–2320 µmol kg^{-1}; SSS: 32–34.5). Such limitations are mainly due to the scarcity of data in periods other than summer and highlight the need for additional efforts to better understand the dynamics of the carbonate system parameters in coastal regions of the Southern Ocean.

4. 4 Results

4. 4. 1 Hydrographic properties and the carbonate system

Negative sea surface temperatures were recorded from April to November (Fig. IV-2a), and the lowest values in summer were observed in the northernmost

part of the strait, where the highest salinities were recorded (Fig. IV-S4). The opposite temperature distribution pattern occurred during spring, when the lowest temperatures were recorded at the southern end of the strait. At the connection between the central basin of the Gerlache Strait and the Bellingshausen Sea (i.e., Schollaert Channel), higher temperatures were associated with lower salinity (Fig. IV-S4). On the other hand, the spatial distributions of temperature and salinity in autumn and winter were more homogeneous than those in summer and spring.

The carbonate system properties also demonstrated distinct spatial distribution patterns among seasons (Figs. IV-S5 to IV-S8). The seasonal variabilities of A_T and C_T followed that of pCO_2^{sw} and were inverse to those of pH and the Ω_{Ca} and Ω_{Ar} throughout the year. A_T was higher than C_T from December to March and was lower than C_T during the rest of the year (Fig. IV-2d). This seasonal pattern was also observed for CO_2 saturation relative to the atmosphere, i.e., the difference (ΔpCO_2) between pCO_2^{sw} and the pCO_2^{air} was positive from April to November and negative from December to March (Fig. IV-2b). Minimum pH values (total scale) of 7.99 ± 0.02 were observed in winter, while in the other seasons, they were equal to or greater than 8.00 (Fig. IV-2c). Undersaturated carbonate calcium conditions (i.e., Ω less than 1) were not observed for either species during the seasonal cycle (Fig. IV-2c), although the lowest surface values of Ω_{Ca} and Ω_{Ar} were recorded in winter, on average.

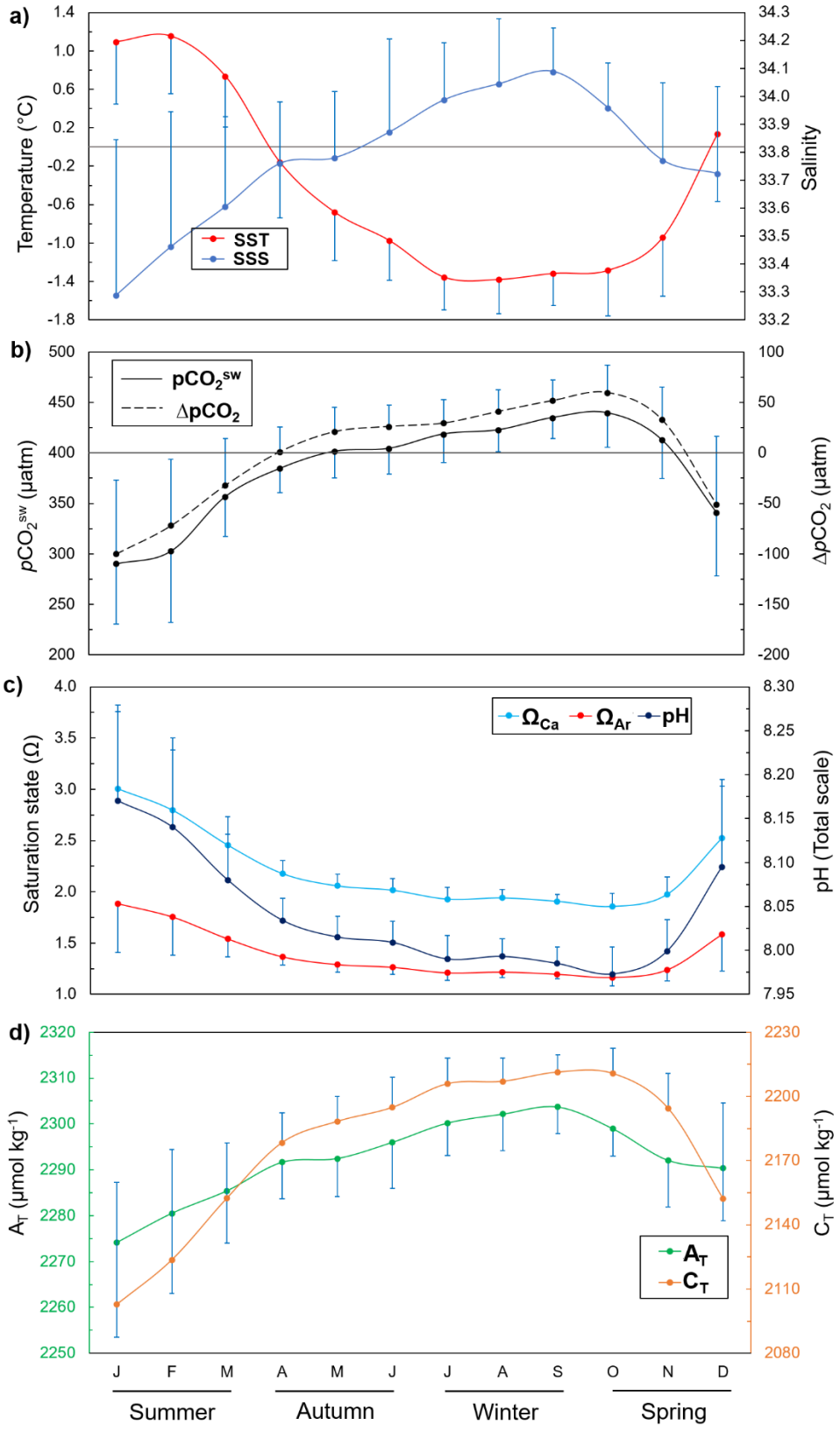

Figure IV-2: Detrended annual cycle of hydrographic and carbonate system properties on the surface of the Gerlache Strait. (a) Temperature and salinity, (b) CO_2 partial pressure in the sea surface (pCO_2^{sw}) and the difference between pCO_2^{sw} and atmospheric pCO_2 (ΔpCO_2), (c) pH (total scale) and saturation states of calcite (Ω_{Ca}) and aragonite (Ω_{Ar}), and (d) total alkalinity (A_T) and total dissolved inorganic carbon (C_T). The blue bars are the standard deviations oriented up or down for visual clarity. The horizontal lines are the boundaries of 0 °C (a) and a ΔpCO_2 equal to 0 (b).

4. 4. 2 Drivers of pCO_2^{sw} seasonal changes

In summer, virtually all processes exerted some influence on the surface CO_2 system, as shown by the wide dispersion of the salinity-normalized A_T and C_T (nA_T and nC_T, respectively; Fig. IV-3a). In general, carbonate dissolution seems to exert a greater influence in autumn and winter than in spring and summer, although sea ice growth also acts to control A_T and C_T in winter.

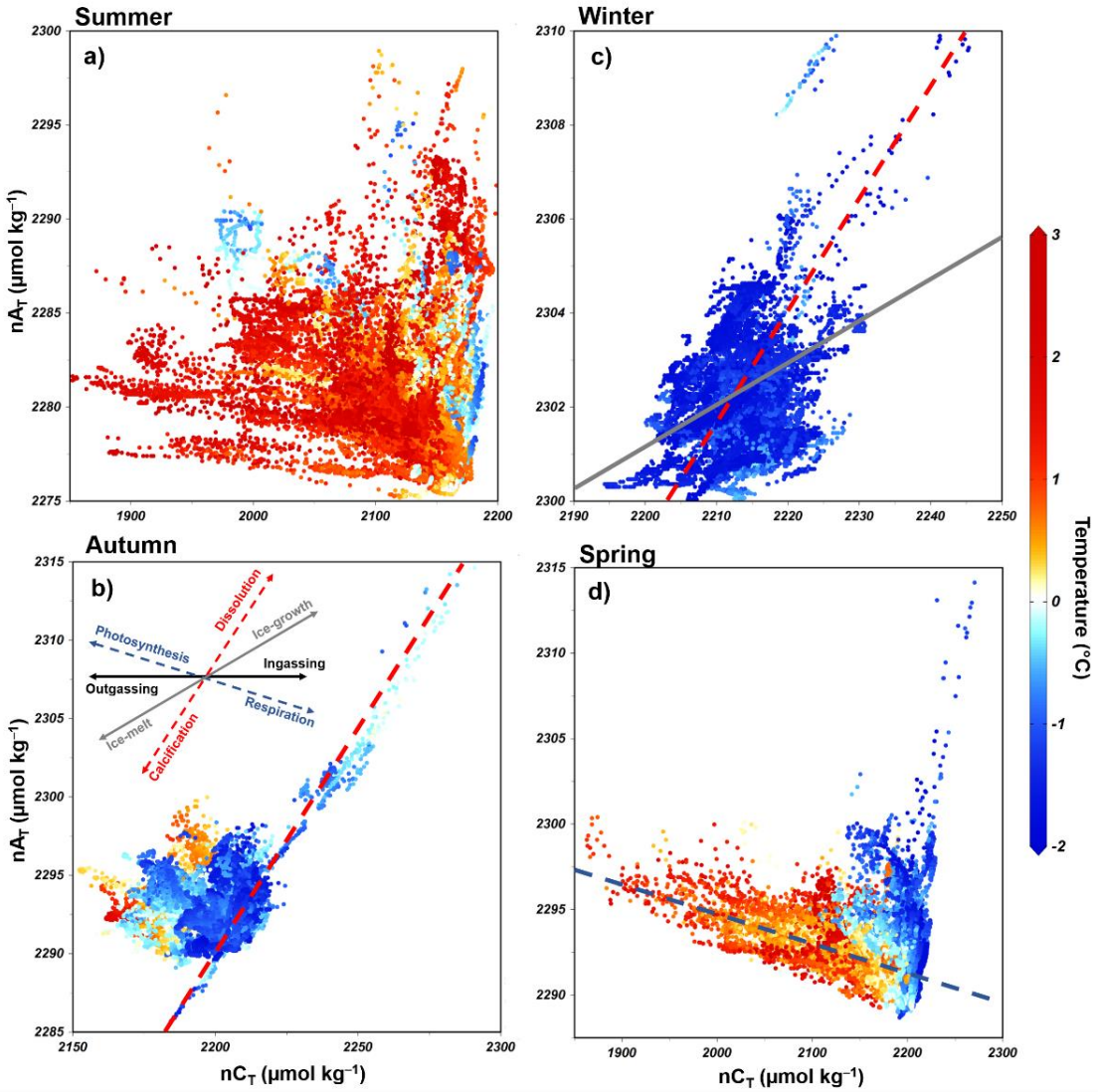

Figure IV-3: Salinity-normalised (average salinity for each season as in Fig. IV-S4) total alkalinity and total dissolved inorganic carbon (nA_T and nC_T, respectively) dispersal diagram for the (a) summer, (b) autumn, (c) winter, and (d) spring. nA_T and nC_T were calculated for non-zero salinities following Friis *et al*. [2003]. Arrows represent the nA_T:nC_T ratio that characterises the physical-biogeochemical processes that affect nA_T and nC_T (adapted from Zeebe [2012]). The theoretical arrow representing the sea ice growth and melt processes was based on the threshold values for A_T and C_T described in Rysgaard *et al*. [2011]. More details about the normalisation of A_T and C_T as well as sea ice growth and melt processes are provided in the Supplementary Material. Note that the magnitudes of the axes are different among subplots.

Carbonate dissolution/calcification processes were observed to play a role in changing the A_T and C_T surface distributions in spring, although sea ice growth and melting processes are also expected to exert an influence, mainly during October and November, in association with low temperatures (Fig. IV-3d) and high pCO_2^{sw}. On the other hand, high temperatures (> 0 °C) in spring were associated with an increased influence of photosynthesis on the A_T and C_T (Fig. IV-3d).

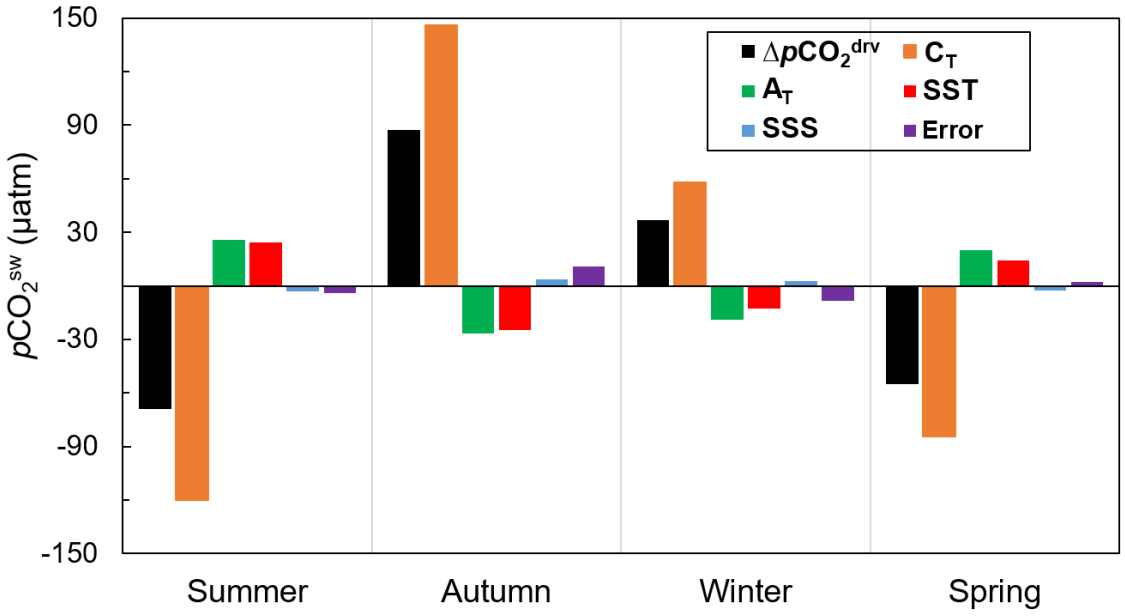

Figure IV-4: Effects of total alkalinity (A_T), total dissolved inorganic carbon (C_T), sea surface temperature (SST) and sea surface salinity (SSS) on seawater pCO_2 (pCO_2^{sw}) for each season in the Gerlache Strait. The variation in each parameter is calculated as the difference between the values of each parameter and their respective averages in previous seasons. The unit of all drivers is the same as that for pCO_2^{sw} (µatm), and their magnitudes represent their influence on pCO_2^{sw} changes. Positive values indicate that an increase in the parameter led to an increase in pCO_2^{sw}; negative values indicate that a decrease in the parameter led to a decrease in pCO_2^{sw}. The only exception to this is A_T because an increase in A_T leads to a decrease in pCO_2^{sw} and vice versa. The error bars (purple) show the difference between the sum of all drivers and the actual variation in pCO_2^{sw} (ΔpCO_2^{drv}), indicating the extent to which the decomposition of pCO_2^{sw} into its drivers differs from ΔpCO_2^{drv}. More details are given in the methods section.

C_T had the dominant effect on changes in pCO_2^{sw} throughout the year. A_T and temperature were secondary drivers of these changes, while salinity had a minor influence on surface pCO_2^{sw} (Fig. IV-4). In summer and spring, there was a considerable decrease in pCO_2^{sw}, mainly due to the C_T drawdown. This

decrease was compensated by the increasing effect on pCO_2^{sw} of the reduction in A_T and the increase in temperature. In winter and autumn, the considerable increase in pCO_2^{sw} was driven by the increase in C_T and partially compensated for by the increase in A_T and decrease in temperature.

4. 4. 3 Seasonal and interannual variability of FCO_2

FCO_2 exhibited distinct seasonality throughout the year, with the region swinging from a strong CO_2 sink ($FCO_2 < -12$ mmol m^{-2} day^{-1}) in summer to a strong CO_2 source ($FCO_2 > 12$ mmol m^{-2} day^{-1}) in winter (Fig. IV-5). During autumn and spring, the behaviour of the region oscillated between the major situations normally observed during winter and summer, resulting in a moderate FCO_2. Despite this well-marked seasonality, the region was an annual weak CO_2 source from 2002 to 2017, with an average estimated FCO_2 of 1.24 ± 4.33 mmol m^{-2} day^{-1}. Notably, with high spatial and temporal variability, this net near-equilibrium condition was achieved because the region switched from a moderate to strong CO_2 ocean sink from December to March to a moderate to strong CO_2 source to the atmosphere throughout the rest of the year (Fig. IV-5). Months with the most intense CO_2 uptake levels (< -12 mmol m^{-2} day^{-1}) have occurred more frequently since 2011, with the peak in January and February of 2016. On the other hand, months with the maximum CO_2 outgassing (> 12 mmol m^{-2} day^{-1}) seem to have become less frequent since 2009 (Fig. IV-5).

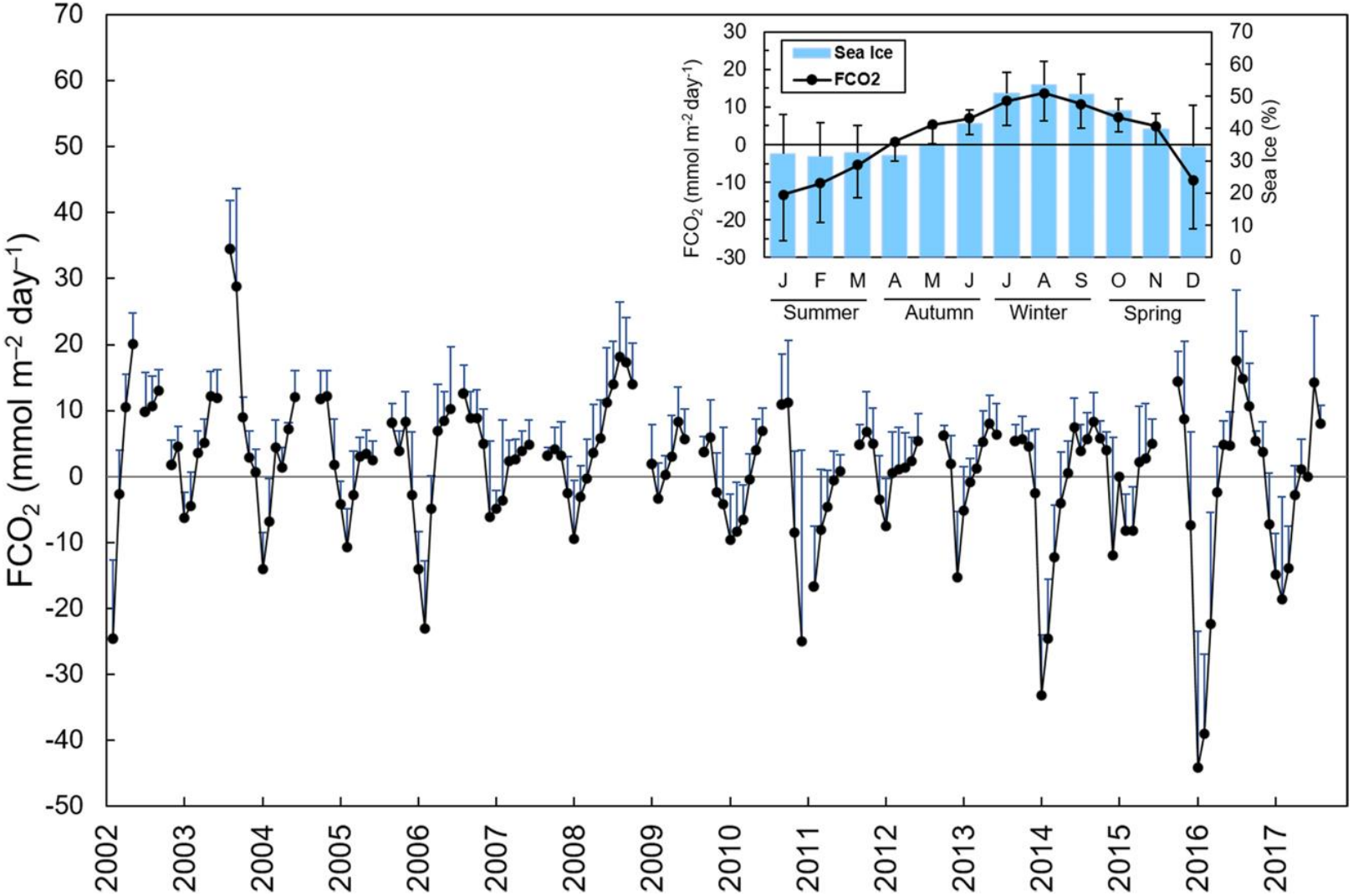

Figure IV-5: Monthly averages of net sea-air CO_2 fluxes (FCO_2) in the Gerlache Strait from January 2002 to December 2017 with an inset showing the variability throughout the year to characterise the seasonal cycle of FCO_2 and the percentage of sea ice cover (filled blue bars). The gaps are from years when there was no winter sampling in the region. The blue bars oriented upwards are the standard deviations from the respective monthly averages, as are the black bars in the inset. Positive FCO_2 values represent the outgassing of CO_2 to the atmosphere, whereas negative FCO_2 values represent CO_2 uptake by the ocean.

Considering all seasons between 2002 and 2017, high seasonal variability in FCO_2 magnitude was identified (Fig. IV-6). However, the behaviour of the Gerlache Strait as a CO_2 sink or source remained almost consistent within each season, as observed in summer (Fig. IV-6b) and winter (Fig. IV-6d). Only two particular exceptions occurred in the autumns of 2011 and 2014, when the region was a weak CO_2 sink (Fig. IV-6c). Exceptions were also identified in spring, when the region behaved as a strong CO_2 source in 2008 and a particularly strong CO_2 sink in 2010 (Fig. IV-6e).

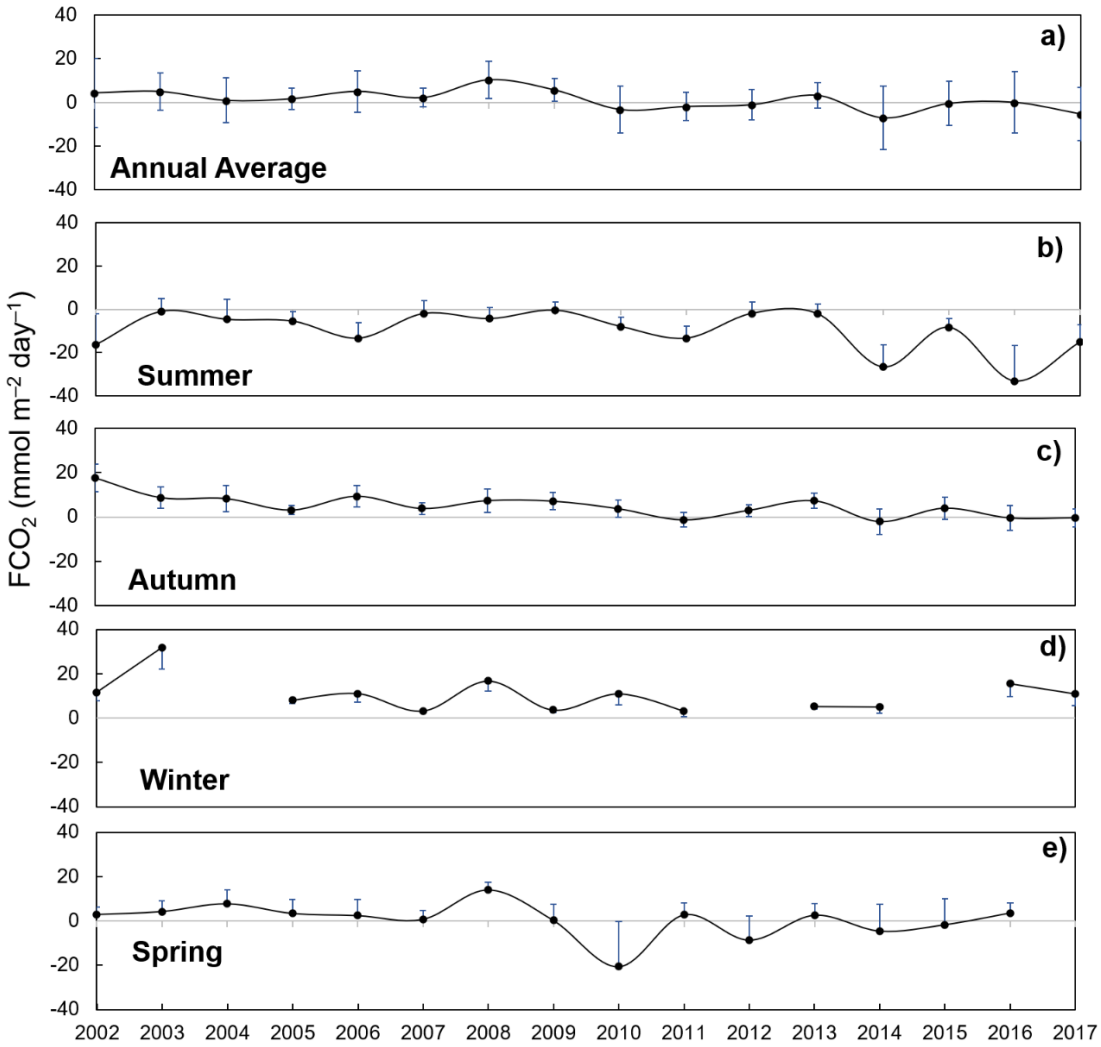

Figure IV-6: Time series of average (a) annual net sea-air CO_2 flux (FCO_2) during (b) summer, (c) autumn, (d) winter and (e) spring in the Gerlache Strait from 2002 to 2017. The gaps are from years when there was no winter sampling in the region. The blue bars oriented upwards are the standard deviations from the respective annual averages. Positive FCO_2 values represent the outgassing of CO_2 to the atmosphere, whereas negative values represent CO_2 uptake by the ocean.

Although the specific episodes in autumn did not appear to influence the average annual FCO_2, the unusual spring FCO_2 magnitudes coincided with increases in the average annual FCO_2 in the respective years (Fig. IV-6a). The Gerlache Strait acted as an absolute annual CO_2 source of 4.4 ± 2.8 mmol m^{-2} day^{-1} from 2002 to 2009 and has become predominantly a net annual CO_2 sink of -2.0 ± 3.0 mmol m^{-2} day^{-1} since 2010 (Fig. IV-6a).

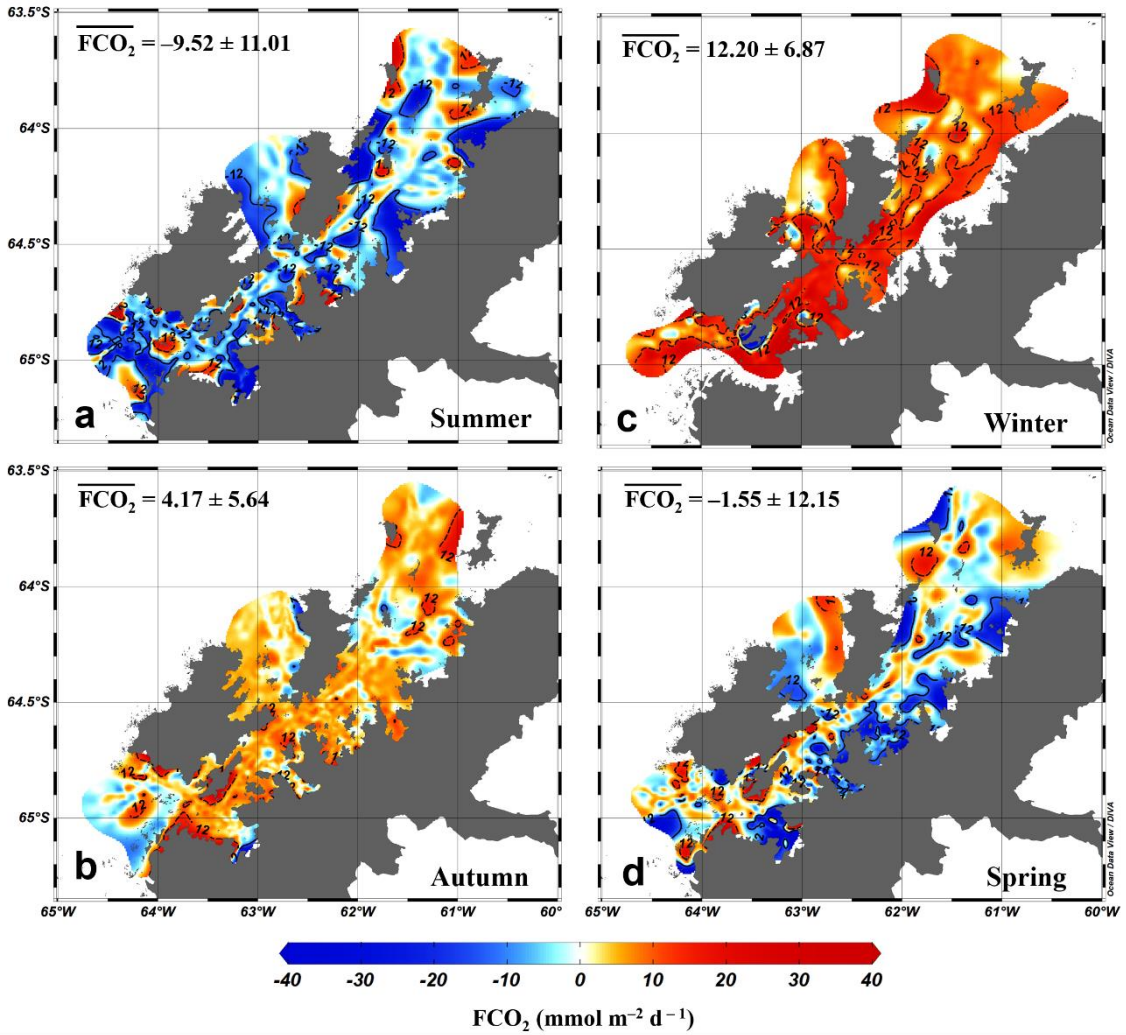

Figure IV-7: Surface distribution of the net sea-air CO_2 flux (FCO_2) in the Gerlache Strait from 2002 to 2017 in (a) summer, (b) autumn, (c) winter and (d) spring. Positive FCO_2 values represent the outgassing of CO_2 to the atmosphere, whereas negative FCO_2 values represent CO_2 uptake by the ocean. The numbers indicate the averages and standard deviations of FCO_2 in each season. The black continuous and dashed isolines depict the FCO_2 values of –12 and + 12 mmol m^{-2} d^{-1}, respectively, for the strong CO_2 sink and outgassing situations. These maps were generated by using the software Ocean Data View (v. 5.3.0, https://odv.awi.de) [Schlitzer 2018].

A seasonal pattern in the spatial distribution of FCO_2 along the Gerlache Strait was also identified. This pattern was characterised by a more homogeneous spatial distribution in autumn and winter (Fig. IV-7b,c) than in summer and spring (Fig. IV-7a,d). Moreover, the northernmost part of the strait, north of 64°S, had a higher annual FCO_2 (3 ± 8 mmol m^{-2} day^{-1}) than the southernmost part of the strait, south of 65°S. In the southernmost part, there was an annual CO_2 uptake of -7 ± 16 mmol m^{-2} day^{-1}.

4. 5 Discussion

4. 5. 1 Seasonal changes in FCO_2

In late spring and summer, the Gerlache Strait is a CO_2 sink, with rates ranging from -13 ± 12 mmol m^{-2} day^{-1} in January to -5 ± 9 mmol m^{-2} day^{-1} in March (Fig. IV-5). This strong CO_2 uptake is driven by an increase in biological activity coupled with meltwater input (Fig. IV-8a) [Brown *et al*. 2019; Monteiro *et al*. 2020; Kerr *et al*. 2018a; Alvarez *et al*. 2002; Mendes *et al*. 2013; Mendes *et al*. 2018] from December until late summer (Fig. IV-5), when sea ice formation becomes gradually more intense [Cavalieri & Parkinson 2008; Parkinson & Cavalieri 2012]. This is revealed by the substantial C_T drawdown (Fig. IV-4), which characterises the influence of photosynthesis on the surface water [Takahashi *et al*. 2014; Lenton *et al*. 2012; Zeebe 2012], associated with a slight decrease in A_T as a result of further respiration (Fig. IV-3b). Phytoplankton growth is favoured by the increased stability of the nutrient-rich shallower mixed layer in summer and late spring (Fig. IV-8a), mainly due to meltwater input [Brown *et al*. 2019; Cape *et al*. 2019; Mendes *et al*. 2013; Mendes *et al*. 2018; Lancelot *et al*. 1993]. This is more evident in the southernmost part of the strait, where intrusions

of warmer mCDW would likely lead to sea ice melting [Prézelin *et al*. 2000] and the higher percentage of meteoric water (Fig. IV-S9) than in the northernmost region, which is comparatively ice-free (Fig. IV-S9). Hence, this could potentially account for the greater CO_2 uptake in the southern region than in the northern region (Fig. IV-7). Nevertheless, the spatial variability of the carbonate system parameters is clearly greater in spring and summer than in autumn and winter. Therefore, it is likely that other oceanographic processes simultaneously have roles in changing the surface nA_T and nC_T.

In fact, during early spring, the carbonate dissolution/precipitation and sea ice growth/melt associated with low temperatures (Fig. IV-3d) seem to influence the carbonate system due to the increase in C_T that is rejected through the sea ice brine. However, the impact of each of these processes, and even the presence of other involved processes, is not yet well understood. The dominant processes in spring (i.e., carbonate dissolution/precipitation or photosynthesis/respiration), as well as during other seasons, can also exhibit interannual variability. For example, during summer, there is variability in CO_2 uptake oscillating between 2 and 4 years, by which FCO_2 in the region alternates between strong CO_2 sink and near-equilibrium conditions [Monteiro *et al*. 2020]. This variability is associated with both intense biological activity and the intrusion of local upwelled CO_2-rich waters (e.g., mCDW). In addition, it is linked to the influence of modes of climate variability, such as ENSO, which decreases the wind intensity, leading to favourable conditions for phytoplankton blooms [Brown *et al*. 2019]. This explains why the most intense CO_2 uptake was recorded in 2016 (Fig. IV-5), as this was the year with the most extreme ENSO since 1998 [Santoso *et al*. 2017], which was associated with biogeochemical changes along

the water column [Avelina *et al*. 2020]. Therefore, the same mechanism underlying the shift in the dominant physical processes may occur in other seasons of the year. This would likely explain why the region was an exceptionally strong CO_2 source in spring 2008 but a strong CO_2 sink in spring 2010 (Fig. IV-6e).

In autumn, the region becomes a moderate CO_2 source to the atmosphere, with the maximum magnitude in August (14 ± 7 mmol m^{-2} day^{-1}). Such behaviour is due to a significant increase in C_T, which leads to an increase in pCO_2^{sw}. This is further partially offset by the effect that the increase in A_T has on pCO_2^{sw} (Fig. IV-4), implicating the upwelling process as a likely cause. In fact, more intense short-term irregular intrusions of mCDW [Couto *et al*. 2017; Moffat *et al*. 2009; Moffat & Meredith 2018] coupled to the deeper mixed layer, which lead to intensified vertical mixing in the winter [Venables & Meredith 2014], are likely to carry CO_2-rich waters to the surface layer of the strait (Fig. IV-8b). Indeed, this has been the process most observed in other Southern Ocean coastal regions [Legge *et al*. 2015; Karl *et al*. 1991; Henley *et al*. 2019]. On the western Antarctic Peninsula shelf, for example, there is no evidence of inorganic macronutrient regeneration in late summer, revealing that the increase in C_T must be more associated with upwelling and/or advection processes [Jones *et al*. 2017]. Although these mCDW intrusions can occur throughout the year and through virtually all connections of the Gerlache Strait [Prézelin *et al*. 2000; Smith *et al*. 1999; García *et al*. 2002], they are expected to be more intense in winter [Venables & Meredith 2014] and at the southern end of the strait [Parra *et al*. 2020]. In addition, the rejection of C_T through sea ice brine [Nomura *et al*. 2006; Rysgaard *et al*. 2011] is an important process (Fig. IV-8b). Despite occurring

more intensely in winter than in other seasons, this process should also contribute to CO_2 release in autumn, as it was also dominant in controlling A_T and C_T (Fig. IV-3c).

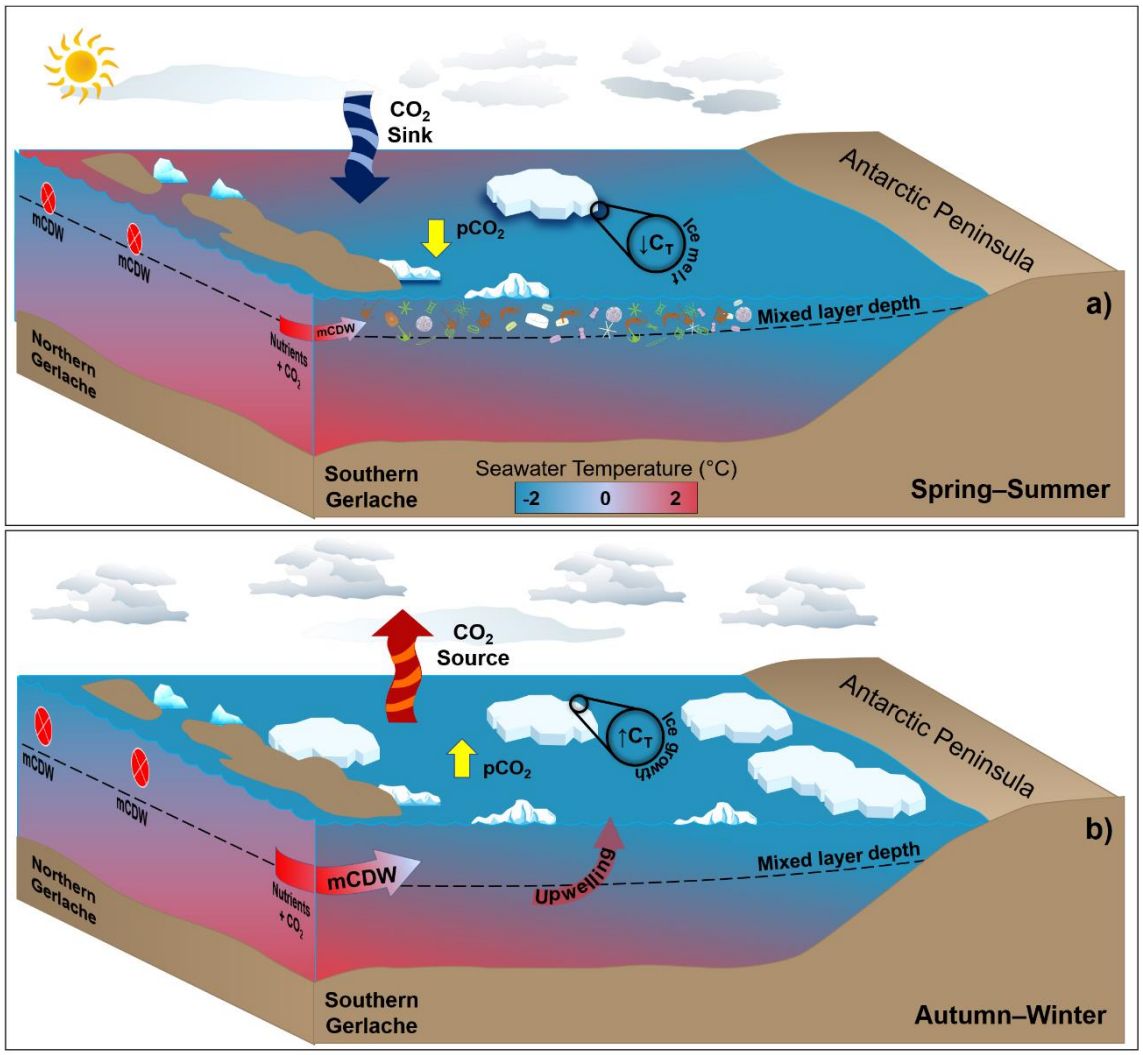

Figure IV-8: Distinct processes driving surface CO_2 partial pressure (pCO_2) and seasonal sea-air CO_2 fluxes in a coastal region of the northern Antarctic Peninsula (NAP). From (a) December to March, sea ice melting provides a shallow mixed layer that leads to phytoplankton growth. This spring–summer scenario coupled with less intense modified Circumpolar Deep Water (mCDW) intrusions into the NAP and a decrease in total dissolved inorganic carbon (C_T) from meltwater causes pCO_2 drawdown. Therefore, in these months, the region behaves as a strong sink of atmospheric CO_2. Conversely, from (b) April to November, under sea ice cover conditions, more intense mCDW intrusions coupled with a deeper mixed layer lead to intensified vertical mixing, resulting in the upwelling of CO_2-rich waters. Such processes, in association with the rejection of C_T through brine release during sea ice growth, lead to a significant increase in surface pCO_2. Then, the region becomes a moderate to strong CO_2 source to the atmosphere during the autumn–winter. The theoretical depth of the shallowest spring–summer mixed layer is approximately 50 m, reaching approximately 150 m in the autumn–winter [Venables & Meredith 2014]. Drawn by Thiago Monteiro. Symbols courtesy of the Integration and Application Network, University of Maryland Center for Envrionmental Science (ian.umces.edu/symbols/).

The increase in C_T due to ice growth, first shown in a laboratory experiment [Nomura *et al*. 2006], occurs in both Arctic and Antarctic regions, where there is an intense sea ice dynamic [Rysgaard *et al*. 2011]. Hence, the increase in C_T leads to high pCO_2^{sw} values but is also related to decreases in Ω_{Ca} and Ω_{Ar} [Hauri *et al*. 2015]. Thus, these conditions contribute to maintaining a relatively low pH (≤ 8.00) until mid-spring, when sea ice begins to melt and both C_T and pCO_2^{sw} decrease towards the summer season.

Although the spatial distribution of FCO_2 is more homogeneous in autumn and winter than in other seasons (Fig. IV-7), there is intense interannual variability in these fluxes (Fig. IV-6). It is not yet clear what drives this variability, but it has been linked to sea ice cover variability in other Antarctic regions [Legge *et al*. 2015; Arrigo & Van Dijken 2007; Keppler & Landschützer 2019]. This link makes sense due to the good correlation ($r^2 = 0.73$; $p = 0.0006$; n = 12) of the FCO_2 seasonal cycle with the sea ice cover seasonality in the Gerlache Strait, mainly in the months when it acts as a CO_2 source ($r^2 = 0.93$; $p = 0.0136$; n = 7) (Fig. IV-S10). Despite the strong CO_2 outgassing during these periods, sea ice cover constrains sea-air CO_2 exchanges [Legge *et al*. 2015; Bakker *et al*. 2008], leading to the conclusion that this CO_2 outgassing could be even more intense under sea ice-free conditions, as observed in the Arctic Ocean [Ouyang *et al*. 2020]. Hence, the FCO_2 dynamics in sea ice-covered periods may be more sensitive than previously thought.

4. 5. 2 Seasonality of the carbonate system and acidification process

The carbonate system parameters on the surface of the strait follow seasonal FCO_2 dynamics, that is, sea ice dynamics. The lower pH, Ω_{Ca} and

Ω_{Ar} values in winter than in other seasons, although expected, reinforce the biogeochemical sensitivity of this season. The low temperatures and the brine released by sea ice growth lead to the dissolution of calcium carbonate and decreases in Ω_{Ca} and Ω_{Ar} [Legge *et al*. 2017]. However, we did not find the calcium carbonate in the surface of the Gerlache Strait to be in a subsaturated state, even in winter when there was high pCO_2^{sw}; this was also the case in Ryder Bay [Jones *et al*. 2017; Legge *et al*. 2017], a region located farther south on the western Antarctic Peninsula shelf, which is under dynamic conditions similar to those of the Gerlache Strait. In summer, carbonate mineral supersaturation is associated with regions where there is strong CO_2 uptake, such as in the southernmost portion of the strait, where meteoric water input is most intense (Fig. IV-S9) and salinity is relatively low (Figs. IV-S4 and IV-S7). This reveals that the intense pCO_2^{sw} drawdown caused by biological activity outweighs the increase in pCO_2^{sw} by the effect of carbonate precipitation [Jones *et al*. 2017], and carbonate dissolution is minimized due to the biological uptake of C_T. Nevertheless, the sensitivity of these parameters should be observed in more detail, as carbonate calcification and dissolution processes also seem to play an important role in controlling A_T and C_T (Fig. IV-3b,c). Furthermore, because we found minimum pH values in winter (7.92) lower than those at Ryder Bay in 1994 (8.11) and 2010 (8.00) [Roden *et al*. 2013] as well as between 2011 and 2014 (7.95) [Legge *et al*. 2017], these waters may be experiencing ocean acidification, although counterintuitive processes may be offsetting the effects in the studied region [Lencina-Avila *et al*. 2018]. In fact, the waters of the Gerlache Strait have previously been reported to show signs of acidification in summer below the

mixed layer [Kerr *et al*. 2018a; Lencina-Avila *et al*. 2018], with surface pH values lower than those found at Ryder Bay (8.21–8.48) [Jones *et al*. 2017].

The effects of intensified summer CO_2 uptake on calcite and aragonite saturation in surface waters may emerge in the coming years. However, supersaturation of these carbonate species is associated with decreased pCO_2^{sw} values in summer [Monteiro *et al*. 2020]. This reveals that these feedback effects need to be further investigated, especially considering the residence time of these waters in coastal regions. As strong summer CO_2 sink periods are extended, an inverse effect of sea surface acidification may occur, as observed in the southernmost portion of the Gerlache Strait. Nevertheless, the acidification process should occur in the deep layers of these strong CO_2 sink regions and in adjacent deep waters due to horizontal advection. Indeed, this will likely be the case because the residence time of surface waters in this region was estimated to be less than 7 days, while the residence time in adjacent larger basins ranges between 13 and 40 days [Zhou *et al*. 2002]. Therefore, assuming a steady increase in both atmospheric CO_2 [Dlugokencky *et al*. 2015] and temperature [Turner *et al*. 2014], the Southern Ocean coastal regions may become intense hotspots of deep-ocean acidification, with some expected implications for organisms throughout the water column and the food web as a whole. For example, on the sea surface, there may be a restructuring of the food web due to a shift in the dominant groups of phytoplankton, such as from diatoms to smaller organisms [Henley *et al*. 2019; Mendes *et al*. 2013, and references therein]. Such changes will potentially decrease the transfer of carbon, energy and nutrients through organisms such as diatoms to pelagic and benthic ecosystems, with complex feedbacks on ocean biogeochemistry and climate

[Henley *et al*. 2019]. In this sense, these findings shed light on the importance of clarifying the real impacts of these changes throughout the water column. This is because, despite showing signs of acidification, most studies provide only snapshots, and coupled ocean–land–ice processes can mask the real ocean acidification state of Southern Ocean coastal regions.

4. 5. 3 Annual budget of FCO_2

We have identified the Gerlache Strait as a weak CO_2 source from 2002 to 2017, with an annual budget of sea-air CO_2 exchanges at near-equilibrium conditions. This contrasts with the expectations for other Antarctic coastal regions, which demonstrate annual CO_2 sink behaviour [Gibson & Trull 1999; Arrigo & Van Dijken 2007; Lenton *et al*. 2006], such as in summer and spring [Karl *et al*. 1991; Brown *et al*. 2019; Ito *et al*. 2018]. The studied region acts as a moderate CO_2 source in autumn and a strong CO_2 source in winter. The CO_2 outgassing that occurs during 8 months of the year (i.e., from April to November) is almost fully compensated for in only 4 months (i.e., from December to March), when the region acts as a moderate to strong CO_2 sink. Although this behaviour is not considered typical for Antarctic coastal regions, the Gerlache Strait lies at approximately 64°S, where Takahashi *et al*. [2012] verified an approximately neutral annual sea-air CO_2 flux. Nevertheless, here, we hypothesise that this scenario is more common to coastal regions of the Southern Ocean than previously thought because incipient signs of this behaviour have already been identified in other Antarctic coastal regions. For example, Bakker *et al*. [2008] found strong supersaturation of seawater CO_2 relative to atmospheric CO_2 in autumn and winter in the Weddell Sea but suggested that the region was

an annual CO_2 sink. These contrasting summer/winter behaviours, with an annual CO_2 sink budget, also extend to other Southern Ocean coastal regions, such as the western Antarctic Peninsula [Gibson & Trull 1999; Roden *et al*. 2013; Legge *et al*. 2015; Karl *et al*. 1991], the Ross Sea [Arrigo & Van Dijken 2007], the Indian Antarctic sector [Metzl *et al*. 2006; Metzl *et al*. 1995] and even the Antarctic Zone south of 62°S as a whole [McNeil *et al*. 2007]. However, the relatively low monthly and interannual coverage in most of these studies may have biased the integrated FCO_2 budget throughout the year. This is particularly true if we take into account recent estimates of FCO_2 from long-term climatology for global coastal regions [Roobaert *et al*. 2019]. In this climatology, the NAP, as well as the Weddell Sea and much of the Atlantic and Indian sectors of the Southern Ocean, was a net CO_2 source between 1998 and 2015. Despite this, the CO_2 uptake by CO_2 sink regions was so intense that the annual FCO_2 budget for this period was approximately − 17 Tg C $year^{-1}$ [Roobaert *et al*. 2019].

4. 5. 4 Expected scenarios for the future of FCO_2

The recent changes observed in the NAP, mainly related to the intensification of the westerly winds [Dinniman *et al*. 2012], rising temperatures [Siegert *et al*. 2019] and the prolongation of ice-free water periods [Shepherd *et al*. 2018; Del Castillo *et al*. 2019], are expected to persist in the coming years [Henley *et al*. 2019; Kerr *et al*. 2018c]. In this sense, two future scenarios for net sea-air CO_2 fluxes can be projected. First, with longer ice-free water periods, these coastal regions could release CO_2 that would otherwise remain in the seawater isolated by sea ice, intensifying the annual CO_2 source. This release may be enhanced by intensified mCDW intrusion into the western Antarctic

Peninsula shelf that have been projected [Henley *et al*. 2019; Barllet *et al*. 2018], although little is known about its periodicity and variability. On the other hand, nutrient-rich mCDW intrusions coupled with the delayed sea ice cover period and rising temperatures should lead to prolonged phytoplankton growth [Del Castillo *et al*. 2019]. Thus, strong CO_2 sink periods should also extend beyond late summer. As CO_2 uptake has intensified in the summer [Brown *et al*. 2019; Monteiro *et al*. 2020] and proved to nearly counteract annual CO_2 evasion, this region could become an annual CO_2 sink in future years, particularly assuming that the Southern Ocean is becoming greener [Del Castillo *et al*. 2019]. Actually, this second scenario seems likely to occur, as the magnitude and frequency of FCO_2 in months when the region is a strong CO_2 sink are increasing and in months when the region is a strong CO_2 source have been less frequent (Fig. IV-5), leading to intensified annual CO_2 uptake since 2010 (Fig. IV-6a).

These scenarios become more complex when we take into account the influence of the modes of climate variability. For example, the positive phase of SAM has been associated with more intense CO_2 outgassing due to the deepening of the mixed layer [Lovenduski *et al*. 2007]. Conversely, it was also associated with higher CO_2 uptake due to the intensification of upwelling, which supplies iron and nutrients to the sea surface and hence increases phytoplankton growth [Hauck *et al*. 2013]. This reveals the sensitivity of sea-air CO_2 exchanges to these feedback mechanisms and the urgent need to broaden investigations for a coupled analysis of ocean-climate systems. Nevertheless, signs of intensifying summer CO_2 sink behaviour [Brown *et al*. 2019; Monteiro *et al*. 2020a] suggest that the influence of SAM should be reversing the flux to encourage annual net CO_2 uptake in Antarctic coastal regions.

Acknowledgements

***** Todos os agradecimentos e financiadores serão listadas ao final deste documento.

References

***** As referências serão listadas ao final deste documento, contendo todas as referências utilizadas nesta dissertação.

APÊNDICE II

Este apêndice contém as seguintes figuras mencionadas no Capítulo IV: Fig. IV-S1; Fig. IV-S2; Fig. IV-S3; Fig. IV-S4; Fig. IV-S5; Fig. IV-S6; Fig. IV-S7; Fig. IV-S8; Fig. IV-S9; Fig. IV-S10.

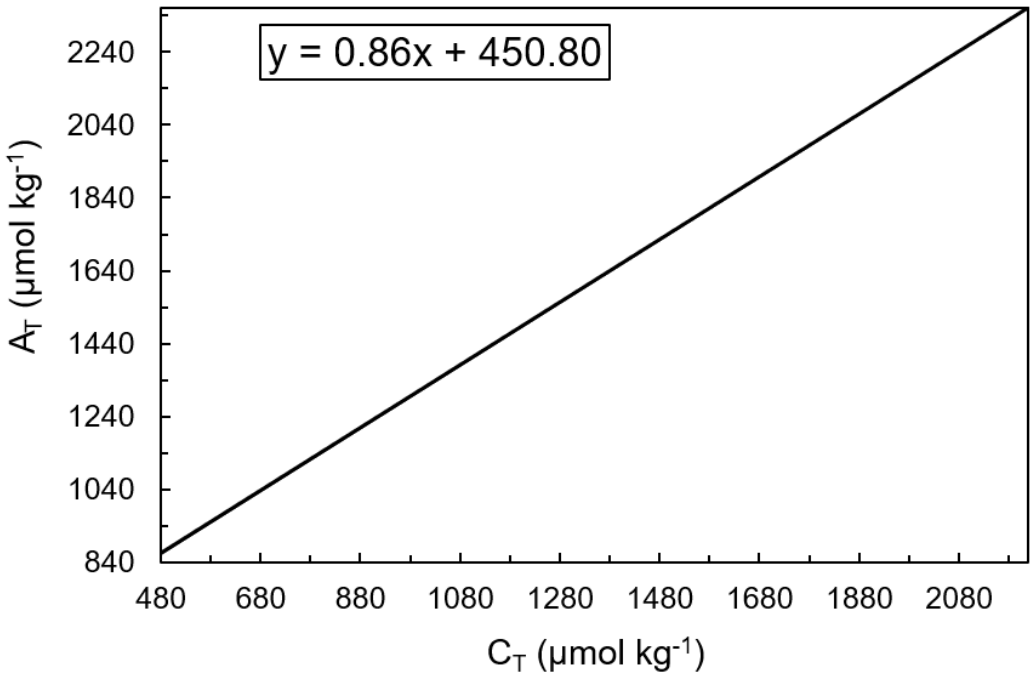

Figure IV-S1: End-members used in the construction of the theoretical line of the sea ice growth/sea ice melt processes (grey arrow) in Fig. IV-3. This line was based on the A_T and C_T values for meltwater (864 µmol kg^{-1} and 480 µmol kg^{-1}, respectively) and for sea ice growth (2361 µmol kg^{-1} and 2219 µmol kg^{-1}, respectively), as suggested by Rysgaard *et al*. [2011] and references therein.

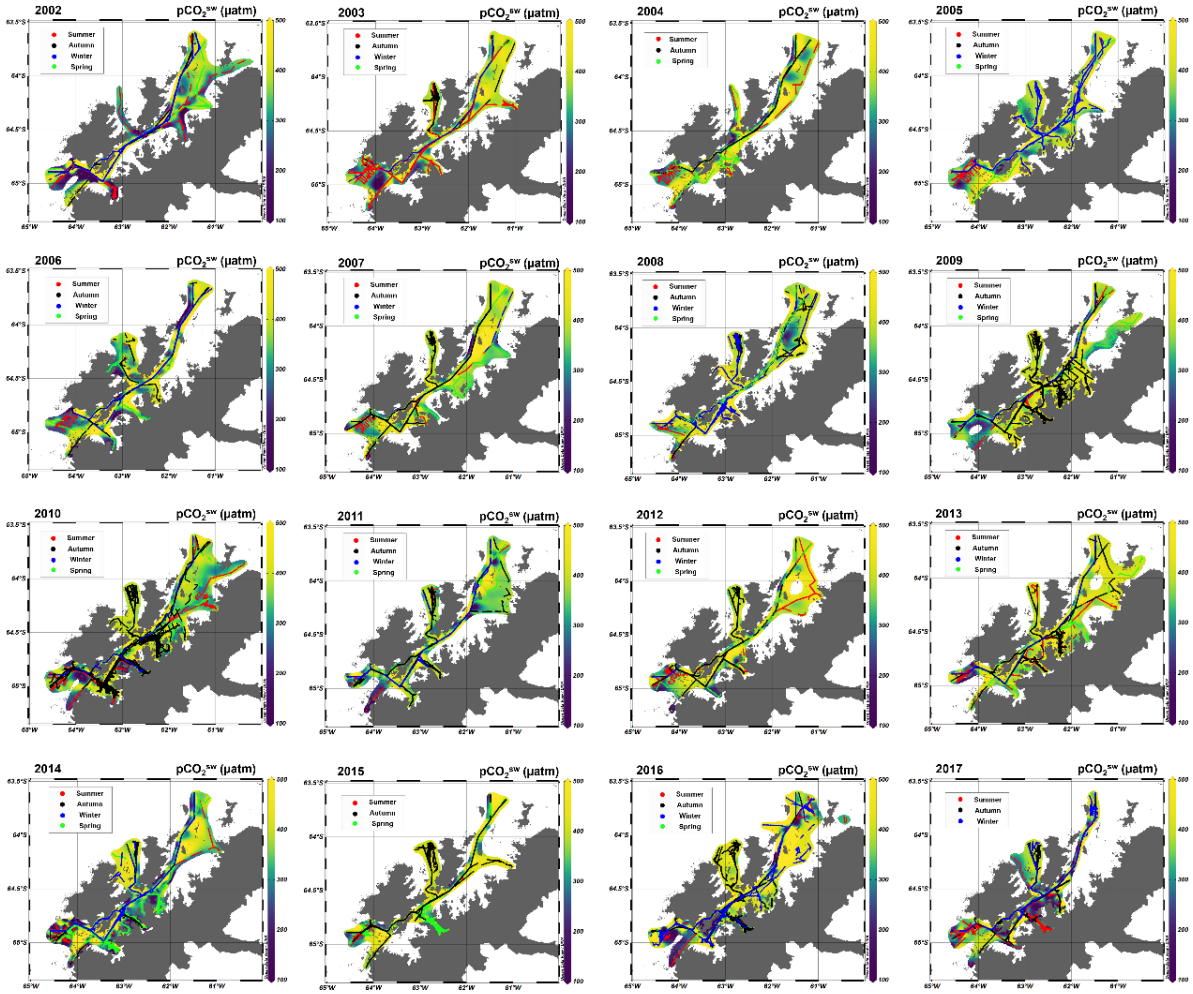

Figure IV-S2: Data coverage of pCO_2^{SW} (with temperature and salinity) per year in each season available for the Gerlache Strait from SOCATv6. The coloured circles indicate the seasons. The percentage of data in each month of the seasons is shown in Fig. IV-S3. These maps were generated by using the software Ocean Data View (v. 5.3.0, http://odv.awi.de).

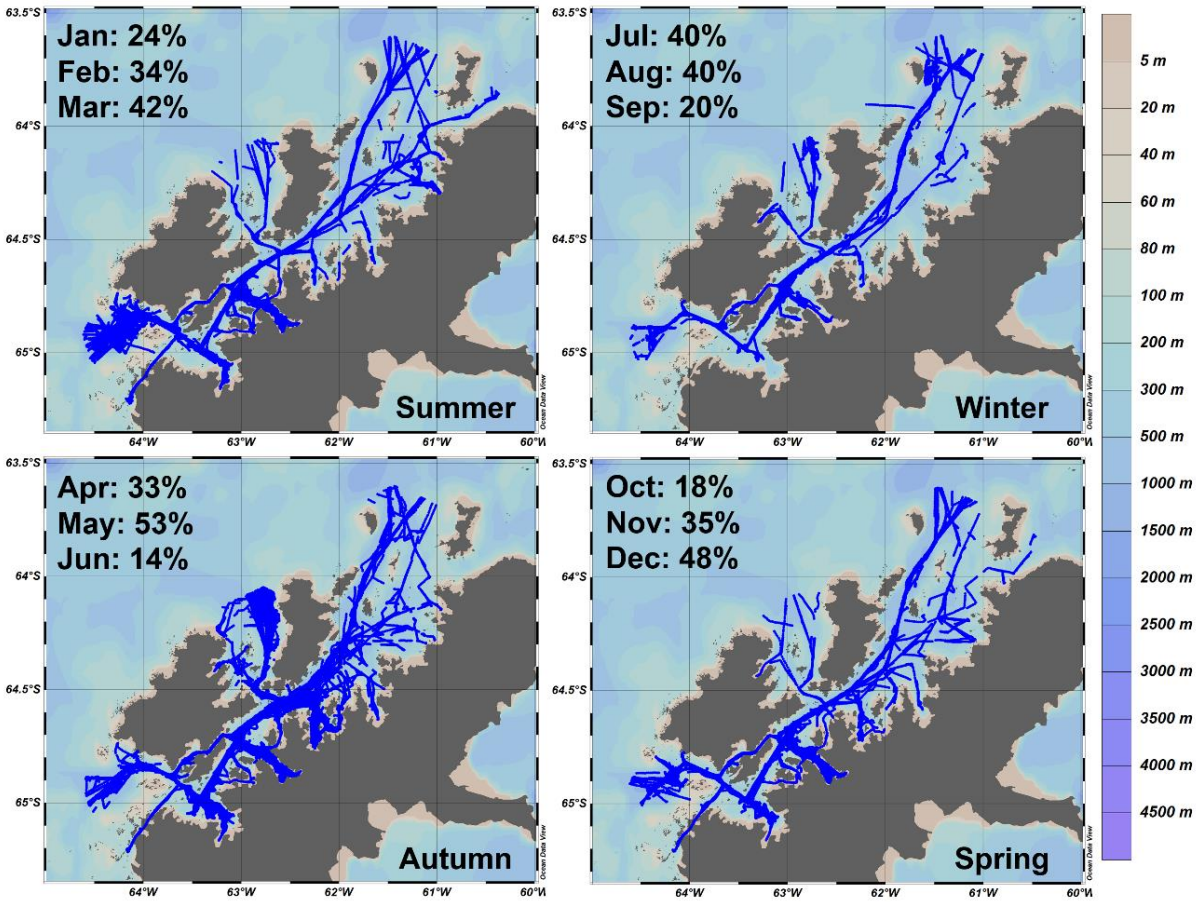

Figure IV-S3: Density and distribution of data in each season with the data percentages within each month. At each point, temperature, salinity and pCO_2^{SW} data were measured and used to derive the other parameters. These maps were generated by using the software Ocean Data View (v. 5.3.0, http://odv.awi.de).

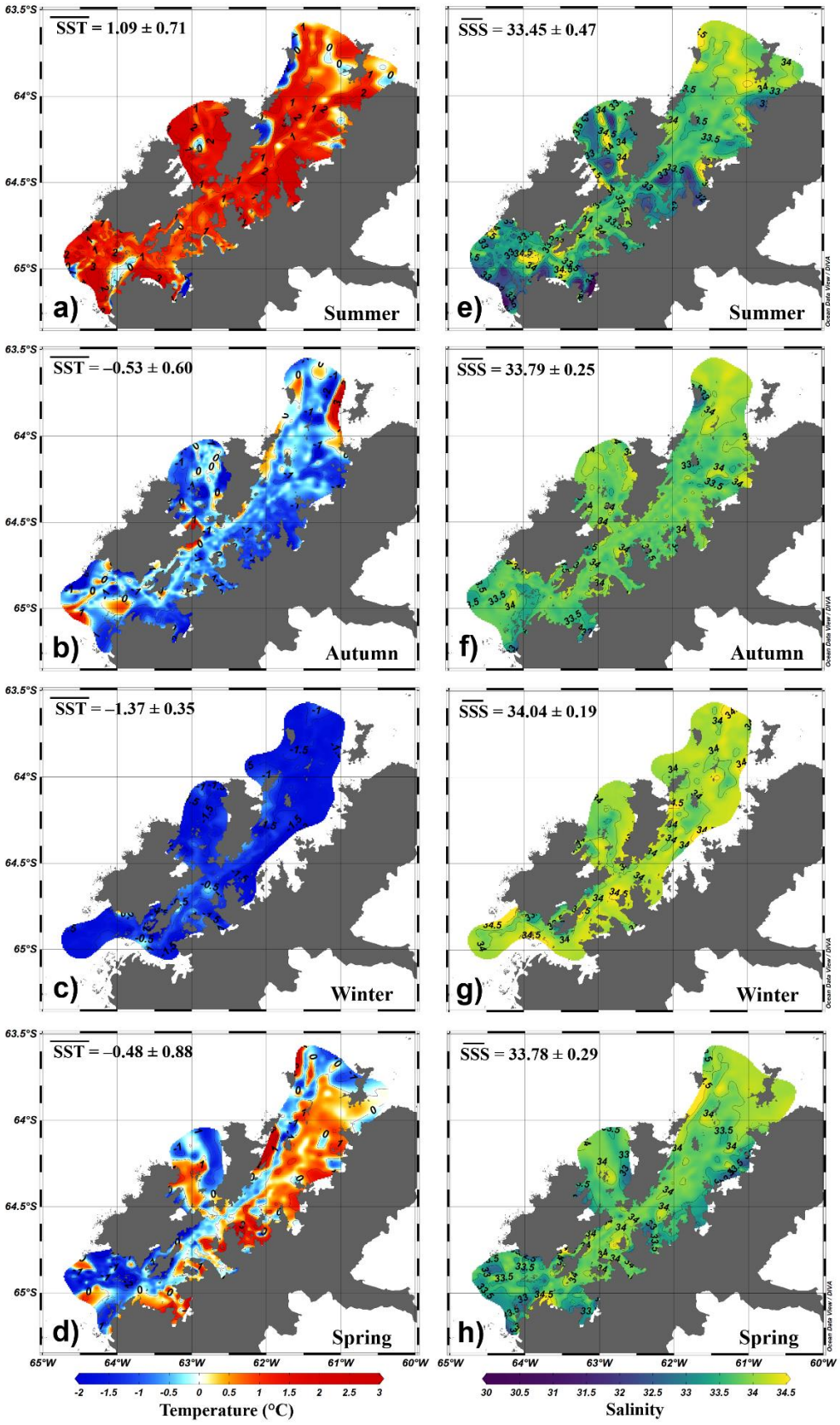

Figure IV-S4: Seasonal surface distribution of temperature (a-d) and salinity (e-h) in the Gerlache Strait from detrended time series from 2002 to 2017. The values indicate the average and standard deviation of each property for the entire area and season. These maps were generated by using the software Ocean Data View (v. 5.3.0, http://odv.awi.de).

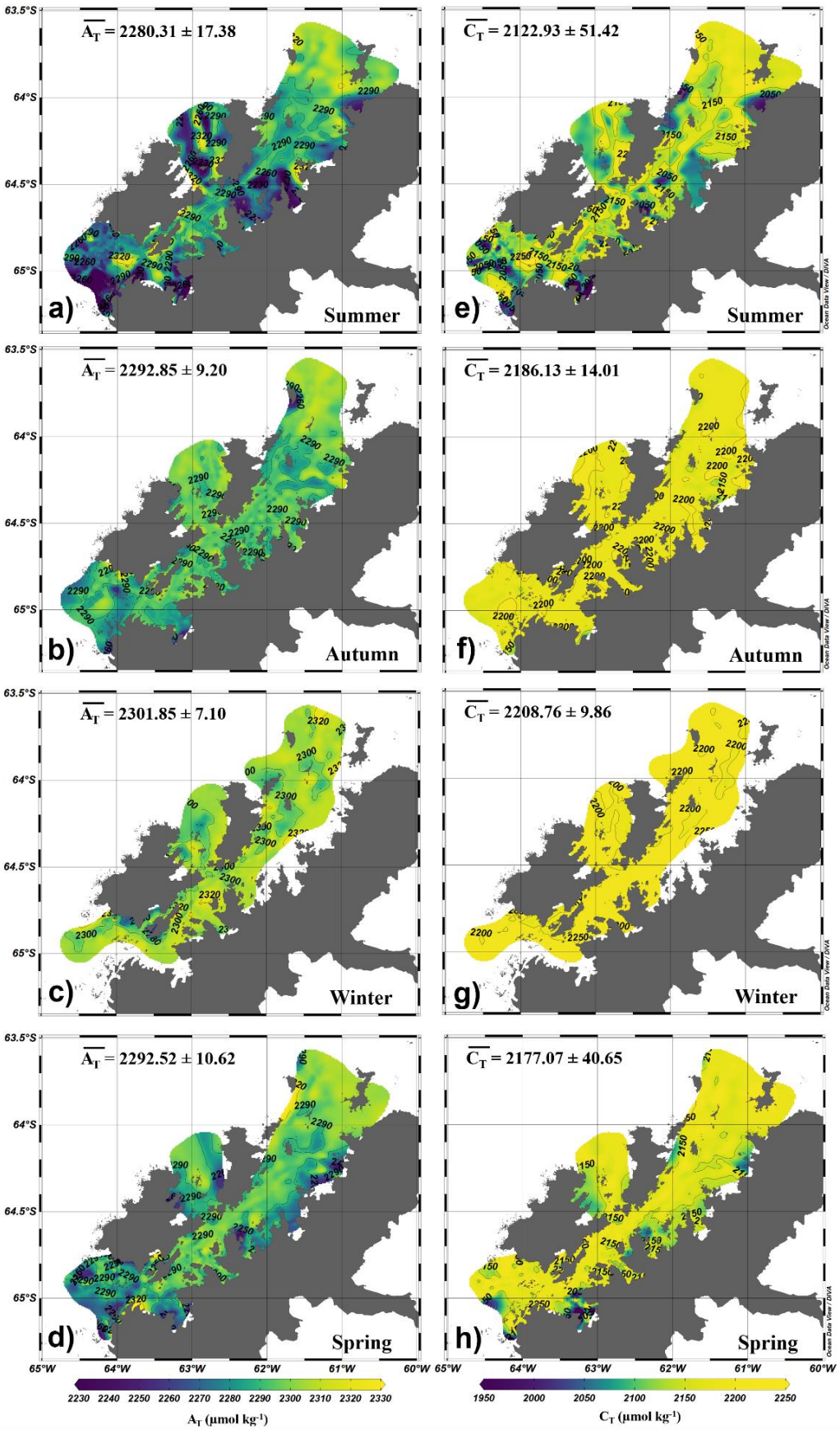

Figure IV-S5: Same as Figure IV-S2 except for total alkalinity–A_T (a-d) and total dissolved inorganic carbon–C_T (e-h). These maps were generated by using the software Ocean Data View (v. 5.3.0, http://odv.awi.de).

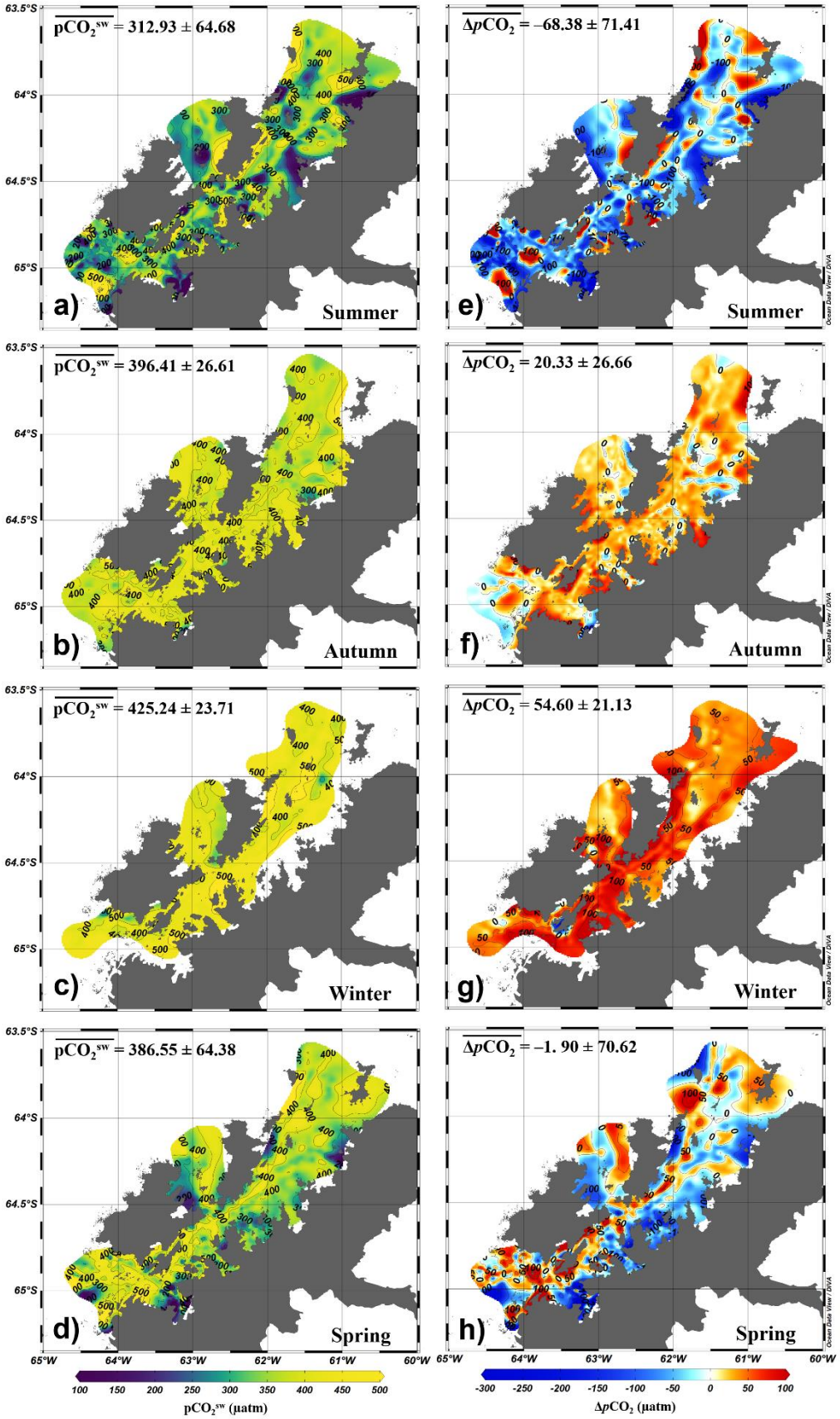

Figure IV-S6: Same as Figure IV-S2 except for pCO_2^{sw} (a-d) and ΔpCO2 (pCO_2^{sw} – pCO_2^{air}) (e-h). These maps were generated by using the software Ocean Data View (v. 5.3.0, http://odv.awi.de).

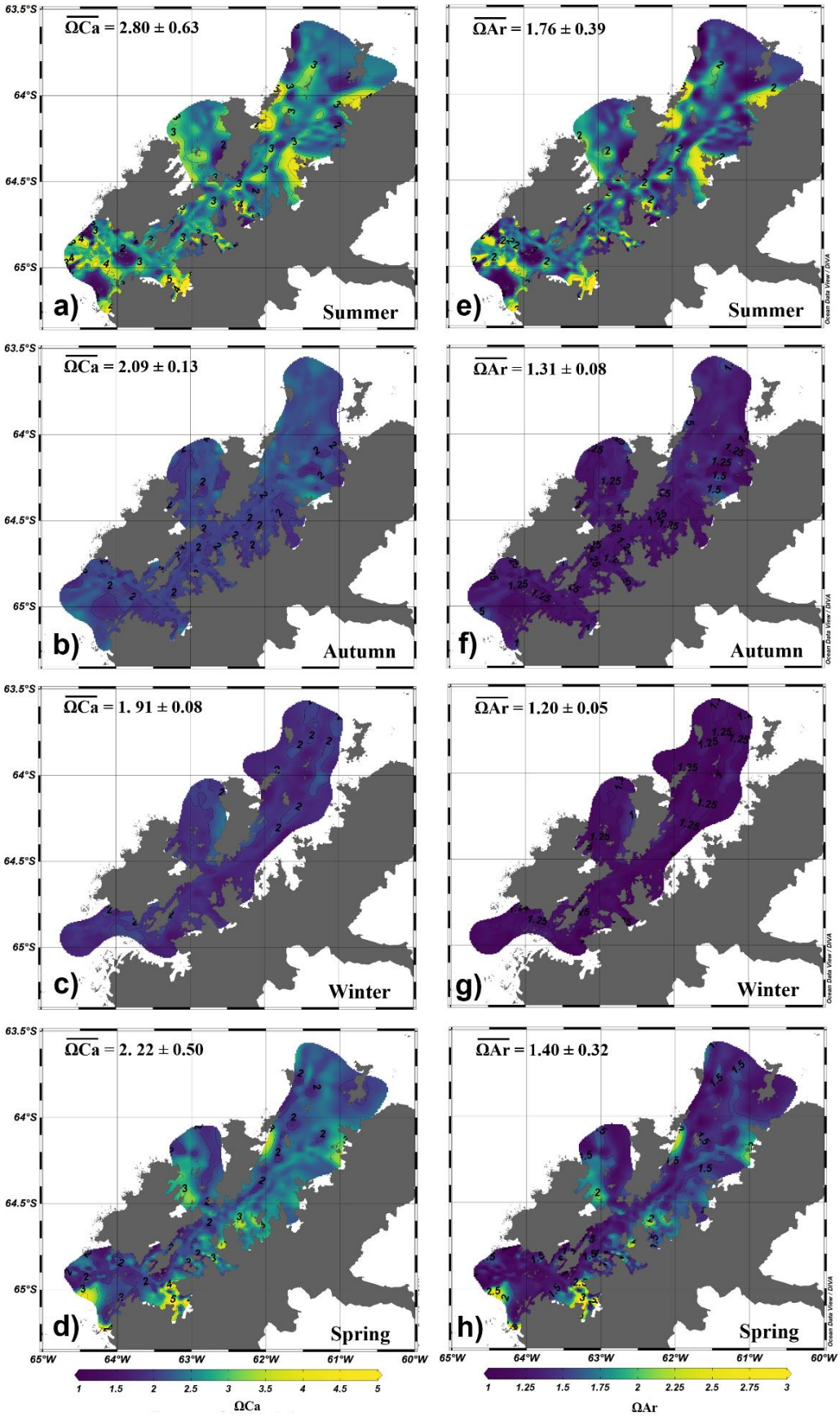

Figure IV-S7: Same as Figure IV-S2 except for the saturation states of calcite–ΩCa (a-d) and aragonite–ΩAr (e-h). These maps were generated by using the software Ocean Data View (v. 5.3.0, http://odv.awi.de).

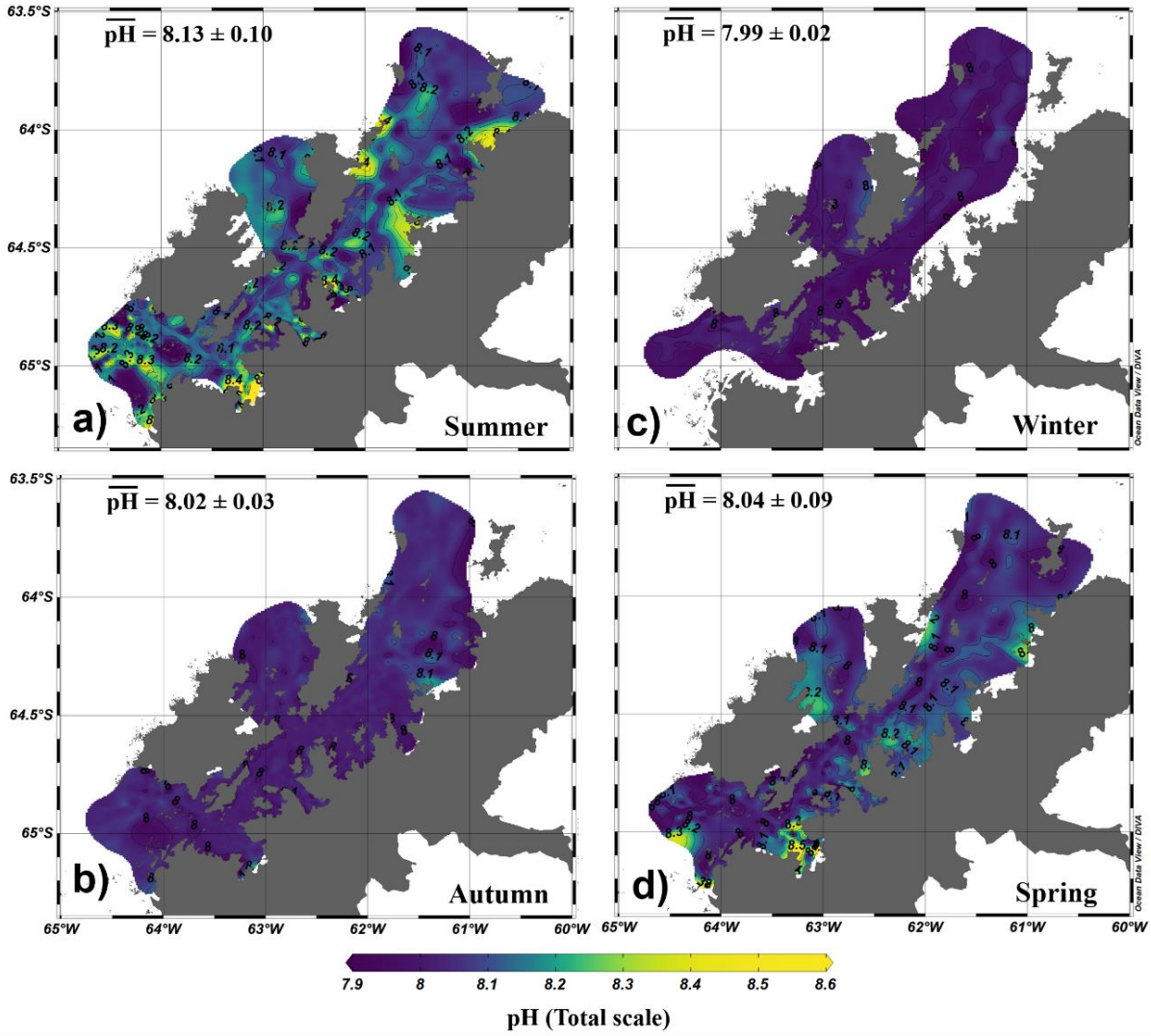

Figure IV-S8: Same as Figure IV-S2 except for pH. These maps were generated by using the software Ocean Data View (v. 5.3.0, http://odv.awi.de).

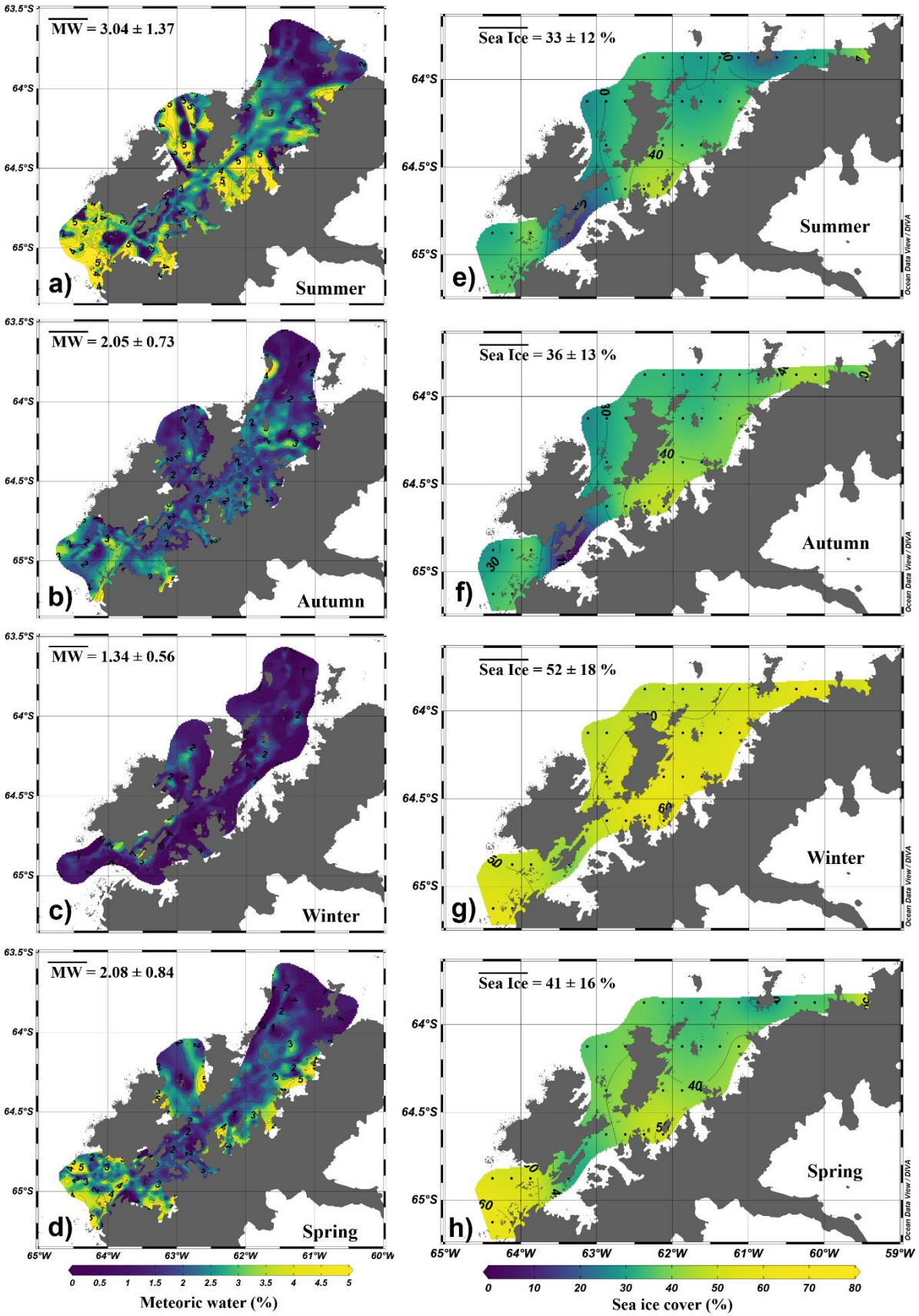

Figure IV-S9: Same as Figure IV-S2 except for meteoric water (a-d) and sea ice cover (e-h) percentage. These maps were generated by using the software Ocean Data View (v. 5.3.0, http://odv.awi.de).

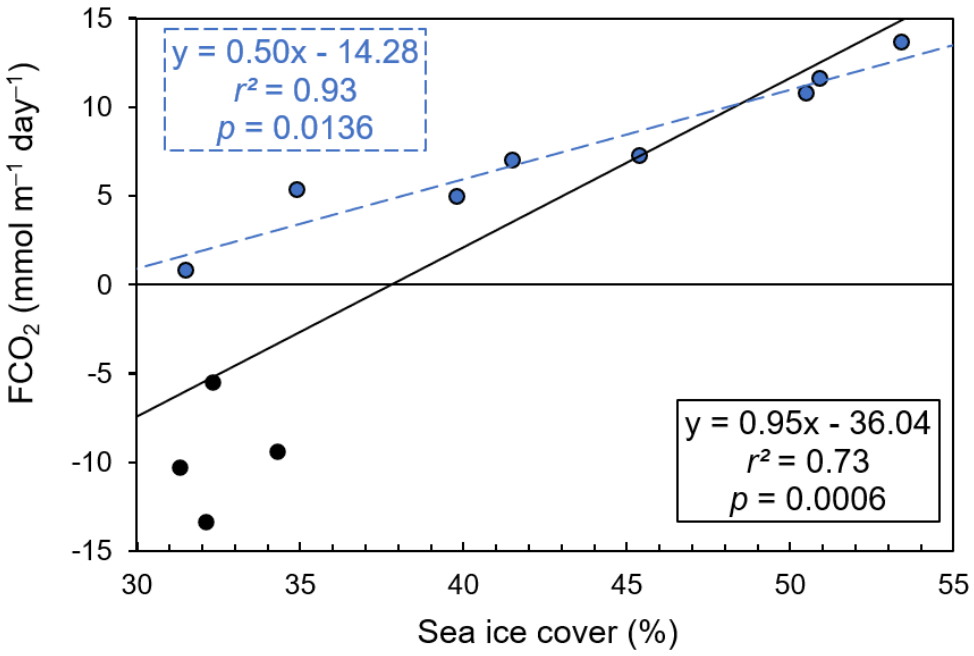

Figure IV-S10: Linear correlation between the seasonal cycle of the net sea-air CO_2 flux (FCO_2) and the percentage of sea ice cover in the Gerlache Strait. Each point represents the monthly averaged values of FCO_2 and sea ice cover between 2002 and 2017. The sea ice data are from the 0.25° daily satellite products from Reynolds *et al*. [2007]. The continuous black line represents the linear fit for all months of the year, and its statistical properties are shown in the continuous black rectangle. The dashed line represents the linear fit only for the months in which the region exhibits CO_2 outgassing (i.e., from April to November; blue-filled circles), and its statistical properties are shown in the dashed blue rectangle.

Capítulo V: Variabilidade espacial e temporal do FCO_2 no WTA

Neste estudo foi demonstrado porque existe divergências nas estimativas de FCO_2 no WTA, qual o papel da ARP na absorção de CO_2 e quais processos controlam o FCO_2 nessa região. A divergência entre os estudos ocorre porque o WTA é dividido em três sub-regiões distintas em termos de FCO_2: a sub-região sob o domínio da NBC, que atua como uma fonte de CO_2 para a atmosfera; a sub-região sob influência da NEC, que atua como sumidouro de CO_2; e a sub-região sob a influência da ARP, que atua como um forte sumidouro de CO_2. Além disso, foi mostrado que a ARP é responsável por 87% da absorção de CO_2 pelo WTA e que essa forte absorção ocorre principalmente devido à alta produtividade primária, alimentada pelas altas concentrações de nutrientes. Este estudo foi publicado no periódico *Global Biogeochemical Cycles* (https://doi.org/10.1029/2022GB007385).

Contrasting sea-air CO_2 exchanges in the western Tropical Atlantic Ocean

Thiago Monteiro, Matheus Batista, Sian Henley, Eunice da Costa Machado, Moacyr Araujo and Rodrigo Kerr

Veja online aqui

5. 1 Introduction

The global ocean plays an essential role in regulating atmospheric CO_2 levels because it takes up about ~25% of atmospheric CO_2 [Friedlingstein *et al*. 2020]. However, the Tropical Atlantic Ocean is the second largest source of CO_2 from the ocean to the atmosphere, mainly due to equatorial upwelling and warm waters [Landschützer *et al*. 2014; Takahashi *et al*. 2009]. The ocean dynamics of the surface current system [e.g., Johns *et al*. 1998; Johns *et al*. 2021; Salisbury *et al*. 2011] and the large freshwater input from the Amazon River [Liang *et al*. 2020], coupled with precipitation dynamics [Ibánhez *et al*. 2015; Utida *et al*. 2019], also add a biogeochemical complexity to the WTA [da Cunha & Buitenhuis 2013].

Such complexity is reflected in the pronounced spatial and temporal variability of the marine carbonate system and particularly in the FCO_2 [Cooley *et al*. 2007; Körtzinger 2003; Lefèvre *et al*. 2010; Louchard *et al*. 2021; Mu *et al*. 2021; Valerio *et al*. 2021]. As a result, some FCO_2 estimates indicate that the WTA acted as a net CO_2 source region [e.g., Cooley *et al*. 2007; Louchard *et al*. 2021; Valerio *et al*. 2021]. Conversely, other studies revealed a net CO_2 sink behavior, mainly due to the high primary productivity driven by optimal nutrient availability supplied by the Amazon River waters [e.g., Ibánhez *et al*. 2015; Ibánhez *et al*. 2016; Körtzinger 2003; Lefèvre *et al*. 2010; Mu *et al*. 2021].

Even when these estimates indicate a FCO_2 in the same direction, the magnitude of these fluxes can vary widely among estimates. For example, estimates of FCO_2 based on satellite data show an average annual CO_2 release

of 4.6 mmol m^{-2} day^{-1} [Valerio *et al*. 2021], while complex biogeochemical models indicate a CO_2 source an order of magnitude lower (0.5 mmol m^{-2} day^{-1}) [Louchard *et al*. 2021] in a vast area of the WTA. Although most studies indicate that the area under the influence of the ARP is an important atmospheric CO_2 sink, the magnitude of ocean CO_2 uptake also varies greatly among them [e.g., Louchard *et al*. 2021; Mu *et al*. 2021].

The great variability in these fluxes is likely associated with sampling that occurs over a limited period and/or with limited geographic scope that does not capture the full extent of variability across the region. This is particularly true because the spreading area of the ARP, as well as the period of maximum freshwater discharge, vary seasonally and interannually [Liang *et al*. 2020]. Furthermore, the surface current system [e.g., Johns *et al*. 1998; Johns *et al*. 2021; Salisbury *et al*. 2011] and the ocean-atmosphere-land coupling [Johns *et al*. 2021; Louchard *et al*. 2021; Utida *et al*. 2019] make it difficult to build an overall picture of sea-air CO_2 exchanges in this region from spatial and temporal snapshots.

5. 1. 1 Oceanographic features of the WTA

Surface dynamics in the WTA are characterized by a complex system of ocean currents (Fig. V-1). The NEC flows westwards in the northern hemisphere, carrying relatively cold waters from the North Atlantic to the WTA (Fig. V-1c) [Johns *et al*. 2021]. On the other hand, the NBC flows northwest along the Brazilian coast [Rodrigues *et al*. 2007; Silva *et al*. 2009; Stramma *et al*. 1995], carrying warm and more saline waters (Figs. V-1b,c) from the equatorial Atlantic to the northern hemisphere [Johns *et al*. 1998, 2021; Salisbury *et al*. 2011]. NBC

waters reach the Amazon River mouth at approximately 5°N, where intense mixing occurs between marine and riverine waters. North of the Amazon River mouth, the NBC retroflects seasonally (Fig. V-1a), carrying waters from both the NBC and the ARP eastwards into the tropical Atlantic, forming the NECC [Fonseca *et al*. 2004; Garzoli *et al*. 2004].

NECC waters reach the easternmost portion of the WTA in September-October [Araujo *et al*. 2017; Lefèvre *et al*. 2020], when their velocity is maximal [Richardson & Reverdin 1987], while there are no clear signs of the NECC in the early months of the year [Johns *et al*. 2021]. Moreover, NBC retroflection can lead to the formation of anticyclonic rings (Fig. V-1a), which transport waters with NBC properties to the northwest of the Tropical Atlantic Ocean [e.g., Aroucha *et al*. 2020; Didden & Schott 1993]. Those eddy-advected waters also carried properties derived from the South Atlantic Ocean, which is influenced by sources in the Indian Ocean [Azar *et al*. 2021; Orselli *et al*. 2019a,b], highlighting important inter-ocean and inter-hemispheric transports.

In addition to its complex ocean surface current system, the WTA is strongly influenced by freshwater input from the Amazon River (Fig. V-S1a), which discharges around 6.6 x 10^3 km^3 of riverine water to the WTA annually [Korosov *et al*. 2015; Salisbury *et al*. 2011]. As it flows into the ocean, the Amazon River develops a plume that can extend over 10^6 km^2 and reach depths of up to 30–35 m, covering a vast portion of the Tropical Atlantic and reaching up to 30°W and 15°N [Coles *et al*. 2013]. The maximum discharge in the inner portion of the Amazon River mouth occurs in March [Liang *et al*. 2020] and there is a delay of around 3 months before these waters spread into the WTA [e.g., Coles *et al*. 2013; Hellweger & Gordon 2002; Korosov *et al*. 2015].

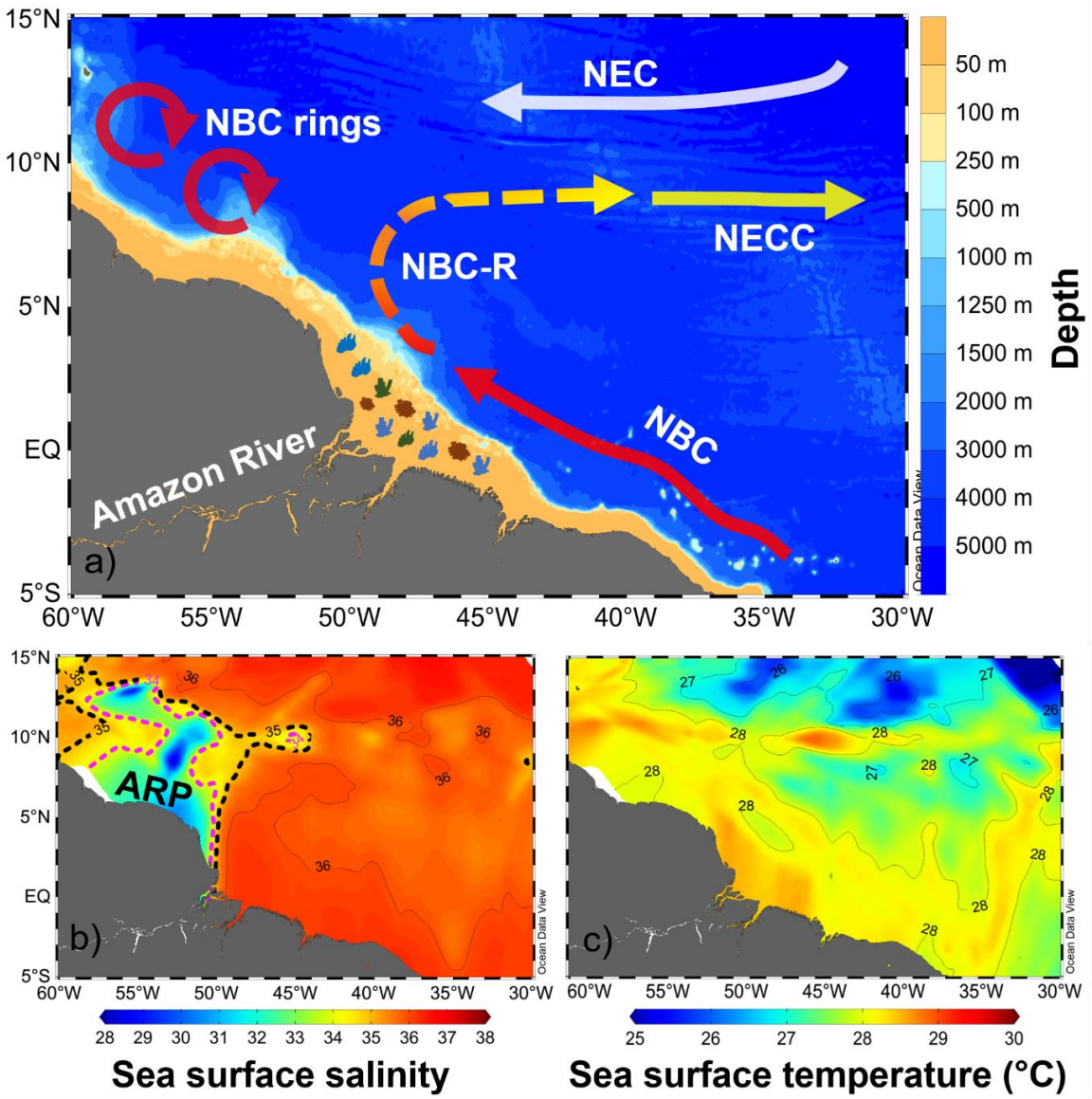

Figure V-1: (a) Western Tropical Atlantic Ocean and the main surface currents that characterise the ocean dynamics in this region (see Johns *et al*. [2021] and references therein): North Equatorial Current (NEC), North Brazil Current (NBC) and the North Equatorial Countercurrent (NECC), which originates from the retroflection of the NBC (NBC-R), as well as the NBC rings. The symbols over the mouth of the Amazon River (a) represent the extensive reef system in this region. (b) Annual climatology of sea surface salinity for the period 1993-2019, with isohalines equal to 35 (dashed black line) and 34 (dashed pink line), representing the Amazon River plume (ARP). (c) Annual climatology of sea surface temperature for the same period in the region.

Although the riverine waters reduce the light penetration in this region due to their relatively high sediment loads, there is an extensive reef system around 0° and 49°W (Fig. V-1a), which almost confines itself to the Amazon River mouth [Moura *et al*. 2016]. The properties of the ARP waters influence the solubility of

CO_2 [Cooley *et al*. 2007] and enhance primary production, both of which lead to under saturation of sea surface CO_2 [Ibánhez *et al*. 2015; Körtzinger 2003; Louchard *et al*. 2021]. Thus, the ARP waters act as a globally relevant atmospheric CO_2 sink [Cooley *et al*. 2007; Ibánhez *et al*. 2015, 2016; Lefèvre *et al*. 2010].

The intense precipitation (Fig. V-S1b) driven by the position of the ITCZ also influences the ocean dynamics in the WTA. The ITCZ varies seasonally, reaching its most northerly position (near 10°N) from June to August and its most southerly (near 4°S) from March to May [Fonseca *et al*. 2004; Utida *et al*. 2019], contributing to the seasonal regulation of sea surface salinity (SSS). In addition, this region is influenced by the El Niño–Southern Oscillation (ENSO), which acts to intensify the drought and flooding periods [Marengo & Espinoza 2016], and by the anomalous warming in the Atlantic Ocean [Tyaquiçã *et al*. 2017]. These events can occur simultaneously, with a range of responses in the physical and chemical properties of the sea surface [Kucharski *et al*. 2016], adding more complexity to biogeochemical cycles in the WTA.

Here, we use a broader set of *in situ* data, with improved spatial and temporal coverage compared to any previous study to investigate why there are contrasting results among the estimates of sea-air CO_2 exchanges. Hence, we have gained a more comprehensive understanding of the CO_2 system and its spatial and temporal variability to explain these contrasting estimates of sea-air CO_2 exchanges in the WTA.

5. 2 Material and Methods

5. 2. 1 Data set and carbonate system properties

We compiled a time series of the hydrographic and carbonate system parameters from the SOCAT version 2020 [Bakker *et al*. 2016] in the WTA spanning 27 years from 1993 to 2019 (Fig. V-S2). The variables used included the SST, SSS and pCO_2. The SOCAT represents a synthesis of quality-controlled sea surface CO_2 fugacity data for the global surface oceans and coastal seas with regular updates. Here we used CO_2 fugacity data from SOCAT with uncertainties <2 µatm (71% of total) and <5 µatm (29% of total). The CO_2 fugacity data extracted from the SOCAT were measured directly using air-water equilibrators and infrared analyzers for CO_2 quantification [Bakker *et al*. 2016]. We converted the CO_2 fugacity data from the SOCAT to pCO_2 using the equations of Weiss [1974].

Since SOCAT only provides SST, SSS and pCO_2 data, we determined the sea surface TA based on the LIAR approach of Carter *et al*. [2018], using SST and SSS as input variables. LIAR is a set of linear regressions capable of estimating TA from different sets of input parameters, considering the depth and coordinates of the measurements. The global uncertainty in the TA estimates using SST and SSS as input variables is expected to be 4.4 µmol kg^{-1} [Carter *et al*. 2018]. The results of LIAR approximations were compared with *in situ* TA data available from GLODAP 2020 [Olsen *et al*. 2020] in the study region (accuracy of ±4.0 µmol kg^{-1}) and RMSE was 6.5 µmol kg^{-1} (r^2 = 0.99, n = 453, p < 0.0001).

The surface DIC was determined using CO2Sys v2.1 [Pierrot & Wallace 2006] based on inputs of SST, SSS, pCO_2 and TA, using the HSO_4^- dissociation constant of Dickson [1990] and the total borate-salinity relationship proposed by

Uppström [1974]. We verified the K1 and K2 constants of Millero *et al*. [2006], Millero [2010], Lueker *et al*. [2000], and Mehrbach *et al*. [1973] refit by Dickson & Millero [1987], as generally recommended for our SSS and SST ranges, and Cai & Wang [1998] for low salinities. The greatest inconsistency for DIC among these constants was 4.64 μmol kg^{-1} between Millero *et al*. [2006] and Cai & Wang [1998], while the smallest inconsistency was −0.13 μmol kg^{-1} between Lueker *et al*. [2000] e Mehrbach *et al*. [1973] refit by Dickson & Millero [1987]. These inconsistencies are lower than the error of ± 6.5 μmol kg^{-1} associated with the estimate of TA by the LIAR approximation. Thus, we used the carbonate constants of Millero *et al*. [2006], which have been widely used in studies in the WTA [e.g., Araujo *et al*. 2018; Bonou *et al*. 2016].

5. 2. 2 Calculation of FCO_2

The FCO_2 was calculated by following Eq. V-1:

$$FCO_2 = K_t \times K_s \times (pCO_2^{sw} - pCO_2^{air}), \quad \text{V-1}$$

where Kt is the CO_2 gas transfer velocity, depending on wind speed [Wanninkhof 2014]; Ks is the CO_2 solubility coefficient, as a function of both SST and SSS [Weiss 1974], pCO_2^{sw} is sea surface pCO_2 and pCO_2^{air} is atmospheric pCO_2. The pCO_2^{air} was calculated from the monthly averages of the atmospheric molar fraction of CO_2 at Barbados Station located at 13.16°N–59.43°W [Dlugokencky *et al*. 2021] and atmospheric pressure from SOCAT. The latter was corrected by the water vapor pressure estimated from SST and SSS by the widely used equations of Weiss & Price [1980]. We used monthly averages of wind speed (m s^{-1}) at 10 m from the atmospheric reanalysis ERA5 (Fig. V-S1d) with a spatial

resolution of 0.25° [Hersbach *et al*. 2020]. We combined the coordinates and sampling month of the sea surface pCO_2 from SOCAT with the reanalysis ERA5 data to ensure that the wind speed covered the same region and the same period.

The spatial distribution maps for sea-air CO_2 flux, SSS and SST were interpolated using the Ocean Data View function of weighted-average gridding [Schlitzer 2018] to construct the climatologies showed in Figs. V-1 and V-2. We used a length scale value of 20‰ for both the X and Y axes to ensure optimal preservation of data structure and smoothness. The averaging and all other calculations performed in this study were based only on the observed data and not on the interpolated data. We made the map interpolation to provide reader-friendly visualization of the results.

5. 2. 3 Drivers of pCO_2 changes

We estimated the drivers of seasonal changes in sea surface pCO_2 (ΔpCO_2^D) between the wet season and the dry season by the approach described in Takahashi *et al*. [2014], which is based on the seasonal amplitudes of the variables, following Eq. V-2:

$$\Delta pCO_2^D = \frac{\partial pCO_2}{\partial DIC}\Delta DIC + \frac{\partial pCO_2}{\partial TA}\Delta TA + \frac{\partial pCO_2}{\partial SST}\Delta SST + \frac{\partial pCO_2}{\partial SSS}\Delta SSS, \qquad \text{V-2}$$

where ΔDIC, ΔTA, ΔSST and ΔSSS are the seasonal amplitudes of the variables (i.e., the difference between averaged values for the wet and dry seasons; Tab. V-1).

Table V-1. Average differences for the sea surface temperature – SST (°C), salinity – SSS, total alkalinity – TA (µmol kg^{-1}), and dissolved inorganic carbon – DIC (µmol kg^{-1}) involved in seasonal pCO_2 changes – ΔpCO_2^D (µatm). The table shows the differences in the average values of the parameters between the wet (April-September) and dry (October-March) seasons in the following regions: North Brazil Current (NBC), North Equatorial Current (NEC) and Amazon Plume region (APR).

	NBC-NECC	**NEC**	**ARP**
ΔSST	0.51	–0.22	–0.09
ΔSSS	–0.08	0.29	–2.75
ΔTA	–17.82	16.68	–168.26
ΔDIC	–19.14	23.35	–128.07
ΔpCO_2^D	–3.15	15.87	–15.88

We calculated the partial derivatives using Eqs. V-3 to V-7 [see details in Sarmiento & Gruber 2006] and the term involving SST using Eq. V-8 [Takahashi *et al*. 2014]. The terms Revelle factor (Eq. V-7) and Alkalinity factor (Eq. V-8) refer to the sensitivity of pCO_2 to changes in DIC and TA, respectively. Here, we used average Revelle and alkalinity factors of 9.13 and −8.5, respectively. The combined influence of the seasonal drivers is consistent with the calculated ΔpCO_2^D, with an average error of 1 µatm.

$$\frac{\partial pCO_2}{\partial DIC} = \frac{pCO_2}{DIC} \times \text{Revelle Factor} \qquad \text{V-3}$$

$$\frac{\partial pCO_2}{\partial TA} = \frac{pCO_2}{TA} \times \text{Alkalinity Factor} \qquad \text{V-4}$$

$$\frac{\partial pCO_2}{\partial SSS} \approx 0.026 \times pCO_2 \qquad \text{V-5}$$

$$\text{Revelle Factor} \approx \frac{3TA \times DIC - 2DIC^2}{(2DIC - TA)(TA - DIC)} \qquad \text{V-6}$$

$$\text{Alkalinity Factor} \approx -\frac{TA^2}{(2DIC - TA)(TA - DIC)} \qquad \text{V-7}$$

$$\frac{\partial pCO_2}{\partial SST} \Delta SST \approx 2\, pCO_2 \times \left[\text{Exp}\left(0.0423 \times \frac{\Delta SST}{2}\right) - 1\right] \qquad \text{V-8}$$

Here, the seasonal periods were defined as wet (April-September) and dry (October-March) following Bonou *et al*. [2016], which includes the months when the waters from the Amazon River spread over a larger area throughout the WTA in the wet season. There is a delay of up to 3 months from the largest freshwater discharge of the Amazon River to the extreme northwest and east spreading that the freshwater plume can reach [e.g., Hellweger & Gordon 2002; Coles *et al*. 2013; Korosov *et al*. 2015]. Therefore, we include both the period of maximum freshwater discharge at the mouth of the Amazon River [Liang *et al*. 2020] and the months in which its waters reach the easternmost point of the WTA [Varona *et al*. 2019; Lefèvre *et al*. 2020].

To assess the effect of SST on the sea surface pCO_2 time series, we removed its thermal component by normalising pCO_2 to the annual average SST (Eq. V-9), following the approach of Takahashi *et al*. [2002]:

$$pCO_{2\ \text{non-thermal}} = pCO_{2\ \text{obs}} \times \exp\left[0.0423 \times (SST_{avg} - SST_{obs})\right], \qquad \text{V-9}$$

where pCO_{2obs} and SST_{obs} are *in situ* sea surface pCO_2 and SST, respectively, and SST_{avg} is the average SST for the entire study period in each sub-region (i.e., NBC-NECC: 27.65 °C, NEC: 26.89 °C, ARP: 28.29 °C).

5. 2. 4 Normalization of TA and DIC by average annual SSS

We normalized TA and DIC to an annual average salinity for each region using a non-zero freshwater end-member according to the Eq. V-10 by Friis *et al*. [2003]:

$$\text{nTA} = \frac{TA^{meas} - TA^{S=0}}{SSS^{meas}} \times SSS^{avg} + TA^{S=0}, \qquad \text{V-10}$$

where TA^{meas} is the measured TA, $TA^{S=0}$ is the TA for a non-zero salinity, SSS_{meas} is the measured salinity and SSS_{avg} is the annual average salinity for each region. We used the same equation to calculate the DIC normalised by salinity. Here we used the linear correlation coefficient between TA/DIC and SSS as the non-zero freshwater end-member terms (i.e., $TA^{s=0}$ and $DIC^{S=0}$). We used the following average salinities, $TA^{S=0}$ and $DIC^{S=0}$ (Tab. V-2).

Table V-2. Values for annual average salinity (SSS), $TA^{s=0}$ (µmol kg^{-1}) and $DIC^{S=0}$ (µmol kg^{-1}) used to calculate the TA and DIC normalised to the average salinity in North Brazil Current-North Equatorial Countercurrent (NBC-NECC), North Equatorial Current (NEC), and Amazon River plume (ARP) regions.

	NBC-NECC	**NEC**	**ARP**
SSS	35.87 ± 1.26	34.71 ± 2.57	32.02 ± 3.39
$TA^{S=0}$	303	346	355
$DIC^{S=0}$	404	290	320

5. 2. 5 Chlorophyll-a trend

Sea surface chlorophyll-a concentrations with a spatial resolution of 4 km and a monthly temporal resolution for the period of 1997–2020 were obtained for the WTA from the European Space Agency (ESA) Ocean-Colour Climate Change Initiative project (OC-CCI v5.0) [Sathyendranath *et al*. 2021] (http://dx.doi.org/10.5285/1dbe7a109c0244aaad713e078fd3059a). This dataset was created by band-shifting and bias-correcting observations from the SeaWiFS, MODIS, VIIRS, and OLCI sensors to match MERIS observations, merging those data in a unique dataset. As the dataset is available in two projections (sinusoidal and geographic) only data from the geographic projection was used for the analysis. We applied the methodology of Kulk *et al*. [2020] to estimate the annual rate of chlorophyll-a changes. Therefore, chlorophyll-a climatologies for each month and the total period were calculated by logging the

chlorophyll-a concentrations, averaging, and then unlogging the results. This step was necessary due to the highly skewed distribution of chlorophyll values, especially in the regions near the coast [Gaube *et al*., 2014]. Subsequently, monthly concentrations were deseasonalized by subtracting the monthly climatologies, and a linear regression was applied to each grid point to evaluate the rate of change over time. Using the slope and intercept from the regression analysis the percentage change per year in chlorophyll-a (%CHL) was calculated as Eq. V-11:

$$\%CHL = 100 \times \frac{12 \times slope}{intercept + climatology} \quad \text{V-11}$$

5. 2. 6 Defined sub-regions in the WTA

We set the ARP sub-region (i.e., the region under the Amazon River plume domain) to SSS < 35 (Fig. V-2) and split the sub-regions under NBC-NECC and NEC domain from a climatology equi- librium isoline of annual average FCO_2 (Fig. V-S3). Since the FCO_2 equilibrium isoline is expected to oscillate regionally over the time series, we used an average isoline for the entire period, so we can observe the signs of this oscillation in our time series.

5. 3 Results

5. 3. 1 Regional variability and main drivers of FCO_2

We identified three distinct sub-regions for annual sea-air CO_2 flux behavior in the WTA from 1993 to 2019, which are maintained both in dry and wet seasons (Fig. V-2).The NBC-NECC sub-region acted as a weak annual source of CO_2 to the atmosphere of 1.5 ± 0.7 mmol m^{-2} day^{-1}, while the NEC

acted as a weak annual CO_2 sink of −2.2 ± 1.0 mmol m^{-2} day^{-1} throughout the analysis period. The ARP (i.e., SSS < 35) acted as a moderate CO_2 sink with an annual average of −5.0 ± 3.0 mmol m^{-2} day^{-1}, while a strengthened CO_2 uptake of −10 mmol m^{-2} day^{-1} is observed where the influence of the ARP is intensified (Fig. V-2c), mainly during the wet season (Fig. V-2b). The sub-region under NBC-NECC influence is outlined by an annual sea-air CO_2 equilibrium isoline around 10°N and is constrained by the ARP sub-region at approximately 50°W. However, the area under the NBC-NECC domain extends beyond 50°W in the dry season and there are signs of its influence beyond 10°N in both the wet and dry seasons (Figs. V-2a and V-2b).

Moreover, we observed signs of CO_2 outgassing northwest of the ARP sub-region in both dry (Fig. V-2a) and wet (Fig. V-2b) seasons. The annual ocean CO_2 uptake is intensified in the northwest, and it is reduced in the southern portion of the NEC sub-region. Despite presenting sub-regions with contrasting sea-air CO_2 flux behavior, the WTA behaved as an oceanic CO_2 sink overall from 1993 to 2019 in both wet and dry seasons, with an annual average of −1.6 ± 1.0 mmol m^{-2} day^{-1}. 87% of this CO_2 uptake occurs in waters under the influence of the ARP, as shown by the average CO_2 net flux dropping notably to −0.2 ± 1.0 mmol m^{-2} day^{-1} when the strong CO_2 uptake at the ARP was not considered in the average.

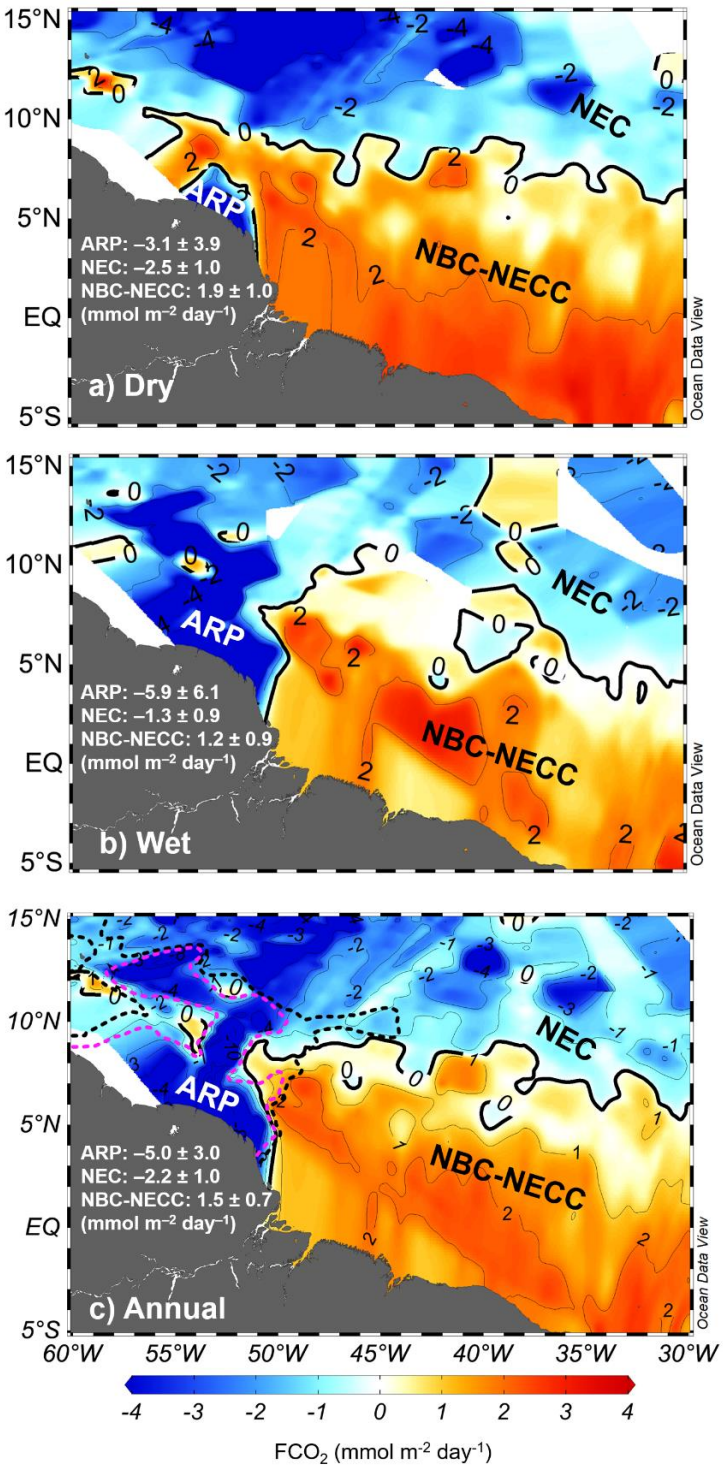

Figure V-2: Climatological distribution of the net sea-air CO_2 flux (FCO_2) in the western Tropical Atlantic Ocean from 1993 to 2019 in the (a) dry and (b) wet seasons, as well as (c) annual average. Positive FCO_2 values (yellow to red) represent the outgassing of CO_2 to the atmosphere, whereas negative FCO_2 values (light to dark blue) represent CO_2 uptake by the ocean. There are three distinct sub-regions for FCO_2: the North Brazil Current-North Equatorial Countercurrent (NBC-NECC), acting as a weak source of CO_2 to the atmosphere; the North Equatorial Current (NEC), acting as a weak sink of atmospheric CO_2; and the Amazon River plume (ARP), which is a moderate sink of atmospheric CO_2. The bold black line represents the isoline for FCO_2 equal to zero, where there is an equilibrium in the sea-air CO_2 exchange. The black dashed isoline in (c) delimits the region under the influence of the ARP, characterised by salinity < 35 and the pink dashed isoline delimits the region with salinity <34, where the influence of the Amazon plume is intensified. The numbers indicate the averages and standard deviations of FCO_2 in each sub-region.

Since atmospheric pCO_2 is more stable seasonally than sea surface pCO_2, we consider seasonal variations in sea surface pCO_2 as the main driver of the sea-air CO_2 fluxes. From the dry to the wet season, sea surface pCO_2 increased by 16 µatm in the NEC sub-region, while it decreased by 16 µatm in the ARP sub-region and by only 3 µatm in the NBC-NECC sub-region (Fig. V-3). DIC and TA were the main drivers of seasonal variations of sea surface pCO_2 in all sub-regions and SSS was a secondary driver in ARP. Both DIC and TA had the same magnitude but with opposite signs, thus almost counteracting each other's effect on sea surface pCO_2 (Fig. V-3a).

However, when we normalized DIC and TA to SSS, SSS appears as the main driver of sea surface pCO_2 drawdown in the wet season in ARP. Such a pCO_2 drawdown is partially counteracted by an increase in salinity-normalized DIC (nDIC) in the wet season, and the influence of salinity-normalized TA (nTA) and SST is negligible (Fig. V-3b). A significant difference was observed in NBC-NECC, where nDIC and SSS led to a sea surface pCO_2 drawdown in the wet season, and this was almost counteracted by the increase in SST. The main change by using nDIC and nTA in NEC was the decrease in the magnitude of TA as a sea surface pCO_2 driver, so virtually every increase in sea surface pCO_2 in the wet season was driven by the increase in DIC (Fig. V-3b).

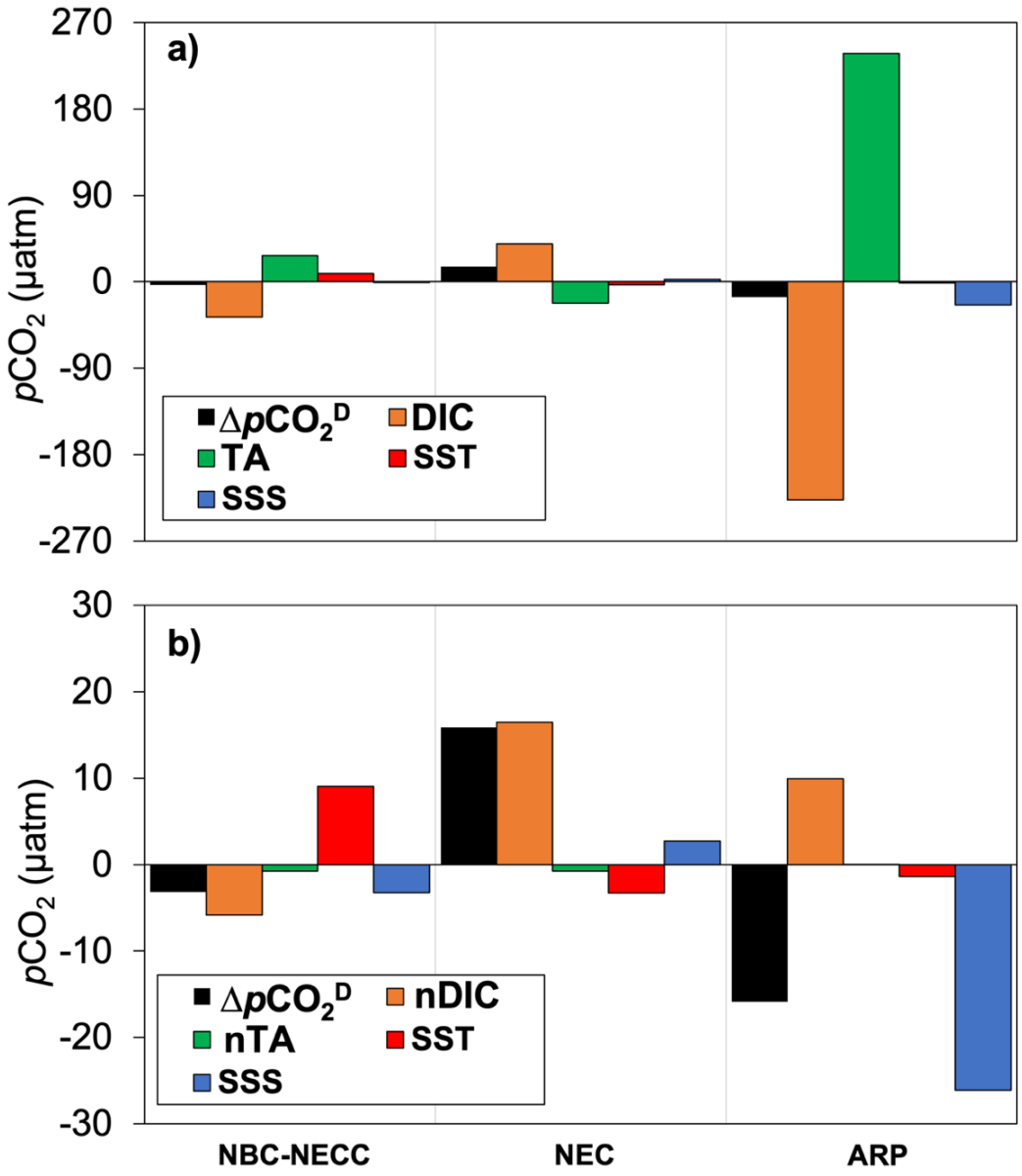

Figure V-3: Effects of seasonal variation sea surface in total alkalinity (TA), dissolved inorganic carbon (DIC), temperature (SST) and salinity (SSS) on the seasonal variation in sea surface pCO_2 (ΔpCO_2^D) for each sub-region of the Western Tropical Atlantic Ocean. In (a) the influence of TA and DIC and in (b) the influence of TA and DIC normalised to the annual average salinity of each sub-region (nTA and nDIC, respectively), following Friis *et al*. [2003]. The annual average salinities used were 35.87, 34.71 and 31.93 for the North Brazil Current-North Equatorial Countercurrent (NBC-NECC), the North Equatorial Current (NEC), and the Amazon River plume (ARP) sub-regions, respectively. The seasonal variation in each parameter is calculated as the difference between the wet (April – September) mean value and the dry (October – March) mean value. The unit of all drivers is the same as that for pCO_2 (µatm), and their magnitudes represent their influence on pCO_2 changes. Positive values indicate that an increase in the parameter led to an increase in pCO_2; negative values indicate that a decrease in the parameter led to a decrease in pCO_2. The only exception to this is TA because an increase in TA leads to a decrease in pCO_2 and vice versa. The combined influence of the seasonal drivers is consistent with the calculated seasonal variation in pCO_2 (ΔpCO_2^D), with an average error of less than 10%. More details are given in the methods section.

The dispersion of TA and DIC and the ratio between these parameters can be used to diagnose the processes influencing them (Fig. V-4), because each process alters TA and DIC with a certain ratio [Zeebe & Wolf-Gladrow 2001]. Here, the TA:DIC ratio for the whole region was 1.13, very close to the 1.12 ratio expected for the sum of all processes acting together (Fig. V-4). This ratio decreases to 0.81 in NEC and to 0.87 in NBC-NECC, revealing that variations in DIC in these sub-regions are likely more important than variations in TA.

In fact, when the effect of SSS on TA and DIC is removed, the CO2 release and uptake processes seem to exert greater influence in waters under the NEC and NBC-NECC domain (Fig. V-4b). On the other hand, in the ARP sub-region the TA:DIC ratio was 1.14, likely revealing that all processes controlling TA and DIC act simultaneously. After removing the SSS effect in the ARP sub-region, dissolution and calcification processes exerted greater influence over a wide range of salinity, while photosynthesis (Fig. V-S8) and CO_2 release/uptake processes can also work to control the changes in nDIC and nTA in waters with salinities <30 (Fig. V-4c).

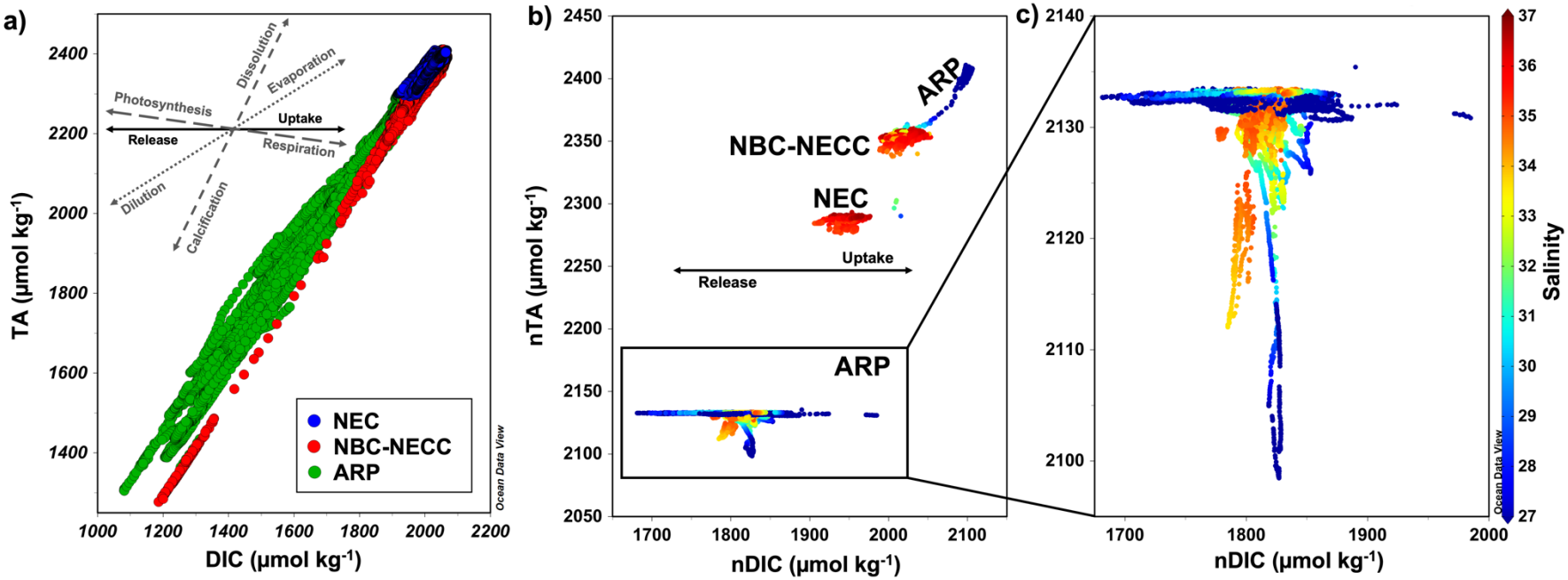

Figure V-4: (a) Total alkalinity (TA) and dissolved inorganic carbon (DIC) dispersion diagram for the North Brazil Current-North Equatorial Countercurrent (NBC-NECC), North Equatorial Current (NEC), and Amazon River plume (ARP) sub-regions. In (b) the diagram is shown considering TA and DIC normalised by the annual average salinity of each sub-region (nTA and nDIC, respectively), following Friis *et al*. [2003] and in (c) the same only for ARP. The annual average salinities used were 35.87, 34.71 and 31.93 for the sub-regions NBC-NECC, NEC and ARP, respectively. The arrows represent the TA:DIC (nTA:nDIC) ratio that characterises the physical-biogeochemical processes that affect these parameters (based on Zeebe & Wolf-Gladrow [2001]) and the colourbar indicates salinity in (b) and (c). Such TA:DIC ratios are as follows: 2:1 for calcification/dissolution, 6:5 for dilution/evaporation, -0.14:1 for photosynthesis/respiration, whereas only DIC is altered in release/uptake processes. Note that the axis scales are different among subplots.

5. 3. 2 Temporal variability and trends in FCO_2

From 1993 to 2019, the temporal variability of the carbonate system parameters and SSS follow similar oscillation and lower amplitude in both NBC-NECC and NEC sub-regions, while much larger interannual variability occurs in the ARP domain (Fig. V-5). On the other hand, SST was the parameter that varied most in NBC-NECC and NEC over the period studied, with amplitude similar to that of ARP (Fig. V-5c). SSS, pCO_2, DIC and TA were markedly higher in NBC-NECC and NEC than in ARP. In the NBC-NECC and NEC sub-regions, sea surface pCO_2 increased significantly at a rate of 2.27 and 2.23 µatm $year^{-1}$ from 1993 to 2019, respectively (Fig. V-5a). This resulted in a sea surface pCO_2 increase of 59 µatm at NBC-NECC and 58 µatm at NEC over the 27-year study period. Such an increasing trend was also observed in the time series of sea surface pCO_2 anomaly in both sub-regions (Fig. V-S4) and in both wet and dry seasons (Fig. V-S5). SST showed a significant increase of 0.06°C $year^{-1}$ in the NEC sub-region, when the anomalous year 2002 (i.e., the warmest year in the time series) is removed (Fig. V-5c). DIC also increased at a rate of 1.22 µmol kg^{-1} $year^{-1}$ in NBC-NECC sub-region (Fig. V-5e).

All hydrographic and carbonate variables showed marked interannual variability in ARP, without any statistically significant trend. The highest interannual amplitude of sea surface pCO_2 in ARP (84 µatm) was found between 2012 and 2017, concurrent with higher amplitudes in SSS (4.67), TA (259 µmol kg^{-1}) and DIC (232 µmol kg^{-1}).

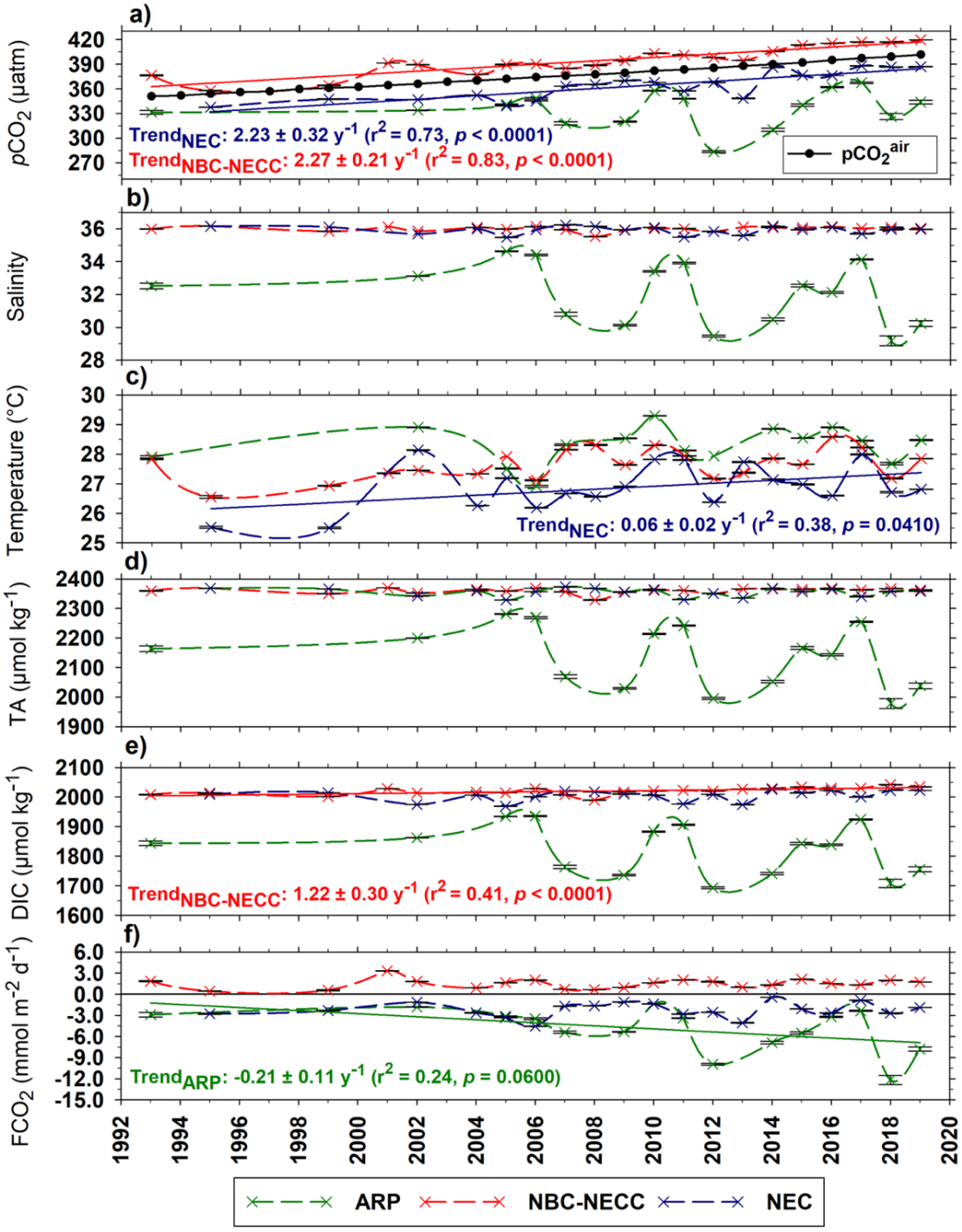

Figure V-5: Time series of annual averages of (a) sea surface (colours) and atmospheric (black) CO_2 partial pressure (pCO_2), (b) salinity, (c) temperature, (d) total alkalinity (TA), (e) dissolved inorganic carbon (DIC) and (f) net sea-air CO_2 flux (FCO_2) in the Western Tropical Atlantic Ocean from 1993 to 2019. Three sub-regions are shown: North Brazil Current-North Equatorial Countercurrent – NBC-NECC (red), North Equatorial Current – NEC (blue), and the Amazon River plume – ARP (green). The dashed lines reflect the temporal trend of the parameters, and their colours are associated with the respective sub-regions. For significant trends (solid lines, with colour depicting sub-region), the trend ± standard deviation as well as its regression statistics are shown. The y-axis error bars (black) are the standard errors of the respective annual averages.

Despite the significant steady increase in sea surface pCO_2 in NBC-NECC and NEC, there was no significant trend in sea-air CO_2 exchanges in these sub-regions (Fig. V-5f). On the other hand, CO_2 uptake in ARP showed a slight increase of −0.21 mmol m^{-2} day^{-1} $year^{-1}$ over the time series, at the 94% confidence level (Fig. V-5f). Over the 27-year study period, these sub-regions maintained their average behavior as a source (NBC-NECC) or sink (NEC and ARP) of CO_2, with variations only in the magnitude of these fluxes.

5. 4 Discussion

5. 4. 1 Main Findings

We demonstrate that the WTA can be split into three distinct sub-regions in terms of sea-air CO_2 exchanges. These contrasting behaviors of the three sub-regions explain why there is such inconsistency in estimates of sea-air CO_2 exchanges in this region (Tab. V-3) since many of them are temporally and/ or spatially restricted to the time of sampling. The sub-region under the NBC-NECC domain is a constant weak annual CO_2 source to the atmosphere, with minor interannual variability. This sub-region is limited by the ARP at approximately 50°W and by the NEC south of 10°N. The NEC sub-region acts as an annual CO_2 sink with greater temporal variability in CO_2 flux than the NBC-NECC sub-region. The Amazon River waters exert a great influence on the spatial variability of sea-air CO_2 exchanges in these two sub-regions. The ARP is the sub-region with the greatest interannual variability in CO_2 fluxes, but it acts as a persistent net oceanic sink for atmospheric CO_2. The CO_2 uptake is twice as high in the ARP core (i.e., SSS < 34), where the influence of the fresh and nutrient-enriched waters from the Amazon River is even greater than in its surroundings.

Several processes act simultaneously to control the CO_2 system in the whole region. However, freshwater discharge seems to exert a strong influence on sea surface pCO_2 in the ARP domain, mainly through dilution and biological activity that is enhanced by riverine nutrient inputs. On the other hand, in the NBC-NECC and NEC domains sea-air CO_2 exchange is likely to be the dominant process. Despite the contrasting behavior among the sub-regions, the entire region acted as a net annual CO_2 sink of −1.6 ± 1.0 mmol m^{-2} day^{-1} from 1993 to 2019. We also found a significant increasing trend in sea surface pCO_2 in NBC-NECC and NEC between 1993 and 2019, which is more pronounced than the increase in atmospheric pCO_2, revealing the sensitivity of carbon dynamics in these sub-regions to ongoing and expected changes in the global climate system.

5. 4. 2 *Regional variability and main drivers of FCO_2*

5. 4. 2. 1 FCO_2 in the NBC-NECC

The sub-region under strong NBC-NECC dominance extends to approximately 50°W, where it is bounded by the waters from the Amazon River and is limited to south of 10°N by an isoline of equilibrium sea-air CO_2 exchanges. This sub-region is homogeneously a CO_2 source to the atmosphere throughout the year, which becomes more intense near the Brazilian coast, where the NBC flow is intensified [e.g., Johns *et al*. 1998; Salisbury *et al*. 2011]. Such CO_2 outgassing behavior is associated with warmer tropical waters (Fig. V-S6) [Azar *et al*. 2021; Johns *et al*. 2021] coupled with equatorial upwelling [Landschützer *et al*. 2014; Takahashi *et al*. 2009]. Moreover, the influence of CO_2-enriched waters from the Indian Ocean [Orselli *et al*. 2019a,b], which are advected by mesoscale

structures along the South Atlantic Ocean [Azar *et al*. 2021; Souza *et al*. 2018], may strengthen the seawater CO_2 supersaturation in this sub-region.

During the wet season, there is a greater influence of the waters from the Amazon River over the WTA [Lefèvre *et al*. 2020; Louchard *et al*. 2021; Mu *et al*. 2021]. This is coupled with increased precipitation due to the northward displacement of the ITCZ [Ibánhez *et al*. 2015; Ibánhez *et al*. 2016; Utida *et al*. 2019], hence leading to a net pCO_2 drawdown in the NBC-NECC sub-region, although it remains supersaturated with respect to atmospheric pCO_2.

The decrease in DIC and SSS (Fig. V-3b) suggests that the pCO_2 drawdown is mainly driven by the physical solubility pump, which has already been suggested as the main driver of pCO_2 changes in this sub-region [Araujo *et al*. 2018]. This is more evident when TA and DIC are normalized to SSS, revealing that pCO_2 drawdown is almost counteracted by the increase in SST, which decreases the CO_2 solubility. This occurs mainly in the NBC-NECC core, where surface waters are typically warmer (Fig. V-S6) [Johns *et al*. 1998; Salisbury *et al*. 2011] and the CO_2 release is doubled near the Brazilian coast (Fig. V-2). In addition, NBC-NECC is a favorable sub-region for calcium carbonate precipitation (Fig. V-4), allowing the development of the extensive reef system at the Amazon River mouth [Francini-Filho *et al*. 2018; Moura *et al*. 2016; Neumann-Leitão *et al*. 2018].

Table V-3: Contrasting magnitudes of net sea-air CO_2 fluxes (FCO_2) recorded in the whole western Tropical Atlantic Ocean as well as in the different sub-regions such as North Brazil Current-North Equatorial Countercurrent (NBC-NECC), North Equatorial Current (NEC) – split by the climatology equilibrium isoline of annual averaged FCO_2 in the region, and Amazon River plume (ARP) – SSS < 35. Positive FCO_2 values indicate the outgassing of CO_2 to the atmosphere, whereas negative FCO_2 values indicate CO_2 uptake by the ocean. In the third column are shown the parameterizations used in the FCO_2 calculations (i.e., Wanninkhof 1992 (W92); Wanninkhof & McGillis 1999 (WM99); Sweeney *et al*. 2007 (S07); Wanninkhof 2014 (W14)) as well as the measure of wind speed used.

References	Temporal coverage	K_t Wind speed	Region domain Latitude; Longitude	**Region** Period	FCO_2 (mmol m^{-2} day^{-1})
This Study	Annual	W14 ERA5 reanalysis	5°S–15°N; 60°W–30°W	**Whole region** 1993-2019	–1.1 ± 1.6
				ARP 1993-2019	–5.0 ± 3.0
				NBC-NECC 1993-2019	1.5 ± 0.7
				NEC 1993-2019	–2.2 ± 1.0
Körtzinger, [2003]	Monthly	W92 Climatology	3°S–18°N; 30°W–60°W	**Whole region** October/November 2002	–1.4 ± 0.5
Cooley *et al*. [2007]	Monthly	WM99 Climatology	6°N–13°N; 48°W–58°W	**Whole region** 1995-1996, 2001-2003	1.4 ± 0.6
Lefèvre *et al*. [2010]	Annual	S07 Scatterometer	5°S–10°N; 65°W–35°W	**Whole region** 2006-2008	–1.0 ± 1.2
Ibánhez *et al*. [2015]	Annual	S07 ERA-interim reanalysis	5°N–14°N; 41°W–52°W	**Whole region** 2006-2013	–0.6 ± 6.1

Continua na próxima página

Valerio *et al*. [2021]	Annual	W14 ECMWF product	5°S–15°N; 45°W–60°W	**Whole region** 2011-2014	4.6 ± 2.5
Carvalho *et al*. [2017]	Monthly	W14 *In situ*/ECMWF product	3°S–5°S; 35.5°W–38.5°W	**NBC-NECC** October 2012	3.3 ± 1.1
			1°S–4°S; 37°W–43°W	**NBC-NECC** September 2014	5.9 ± 3.1
Araujo *et al*. [2017]	Monthly	S07 Scatterometer	0°–8°N; 37°W–51°W	**NBC-NECC** October 2012	1.6 ± 3.4
Araujo *et al*. [2018]*	Monthly	W14 *In situ*	15ºS–5ºN; 30°W–51ºW	**NBC-NECC** 1995-2001	0.3 ±1.7
Lefèvre *et al*. [2020]	Monthly	S07 ERA5	8°N; 38°W	**NBC-NECC** June-September 2013	0.6 ± 0.5
Mu *et al*. [2021]	Monthly	S07 *In situ/* ERA-interim reanalysis	0°–13°N; 45°W–60°W	**Whole region** September 2011	–0.4 ± 0.8
				ARP June 2010	–2.4 ± 1.3
				ARP/NBC-NECC July 2012	0.3 ± 0.6
Louchard *et al*. [2021]	Annual	Uninformed ERA-Interim reanalysis	0.5°–24°N; 30°W–70°W	**Whole region** 1998-2018	0.5
				ARP** 1998-2018	–0.9

*In this study sea surface pCO_2 was estimated from SST and SSS.
**For Louchard *et al*. [2021] the area of the ARP (~1.1 x 10^6 km^{-2}) was estimated at 12% of the total area of the western Tropical Atlantic (9.6 x 10^6 km^{-2}) for the FCO_2 calculation.

5. 4. 2. 2 FCO_2 in the NE

The NEC sub-region is a moderate CO_2 sink, but with greater internal variability than NBC-NECC. This is evidenced by higher spatial heterogeneity in the sea-air CO_2 flux in the NEC sub-region, which is intensified to the northwest where the influence of waters from the Amazon River is greater. In fact, the waters from the Amazon River are expected to have influence on the position of the sea-air CO_2 equilibrium isoline that demarcates the NEC and NBC-NECC sub-regions, due to the NBC retroflection transporting riverine waters in the wet season [Garzoli *et al*. 2004; Goes *et al*. 2005; Lefèvre *et al*. 2020]. However, the increase in sea surface pCO_2 driven by the increase in DIC during the wet season (Fig. V-3) indicates that the influence of NBC-NECC waters supersaturated in CO_2 overlaps with the influence of Amazon River waters in this period.

Furthermore, this increase in pCO_2 may be associated with the influence of CO_2-rich waters from the Canary upwelling system [Landschützer *et al*. 2020], which influences the NEC before reaching the WTA [Ibánhez *et al*. 2017]. This leads to a net increase in pCO_2 over the whole NEC (Fig. V-3) during maximum NBC retroflection, despite the nutrient- and carbon-enriched waters from the Amazon River [Lefèvre *et al*. 2020]. During the dry season, instead of being transported to the east, the waters from the Amazon River are mainly advected to the northwest, decreasing pCO_2 in the NEC sub-region due to high primary productivity [Bonou *et al*. 2016; Ibánhez *et al*. 2015; Mu *et al*. 2021; Louchard *et al*. 2021], hence intensifying the biological uptake of CO_2 (Fig 2a). Indeed, model estimates suggested that without the influence of the Amazon River, much of the WTA, including part of the NEC sub-region, would be a CO_2 source year-round [Louchard *et al*. 2021].

Nevertheless, CO_2 uptake is reduced east of the NEC sub-region, where sea-air CO_2 exchange is close to ocean-atmosphere equilibrium (Fig. V-2c). It is a note of mention that previous studies have recorded a CO_2 release during the wet season in the NEC sub-region [Lefèvre *et al*. 2014; Ibánhez *et al*. 2015; Ibánhez *et al*. 2017]. These records were associated with the influence of extreme events driven by ENSO (i.e., 2009 and 2010), leading to anomalous SST and consequent increase in sea surface pCO_2. We also observed these signs of CO_2 release in 2009, 2010 and 2014 (Fig. V-S3), but further investigations are needed to assess to what extent this behaviour should be considered anomalous as well as its periodicity, which might also be associated with the influence of the Canary upwelling system [Landschützer *et al*. 2020].

Although the ITCZ lies to the north during most of the wet season [Utida *et al*. 2019], precipitation does not seem to exert a strong influence on pCO_2 seasonality in the NEC. Otherwise, the increase in pCO_2 would be partially attenuated, due to the dilution process [Ho & Schanze 2020], and SSS would decrease rather than increase during the wet season (Fig. V-3b). This suggests that the hydrographic and biogeochemical properties in the NEC vary with ocean circulation [e.g., Bruto *et al*. 2017] rather than precipitation. Thus, the seasonal changes in pCO_2, and hence in sea-air CO_2 exchanges, in NEC are likely driven by CO_2 release and uptake processes controlled by the variability of ocean dynamics and to some extent by the Canary upwelling system.

5. 4. 2. 3 FCO_2 in the ARP

The ARP is the most complex sub-region for understanding the changes in the marine carbonate system, since several processes act together, with often

contrasting influences on sea surface pCO_2. The strength of each of these processes is likely coupled with the balance between freshwater discharge and seawater influence since there was a great difference in sea surface pCO_2 drivers after normalization to SSS. For instance, sea surface pCO_2 drawdown in the wet season (Fig. V-3) is driven by the dilution of riverine waters through mixing with seawater [Bonou *et al*. 2016; Varona *et al*. 2018; Mu *et al*. 2021; Louchard *et al*. 2021]. In addition, the calcium carbonate calcification and dissolution processes are also intensified as SSS increases (Fig. V-4c), although their net effect on sea surface pCO_2 is not clear.

Moreover, the pronounced sea surface pCO_2 drawdown in the wet season is also due to the uptake of CO_2 during phytoplankton growth, mainly diatoms and diatom-diazotroph-assemblages [Louchard *et al*. 2021], driven by nutrient enrichment from Amazon River waters [Smith & Demaster 1996; Dagg *et al*. 2004; da Cunha & Buitenhuis 2013; Louchard *et al*. 2021]. Although the relative influence of each of these processes (i.e., dilution and photosynthesis) on pCO_2 remains unclear, most studies conducted in the ARP sub-region indicate that biological activity is the main driver for the sea surface pCO_2 drawdown [Kortzinger 2003; Bonou *et al*. 2016; Lefèvre *et al*. 2017; Mu *et al*. 2021; Louchard *et al*. 2021].

However, we identified a decrease in TA in the wet season (Fig. V-3a), rather than a small increase expected as a result of photosynthesis, revealing the influence of TA dilution through mixing of marine and riverine waters [Bonou *et al*. 2016; Araujo *et al*. 2018; Louchard *et al*. 2021]. Furthermore, the increase only in normalized DIC (Fig. V-3b) reveals the influence of carbon remineralized from particulate and dissolved organic matter, transported by the waters of the

Amazon River during the wet season [Ward *et al*. 2013; Mu *et al*. 2021; Louchard *et al*. 2021]. Thus, both the increase in DIC from remineralisation and the decrease in TA from dilution lead to an increase in sea surface pCO_2, but this is not sufficient to counteract the pCO_2 drawdown by primary production.

Therefore, photosynthesis is the main driver of sea surface pCO_2 drawdown in the ARP (Fig. V-S8), as has been suggested in a number of previous studies [Kortzinger 2003; Bonou *et al*. 2016; Lefèvre *et al*. 2017; Mu *et al*. 2021; Louchard *et al*. 2021]. Moreover, both CO_2 solubility and calcium carbonate dissolution by riverine waters likely exert some influence on the marine carbonate system. This may have some effect on the extent of the reef system, as it appears to be limited to the warmer and more saline waters under the NBC-NECC domain [e.g., Moura *et al*. 2016; Francini-Filho *et al*. 2018; Neumann-Leitão *et al*. 2018].

The annual average net CO_2 flux across the whole region drops considerably from –1.6 to –0.2 mmol m^{-2} day^{-1} when we remove the ARP sub-region. Thus, the waters derived from ARP are responsible for 87% of the CO_2 uptake by the WTA, a greater contribution than the 60% showed by biogeochemical models [Louchard *et al*. 2021]. Hence, further observational efforts are needed to broaden our understanding of this biogeochemically complex region, and thus to improve ocean and climate model estimates.

5. 4. 3 Temporal variability and trends in FCO_2

The progressive increase in sea surface pCO_2 is likely associated mainly with the increase in SST in both NEC and NBC-NECC waters and DIC in the NBC-NECC domain (Fig. V-5c,e). For instance, the sea surface pCO_2 growth trend decreased by 35% in NEC and by 31% in NBC-NECC waters when we

removed its thermal effect (Fig. V-6). Indeed, an increase in SST has been reported in the North Atlantic [Bates & Johnson 2020], where NEC waters originate before being advected to the Tropical Atlantic [e.g., Lefèvre *et al*. 2014]. The NBC-NECC sub-region is influenced by both CO_2-rich waters from the equatorial upwelling [e.g., Lefèvre *et al*. 2014] and warmer, more saline upper waters from the South Atlantic Ocean. Those waters comprise a considerable contribution (34%) derived from the Indian Ocean, which are transported through the Agulhas eddies along the South Atlantic Ocean [Souza *et al*. 2018; Azar *et al*. 2021].

In fact, around 20% of those waters that reach the NBC system through the southern South Equatorial Current bifurcation is sourced from the Indian Ocean [Azar *et al*. 2021]. Thus, the mesoscale activity along the South Atlantic Ocean likely acts as an interhemispheric coupling component also influencing the CO_2 behaviour in the NBC-NECC sub-region through the transfer of biogeochemical properties between ocean basins [Orselli *et al*. 2019a,b]. For instance, the Agulhas eddies typically intensify the ocean CO_2 uptake along their pathway in the South Atlantic [Orselli *et al*. 2019a], increasing their initial DIC storage from Indian Ocean waters. Hence, those structures also contain more anthropogenic carbon than the surrounding waters [Orselli *et al*. 2019b]. Since the release of the Agulhas eddies has been intensifying [Biastoch *et al*. 2009; Lübbecke *et al*. 2015], it is likely that part of the increase in DIC and sea surface pCO_2 in the NBC-NECC domain is explained by the increasing influence of these waters being transferred to the NBC current system.

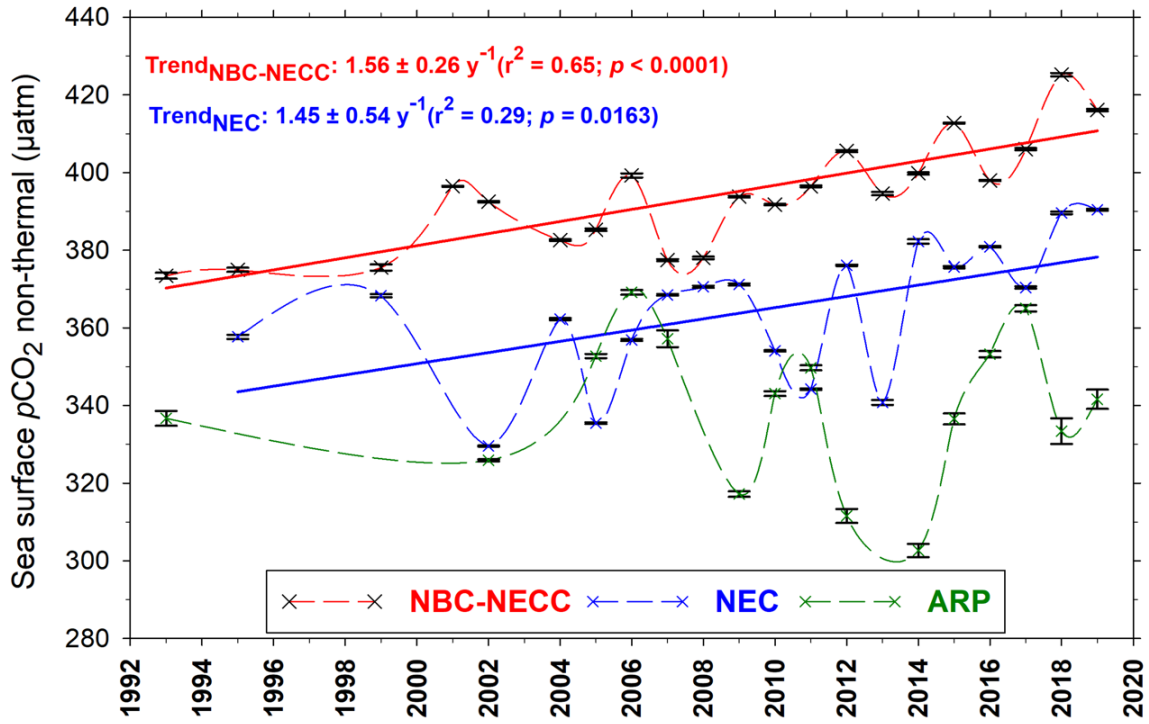

Figure V-6: Time series of annual averages of sea surface CO_2 partial pressure normalised to annual average surface temperature in North Brazil Current-North Equatorial Countercurrent – NBC-NECC (red), North Equatorial Current – NEC (blue), and Amazon River plume – ARP (green) sub-regions. For significant trends (solid lines, with colour depicting sub-region), the trend ± standard deviation as well as their regression statistics are shown. The y-axis error bars (black) are the standard errors of the respective annual averages.

A sea surface pCO_2 increase of 1.20 ± 0.02 µatm year^{-1} in the NBC-NECC sub-region was reported for 1983-2010 but was lower than the increase in atmospheric pCO_2 of 1.70 µatm year^{-1} over the same period [Araujo *et al*. 2018]. This trend in sea surface pCO_2 has increased rapidly to the current estimate of 2.27 ± 0.21 µatm year^{-1} from 1993 to 2019 (Fig. V-5a), indicating that it is likely to continue to accelerate in the coming years. This is also observed in the NEC sub-region (Fig. V-5a), as it is influenced by the circulation and ocean dynamics of the NBC-NECC system [Garzoli *et al*. 2004; Goes *et al*. 2005; Varona *et al*. 2018; Lefèvre *et al*. 2020].

In fact, Park & Wanninkhof [2012] identified a sea surface pCO_2 growth rate (0.17 ± 1.23 µatm year^{-1}) north of 18°N that was lower than atmospheric pCO_2 growth (2.05 ± 0.09 µatm year^{-1}) until 2009, mainly during the boreal winter

(dry season). However, they identified a higher sea surface pCO_2 growth (1.57 ± 0.86 µatm $year^{-1}$) in boreal summer (wet season), which is in agreement with our findings of higher sea surface pCO_2 growth during the wet season (Fig. V-S5). Furthermore, the sea surface pCO_2 growth in NEC has intensified from 2009, as well as in the NBC-NECC sub-region. In both sub-regions, the rate of increase in sea surface pCO_2 is greater than that of atmospheric pCO_2 (1.93 ± 0.02 µatm $year^{-1}$; $p < 0.0001$). Therefore, CO_2 outgassing is intensifying in the NBC-NECC while the NEC sub-region can be expected to show a trend towards CO_2 equilibrium with the atmosphere.

Assuming a growth in atmospheric pCO_2 at current levels (1.93 µatm $year^{-1}$), these trends suggest that it will take around 50 years for sea surface pCO_2 in the NEC to reach equilibrium with atmospheric pCO_2 and from there begin predominantly releasing CO_2. At the same time, the disequilibrium between sea-air CO_2 in NBC-NECC is expected to double, intensifying the CO_2 outgassing. Indeed, although this sub-region is relatively resilient to decreased seawater buffering capacity [Jiang *et al*. 2019], we observed a small yet significant increasing trend in Revelle Factor (Fig. V-S7), indicating a likely reduction in buffering capacity in both NEC and NBC-NECC waters. However, since this trend in sea surface pCO_2 in NBC-NECC increased rapidly by 33% from 2010 to 2019, it is likely that this equilibrium point in NEC and intensification in NBC-NECC will be reached even before the 50 years projected based on a linear increase in atmospheric pCO_2.

The timing of these changes will depend on global CO_2 emissions and the future evolution of atmospheric pCO_2 in the coming years, as reflected in the Shared Socioeconomic Pathways (SSP) [Meinshausen *et al*. 2020] used in the

latest IPCC report [IPCC 2021]. For instance, if global CO_2 emissions are cut to net zero by around 2050, in the most optimistic scenario (SSP1-1.9), the NEC sub-region would switch to releasing instead of taking up CO_2 and NBC-NECC would double its CO_2 outgassing in approximately 20 years, assuming the current sea surface pCO_2 trend.

However, it remains difficult to predict an accurate response of the marine carbonate system to different scenarios, because sea-air CO_2 exchanges are an important driver for sea surface pCO_2 in these sub-regions [e.g., Araujo *et al*. 2018]. In any case, the increase in sea surface pCO_2 can further lead to changes in seawater pH and hence affect the extensive reef system at the Amazon River mouth along the continental shelf [Moura *et al*. 2016], which is highly sensitive to changes in biogeochemical conditions [Francini-Filho *et al*. 2018; Neumann-Leitão *et al*. 2018].

The ARP sub-region exhibits high interannual variability but no trend in sea surface pCO_2. However, there is a trend (at the 94% confidence level) towards an increase in CO_2 uptake in this sub-region (Fig. V-5f) because of the increase in atmospheric pCO_2 (Fig. V-5a) and therefore the sea-air CO_2 disequilibrium. The ARP waters have been experiencing an increasing trend in the concentration of chlorophyll-a from 1997 to 2020 (Fig. V-S8), which is likely associated with the amplification of the hydrological cycle in this sub-region [Liang *et al*. 2020], characterized by an increase in precipitation and discharge from the Amazon River. The waters exported from the Amazon River are the main source of nutrients that enrich the ARP sub-region for phytoplankton growth [Bonou *et al*. 2016; Ibánhez *et al*. 2015; Mu *et al*. 2021; Louchard *et al*. 2021]. Hence, the increasing trend in ARP sea surface pCO_2 expected due to both the increase in

atmospheric pCO_2 and sea surface pCO_2 in the surroundings is completely counteracted by the increase in biological CO_2 uptake.

The strong interannual variability of the carbonate system in the ARP sub-region is matched by the variability in SSS (Fig. V-5). However, it remains unclear which is the main driver of this strong interannual variability, since several processes act together and decomposing them is still a challenge [Bonou *et al*. 2016; Ibánhez *et al*. 2015; Mu *et al*. 2021; Louchard *et al*. 2021; Valerio *et al*. 2020]. For example, although precipitation driven by the ITCZ position intensifies in the wet season south of 10°N, it has not been associated with interannual pCO_2 variability in this sub-region [Lefèvre *et al*. 2020]. Nevertheless, the years with the highest SSS and pCO_2 (2005, 2010 and 2011) were those with the most significant droughts due to the coupled influence of the El Niño phase of ENSO with warming of the tropical North Atlantic [Marengo & Espinoza 2016; Tyaquiçã *et al*. 2017].

Conversely, the lowest SSS and pCO_2 were found in years (2009 and 2012-2014) marked by heavy flooding associated with the La Niña phase and warming of the tropical South Atlantic [Marengo & Espinoza 2016; Tyaquiçã *et al*. 2017]. Such climatic events add complexity to the dynamics of the carbon cycle in the WTA [Kucharski *et al*. 2016] and require further investigation using observations, models [Louchard *et al*. 2021], reanalysis products and satellite imagery [e.g., Valerio *et al*. 2021; Liutti *et al*. 2021] to constrain their relative importance to regional biogeochemistry.

5. 5 Caveats and limitations

Although the contrasting behavior of sea-air CO_2 exchanges in the sub-regions of the WTA is evident, the marine carbonate system sampling is limited before the 2000s. As such, the increasing trends in sea surface pCO_2 may be even greater than those we found here. However, this limits us to associating the interannual variability of sea surface pCO_2 in the ARP sub-region with its likely drivers, such as precipitation, river discharge and chlorophyll-a concentrations (Fig. V-S1).

Despite our findings suggesting that the behaviour of the NBC-NECC, NEC and ARP sub-regions is consistent in the dry and wet seasons in terms of average FCO_2, our time series is limited to just one season in some years, mainly until 2009 (Fig. V-S2). Nevertheless, the CO_2 source or CO_2 sink behavior in each sub-region is evident in the years in which there is sampling in both dry and wet seasons (Fig. V-S3).

The ARP is the sub-region with the lowest spatial and temporal data coverage. Although temporal coverage has increased since 2006, when both dry and wet season data are available more frequently, the temporal variability of the average annual pCO_2 in the ARP may be biased by the greater amount of data in the wet season (Fig. V-S5). This demonstrates that the ARP is a priority sub-region to focus efforts on future studies to solve the issue of seasonal biases in data coverage.

Another complication is that organic substances influence alkalinity measurements, mainly in estuarine waters [e.g., Kerr *et al*. 2021]. Moreover, although the organic fraction of alkalinity over a vast area of the WTA is estimated to be less than 5 µmol kg^{-1} [Kerr *et al*. 2021], this fraction may be higher in ARP

waters, because of riverine transport. Since the TA that we estimated from SSS, SST and location [Carter *et al*. 2018] does not consider the organic fraction of alkalinity, the TA may be underestimated, and this could influence the TA:DIC ratios to some extent. This may be an explanation for the lack of a clearly observed increase in TA as a result of photosynthesis (Fig. V-4c). In fact, the organic fraction in TA has been a global challenge in studies of the carbonate system in coastal regions [Kerr *et al*. 2021] and a limitation shared among several studies conducted to date in the WTA [e.g., Kortzinger 2003; Lefèvre *et al*. 2010; Araujo *et al*. 2014; Lefèvre *et al*. 2014; Bonou *et al*. 2016; Araujo *et al*. 2017; Lefèvre *et al*. 2017; Araujo *et al*. 2018].

Furthermore, other biogeochemical aspects need to be investigated in future studies to elucidate the consequences of the increase in sea surface pCO_2 in the NEC and NBC-NECC sub-regions, and what has been driving the resilience of the ARP to this increase. Since little is known about the temporal and spatial variability of the carbonate system properties in the whole region, separating the main processes driving the sea surface pCO_2 changes remains a challenge, as several processes act simultaneously.

5. 6 Conclusions and closing remarks

The contrasting estimates in sea-air CO_2 exchanges in the WTA occur because this region is composed of three distinct sub-regions in terms of these exchanges. The sub-region under the NBC domain is a net annual CO_2 source to the atmosphere, while the sub-region under the NEC influence is a net annual CO_2 sink. The ARP waters are a strong net CO_2 sink, being responsible for 87% of the CO_2 uptake in the WTA. Since several studies have only used snapshots

of sea-air CO_2 exchanges in this region, the comprehensive approach of this study expands our knowledge about their spatial and temporal dynamics.

Our findings shed light on the risk of extrapolation in estimating sea-air CO_2 exchanges from geographic or temporal snapshots. Hence, in addition to pointing out questions that still need to be answered on the marine carbonate system, our study may be useful for informing the sampling design of future studies in this region. Increased availability of observational data should significantly improve the performance of complex coupled models (e.g., ocean-biogeochemical and climate models) to provide more robust information about the natural behaviour and changes underway and anticipated in the WTA. Finally, the significant increase in sea surface pCO_2 in both the NBC and NEC reveals the sensitivity of carbon dynamics in these sub-regions to global climate change.

Acknowledgements

***** Todos os agradecimentos e financiadores serão listadas ao final deste documento.

References

***** As referências serão listadas ao final deste documento, contendo todas as referências utilizadas nesta dissertação.

APÊNDICE III

Este apêndice contém as seguintes figuras mencionadas no capítulo V: Fig. V-S1; Fig. V-S2; Fig. V-S3; Fig. V-S4; Fig. V-S5; Fig. V-S6; Fig. V-S7.

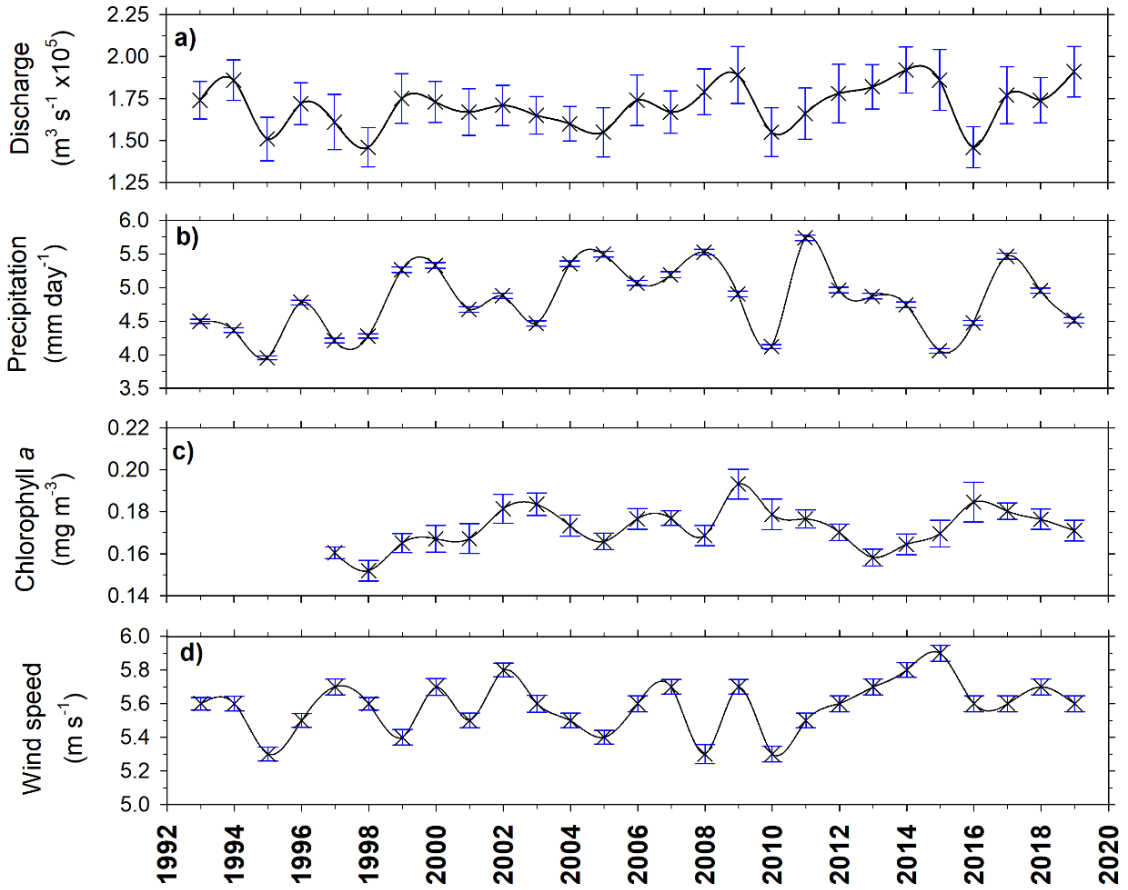

Figure V-S1. Time series of annual averages (crosses) of the (a) Amazon River water discharge at the Óbidos station, (b) precipitation, (c) chlorophyll-a concentration and (d) wind speed in the western Tropical Atlantic Ocean. The blue bars oriented up and down are the standard errors of the respective annual averages. Data from the Óbidos station were obtained from the Brazilian National Water Agency (http://www.snirh.gov.br/hidrotelemetria/Mapa.aspx), while precipitation and wind speed data were extracted from the ERA 5 reanalysis [Hersbach *et al*. 2020].

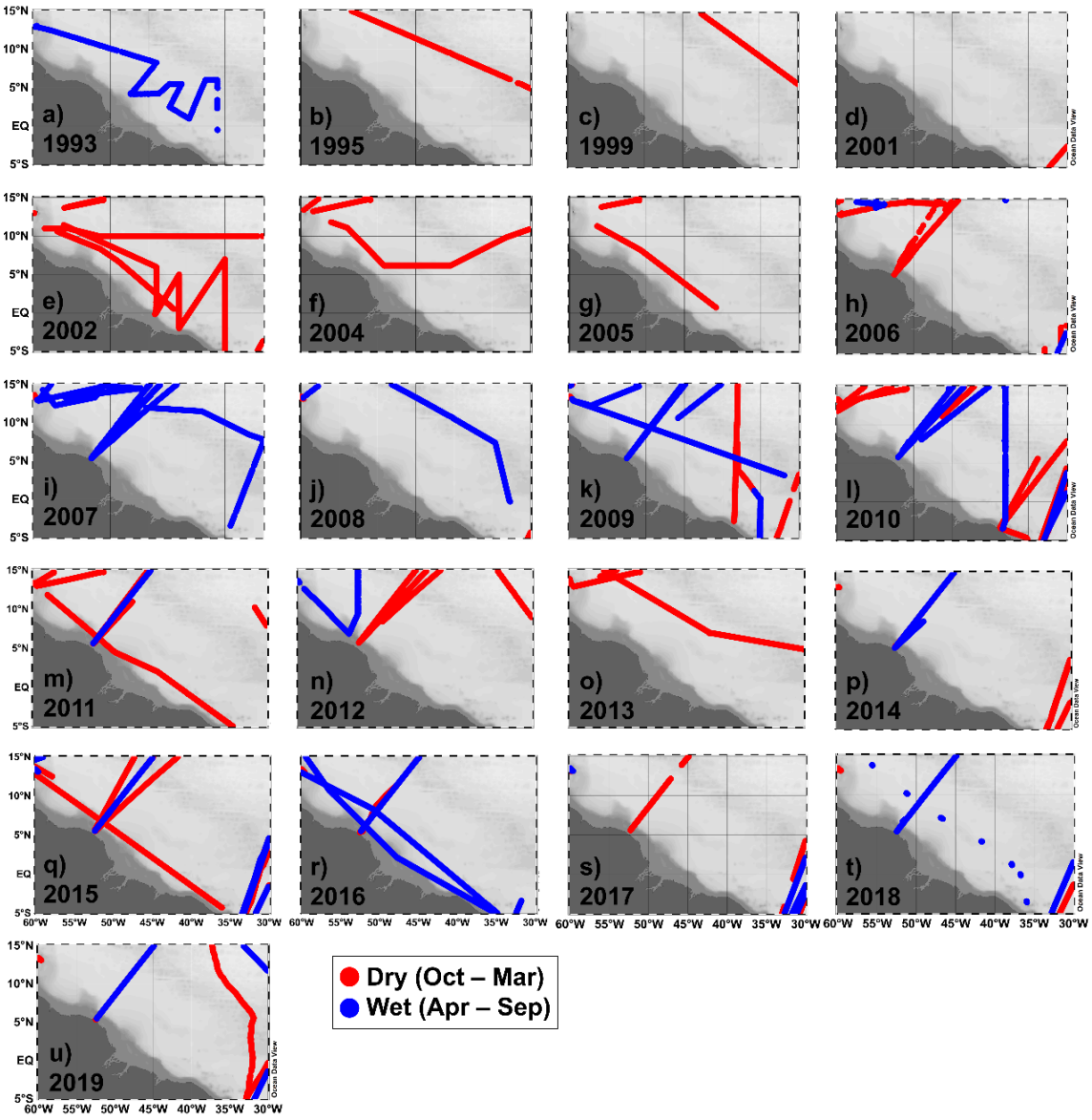

Figure V-S2. Density and distribution of data from SOCAT version 2020 per year over the western Tropical Atlantic Ocean from 1993 to 2019 (a-u). The colours indicate the seasons: dry (October – March; red) and wet (April – September; blue). The data density (n = 142,942 for the entire period) for the seasons was as follows: 59.39% during dry period and 40.60% during wet period.

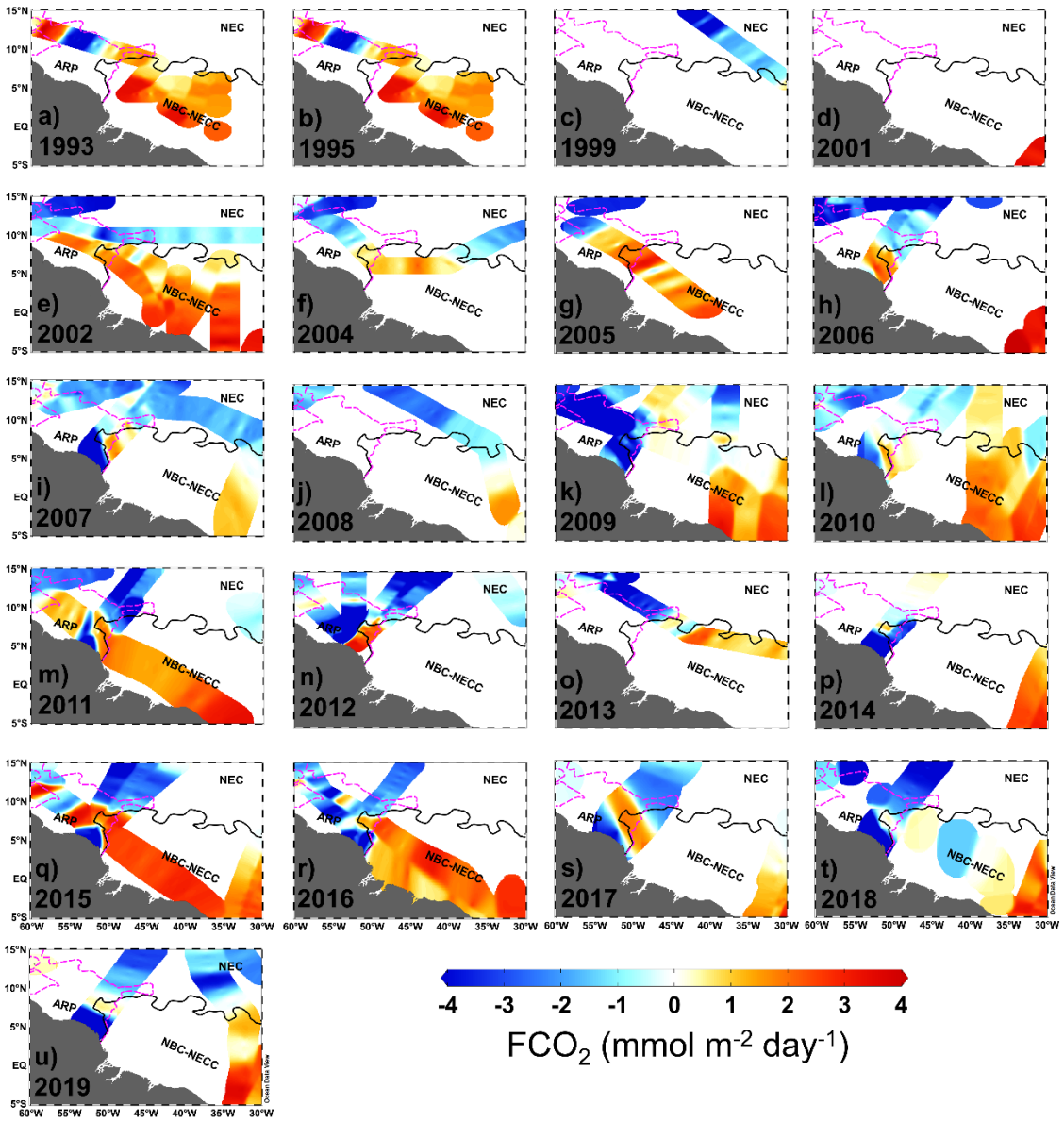

Figure V-S3. Annual average CO_2 flux (FCO_2) per year over the western Tropical Atlantic Ocean from 1993 to 2019 (a-u). The solid black line represents the climatology equilibrium isoline of annual average FCO_2 (i.e., FCO_2=0) that divides the North Brazil Current-North Equatorial Countercurrent (NBC-NECC) and North Equatorial Current (NEC) regions. The pink dashed line represents the annual climatological isoline of SSS = 35, which delimits the ARP region.

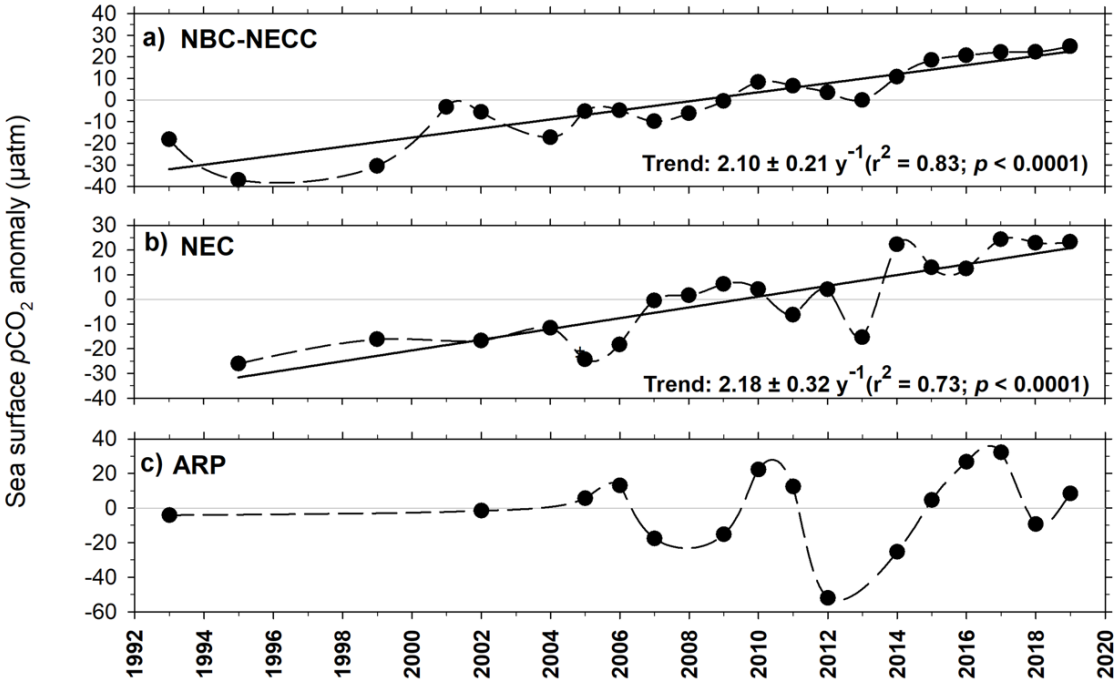

Figu**re V**-S4. Annual average (dots) and trends (full line) of sea surface *p*CO2 anomaly in the (a) North Brazil Current-North Equatorial Countercurrent (NBC-NECC), (b) North Equatorial Current (NEC), and (c) Amazon River plume (ARP) regions.

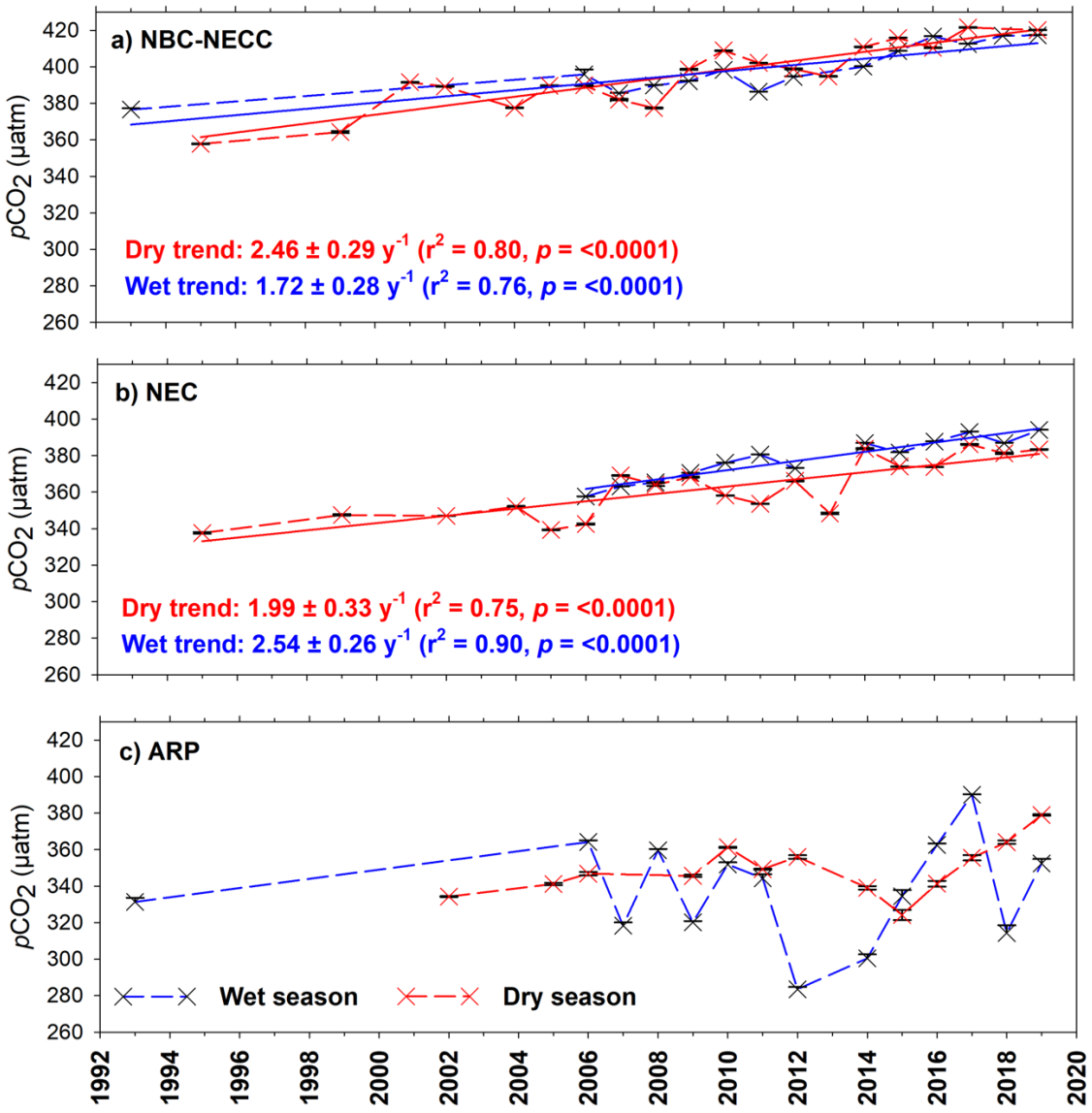

Figure V-S5. Time series of seasonal average and trends (full line) of sea surface pCO2 in the (a) North Brazil Current-North Equatorial Countercurrent (NBC-NECC), (b) North Equatorial Current (NEC), and (c) Amazon River plume (ARP) regions during the wet (blue) and dry (red) seasons. For significant trends (solid lines), the trend ± standard deviation as well as its statistical characteristics are shown. The y-axis error bars (black) are the standard errors of the respective seasonal averages.

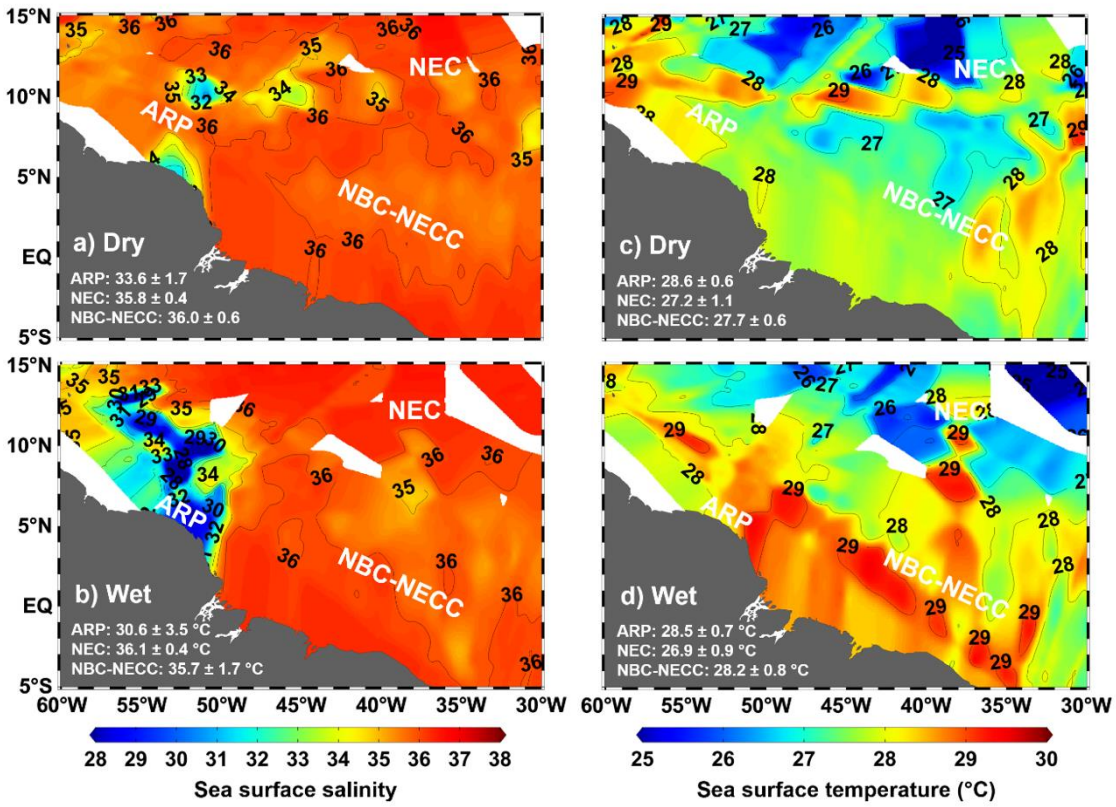

Figure V-S6. Climatological distribution of sea surface (a,b) salinity and (c,d) temperature in the western Tropical Atlantic Ocean from 1993 to 2019 in the dry and wet seasons. The numbers indicate the averages and standard deviations of each variable in each sub-region: North Brazil Current-North Equatorial Countercurrent (NBC-NECC), North Equatorial Current (NEC), and the region under the influence of the Amazon River plume (ARP).

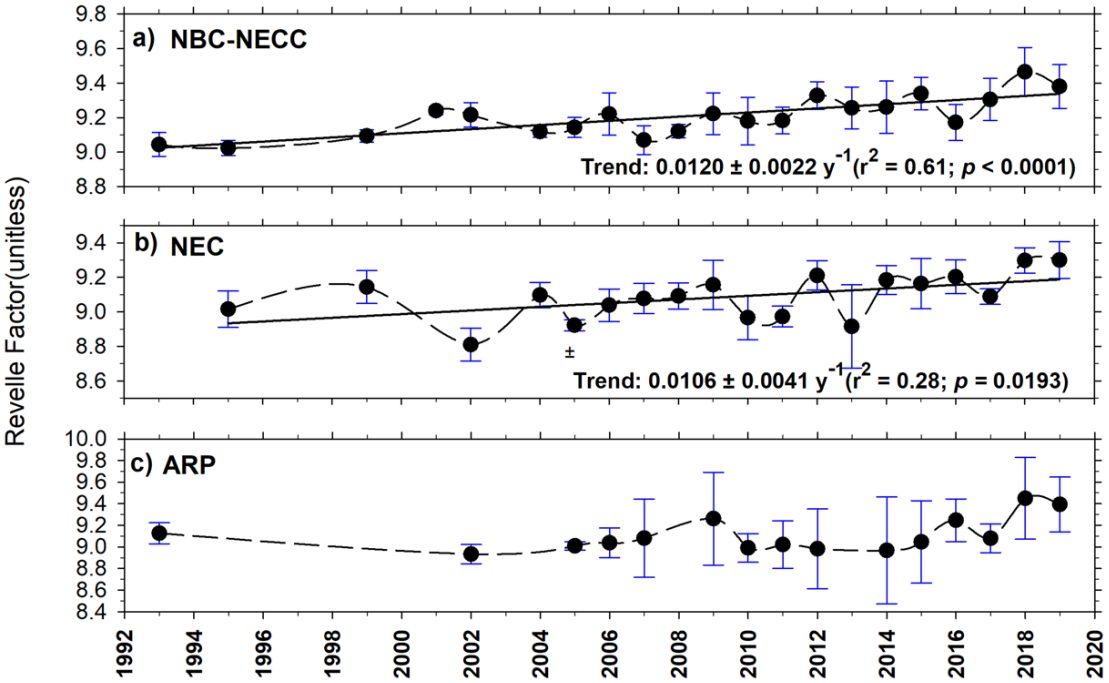

Figure V-S7. Annual average (dots) and trends (full lines) of Revelle Factor in the (a) North Brazil Current-North Equatorial Countercurrent (NBC-NECC), (b) North Equatorial Current (NEC), and (c) Amazon River plume (ARP) regions. There is no significant trend in ARP (c). The blue bars oriented up and down are the standard deviation of the respective annual averages.

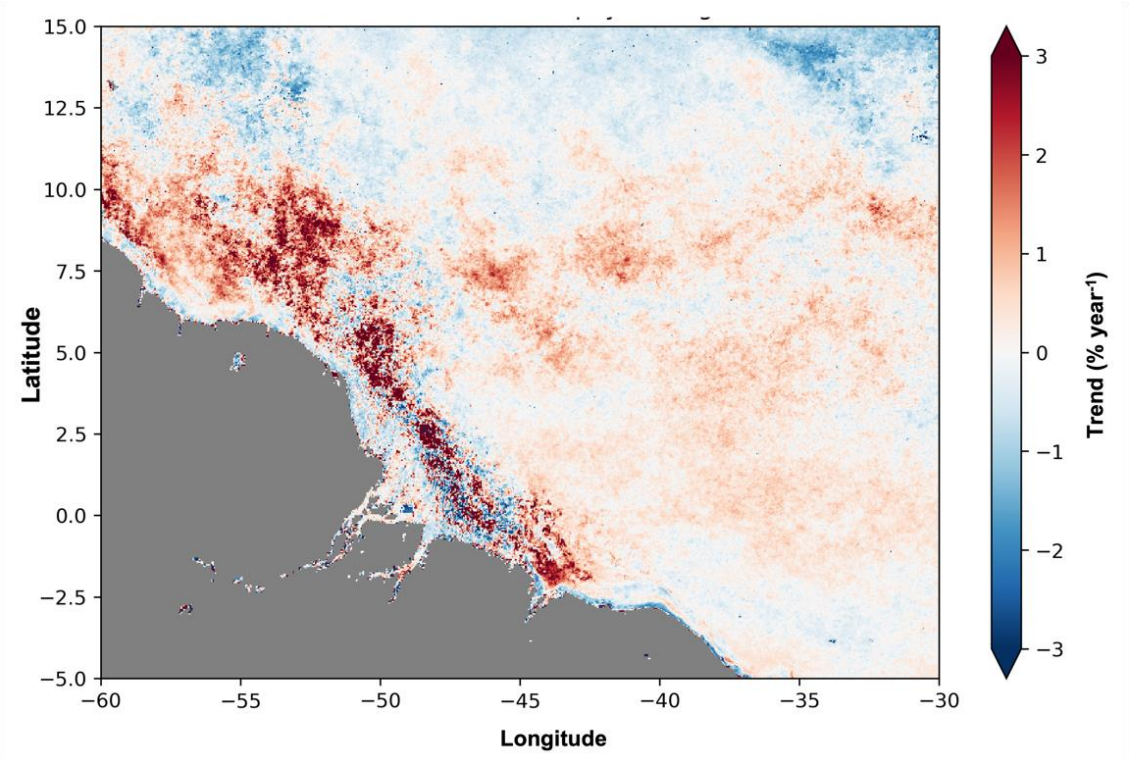

Figure V-S8. Trend in chlorophyll-a concentration from 1997 to 2020 derived from satellite images. Trend are expressed in % per year, with positive trends in red and negative trends in blue.

Capítulo VI: Síntese dos Resultados e Conclusões

Aqui são destacados os principais pontos de discussão e conclusões dos artigos científicos apresentados nos Capítulos III, IV e V. Primeiramente, os artigos serão abordados individualmente e, por fim, a tese será concluída através da verificação da hipótese formulada e das considerações finais.

6. 1 Variabilidade espeço-temporal dos macronutrientes e ambiente chave para a absorção de CO_2 no NAP

Neste estudo, os principais processos que controlam a variabilidade espacial e temporal dos macronutrientes inorgânicos dissolvidos foram investigados ao longo do NAP, desde o estreito de Gerlache, no extremo sul, até a bacia leste do estreito de Bransfield, no extremo norte do NAP. A principal fonte de nutrientes (i.e., DIN, ácido silícico e fosfato) para o NAP é a intrusão de CDW em camadas intermediárias (200 - 500 m), principalmente a partir do estreito de

Gerlache e da bacia oeste do estreito de Bransfield. Alguns processos locais como a remineralização após as florações de fitoplâncton, a presença de estruturas de mesoescala (i.e., vórtices) e o aporte regional a partir de *fjords* também podem adicionar nutrientes para o NAP. Por isso, altas concentrações de nutrientes foram identificadas ao longo do NAP, até mesmo na superfície e sob condições de intensas florações de fitoplâncton durante o verão austral.

No estudo também foi observado que a mistura de CDW com a DSW proveniente do mar de Weddell é responsável pela variabilidade interanual na concentração desses nutrientes, pois a DSW é uma água recentemente ventilada comparada à CDW e, portanto, com menores concentrações de nutrientes. Tal diferença é ainda mais evidente na concentração de ácido silícico, que é abundantemente utilizado durante as florações de diatomáceas. A mistura entre CDW e DSW, por sua vez, é fortemente influenciada pela circulação local, que é modulada pelos modos de variabilidade climática SAM e ENSO. Isso ocorre porque quando o índice SAM é positivo as intrusões de CDW são intensificadas, aumentando a concentração de nutrientes ao longo do NAP. O oposto ocorre quando o índice ENSO é positivo, embora com menor influência sobre a concentração dos nutrientes do que o SAM.

Além disso, a redução dos nutrientes entre o inverno e o verão austral foi estimada ao longo do NAP, revelando-se um claro gradiente espacial, com maiores reduções em todos os nutrientes no estreito de Gerlache e menores reduções na bacia leste do estreito de Bransfield. Na verdade, a redução entre o inverno e o verão em todos os nutrientes no estreito de Gerlache é o dobro da que é observada na bacia leste do estreito de Bransfield. Este é um resultado importante porque demonstra que apesar de toda o NAP ser rica em nutrientes,

o estreito de Gerlache é provavelmente a região onde há melhores condições para o desenvolvimento de florações de fitoplâncton. Tais condições estão associadas ao maior aporte de água de degelo continental e derretimento de gelo marinho, proporcionando uma maior estabilidade na camada superior do oceano, o que favorece as florações de fitoplâncton. Além disso, o estreito de Gerlache é uma das regiões mais abrigadas do NAP, tornando-a relativamente protegida às condições de ventos extremos, que impacta diretamente a estabilidade da coluna de água. Como alguns estudos sugerem que o NAP não deve experimentar limitações por ferro, o estreito de Gerlache pode ser considerado como uma região altamente favorável ao crescimento do fitoplâncton.

As intensas florações de fitoplâncton, principalmente de diatomáceas, já foram associados à intensa absorção de CO_2 atmosférico ao sul do NAP e no estreito de Gerlache durante o verão austral. Além disso, o estreito de Gerlache absorve desproporcionalmente mais CO_2 do que regiões ao redor da Antártica com áreas maiores, como o estreito de Bransfield. Apenas as altas concentrações de nutrientes e a disponibilidade de luz no verão não explicam tal desproporcionalidade na absorção CO_2, pois em geral todas as regiões ao redor da Antártica experimentam essas mesmas condições durante o verão astral. Portanto, nesse estudo, foi demonstrado porque o estreito de Gerlache, e provavelmente outras regiões costeiras abrigadas ao redor da Antártica, são consideradas regiões-chave para a absorção de CO_2. No entanto, as conclusões até o momento eram restritas ao comportamento dessa região durante o verão austral, de modo que uma questão ainda permanecia em aberto: o que ocorre com o FCO_2 no estreito de Gerlache nas outras estações do ano?

6. 2 Variabilidade sazonal e interanual do FCO_2 no estreito de Gerlache

A variabilidade sazonal do FCO_2 nas regiões costeiras da Antártica ainda é muito pouco conhecida, principalmente devido à dificuldade de acesso a essas regiões, especialmente durante o inverno austral. Por isso, nesse estudo foi investigado como o estreito de Gerlache se comporta em relação ao FCO_2 ao longo do ano, já que durante o verão essa região é um importante sumidouro de CO_2 atmosférico, e quais processos controlam esses fluxos. Isso foi possível por meio da análise de uma série temporal do FCO_2 de 2002 a 2017, incluindo as variabilidades sazonais e interanuais. Durante oito meses do ano (i.e., de abril a novembro) o estreito de Gerlache se comporta como uma fonte de CO_2 para a atmosfera, com uma forte liberação de CO_2 durante o inverno (i.e., de julho a setembro). No entanto, em apenas quatro meses (i.e., de dezembro a março), a absorção de CO_2 pelo oceano é tão intensa que ela quase compensa os oito meses em que a região se comporta liberando CO_2 para a atmosfera.

A média anual do FCO_2 entre 2002 e 2017 foi $1{,}24 \pm 4{,}33$ mmol m^{-2} dia^{-1}, relevando que o estreito de Gerlache é uma região bastante sensível às alterações climáticas que influenciam o ciclo do carbono. A desproporcionalidade na intensa absorção de CO_2 durante o verão tem ficado ainda mais evidente nos últimos anos à medida em que a magnitude da absorção de CO_2 no verão tem aumentado desde 2011. Assim, houve uma mudança no FCO_2 médio anual de $4{,}4 \pm 2{,}8$ mmol m^{-2} dia^{-1} até 2009 para -2.0 ± 3.0 mmol m^{-2} dia^{-1} a partir de 2010, revelando que a região era uma fonte anual de CO_2 para a atmosfera e desde 2010 tem se comportado predominantemente como sumidouro anual de CO_2 atmosférico.

Diversos processos podem estar associados a essa mudança e alguns cenários são esperados para o futuro, inclusive contrastantes. Por exemplo, o aumento das intrusões de CDW devido à intensificação dos ventos de oeste e sua migração para sul podem diminuir o desequilíbrio entre a pCO_2^{mar} e pCO_2^{ar}, minimizando a absorção de CO_2 no verão. No entanto, o mais provável é que a absorção de CO_2 seja intensificada devido à extensão do período livre de gelo marinho, começando mais cedo na primavera e se prolongando até depois do verão.

Durante o outono e, principalmente, no inverno austral, parte do fluxo de CO_2 entre o oceano e atmosfera é minimizada devido à cobertura de gelo marinho. As intrusões de CDW e a ressurgência dessas águas são intensificadas nessas estações do ano, aumentando a pCO_2^{mar} e ao mesmo tempo propiciando o derretimento de gelo marinho, devido à maior temperatura da CDW. Além disso, a camada de mistura é mais profunda, proporcionando uma maior mistura vertical, incrementando a pCO_2^{mar} devido à remineralização de matéria orgânica. Essas condições levam a região a se comportar como uma moderada a forte fonte de CO_2 para a atmosfera. No final da primavera (dezembro) e durante o verão austral a disponibilidade de luz associada à maior estabilidade da coluna de água, devido ao derretimento de gelo marinho, favorece o crescimento do fitoplâncton, especialmente diatomáceas, que reduzem drasticamente a pCO_2^{mar}.

Embora diversos processos atuem simultaneamente no controle da pCO_2^{mar} no estreito de Gerlache, a redução significativa de C_T no verão sugere que o consumo de CO_2 pelo crescimento do fitoplâncton se sobrepõe aos demais processos como a solubilidade, a calcificação e o derretimento de gelo marinho.

Isso fica mais evidente quando, na primavera, a razão A_T:C_T sob maiores temperaturas na superfície do mar (>0 ºC), principalmente em dezembro, indica o processo de fotossíntese, enquanto sob menores temperaturas (<0 ºC) essa razão reflete processos de calcificação/dissolução de $CaCO_3$ e formação de gelo marinho.

O intenso aporte de água doce de degelo durante o verão aumenta a estabilidade na camada superior do oceano, favorecendo o crescimento do fitoplâncton. Portanto a fotossíntese deve exercer maior influência direta sobre a absorção de CO_2 do que o aporte de água doce, no estreito de Gerlache. No entanto, o estreito de Gerlache é uma região relativamente pequena e protegida do NAP, cujos aportes de água doce de degelo são consideravelmente menores do que o aporte de água doce que o rio Amazonas descarrega sobre o WTA. Ou seja, será que a fotossíntese também é um processo dominante na absorção de CO_2 nas águas da ARP, com uma extensão e um aporte de água doce significativamente maiores do que no estreito de Gerlache?

6. 3 Variabilidade espacial e temporal do FCO_2 no WTA

Apesar de a ARP ser uma importante feição oceanográfica no oceano Atlântico Tropical, pouco ainda é conhecido sobre o seu impacto na biogeoquímica dessa região. Há uma grande divergência entre a maioria dos estudos que abordam o FCO_2 no WTA. Mesmo na ARP, onde os estudos convergem em relação ao seu comportamento de sumidouro de CO_2 atmosférico, há uma enorme variabilidade na magnitude desses fluxos. Nesse estudo foi possível demostrar porque existe essa divergência entre os estudos,

tanto sobre o comportamento da região em relação ao FCO_2 quanto sobre a variabilidade na magnitude da absorção de CO_2 pela ARP.

No presente estudo foi demonstrado que a divergência no FCO_2 do WTA ocorre porque essa região é caracterizada por três sub-regiões com comportamentos distintos em relação ao FCO_2. A região sob domínio da NBC atua como uma fonte de CO_2 para atmosfera, enquanto as águas sob domínio da NEC atuam predominantemente como um sumidouro de CO_2 ao longo do ano. As águas sob domínio da ARP atuam como um forte sumidouro de CO_2 atmosférico, tanto no período seco quanto no chuvoso, sendo responsáveis por cerca de 87% da absorção de CO_2 pelo WTA. Tais comportamentos distintos levavam os estudos a resultados contrastantes sobre o FCO_2 quando as amostragens se restringiam majoritariamente em determinadas sub-regiões.

Além disso, foi identificada uma tendência de aumento significativo na pCO_2^{mar}, tanto nas águas da NBC quanto nas águas da NEC. Essas tendências de aumento da pCO_2^{mar} já haviam sido identificadas até 2010 em outros estudos, no entanto elas aumentaram em 42% na NEC e em 89% na NBC entre 2010 e 2019, enquanto a tendência de aumento da pCO_2^{ar} aumentou apenas 14% no mesmo período. Como consequência, atualmente, a tendência de aumento da pCO_2^{mar} na NEC e na NBC é maior do que o aumento da pCO_2^{ar}. Isso significa que se essas tendências persistirem nos próximos anos, em torno de 50 anos a NEC pode começar a liberar ao invés de absorver CO_2 e a NBC pode dobrar a quantidade de CO_2 liberada para a atmosfera, impactando o equilíbrio biogeoquímico da região.

Parte do aumento da pCO_2^{mar} na NBC (31%) e, principalmente na NEC (35%), é devido ao aumento da SST. No entanto, não está claro quais processos

são responsáveis pela maior parte desse aumento. Na NBC, o aumento de pCO_2^{mar} deve estar associado ao aumento significativo de C_T, que foi associado à intensificação na liberação dos vórtices das Agulhas do oceano Índico. Essa associação foi pensada porque essas estruturas são importantes sumidouros de CO_2, possuem maior C_T em seu interior do que nas águas ao redor e já foi demostrado que elas podem atingir as águas da NBC antes de serem advectadas para o WTA.

A ARP é a região onde a biogeoquímica é mais complexa porque diversos processos atuam simultaneamente controlando a pCO_2^{mar}. As águas da ARP têm altas concentrações de nutrientes e uma alta estabilidade nos primeiros metros, devido à baixa SSS. Tais condições favorecem o crescimento do fitoplâncton, especialmente as assembleias de diatomáceas diazotróficas, que são muito eficientes na absorção de CO_2. A diminuição da SSS também aumenta a solubilidade do CO_2, o que facilita a difusão desse gás entre o oceano e atmosfera. Até o momento não está claro qual o real impacto desses processos (fotossíntese e solubilidade) na redução da pCO_2^{mar} das águas da ARP, embora a maioria dos estudos apontem que a fotossíntese sejam o principal processo.

Durante o período chuvoso, quando há maior influência das águas do rio Amazonas, há uma intensa diminuição de C_T e A_T associada à maior diminuição de pCO_2^{mar} na ARP. A diminuição de A_T ocorre devido à diluição da água do mar com as águas da ARP, onde há intensa remineralização de matéria orgânica proveniente do rio Amazonas, o que deveria aumentar o C_T. Tanto a diminuição da A_T quanto o aumento do C_T causam um aumento da pCO_2^{mar}. No entanto, foi observada uma redução líquida de C_T e de pCO_2^{mar} na ARP no período chuvoso. Isso releva que, de fato, a fotossíntese parece ser o principal controlador da

redução de pCO_2^{mar} e, consequentemente, da intensa absorção de CO_2 pelas águas da ARP.

Além disso, nenhuma tendência na pCO_2^{mar} foi identificada nas águas da ARP, como foi observada na NBC e na NEC. Em vez disso, foi identificada uma tendência de aumento na absorção de CO_2, como resposta ao aumento da pCO_2^{ar}. Essa maior resiliência das águas da ARP em relação ao aumento de pCO_2^{mar} provavelmente está associada à intensa produtividade primária, pois nessa região há uma tendência de aumento da clorofila *a*, indicando que a intensificação da fotossíntese está neutralizando o aumento de pCO_2^{mar} que seria esperado devido à mistura com as águas da NBC.

6. 4 Considerações finais e direcionamentos futuros

A hipótese testada nesta tese foi que "a alta produtividade primária proporcionada pelas altas concentrações de nutrientes é o principal controlador da absorção de CO_2 no estreito de Gerlache, no NAP, e na ARP." A parte da hipótese associada ao estreito de Gerlache foi aceita porque nessa região se observa as maiores concentrações de nutrientes ao longo do NAP e a maior redução entre o inverno e o verão, nos primeiros 50 m, em todos os macronutrientes analisados. Essa maior redução nos macronutrientes está associada à maior produtividade primária, que é proporcionada pela maior estabilidade na coluna de água, já que o estreito de Gerlache é a região mais abrigada e sob maior influência de degelo continental e de gelo marinho ao longo do NAP. Tais condições altamente favoráveis ao crescimento e às episódicas florações de fitoplâncton tornam o estreito de Gerlache uma região bastante importante para a absorção de CO_2 no verão (Fig. VI-1).

Em relação à ARP, a hipótese foi parcialmente aceita porque nessa região a razão A_T:C_T indicou a fotossíntese como o principal controlador desses parâmetros, os quais foram identificados como os principais controladores da pCO_2^{mar}. Contudo, a fotossíntese foi identificada como o principal processo controlando A_T e C_T após sua normalização pela SSS, ou seja, após a remoção do efeito da diluição pelas águas do rio Amazonas. A distribuição de A_T e C_T não normalizados revelou que diversos processos atuam simultaneamente controlando esses parâmetros e a alteração nessa distribuição após a normalização revela que a diluição tem um papel importante sobre A_T e C_T. Portanto, embora os resultados indiquem que a fotossíntese seja o principal processo controlando a absorção de CO_2 (Fig. VI-1), mais estudos são necessários para identificar o papel da diluição e da solubilidade nessa absorção.

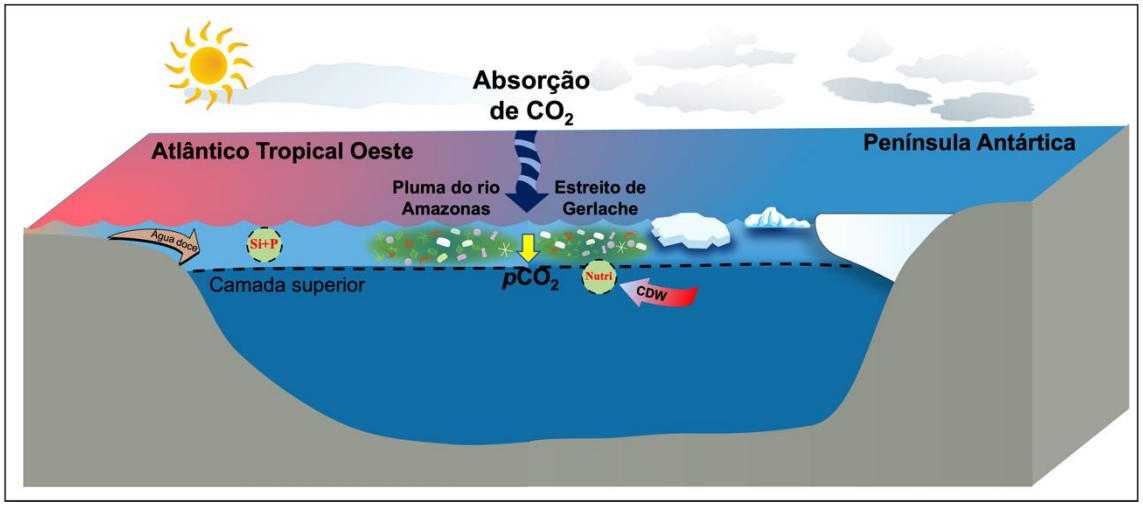

Fig. VI-1: Esquema representativo dos principais processos controlando a pressão parcial do CO_2 (pCO_2) na superfície do mar no estreito de Gerlache, localizado no norte da Península Antártica, e na pluma do rio Amazonas, no oceano Atlântico Tropical oeste. O esquema destaca o intenso processo de fotossíntese, indicador da alta produtividade primária, como o principal controlador da redução da pCO_2, que leva à forte absorção de CO_2 em ambas as regiões. E alta produtividade ocorre devido às altas concentrações de nutrientes (Nutri) e o aporte de água doce é um controlador secundário da absorção de CO_2, através da diluição e da solubilidade. A siglas Si e P significam os nutrientes silicato e fosfato, respectivamente, enquanto CDW significa Água Profunda Circumpolar.

Ambas as regiões estudadas são caracterizadas por altas concentrações de nutrientes, que sustenta uma alta produtividade primária. O crescimento do fitoplâncton, por sua vez, é um dos principais mecanismos que reduzem a pCO_2^{mar}, fazendo as águas superficiais absorverem CO_2 da atmosfera (Fig. VI-1). Porém, outra característica importante dessas regiões é o intenso aporte sazonal de água doce, embora por motivos distintos: no NAP por degelo continental e de gelo marinho e no WTA pela descarga do rio Amazonas. Tais condições reforçam o crescimento do fitoplâncton e influenciam diretamente a solubilidade do CO_2 na água, facilitando a troca de CO_2 entre o oceano e atmosfera.

Embora os estudos apresentados nesta tese tenham fortes indícios de que a produtividade primária seja o principal processo que controla a absorção de CO_2 em ambas as regiões estudadas, não está muito claro qual a magnitude do papel da diluição e da solubilidade nessas trocas. No NAP há mais estudos que buscaram resolver esse dilema, utilizando dados de diferentes grupos de fitoplâncton e os associando ao FCO_2. Porém, ainda é muito difícil separar o papel da SST e da SSS do papel da fotossíntese sobre a pCO_2^{mar}, já que a SST e a SSS também são variáveis importantes para o crescimento do fitoplâncton.

Descobrir a magnitude da influência dos processos físicos e biogeoquímicos sobre as mudanças na pCO_2^{mar} parece ser ainda mais complexo na região sob influência da ARP. Tal complexidade ocorre porque, além de nutrientes, o rio Amazonas transporta altas concentrações de matéria orgânica em decomposição, que influencia a pCO_2^{mar}, e material e suspensão, que aumenta a turbidez da água e influencia a produtividade primária. Todos esses processos atuam simultaneamente com precipitação/dissolução de $CaCO_3$,

fotossíntese/respiração, absorção/liberação de CO_2, diluição/evaporação, tornando a compreensão da magnitude de cada um deles um desafio para os futuros estudos.

Um dos maiores desafios para se compreender melhor a magnitude de cada um desses processos e para desacoplar um dos outros é a escassez de dados físicos e, principalmente, biogeoquímicos nessas regiões estudadas. Nesse sentido, o GOAL tem tido um papel fundamental no monitoramento das propriedades físicas e biogeoquímicas ao longo do NAP, o que contribuiu significativamente para o desenvolvimento dos estudos apresentados nessa tese. Além disso, a disponibilidade de dados em plataformas com livre acesso, como o SOCAT e o GLODAP, são essenciais para melhorar nossa compreensão dos processos oceanográficos em diversas regiões oceânicas. Sem esses bancos de dados, esses estudos não seriam possíveis e o entendimento sobre o ciclo do carbono e a biogeoquímica marinha seriam ainda mais limitados. Portanto, uma das ações que devem ser encorajadas em projetos e estudos futuros é o monitoramento dessas e de outras importantes regiões, a manutenção das plataformas de dados disponibilizados livremente e a ampla utilização desses dados. Assim, poderemos aprofundar e ampliar nosso entendimento sobre os processos biogeoquímicos sob um ponto de vista interdisciplinar.

AGRADECIMENTOS GERAIS

Capítulo III

This study contributes to the activities of the CARBON Team (www.carbonteam.furg.br), the Brazilian Ocean Acidification Network (BrOA; www.broa.furg.br) and the Brazilian High Latitude Oceanography Group (GOAL; www.goal.furg.br), which is part of the Brazilian Antarctic Program (PROANTAR). GOAL has been funded by and/or has received logistical support from the Brazilian Ministry of the Environment (MMA), the Brazilian Ministry of Science, Technology, and Innovation (MCTI), the Brazilian Navy, the Secretariat of the Interministerial Commission for the Resources of the Sea (SECIRM), and the Council for Research and Scientific Development of Brazil (CNPq) through grants from the Brazilian National Institute of Science and Technology of Cryosphere (INCT-CRIOSFERA; CNPq Grants Nos. 573720/2008-8 and 465680/2014-3; FAPERGS Grant no. 17/2551-0000518-0), NAUTILUS, INTERBIOTA, PROVOCCAR and ECOPELAGOS projects (CNPq Grants Nos. 405869/2013-4, 407889/2013-2, 442628/2018-8 and 442637/2018-7, respectively), and Higher Education Personnel Improvement Coordination (CAPES Grant No. 23038.001421/2014-30). T.M. received financial support from the Brazilian Improving Coordination of Higher Education Personnel (CAPES, PhD Grant No. 88887.360799/2019-00), and from CNPq Grant No. 200649/2020-5 for an abroad PhD period supervised by S.H. R.K. received financial support from CNPq researcher Grant Nos. 304937/2018-5 and 309978/2021-1. We are thankful for the support provided by CAPES to the Graduate Program in Oceanology and the

FURG project CAPES-PrInt. We appreciate the availability of high-quality data from GLODAP (https://www.glodap.info/).

Capítulo IV

This study contributes to the activities of the Brazilian Ocean Acidification Network (BrOA; www.broa.furg.br) and the Brazilian High Latitude Oceanography Group (GOAL; www.goal.furg.br), which is part of the Brazilian Antarctic Program (PROANTAR). GOAL has been funded by and/or has received logistical support from the Brazilian Ministry of the Environment (MMA), the Brazilian Ministry of Science, Technology, and Innovation (MCTI), the Brazilian Navy, the Secretariat of the Interministerial Commission for the Resources of the Sea (SECIRM), and the Council for Research and Scientific Development of Brazil (CNPq) through grants from the Brazilian National Institute of Science and Technology of Cryosphere (INCT-CRIOSFERA; CNPq Grants Nos. 573720/2008-8 and 465680/2014-3; FAPERGS Grant no. 17/2551-0000518-0), NAUTILUS, INTERBIOTA, PROVOCCAR and ECOPELAGOS projects (CNPq Grants Nos. 405869/2013-4, 407889/2013-2, 442628/2018-8 and 442637/2018-7, respectively), and Higher Education Personnel Improvement Coordination (CAPES Grant No. 23038.001421/2014-30). T.M. received financial support from PhD Grant No. 88887.360799/2019-00 from CAPES. R.K. received financial support from researcher Grant No. 304937/2018-5 from CNPq and 888881.195000/2018-01 from CAPES. We are thankful for the resources provided by CAPES to support the Graduate Program in Oceanology. We appreciate the availability of high-quality data from the SOCATv6, PANGAEA and Palmer Station datasets. Special thanks to the scientists (Taro Takahashi, Colm

Sweeney, David Munro, Stu Sutherland, Timothy Newberger, Steven van Heuven, Mario Hoppema, Vassilis Kitidis and Ian Brown) onboard the RV Lawrence M. Gould, Nathaniel B. Palmer, Polarstern and James Clark Ross, who provided the surface ocean pCO2 measurements publicly available via the SOCAT dataset. We thank all researchers and students from LEOC/FURG and other GOAL groups for their contributions to cruise planning, sampling, and analyses. We also thank the Brazilian Navy, especially the crew onboard the RV Almirante Maximiano, for providing logistical and sampling support during the NAUTILUS and INTERBIOTA cruises.

Capítulo V

This study contributes to the activities of the Brazilian Ocean Acidification Network (BrOA; www.broa.furg.br) and the CARBON Team (www.carbonteam.furg.br). T.M. received financial support from the Brazilian Improving Coordination of Higher Education Personnel (CAPES, PhD Grant No. 88887.360799/2019-00), allowed by the PROVOCCAR project and sponsored by the Brazilian National Council for Scientific and Technological Development (CNPq) Grant No. 442628/2018-8; and from CNPq Grant No. 200649/2020-5 for an abroad PhD period supervised by S.H. R.K. received financial support from CNPq researcher Grant Nos. 304937/2018-5 and 309978/2021-1. M.A. thanks the Brazilian Research Network on Global Climate Change - Rede CLIMA (FINEP-CNPq 437167/2016-0) and the Brazilian National Institute of Science and Technology for Tropical Marine Environments - INCT AmbTropic (CNPq/FAPESB 565054/2010-4 and 8936/2011) for their support. We are thankful for the support provided by CAPES to the Graduate Program in

Oceanology and the FURG project CAPES-PrInt. We appreciate the availability of high-quality data from the SOCAT (https://www.socat.info/), GLODAP (https://www.glodap.info/) and Barbados Station datasets https://gml.noaa.gov/dv/data/index.php?category=Greenhouse%2BGases&parameter_name=Carbon%2BDioxide&site=RPB). Special thanks to the scientists Dorothee Bakker, Wanninkhof, R.; Lefèvre, N.; Pierrot, D.; Ritschel, M; González-Dávila, M.; Santana-Casiano, J. M.; Goyet, C.; Gutekunst, S.; Ríos, A. F.; Schuster, U.; Tanhua, T.; Wallace, D. and Diverrès, D., who have made the invaluable surface ocean pCO_2 measurements publicly available via the SOCAT dataset. We thank Andrés Pinãngo for his help in obtaining and analysing satellite chlorophyll data.

Capítulo VII: Referências Bibliográficas

Abril G, Martinez J-M, Artigas LF, Moreira-Turcq P, Benedetti MF, Vidal L et al (2014) Amazon River carbon dioxide outgassing fuelled by wetlands. Nature 505:395–398. https://doi.org/10.1038/nature12797

Ackley SF, Buck KR, Taguchi, S (1979) Standing crop of algae in the sea ice of Weddell Sea region. Deep-Sea Res Pt I 26:269–281. https://doi.org/10.1016/0198-0149(79)90024-4

Alcaraz M, Saiz E, Fernandez JA, Trepat I, Figueiras F, Calbet A, Bautista B (1998) Antarctic zooplankton metabolism: carbon requirements and ammonium excretion of salps and crustacean zooplankton in the vicinity of the Bransfield Strait during January 1994 J Mar Syst 17:347–359. https://doi.org/10.1016/S0924-7963(98)00048-7

Álvarez M, Ríos AF Rosón G (2002) Spatio-temporal variability of air–sea fluxes of carbon dioxide and oxygen in the Bransfield and Gerlache Straits during austral summer 1995–96. Deep-Sea Res Pt II 49:643–662. https://doi.org/10.1016/S0924-7963(98)00048-7

Aminot A, Chaussepied M (1983) Manuel des analyses chimiques en milieu marin. Centre National pour L'Exploitation des Oceans (CNEXO, Brest, 1983).

Anadón R, Estrada M (2002) The FRUELA cruises: a carbon flux study in productive areas in the Antarctic Peninsula (December 1995–January 1996). Deep Sea Res Pt II 49:567–583. https://doi.org/10.1016/S0967-0645(01)00112-6

Annett AL, Fitzsimmons JN, Séguret MJM, Lagerström M, Meredith MP, Schofield O, Sherrell RM (2017) Controls on dissolved and particulate iron

distributions in surface waters of the Western Antarctic Peninsula shelf. Mar Chem 196:81–97. https://doi.org/10.1016/j.marchem.2017.06.004

Araujo M, Noriega C, Hounsou-Gbo GA, Veleda D, Araujo J, Bruto L, et al (2017) A Synoptic Assessment of the Amazon River-Ocean Continuum during Boreal Autumn: From Physics to Plankton Communities and Carbon Flux. Front Microbiol 8:1358. https://doi.org/10.3389/fmicb.2017.01358

Araujo M, Noriega C, Medeiros C, Lefèvre N, Ibánhez JSP, Montes, MF et al (2018) On the variability in the CO_2 system and water productivity in the western tropical Atlantic off North and Northeast Brazil. J Mar Syst 189:62–77. https://doi.org/10.1016/j.jmarsys.2018.09.008

Araujo M, Noriega CED, Lefèvre N (2014) Nutrients and carbon fluxes in the estuaries of major rivers flowing into the tropical Atlantic. Front Mar Sci 1:10. https://doi.org/10.3389/fmars.2014.00010

Ardelan MV (2010) Natural iron enrichment around the Antarctic Peninsula in the Southern Ocean. Biogeosciences 7:11–25. https://doi.org/10.5194/bg-7-11-2010

Aroucha LC, Veleda D, Lopes FS, Tyaquiçã P, Lefèvre N, Araujo M (2020). Intra- and Inter-Annual Variability of North Brazil Current Rings Using Angular Momentum Eddy Detection and Tracking Algorithm: Observations From 1993 to 2016. J Geophys Res Oceans 125: 1:20. https://doi.org/10.1029/2019JC015921

Arrigo KR, Van Dijken GL (2007) Interannual variation in air-sea CO_2 flux in the Ross Sea, Antarctica: a model analysis. J Geophys Res Oceans 112:1–16. https://doi.org/10.1029/2006JC003492

Arrigo KR, van Dijken G, Long M (2008) Coastal Southern Ocean: a strong anthropogenic CO_2 sink. Geophys Res Lett 35:1–6. https://doi.org/10.1029/2008GL035624

Arrigo KR, Robinson DH, Worthen DL, Dunbar RB, DiTullio GR, VanWoert M, Lizotte MP (1999) Phytoplankton community structure and the drawdown of nutrients and CO_2 in the Southern Ocean. Science 283:365–367. DOI: 10.1126/science.283.5400.365

Avelina R, da Cunha LC, Farias CO, Hamacher C, Kerr R, Mata, MM (2020) Contrasting dissolved organic carbon concentrations in the Bransfield Strait, northern Antarctic Peninsula: insights into ENSO and SAM effects. J Marine Syst 212:103457. https://doi.org/10.1016/j.jmarsys.2020.103457

Azar E, Piñango A, Wallner-Kersanach M, Kerr R (2020) Source waters contribution to the tropical Atlantic central layer: new insights on the Indo-Atlantic exchanges. Deep Sea Res Part I Oceanogr Res Pap 168:103450. https://doi.org/10.1016/j.dsr.2020.103450

Bakker DCE, Pfeil B, Landa CS, Metzl N, O'Brien KM, Olsen A, Smith K et al (2016) A multi-decade record of high quality fCO_2 data in version 3 of the Surface Ocean CO_2 Atlas (SOCAT). Earth Syst Sci Data 8: 383–413. https://doi.org/10.5194/essd-8-383-2016

Bakker DCE, Hoppema M, Schröder M, Geibert W, de Baar HJW (2008) A rapid transition from ice covered CO_2–rich waters to a biologically mediated CO_2 sink in the eastern Weddell Gyre. Biogeosciences 5:1373–1386. https://doi.org/10.5194/bg-5-1373-2008

Barbat MM, Mata MM (2022) Iceberg drift and melting rates in the northwestern Weddell Sea, Antarctica: Novel automated regional estimates through machine learning. An Acad Bras Ciênc 94:e20211586. https://doi.org/10.1590/0001-3765202220211586

Barlett EMR, Tosonotto GV, Piola AR, Sierra ME, Mata MM (2018) On the temporal variability of intermediate and deep waters in the Western Basin of the Bransfield Strait. Deep Sea Res Part II Top Stud Oceanogr 149:31–46. https://doi.org/10.1016/j.dsr2.2017.12.010

Bates NR, Johnson RJ (2020) Acceleration of ocean warming, salinification, deoxygenation and acidification in the surface subtropical North Atlantic Ocean. Commun Earth Environ 1:33. https://doi.org/10.1038/s43247-020-00030-5

Biastoch A, Beal L, Lutjeharms J, Casal T (2009) Variability and coherence of the Agulhas Undercurrent in a high-resolution ocean general circulation model. J Phys Oceanogr 39:2417–2435. https://doi.org/10.1175/2009JPO4184.1

Bonou FK, Noriega C, Lefèvre N, Araujo M (2016) Distribution of CO_2 parameters in the Western Tropical Atlantic Ocean. Dyn Atmos Oceans 73:47–60. https://doi.org/10.1016/j.dynatmoce.2015.12.001

Brown L, Sanders R, Savidge G (2006). Relative mineralisation of C and Si from biogenic particulate matter in the upper water column during the Northeast Atlantic diatom bloom in spring 2001. J Mar Syst 63:79–90. https://doi.org/10.1016/j.jmarsys.2006.03.001

Brown MS, Munro DR, Feehan CJ, Sweeney C, Ducklow HW, Schofield OM (2019) Enhanced oceanic CO_2 uptake along the rapidly changing West Antarctic Peninsula. Nat Clim Change 9:678–683. https://doi.org/10.1038/s41558-019-0552-3

Bruto L, Araujo M, Noriega C, Veleda D, Lefèvre N (2017) Variability of CO_2 fugacity at the western edge of the tropical Atlantic Ocean from the 8°N to 38°W PIRATA buoy. Dyn Atmos Oceans 78:1–13. https://doi.org/10.1016/j.dynatmoce.2017.01.003

Mendes CRB, Tavano VM, Kerr R, Dotto TS, Maximiano T, Secchi ER (2018) Impact of sea ice on the structure of phytoplankton communities in the northern Antarctic Peninsula. Deep Res Part II Top Stud Oceanogr 149:111–123. https://doi.org/10.1016/j.dsr2.2017.12.003

Caetano LS, Pollery RCG, Kerr R, Magrani F, Neto AA, Vieira R, Marotta H (2020) High-resolution spatial distribution of pCO_2 in the coastal Southern Ocean in late spring. Antarct Sci 1:1–10. https://doi.org/10.1017/S0954102020000334

Cai WJ, Wang Y (1998) The chemistry, fluxes, and sources of carbon dioxide in the estuarine waters of the Satilla and Altamaha Rivers, Georgia. Limnol Oceanogr 43:657–668. https://doi.org/10.4319/lo.1998.43.4.0657

Cape MR, Vernet M, Pettit EC, Wellner J, Truffer M, Akie G, Domack E et al (2019) Circumpolar Deep Water impacts glacial meltwater export and coastal biogeochemical cycling along the West Antarctic Peninsula. Front Mar Sci 6:144. https://doi.org/10.3389/fmars.2019.00144

Carter BR, Feely RA, Williams NL, Dickson AG, Fong MB, Takeshita Y (2018) Updated methods for global locally interpolated estimation of alkalinity, pH, and nitrate. Limnol Oceanogr Methods 16:119–131. https://doi.org/10.1002/lom3.10232

Carvalho ACO, Marins RV, Dias FJS, Rezende CE, Lefèvre N, Cavalcante MS, Eschrique SA (2017) Air-sea CO_2 fluxes for the Brazilian northeast continental shelf in a climatic transition region. J Mar Syst 173:70–80. https://doi.org/10.1016/j.jmarsys.2017.04.009.

Cavalieri DJ, Parkinson CL (2008) Antarctic sea ice variability and trends, 1979–2006. J Geophys Res 113:C07004. https://doi.org/10.1029/2007JC004558

Coles VJ, Brooks MT, Hopkins J, Stukel MR, Yager PL, Hood RR (2013) The pathways and properties of the Amazon River plume in the tropical North Atlantic Ocean. J Geophys Res Oceans 118:6894–6913. https://doi.org/10.1002/2013JC008981

Collares LL, Mata MM, Kerr R, Arigony-Neto J, Barbat MM (2018) Iceberg drift and ocean circulation in the northwestern Weddell Sea, Antarctica. Deep Res Part II Top Stud Oceanogr 149: 10–24. https://doi.org/10.1016/j.dsr2.2018.02.014

Cook AJ, Holland, PR, Meredith MP, Murray T, Luckman A, Vaughan DG (2016) Ocean forcing of glacier retreat in the western Antarctic Peninsula. Science 353:283–286. 10.1126/science.aae0017

Cooley SR, Coles VJ, Subramaniam A, Yager PL (2007) Seasonal variations in the Amazon plume-related atmospheric carbon sink. Glob Biogeochem Cycles 21:1–15. http://doi.org/10.1029/2006GB002831

Costa RR, Mendes CRB, Ferreira A, Tavano VM, Dotto TS, Secchi ER (2021) Large diatom bloom off the Antarctic Peninsula during cool conditions associated with 2015/2016 El Niño. Commun Earth Environ 2: 252. https://doi.org/10.1038/s43247-021-00322-4

Costa RR, Mendes CRB, Tavano VM, Dotto TS, Kerr R, Monteiro T, Odebrecht C, Secchi ER (2020) Dynamics of an intense diatom bloom in the Northern Antarctic Peninsula, February 2016. Limnol Oceanogr 66:1–20. https://doi.org/10.1002/lno.11437

Couto N, Martinson DG, Kohut J, Schofield O (2017) Distribution of upper circumpolar deep water on the warming continental shelf of the West Antarctic

Peninsula. J Geophys Res Oceans 122:5306–5315. https://doi.org/10.1002/2017JC012840

da Cunha LC, Hamacher C, Farias CO, Kerr R, Mendes CRB, Mara M (2018) Contrasting end-summer distribution of organic carbon along the Gerlache Strait, Northern Antarctic Peninsula: Bio-physical interactions. Deep Sea Res Part II Top Stud Oceanogr 149:206–217. https://doi.org/10.1016/j.dsr2.2018.03.003

da Cunha LC, Buitenhuis ET (2013). Riverine influence on the tropical Atlantic Ocean biogeochemistry. Biogeosciences 10:6357–6373. https://doi.org/10.5194/bg-10-6357-2013

Dagg M, Benner R, Lohrenz S, Lawrence D (2004) Transformation of dissolved and particulate materials on continental shelves influenced by large rivers: Plume processes. Cont Shelf Res 24(7–8):833–858. https://doi.org/10.1016/j.csr.2004.02.003.

Dai A, Trenberth KE (2002) Estimates of freshwater discharge from continents: Latitudinal and seasonal variations. J Hydrometeorol 3(6):660–687. https://doi.org/10.1175/1525-7541(2002)003<0660:EOFDFC>2.0.CO;2

Dai Y, Yang S, Zhao D, Hu C, Xu W, Anderson DM, Li Y (2023) Coastal phytoplankton blooms expand and intensify in the 21st century. Nature 615:280–284. https://doi.org/10.1038/s41586-023-05760-y

Dalla Rosa L, Secchi ER, Maia YG, Zerbini AN, Heide-Jørgensen MP (2008) Movements of satellite-monitored humpback whales on their feeding ground along the Antarctic Peninsula. Polar Biol 31:771–781. https://doi.org/10.1007/s00300-008-0415-2

Damini BY, Kerr R, Dotto TS, Mata MM (2022) Long-term changes on the Bransfield Strait deep water masses: Variability, drivers and connections with the northwestern Weddell Sea. Deep Sea Res Part I Oceanogr Res Pap 179: 103667. https://doi.org/10.1016/j.dsr.2021.103667

Damini BY, Costa RR, Dotto TS, Mendes CRB, Torres-lasso JC, Azaneu MVC, Mata MM, Kerr R (2023) Antarctica Slope Front bifurcation eddy: A stationary feature influencing CO_2 dynamics in the northern Antarctic Peninsula. Progress in Oceanography 212:102985. https://doi.org/10.1016/j.pocean.2023.102985

de Baar HJW, De Jong JTM, Bakker DCE, Löscher BM, Veth C, Bathmann U, Smetacek U (1995) Importance of iron for plankton blooms and carbon dioxide drawdown in the Southern Ocean. Nature 373:412–415. https://doi.org/10.1038/373412a0

De Jong J, Schoemann V, Lannuzel D, Croot P, De Baar H, Tison J.-L (2012) Natural iron fertilization of the Atlantic sector of the Southern Ocean by continental shelf sources of the Antarctic Peninsula. J Geophys Res Biogeosci 117:G01029. https://doi.org/10.1029/2011JG001679

Deacon EL (1977) Gas transfer to and across an air–water interface. Tellus 29(4): 363–374. https://doi.org/10.1111/j.2153-3490.1977.tb00724.x

Dejong HB, Dunbar RB (2017) Air-sea CO_2 exchange in the Ross Sea, Antarctica. J Geophys Res Ocean 122:8167–8181. https://doi.org/10.1002/2017JC012853

Del Castillo CE, Signorini SR, Karaköylü EM, Rivero-Calle S (2019) Is the Southern Ocean getting greener? Geophys Res Lett 46:6034–6040. https://doi.org/10.1029/2019GL083163

Del Vecchio R, Subramaniam A (2004) Influence of the Amazon River on the surface optical properties of the western tropical North Atlantic Ocean. J Geophys Res 109:C11001. https://doi.org/10.3389/fmars.2018.00343

Dickson AG (1990) Termodynamics of the dissociation of boric acid in synthetic seawater from 273.15 to 318.15 K. Deep Sea Res 37:755–766. https://doi.org/10.1016/0198-0149(90)90004-F

Dickson AG, Millero FJ (1987) A comparison of the equilibrium constants for the dissociation of carbonic acid in seawater media, Deep-Sea Res I: Oceanogr Res Pap 34:1733– 1743. https://doi.org/10.1016/0198-0149(87)90021-5

Didden, N. and F. Schott. (1993). Eddies in the North Brazil Current retroflection region observed by Geosat altimetry. *Journal of Geophysical Research: Oceans*, 98, C11, 20121-20131. https://doi.org/10.1029/93JC01184.

Dinniman MS, Klinck JM, Hofmann EE (2012) Sensitivity of Circumpolar Deep Water transport and ice shelf basal melt along the west Antarctic Peninsula to changes in the winds. J Clim 25(14):4799–4816. https://doi.org/10.1175/JCLI-D-11-00307.1

Dlugokencky EJ, Lang PM, Masarie KA, Crotwell AM, Crotwell MJ (2015) Atmospheric Carbon Dioxide Dry Air Mole Fractions from the NOAA ESRL Carbon Cycle Cooperative Global Air Sampling Network, 1968–2014, Version: 2015–09–08. ftp://aftp.cmdl.noaa.gov/data/trace_gases/co2/flask/surface

Dlugokencky EJ, Mund JW, Crotwell AM, Crotwell MJ, Thoning KW (2021) Atmospheric Carbon Dioxide Dry Air Mole Fractions from the NOAA GML Carbon Cycle Cooperative Global Air Sampling Network, 1968-2020, Version: 2021-07-30. https://doi.org/10.15138/wkgj-f215

Doney SC, Fabry VJ, Feely RA, Kleypas JA (2009) Ocean acidification: the other CO_2 problem. Ann Rev Mar Sci 1:169–92. https://doi.org/10.1146/annurev.marine.010908.163834

Doney SC, Busch DS, Cooley SR, Kroeker KJ (2020) The Impacts of Ocean Acidification on Marine Ecosystems and Reliant Human Communities. Annu Rev Environ Resour 45:83–112. https://doi.org/10.1146/annurev-environ-012320-083019

Dotto TS, Kerr R, Mata MM, Garcia CA (2016) Multidecadal freshening and lightening in the deep waters of the Bransfield Strait, Antarctica. J Geophys Res Oceans 121(6):3741–3756. https://doi.org/10.1002/2015JC011228

Dotto TS, Mata MM, Kerr R, Garcia CA (2021) A novel hydrographic gridded data set for the Northern Antarctic Peninsula. Earth Syst Sci Data 13(2):671–696. https://doi.org/10.5194/essd-13-671-2021

Dufois F, Hardman-Mountford NJ, Greenwood J, Richardson AJ, Feng M, Herbette S, Matear R (2014) Impact of eddies on surface chlorophyll in the South Indian Ocean. J Geophys Res Oceans 119:8061–8077, https://doi.org/10.1002/2014JC010164

Seyboth E, Groch KR, Dalla-Rosa L, Reid K, Flores PAC, Secchi ER (2016) Southern Right Whale (Eubalaena australis) Reproductive Success is Influenced by Krill (Euphausia superba) Density and Climate. Sci Rep 6:1–8. https://doi.org/10.1038/srep28205

Ferreira A, Costa RR, Dotto TS, Kerr R, Tavano VM, Brito AC, Brotas V, Secchi ER, Mendes CRB (2020) Changes in Phytoplankton Communities Along the Northern Antarctic Peninsula: Causes, Impacts and Research Priorities. Front Mar Sci 7:576254. https://doi.org/10.3389/fmars.2020.576254

Ferreira, MLC, Kerr R (2017) Source water distribution and quantification of North Atlantic deep water and Antarctic bottom water in the Atlantic Ocean. Prog Oceanogr 153:66–83. https://doi.org/10.1016/j.pocean.2017.04.003

Flynn RF, Bornman TG, Burger JM, Smith S, Spence KAM, Fawcett SE (2021) Summertime productivity and carbon export potential in the Weddell Sea, with a focus on the waters adjacent to Larsen C Ice Shelf. Biogeosciences 18:6031–6059. https://doi.org/10.5194/bg-18-6031-2021

Fonseca CA, Campos E, Goni GJ, Johns WE (2004) Investigation of the North Brazil Current retroflection and North Equatorial Countercurrent variability. Geophys Res Lett 31:1–5. https://doi.org/10.1029/2004GL020054

Forsch KO, Hahn-Woernle L, Sherrell RM, Roccanova VJ, Bu K, Burdige D, Vernet M, Barbeau KA (2021) Seasonal dispersal of fjord meltwaters as an important source of iron and manganese to coastal Antarctic phytoplankton. Biogeosciences 18:6349–6375. https://doi.org/10.5194/bg-18-6349-2021

Fractions from the NOAA ESRL Carbon Cycle Cooperative Global Air Sampling Network, 1968–2014, Version: 2015–09–08, fp://afp.cmdl.noaa.gov/data/trace_gases/co2/fask/surface

Francini-Filho R, Asp NE, Siegle E, Hocevar J, Lowyck K, D'Avila N, Vasconcelos AA (2018) Perspectives on the Great Amazon Reef: Extension, biodiversity, and threats. Front Mar Sci 5:142. https://doi.org/10.3389/fmars.2018.00142

Friedlingstein P, O'Sullivan, M, Jones MW, Andrew RM, Hauck J, Olsen A, Peters GP (2020) Global carbon budget 2020. Earth Syst Sci Data 12:3269–3340. https://doi.org/10.5194/essd-12-3269-2020

Friis K, Körtzinger A, Wallace DWR (2003) The salinity normalization of marine inorganic carbon chemistry data. Geophys Res Lett 30(2):1085. https://doi.org/10.1029/2002GL015898

Fripiat F, Klaus MM, Vancoppenolle M, Papadimitriou S, Thomas DN, Ackley SF, Arrigo KR (2017) Macro-nutrient concentrations in Antarctic pack ice: Overall patterns and overlooked processes. Elementa-Sci Anthropocene 5:13. https://doi.org/10.1525/elementa.217

García MA, Castro CG, Ríos AF, Doval MD, Rosón G, Gomis D, López O (2002) Water masses and distribution of physico-chemical properties in the Western Bransfeld Strait and Gerlache Strait during Austral summer 1995/96. Deep Sea Res Part II Top Stud Oceanogr 49:585–602. https://doi.org/10.1016/S0967-0645(01)00113-8

Garzoli SL, Ffield A, Johns WE, Yao Q (2004) North Brazil Current retroflection and transports. J Geophys Res 109:1–13. http://dx.doi.org/10.1029/2003JC001775

Gaube P, McGillicuddy DJ, Chelton DB, Behrenfeld MJ, Strutton PG (2014) Regional variations in the influence of mesoscale eddies on near-surface chlorophyll. J Geophys Res Oceans 119(12):8195–8220. https://doi.org/10.1002/2014JC010111

Gibson JAE, Trull TW (1999) Annual cycle of fCO_2 under sea-ice and in open water in Prydz Bay, East Antarctica. Mar Chem 66:187–200. https://doi.org/10.1016/S0304-4203(99)00040-7

Goes M, Molinari R, Silveira I, Wainer I (2005) Retroflections of the North Brazil Current during February 2002. Deep Sea Res I: Oceanogr Res Pap 52:647–667. https://doi.org/10.1016/j.dsr.2004.10.010

Goeyt C, Poisson A (1989) New determination of carbonic acid dissociation constants in seawater as a function of temperature and salinity. Deep Sea Res Part A Ocean Res Pap 36:1635–1654. https://doi.org/10.1016/0198-0149(89)90064-2

Gomes HdR, Xu Q, Ishizaka J, Carpenter EJ, Yager PL, Goes JI (2018) The Influence of Riverine Nutrients in Niche Partitioning of Phytoplankton Communities–A Contrast Between the Amazon River Plume and the Changjiang (Yangtze) River Diluted Water of the East China Sea. Front Mar Sci 5:343. https://doi.org/10.3389/fmars.2018.00343

Gonçalves-Araujo R, Souza MA, Tavano VM, Garcia CAE (2015) Garcia Influence of oceanographic features on spatial and interannual variability of phytoplankton in the Bransfield Strait, Antarctica. J Mar Syst 142:1–15. https://doi.org/10.1016/j.jmarsys.2014.09.007

Gouveia NA, Gherardi DFM, Wagner FH, Paes ET, Coles VJ, Aragão LEOC (2019) The salinity structure of the Amazon River plume drives spatiotemporal variation of oceanic primary productivity. J Geophys Res Biogeosci 124:147–165. https://doi.org/10.1029/2018JG004665

Grumbine RW (1996) Automated passive microwave sea ice concentration analysis at NCEP. NOAA Tech. Note 120, 13 pp. [Available from NCEP/NWS/NOAA, 5200 Auth Road, Camp Springs, MD 20746].

Ducklow H, Vernet M, Prezelin B (2019) Palmer Station Antarctica LTER. Dissolved inorganic nutrients including 5 macro nutrients: silicate, phosphate, nitrate, nitrite, and ammonium from water column bottle samples collected between October and April at Palmer Station, 1991 - 2019. ver 9. Environmental Data Initiative. https://doi.org/10.6073/pasta/8f9b7a10633d6eed2e8c0f2eefb8ac0c

Hatta M, Measures CI, Selph KE, Zhou M, Hiscock WT (2013) Iron fluxes from the shelf regions near the South Shetland islands in the drake passage during the austral-winter 2006. Deep Sea Res Part II Top Stud Oceanogr 90:89–101. https://doi.org/10.1016/j.dsr2.2012.11.003

Hauck J, Völker C, Wolf-Gladrow DA, Laufkötter C, Vogt M, Aumont O, Bopp L, Buitenhuis ET (2015) On the Southern Ocean CO_2 uptake and the role of the biological carbon pump in the 21st century. Glob Biogeochem Cycles 29:1451–1470. https://doi.org/10.1002/2015GB005140

Hauck J, Völker C, Wang T, Hoppema M, Losch M, Wolf-Gladrow DA (2013) Seasonally different carbon flux changes in the Southern Ocean in response to the southern annular mode. Glob Biogeochem Cycles 27:1236–1245. https://doi.org/10.1002/2013GB004600

Hauri C, Doney SC, Takahashi T, Erickson M, Jiang G, Ducklow HW (2015) Two decades of inorganic carbon dynamics along the West Antarctic Peninsula. Biogeosciences 12:6761–6779. https://doi.org/10.5194/bg-12-6761-2015

Hawkings J, Wadham J, Benning L, Hendry KR, Tranter M, Tedstone A, Nienow P, Raiswell R (2017) Ice sheets as a missing source of silica to the polar oceans. Nat Commun 8:14198. https://doi.org/10.1038/ncomms14198

Hellmer HH, Rohardt G (2010) Physical oceanography during Ary Rongel cruise AR01. Alfred Wegener Institute, Helmholtz Center for Polar and Marine Research, Bremerhaven. PANGAEA. https://doi.org/10.1594/PANGAEA.735276

Hellweger F, Gordon A (2002) Tracing Amazon River water into the Caribbean Sea. J Mar Res 60:537–549. https://doi.org/10.1357/002224002762324202

Henley SF, Cavan EL, Fawcett SE, Kerr R, Monteiro T, Sherrell RM, Bowie AR (2020) Changing Biogeochemistry of the Southern Ocean and Its Ecosystem Implications. Front Mar Sci 7:581. https://doi.org/10.3389/fmars.2020.00581

Henley SF, Schofield OM, Hendry KR, Schloss IR, Steinberg DK, Moffat C, Peck LS (2019) Variability and change in the west Antarctic Peninsula marine system: research priorities and opportunities. Prog Oceanogr 173:208–237. https://doi.org/10.1016/j.pocean.2019.03.003

Henley SF, Jones EJ, Venables HJ, Meredith MP, Firing YL, Dittrich R, Heiser S (2018) Macronutrient and carbon supply, uptake and cycling across the Antarctic

Peninsula shelf during summer. Philos Trans A Math Phys Eng Sci 376: 20170168. https://doi.org/10.1098/rsta.2017.0168

Henley SF, Tuerena RE, Annett AL, Fallick AE, Meredith MP, Venables HJ, Clarke A, Ganeshram RS (2017) Macronutrient supply, uptake and recycling in the coastal ocean of the west Antarctic Peninsula. Deep Sea Res Part II Top Stud Oceanogr 139:58–76. https://doi.org/10.1016/j.dsr2.2016.10.003

Hersbach H, Bell B, Berrisford P, Hirahara S, Horányi A, Muñoz-Sabater J, Nicolas J (2020) The ERA5 global reanalysis. Q J R Meteorol Soc 146:1999–2049. https://doi.org/10.1002/qj.3803

Ho DT, Schanze JJ (2020) Precipitation-induced reduction in surface ocean pCO2: observations from the eastern tropical Pacific Ocean. Geophys Res Lett 47: e2020GL088252. https://doi.org/10.1029/2020GL088252

Höfer J, Giesecke R, Hopwood MJ, Carrera V, Alarcón E, González HE (2019) The Role of Water Column Stability and Wind Mixing in the Production/Export Dynamics of Two Bays in the Western Antarctic Peninsula. Prog Oceanogr 174:105–116. https://doi.org/10.1016/j.pocean.2019.01.005

Hogg, A, Gudmundsson G (2017) Impacts of the Larsen-C Ice Shelf calving event. Nat Clim Change 7:540–542. https://doi.org/10.1038/nclimate3359

Hoppema M, Bakker K, van Heuven SMAC, Ooijen JC, de Baar HJ (2015) Distributions, trends and inter-annual variability of nutrients along a repeat section through the Weddell Sea (1996–2011). Mar Chem 177:545–553 https://doi.org/10.1016/j.marchem.2015.08.007

Hopwood MJ, Cantoni C, Clarke JS, Cozzi S, Achterberg EP (2017) The heterogeneous nature of Fe delivery from melting icebergs. Geochem Perspect Lett 3:200–209. doi:10.7185/geochemlet.1723

Ibánhez JS, Araujo M, Lefèvre N (2016) The overlooked tropical oceanic CO_2 sink. Geophys Res Lett 43(8): 3804-3812. https://doi.org/10.1002/2016GL068020

Ibánhez JS, Diverrès D, Araujo M, Lefèvre N (2015) Seasonal and interannual variability of sea-air CO_2 fluxes in the tropical Atlantic affected by the Amazon River plume. Glob Biogeochem Cycles 29(10):1640–1655 https://doi.org/10.1002/2015GB005110

Ibánhez J, Flores M, Lefèvre N (2017) Collapse of the tropical and subtropical North Atlantic CO_2 sink in boreal spring of 2010. Sci Rep 7:41694 https://doi.org/10.1038/srep41694

IPCC (2021) Climate Change 2021: The Physical Science Basis. Contribution of Working Group I to the Sixth Assessment Report of the Intergovernmental Panel on Climate Change [Masson-Delmotte V, Zhai P, Pirani A, Connors SL, Péan C, Berger S, Caud N, Chen Y, Goldfarb L, Gomis MI, Huang M, Leitzell K, Lonnoy E, Matthews JBR, Maycock TK, Waterfield T, Yelekçi O, Yu R, and Zhou B (eds.)]. Cambridge University Press. In Press.

Ito RG, Tavano VM, Mendes CRB, Garcia CAE (2018) Sea-air CO_2 fluxes and pCO_2 variability in the Northern Antarctic Peninsula during 3 summer periods (2008–2020). Deep Sea Res Part II Top Stud Oceanogr 149:84–98. https://doi.org/10.1016/j.dsr2.2017.09.004

Jiang LQ, Carter BR, Feely RA, Lauvset SK, Olsen A (2019) Surface ocean pH and buffer capacity: past, present and future. Sci Rep 9:18624. https://doi.org/10.1038/s41598-019-55039-4

Johns WE, Lee T, Beardsley RC, Candela J, Limeburner R, Castro BM (1998) Annual cycle and variability of the North Brazil Current. J Phys Oceanogr 28:103–128. https://doi.org/10.1175/1520-0485(1998)028<0103:ACAVOT>2.0.CO;2

Johns W, Speich S (2021) Tropical Atlantic Observing System (TAOS) Review Report. *CLIVAR-01/202*1, 218. https://archimer.ifremer.fr/doc/00696/80787/.

Jones EM, Fenton M, Meredith MP, Clargo NM, Ossbaar S, Ducklow HW, Venables HJ, de Baar HJW (2017) Ocean acidifcation and calcium carbonate saturation states in the coastal zone of the West Antarctic Peninsula Peninsula. Deep Sea Res Part II Top Stud Oceanogr 139:181–194. https://doi.org/10.1016/j.dsr2.2017.01.007

Jones EM, Hoppema M, Strass V, Hauck J, Salt L, Ossebaar S, Klaas C et al (2015) Mesoscale features create hotspots of carbon uptake in the Antarctic Circumpolar Current. Deep Sea Res Part II Top Stud Oceanogr 138:39– 51. https://doi.org/10.1016/j.dsr2.2015.10.006

Karl, D. M., Tilbrook, B. D. & Tien, G. Seasonal coupling of organic matter production and particle flux in the western Bransfield Strait, Antarctica. Deep-Sea Res. 38, 1097–1126 (1991). https://doi.org/10.1016/0198-0149(91)90098-Z

Keppler, L. & Landschützer, P. Regional wind variability modulates the Southern Ocean carbon sink. Sci. Rep. 9, 7384 (2019). https://doi.org/10.1038/s41598-019-43826-y

Kerr, D. E., Brown, P. J., Grey, A., Kelleher, B. P. The Influence of Organic Alkalinity on the Carbonate System in Coastal Waters. Mar. Chem. 2021, 104050. DOI: 10.1016/j.marchem.2021.104050

Kerr R, Goyet C, da Cunha LC, Orselli IBM, Lencina-Avila JM, Mendes CRB, Carvalho-Borges M, Mata MM, Tavano VM (2018b). Carbonate system properties in the Gerlache Strait, Northern Antarctic Peninsula (February 2015): II. Anthropogenic CO_2 and seawater acidification. Deep. Res. Part II., 149, pp. 182-192. https://doi.org/10.1016/j.dsr2.2017.07.007

Kerr, R. et al. Carbonate system properties in the Gerlache Strait, Northern Antarctic Peninsula (February 2015): I. Sea-Air CO_2 fluxes. Deep Sea Res. Part II Top. Stud. Oceanogr., 149 (2018), pp. 171-181. https://doi.org/10.1016/j.dsr2.2017.02.008

Kerr, R. et al (2018) Carbonate system properties in the Gerlache Strait, Northern Antarctic Peninsula (February 2015): II. Anthropogenic CO_2 and seawater

acidification. Deep Res. Part II 149, 182–192. https://doi.org/10.1016/j.dsr2.2017.07.007

Kerr, R., Mata, M. M., Mendes, C. R. B. & Secchi E. R (2018) Northern Antarctic Peninsula: a marine climate hotspot of rapid changes on ecosystems and ocean dynamics. Deep Res. Part II Top. Stud. Oceanogr. 149, 4–9. https://doi.org/10.1016/j.dsr2.2018.05.006

Khatiwala, F. Primeau, T. Hall. Reconstruction of the history of anthropogenic CO2 concentrations in the ocean. Nature, 462 (2009), pp. 346-349. https://doi.org/10.1038/nature08526

Kim, H. et al. Inter-decadal variability of phytoplankton biomass along the coastal West Antarctic Peninsula. Philos. Trans. R. Soc. A Math. Phys. Eng. Sci. 376(2122), 20170174 (2018). https://doi.org/10.1098/rsta.2017.0174

Kim, H., Doney, S.C., Iannuzzi, R.A., Meredith, M.P., Martinson, D.G., Ducklow, H.W., 2016. Climate forcing for dynamics of dissolved inorganic nutrients at Palmer Station, Antarctica: An interdecadal (1993–2013) analysis. J. Geophys. Res.- Biogeosci. 121, 2369–2389. https://doi.org/10.1002/2015JG003311.

Klinck, J.M., Hofmann, E.E., Beardsley, R.C., Salihoglu, B., Howard, S., 2004. Water-mass properties and circulation on the west Antarctic Peninsula Continental Shelf in Austral Fall and Winter 2001. Deep-Sea Res. Part II-Topical Stud. Oceanography 51, 1925–1946. https://doi.org/10.1016/j.dsr2.2004.08.001

Korosov, A., Counillon, F., Johannessen, J. A. (2015). Monitoring the spreading of the Amazon freshwater plume by MODIS, SMOS, Aquarius, and TOPAZ. *Journal of Geophysical Research: Oceans*, 120, 268–283. https://doi.org/10.1002/2014JC010155

Körtzinger, A. (2003). A significant CO2 sink in the tropical Atlantic Ocean A significant CO2 sink in the tropical Atlantic Ocean associated with the Amazon Plume River plume. *Geophysical Research Letters*, 30, 1–4. http://dx.doi.org/10.1029/2003GL018841.

Kucharski, F., Parvin, A., Rodriguez-Fonseca, B., Farneti, R., Martin-Rey, M., Polo, I., Losada, T. (2016). The teleconnection of the tropical Atlantic to indo-Pacific Sea surface temperatures on inter-annual to centennial time scales: A review of recent findings. *Atmosphere*, 7, 2, 29. https://doi.org/10.3390/atmos7020029.

Kulk, G., Platt, T., Dingle, J., Jackson, T., Jönsson, B. F., Bouman, H. A., et al. (2020). Primary Production, an Index of Climate Change in the Ocean: Satellite-Based Estimates over Two Decades. *Remote Sensing*, 12, 5, 826. https://doi.org/10.3390/rs12050826.

Laika, H. E. et al. Interannual properties of the CO_2 system in the Southern Ocean south of Australia. Antarct. Sci. 21, 663 (2009). https://doi.org/10.1017/S0954102009990319

Lancelot, C., Mathot, S., Veth, C. & de Baar, H. Factors controlling phytoplankton ice-edge blooms in the marginal ice-zone of the northwestern Weddell Sea during sea ice retreat 1988: feld observations and mathematical modelling. Polar Biol. 13, 377–387 (1993). https://doi.org/10.1007/BF01681979

Landschützer, P., et al. 2015. The reinvigoration of the Southern Ocean carbon sink. Science (80-.). 349, 1221–1224. DOI:10.1126/science.aab26

Landschützer, P., Gruber, N., Bakker, D.C.E., Schuster U. (2014). Recent variability of the global ocean carbon sink. *Global Biogeochemical Cycles*, 28, 9, 927–949. https://doi.org/10.1002/2014GB004853

Landschützer, P., Laruelle, G. G., Roobaert, A., and Regnier, P. (2020). A uniform pCO_2 climatology combining open and coastal oceans, *Earth System Science Data*, 12, 2537–2553. https://doi.org/10.5194/essd-12-2537-2020

Laufkötter, C., Stern, A. A., John, J. G., Stock, C. A., and Dunne, J. P. (2018). Glacial iron sources stimulate the Southern Ocean carbon cycle. Geophys. Res. Lett. 13:385. https://doi.org/10.1029/2018GL079797

Lauvset, S. K., Carter, B. R., Perez, F. F., Jiang, L.-Q., Feely, R. A., Velo, A., & Olsen, A. (2020). Processes driving global interior ocean pH distribution. Global Biogeochemical Cycles, 34, e2019GB006229. https://doi.org/10.1029/2019GB006229

Lefèvre, N., Diverrès, D., Francis, G. (2010). Origin of CO_2 undersaturation in the western tropical Atlantic. *Tellus B: Chemical and Physical Meteorology*, 62, 595–607. http://dx.doi.org/10.1111/j.1600-0889.2010.00475.x.

Lefèvre, N., Flores Montes, M., Gaspar, F.L., Rocha, C., Jiang, S., De Araújo, M.C., Ibánhez, J.S.P. (2017). Net heterotrophy in the Amazon continental shelf changes rapidly to a sink of CO_2 in the outer Amazon plume. *Frontiers in Marine Science*, 4, 278. https://doi.org/10.3389/fmars.2017.00278.

Lefèvre, N., Tyaquiçã, P., Veleda, D., Perruche, C., & Van Gennip, S. J. (2020). Amazon River propagation evidenced by a CO_2 decrease at 8° N, 38° W in September 2013. *Journal of Marine Systems*, *211*, 103419, https://doi.org/10.1016/j.jmarsys.2020.103419.

Lefèvre, N., Urbano, D.F., Diverrès, D., Francis, G. (2014). Impact of physical processes on the seasonal distribution of the fugacity of CO_2 in the western tropical Atlantic. *Journal of Geophysical Research,* 119, 646–663. https://doi.org/10.1002/2013JC009248.

Legge, O. J. et al. The seasonal cycle of carbonate system processes in Ryder Bay, West Antarctic Peninsula. Deep Sea Res. Part II Top. Stud. Oceanogr. 139, 167–180 (2017). https://doi.org/10.1016/j.dsr2.2016.11.006

Legge, O. J. et al. The seasonal cycle of ocean-atmosphere CO_2 flux in Ryder Bay, West Antarctic Peninsula. Geophys. Res. Lett. 42, 2934–2942 (2015). https://doi.org/10.1002/2015GL063796

Lencina-Avila, J. M. et al. Past and future evolution of the marine carbonate system in a coastal zone of the Northern Antarctic Peninsula. Seep Res. Part II Top. Stud. Oceanogr. 149, 193–205 (2018). https://doi.org/10.1016/j.dsr2.2017.10.018

Lenton, A. et al. Sea-air CO_2 fuxes in the Southern Ocean for the period 1990–2009. Biogeosci. Discuss. 10, 285–333 (2013). https://doi.org/10.5194/bg-10-4037-2013

Lenton, A. et al. The observed evolution of oceanic pCO_2 and its drivers over the last two decades. Glob. Biogeochem. Cycles 26, 1–14 (2012). https://doi.org/10.1029/2011GB004095

Lenton, A., Matear, R. J. & Tilbrook, B. Design of an observational strategy for quantifying the Southern Ocean uptake of CO_2. Glob. Biogeochem. Cycles 20, GB4010 (2006). https://doi.org/10.1029/2005GB002620

Lewis, E., Wallace, D. & Allison, L. J. Program Developed for CO_2 System Calculations System Calculations 38 (Carbon Dioxide Information Analysis Center, USA, 1998).

Liang, Y.C., Lo, M.H., Lan, C.W., Seo, H., Ummenhofer, C. C., Yeager, S., et al. (2020). Amplified seasonal cycle in hydroclimate over the Amazon River basin and its plume region. *Nature Communications*, 11, 1, 4390. https://doi.org/10.1038/s41467-020-18187-0

Liutti, C. C. et al. (2021). Sea surface CO_2 fugacity in the southwestern South Atlantic Ocean: An evaluation based on satellite-derived images. *Marine Chemistry*, 104020. https://doi.org/10.1016/j.marchem.2021.104020

Louchard, D., Gruber, N., & Münnich, M. (2021). The impact of the Amazon on the biological pump and the air-sea CO2 balance of the Western Tropical Atlantic. *Global Biogeochemical Cycles*, 35, 6, e2020GB006818. https://doi.org/10.1029/2020GB006818.

Lovenduski, N. S., Gruber, N., Doney, S. C. & Lima, I. D. Enhanced CO_2 outgassing in the Southern Ocean from a positive phase of the Southern annular mode. Glob. Biogeochem. Cycles 21, GB2026 (2007). https://doi.org/10.1029/2006GB002900

Lübbecke, J. F., Durgadoo, J. V., & Biastoch, A. (2015). Contribution of increased Agulhas leakage to tropical Atlantic warming. *Journal of Climate*, 28, 24, 9697-9706. https://doi.org/10.1175/JCLI-D-15-0258.1

Lueker, T. J., Dickson, A. G., & Keeling, C. D. (2000). Ocean pCO_2 calculated from dissolved inorganic carbon, alkalinity, and equations for K1 and K2: validation based on laboratory measurements of CO_2 in gas and seawater at equilibrium. *Marine chemistry*, 70,1-3, 105-119. https://doi.org/10.1016/S0304-4203(00)00022-0

Marengo, J. A., & Espinoza, J. C. (2016). Extreme seasonal droughts and floods in Amazonia: causes, trends and impacts. *International Journal of Climatology*, 36, 1033–1050, https://doi.org/10.1002/joc.4420

Marshall, G. J. Trends in the Southern annular mode from observations and reanalyses. J. Clim., 16 (2003), pp. 4134-4143. https://doi.org/10.1175/1520-0442(2003)016<4134:TITSAM>2.0.CO;2

Marshall, G. J., Orr, A., van Lipzig, N. P. M., & King, J. C. (2006). The impact of a changing Southern Hemisphere annular mode on Antarctic Peninsula summer temperatures. Journal of Climate, 19(20), 5388– 5404. https://doi.org/10.1175/JCLI3844.1

Mascioni, M. et al. Microplanktonic diatom assemblages dominated the primary production but not the biomass in an Antarctic fjord. J. Marine Syst. 224, 103624 (2021). https://doi.org/10.1016/j.jmarsys.2021.103624

Mata, M. M., Tavano, V. M. & García, C. A. E. 15 years sailing with the Brazilian High Latitude Oceanography Group (GOAL). Deep Res. Part II Top. Stud. Oceanogr. 149, 1–3 (2018). https://doi.org/10.1016/j.dsr2.2018.05.007

McNeil, B. I., Metzl, N., Key, R. M., Matear, R. J. & Corbiere, A. An empirical estimate of the Southern Ocean air-sea CO_2 flux. Glob. Biogeochem. Cycles 21, GB3011 (2007). https://doi.org/10.1029/2007GB002991

Mehrbach, C., Culberson, C. H., Hawley, J. E., & Pytkowicz R. M. (1973). Measurements of the apparent dissociation constants of carbonic acid in seawater at atmospheric pressure. *Limnology and Oceanography*, 18, 897– 907. https://doi.org/10.4319/lo.1973.18.6.0897

Meinshausen, M., Nicholls, Z. R., Lewis, J., Gidden, M. J., Vogel, E., Freund, M., et al. (2020). The shared socio-economic pathway (SSP) greenhouse gas concentrations and their extensions to 2500. *Geoscientific Model Development*, 13, 8, 3571-3605. https://doi.org/10.5194/gmd-13-3571-2020

Mendes, C. R. B. et al. New insights on the dominance of cryptophytes in Antarctic coastal waters: a case study in Gerlache Strait. RDeep Res. Part II Top. Stud. Oceanogr. 149, 161–170 (2018). https://doi.org/10.1016/j.dsr2.2017.02.010

Mendes, C. R. B., M. S. de Souza, V. M. T. Garcia, M. C. Leal, V. Brotas, and C. A. E. Garcia. 2012. Dynamics of phytoplankton communities during late summer around the tip of the Antarctic Peninsula. Deep-Sea Res. Part I Oceanogr. Res. Pap. 65: 1– 14. https://doi.org/10.1016/j.dsr.2012.03.002

Mendes, C. R. B., V. M. Tavano, M. C. Leal, M. S. de Souza, V. Brota, and C. A. E. Garcia. 2013. Shifts in the dominance between diatoms and cryptophytes during three late summers in the Bransfield Strait (Antarctic Peninsula). Polar Biol. 36: 537– 547. doi: https://doi.org/10.1007/s00300-012-1282-4

Mendes, C. R. B., V. M. Tavano, R. Kerr, T. S. Dotto, T. Maximiano, and E. R. Secchi. 2018. Impact of sea ice on the structure of phytoplankton communities in

the northern Antarctic Peninsula. Deep-Sea Res. Part II Top. Stud. Oceanogr. 149: 111– 123. https://doi.org/10.1016/j.dsr2.2017.12.003

Meredith et al. 2022. Internal tsunamigenesis and ocean mixing driven by glacier calving in Antarctica. Science Adcances. 8, eadd0720. https://doi.org/10.1126/sciadv.add0720

Meredith, M. P. & King, J. C. Rapid climate change in the ocean west of the Antarctic Peninsula during the second half of the 20th century. Geophys. Res. Lett. 32, 1–5 (2005). https://doi.org/10.1029/2005GL024042

Meredith, M. P. et al. On the interannual variability of ocean temperatures around South Georgia, Southern Ocean: forcing by El Niño/southern oscillation and the southern annular mode. Deep-Sea Res. II Top. Stud. Oceanogr., 55 (18–19) (2008), pp. 2007-2022. https://doi.org/10.1016/j.dsr2.2008.05.020

Meredith, M. P. et al. Variability in the freshwater balance of northern Marguerite Bay, Antarctic Peninsula: Results from δ18O. Deep Res. Part II Top. Stud. Oceanogr. 55, 309–322 (2008). https://doi.org/10.1016/j.dsr2.2007.11.00

Meredith, M. P., Stefels, J., & van Leeuwe, M. Marine studies at the western Antarctic Peninsula: priorities, progress and prognosis. Deep–Sea Res. Pt II, 139 (2017), pp. 1-8. https://doi.org/10.1016/j.dsr2.2017.02.002.

Metzl, N. et al. Spatio-temporal distributions of air-sea fuxes of CO_2 in the India and Antarctic oceans. Tellus 47B, 56–69 (1995). https://doi.org/10.3402/tellusb.v47i1-2.16006

Metzl, N., Bunet, C., Jabaud-Jan, A., Poisson, A. & Schauer, B. Summer and winter air–sea CO_2 fluxes in the Southern Ocean. Deep Res. I 53, 1548–1563 (2006). https://doi.org/10.1016/j.dsr.2006.07.006

Millero, F. J. The marine inorganic carbon cycle. *Chem. Rev.* **107,** 308–341 (2007). https://doi.org/10.1021/cr0503557

Millero, F. J. The carbonate system. In: Chemical Oceanography (CRC Press 2013.

Millero, F. J. (2010). Carbonate constants for estuarine waters. *Marine and Freshwater Research*, 61, 2, 139-142. https://doi.org/10.1071/MF09254

Millero, F. J. et al. Dissociation constants for carbonic acid determined from field measurements. Deep Res. Part I 49, 1705–1723 (2002). https://doi.org/10.1016/S0967-0637(02)00093-6

Millero, F.J., Graham, T.B., Huang, F., Bustos-Serrano, H., Pierrot, D. (2006). Dissociation constants of carbonic acid in seawater as a function of salinity and temperature. *Marine Chemistry*, 100, 80–94. http://dx.doi.org/10.1016/j.marchem.2005.12.001

Mofat, C., Owens, B. & Beardsley, R. C. On the characteristics of circumpolar deep water intrusions to the west Antarctic Peninsula continental shelf. J. Geophys. Res. Ocean. 114, 1–16 (2009). https://doi.org/10.1029/2008JC004955

Moffat, C., & Meredith, M. (2018). Shelf–ocean exchange and hydrography west of the Antarctic peninsula: A review. Philosophical Transac- tions of the Royal Society A: Mathematical, Physical & Engineering Sciences, 376(2122), 20170164. https://doi.org/10.1098/rsta.2017.0164

Monteiro, T., Kerr, R. & Machado, E.d. Seasonal variability of net sea-air CO_2 fluxes in a coastal region of the northern Antarctic Peninsula. Sci Rep 10, 14875 (2020b). https://doi.org/10.1038/s41598-020-71814-0

Monteiro, T., Kerr, R., Orselli, I. B. M. & Lencina-Avila, J. M. Towards an intensified summer CO2 sink behaviour in the Southern Ocean coastal regions. Prog. Oceanogr. 183, 102267 (2020a). https://doi.org/10.1016/j.pocean.2020.102267

Monteiro, Thiago, Kerr, Rodrigo, Pollery, Ricardo César Gonçalves, Mendes, Carlos Rafael Borges, Henley, Sian, Tavano, Virginia Maria, Garcia, Carlos Alberto Eiras, & Mata, Mauricio. (2022). BGQNAPv1.0: A summer macronutrients binned data set for the Northern Antarctic Peninsula, Southern Ocean (1.0) [Data set]. Zenodo. https://doi.org/10.5281/zenodo.7384423

Moreau, S. et al. Climate change enhances primary production in the western Antarctic Peninsula. Glob. Change Biol. 21, 2191–2205 (2015). https://doi.org/10.1111/gcb.12878

Moura, R. L., Amado-Filho, G. M., Moraes, F. C., Brasileiro, P. S., Salomon, P. S., Mahiques, M. M. et al. (2016). An extensive reef system at the Amazon River mouth. *Science Advances,* 2, 4, e1501252. http://dx.doi.org/10.1126/sciadv.1501252

Mu, L., Gomes, H. D. R., Burns, S. M., Goes, J. I., Coles, V. J., Rezende, C. E., et al. (2021). Temporal Variability of Air-Sea CO2 flux in the Western Tropical North Atlantic Influenced by the Amazon River Plume. *Global Biogeochemical Cycles*, *35*, 6, e2020GB006798. https://doi.org/10.1029/2020GB006798

Murphy EJ, Johnston NM, Hofmann EE, Phillips RA, Jackson JA, Constable AJ, Henley SF, Melbourne-Thomas J, Trebilco R, Cavanagh RD, Tarling GA, Saunders RA, Barnes DKA, Costa DP, Corney SP, Fraser CI, Höfer J, Hughes KA, Sands CJ, Thorpe SE, Trathan PN and Xavier JC (2021) Global Connectivity of Southern Ocean Ecosystems. Front. Ecol. Evol. 9:624451. https://doi.org/10.3389/fevo.2021.624451

Neumann-Leitão, S., Melo, P. A. M. C., Schwamborn, R., Diaz, X. F. G., Figueiredo, L. G. P., Silva, A. P., et al. (2018). Zooplankton from a reef system under the influence of the Amazon River plume. *Frontiers in microbiology,* 9, 355. https://doi.org/10.3389/fmicb.2018.00355

Niiler, P. P., Amos, A., & Hu, J.-H. (1991). Water masses and 200 m relative geostrophic circulation in the western Bransfield Strait region. Deep Sea

Research Part A. Oceanographic Research Papers, 38(8–9), 943–959. https://doi.org/10.1016/0198-0149(91)90091-S

Nomura, D. et al. Winter-to-summer evolution of pCO_2 in surface water and air–sea CO_2 flux in the seasonal ice zone of the Southern Ocean. Biogeosciences 11, 5749–5761 (2014). https://doi.org/10.5194/bg-11-5749-2014

Nomura, D., Inoue, H. Y. & Toyota, T. The effect of sea-ice growth on air-sea CO_2 flux in a tank experiment. Tellus 58B, 418–426 (2006). https://doi.org/10.1111/j.1600-0889.2006.00204.x

Nowacek, D. P. et al. Super-aggregations of Krill and Humpback Whales in Wilhelmina Bay, Antarctic Peninsula. PLoS ONE 6, e19173 (2011). https://doi.org/10.1371/journal.pone.0019173

Olsen, A., Lange, N., Key, R. M., Tanhua, T., Bittig, H. C., Kozyr, A., et al. (2020). An updated version of the global interior ocean biogeochem- ical data product, GLODAPv2.2020. Earth System Science Data, 12(4), 3653–3678. https://doi.org/10.5194/essd-12-3653-2020

Orr JC, Fabry VJ, Aumont O, Bopp L, Doney SC, et al. 2005. Anthropogenic ocean acidification over the twenty-first century and its impact on calcifying organisms. Nature 437:681–86. https://doi.org/10.1038/nature04095

Orr, J. C., Epitalon, J., Dickson, A. & Gattuso, J. Routine uncertainty propagation for the marine carbon dioxide system. Mar. Chem. 207, 84–107 (2018). https://doi.org/10.1016/j.marchem.2018.10.006

Orselli, I. B. M., Goyet, C., Kerr, R., Azevedo, J. L. L. de Araujo, M., Galdino, F., et al. (2019). The effect of Agulhas eddies on absorption and transport of anthropogenic carbon in the South Atlantic Ocean. *Climate*, 7, 6, 84. https://doi.org/10.3390/cli7060084

Orselli, I. B. M., Kerr, R., Azevedo, J. L. L. d., Galdino, F., Araujo, M. & Garcia, C. A. E. (2019). The sea-air CO_2 net fluxes in the South Atlantic Ocean and the role played by Agulhas eddies. *Progress in Oceanography*, 170, 40-52. https://doi.org/10.1016/j.pocean.2018.10.006

Orselli, I. B. M.et al. 2022. The marine carbonate system along the northern Antarctic Peninsula: current knowledge and future perspectives. An Acad Bras Cienc 94: e20210825. https://doi.org/10.1590/0001-3765202220210825

Ouyang, Z. et al. Sea-ice loss amplifies summertime decadal CO_2 increase in the western Arctic Ocean. Nat. Clim. Change 10, 678–684 (2020). https://doi.org/10.1038/s41558-020-0784-2

Park, G.-H., & Wanninkhof, R. (2012). A large increase of the CO_2 sink in the western tropical North Atlantic from 2002 to 2009. Journal of Geophysical Research, 117, C08029. https://doi.org/10.1029/2011JC007803

Parkinson, C. L. & Cavalieri, D. J. Antarctic sea ice variability and trends, 1979–2010. Cryosphere 6, 871–880 (2012). https://doi.org/10.5194/tc-6-871-2012

Parra, R. R. T., Laurido, A. L. C. & Sánchez, J. D. I. Hydrographic conditions during two austral summer situations (2015 and 2017) in the Gerlache and Bismarck straits, northern Antarctic Peninsula. *Deep Res. Part I* **161**, 103278 (2020). https://doi.org/10.1016/j.dsr.2020.103278

Patil, G. P. & Rao, C. R. Handbook of Statistics v 12 927 (Amsterdan, Environmental Statistics, 1994).

Pierrot, D., Lewis, E. & Wallace, D. W. R. MS Excel Program Developed for CO2 System Calculations, ORNL/CDIAC-105a (Carbon Dioxide Information Analysis Center. Oak Ridge National Laboratory, U.S. Department of Energy, Tennessee, 2006). doi: 10.3334/CDIAC/otg.CO2SYS_XLS_CDIAC105a

Pitman, R.L., Durban, J.W. Killer whale predation on penguins in Antarctica. Polar Biol 33, 1589–1594 (2010). https://doi.org/10.1007/s00300-010-0853-5

Plum, C., Hillebrand, H. & Moorthi, S. Krill vs salps: dominance shift from krill to salps is associated with higher dissolved N:P ratios. Sci Rep 10, 5911 (2020). https://doi.org/10.1038/s41598-020-62829-8

Pollard, R., P. Tre´guer, and J. F. Read (2006), Quantifying nutrient supply to the Southern Ocean, J. Geophys. Res., 111, C05011, https://doi.org/10.1029/2005JC003076

Pondaven, P., Ragueneau, O., Treguer, P., Hauvespre, A., Dezileau, L., and Reyss, J. L. (2000). Resolving the 'opal paradox' in the Southern Ocean. Nature 405, 168–172. https://doi.org/10.1038/35012046

Prézelin, B. B. et al. Physical forcing of phytoplankton community structure and primary production in continental shelf waters of the Western Antarctic Peninsula. J. Mar. Res., 62 (2004), pp. 419-460. https://doi.org/10.1357/0022240041446173

Prézelin, B. B. et al. The linkage between upper circumpolar deep water (UCDW) and phytoplankton assemblages on the west Antarctic Peninsula continental shelf. J. Mar. Res. 58, 165–202 (2000). https://doi.org/10.1357/002224000321511133

Ratnarajah, L. & Bowie, A. R. Nutrient cycling: are antarctic krill a previously overlooked source in the marine iron cycle? Curr. Biol. 26, R884–R887 (2016). https://doi.org/10.1016/j.cub.2016.08.044

Reynolds, R. W. et al (2007) Daily high-resolution-blended analyses for sea surface temperature. J. Clim. 20(22), 5473–5496. https://doi.org/10.1175/2007JCLI1824.1

Richardson, P.L., & Reverdin, G. (1987). Seasonal Cycle of Velocity in the Atlantic North Equatorial Countercurrent as Measured by Surface Drifters,Current Meters, and Ship Drifts. *Journal of Geophysical Research*, 92, C4, 3691-3708. https://doi.org/10.1029/JC092iC04p03691

Rivaro, P. et al. Distribution of dissolved labile and particulate iron and copper in Terra Nova Bay polynya (Ross Sea, Antarctica) surface waters in relation to

nutrients and phytoplankton growth. Continental Shelf Research. 31, 879–889 (2011). https://doi.org/10.1016/j.csr.2011.02.013

Rivaro, P. et al. Distribution of total alkalinity and pH in the Ross Sea (Antarctica) waters during austral summer 2008. Polar Research, 33, 20403 (2014). https://doi.org/10.3402/polar.v33.20403

Roden, N. P., Shadwick, E. H., Tilbrook, B. & Trull, T. W. Annual cycle of carbonate chemistry and decadal change in coastal Prydz Bay, East Antarctica. Mar. Chem. 155, 135–147 (2013). https://doi.org/10.1016/j.marchem.2013.06.006

Rodrigues, R.R., Rothstein, L.M., Wimbush, M. (2007). Seasonal variability of the South Equatorial Current bifurcation in the Atlantic Ocean: A numerical study. *Journal of Physical Oceanography,* 37, 16-37. https://doi.org/10.1175/JPO2983.1.

Roobaert, A. et al (2019) The spatiotemporal dynamics of the sources and sinks of CO_2 in the global coastal ocean. Glob. Biogeochem. Cycles https://doi.org/10.1029/2019GB006239

Rysgaard. S. et al. Sea ice contribution to the air–sea CO_2 exchange in the Arctic and Southern Oceans. Tellus. 63B, 823–830 (2011). https://doi.org/10.1111/j.1600-0889.2011.00571.x

Saba, G. K., et al. (2014), Winter and spring controls on the summer food web of the coastal West Antarctic Peninsula, Nat. Commun., 5, 4318. https://doi.org/10.1038/ncomms5318

Salisbury, J., Vandemark, D., Campbell, J., Hunt, C., Wisser, D. et al. (2011). Spatial and temporal coherence between Amazon River discharge, salinity, and light absorption by colored organic carbon in western tropical Atlantic surface waters. *Journal of Geophysical Research: Oceans*, 116, C00H02. https://doi.org/10.1029/2011JC006989

Sangrà, P., Gordo, C., Hernández-Arencibia, M., Marrero-Díaz, A., Rodríguez-Santana, A., Stegner, A., & Pichon, T. (2011). The Bransfield current system. Deep-Sea Research Part I Oceanographic Research Papers, 58(4), 390–402. https://doi.org/10.1016/j.dsr.2011.01.011

Sangrà, P., Stegner, A., Hernández-Arencibia, M., Marrero-Díaz, Á., Salinas, C., et al. (2017). The Bransfield gravity current. Deep Sea Research Part I: Oceanographic Research Papers, 119, 1–15. https://doi.org/10.1016/j.dsr.2016.11.003

Santos-Andrade, M., Kerr, R., Orselli,I. B. M., Monteiro, T., Mata, M.M., & Goyet, C. (2023). Drivers ofmarine CO2-carbonate chemistry inthe northern Antarctic Peninsula.Global Biogeochemical Cycles,37, e2022GB007518. https://doi.org/10.1029/2022GB007518

Santoso, A., Mcphaden, M. J. & Cai, W. The Defining Characteristics of ENSO extremes and the Strong 2015/2016 El Niño. Rev. Geophys. 55, 1079–1129 (2017). https://doi.org/10.1002/2017RG000560

Sarmiento, J. L., and N. Gruber (2006), Ocean Biogeochemical Dynamics, Princeton Univ. Press, Princeton, Woodstock.

Sathyendranath, S., Jackson, T., Brockmann, C. et al. (2021). ESA Ocean Colour Climate Change Initiative (Ocean_Colour_cci): Version 5.0 Data. NERC EDS Centre for Environmental Data Analysis, 19 May 2021. http://dx.doi.org/10.5285/1dbe7a109c0244aaad713e078fd3059a

Savidge, D. K., & Amft, J. A. (2009). Circulation on the west Antarctic peninsula derived from 6 years of shipboard ADCP transects. Deep Sea Research Part I: Oceanographic Research Papers, 56(10), 1633–1655. https://doi.org/10.1016/j.dsr.2009.05.011

Schlitzer, R. (2018). Ocean Data View, v. 5.3.0. https://odv.awi.de.

Secchi, E. R. et al. Encounter rates and abundance of humpback whales (Megaptera novaeangliae) in Gerlache and Bransfield Straits, Antarctic Peninsula. J. Cetacean Res. Manag. 3, 107–111 (2011). https://doi.org/10.47536/jcrm.vi.312

Shepherd, A. et al. Mass balance of the Antarctic ice sheet from 1992 to 2017. Nature 558, 219–226 (2018). https://doi.org/10.1038/s41586-018-0179-y.

Sherrell, R.M., Annett, A.L., Fitzsimmons, J.N., Roccanova, V.J., Meredith, M.P., 2018. A 'shallow bathtub ring' of local sedimentary iron input maintains the Palmer Deep biological hotspot on the West Antarctic Peninsula shelf. Philos. Trans. R. Soc. A- Math. Phys. Eng. Sci. 376. https://doi.org/10.1098/rsta.2017.0171

Siegert, M. et al. The Antarctic Peninsula under a 1.5°C global warming scenario. Front. Environ. Sci. 7, 102 (2019). https://doi.org/10.3389/fenvs.2019.00102

Silva, A. B.et al. 2020. Spatial and temporal analysis of changes in the glaciers of the Antarctic Peninsula. Glob. Planet. Chang. 2020, 184, 103079. https://doi.org/10.1016/j.gloplacha.2019.103079

Silva, M., Araujo, M., Servain, J., Penven, P., Lentini, C.A.D. (2009). High-Resolution Regional Ocean Dynamics Simulation in the Southwestern Tropical Atlantic. *Ocean Modelling,* 30, 256-269. https://doi.org/10.1016/j.ocemod.2009.07.002

Smith, W. O., Anderson, R. F., Keith Moore, J., Codispoti, L. A., and Morrison, J. M. (2000). The US southern ocean joint global ocean flux study: an introduction to AESOPS. Deep Sea Res. Part II Top. Stud. Oceanogr. 47, 3073–3093. https://doi.org/10.1016/S0967-0645(00)00059-X

Smith, D. A., Hofmann, E. E., Klinck, J. M. & Lascara, C. M. Hydrography and circulation of the West Antarctic Peninsula continental shelf. Deep. Res. Part I 46, 925–949 (1999). https://doi.org/10.1016/S0967-0637(98)00103-4

Smith, W. O., Jr, & Demaster, D. J. (1996). Phytoplankton biomass and productivity in the Amazon River plume: Correlation with seasonal river discharge. *Continental Shelf Research*, 16, 3, 291–319. https://doi.org/10.1016/0278-4343(95)00007-N.

Souza, A. D., Kerr, R., & Azevedo, J. D. (2018). On the influence of subtropical mode water on the South Atlantic Ocean. *Journal of Marine Systems*, 185, 13–24 https://doi.org/10.1016/j.jmarsys.2018.04.006.

Stammerjohn, S. E., Martinson, D. G., Smith, R. C., Yuan, X. & Rind, D. Trends in Antarctic annual sea ice retreat and advance and their relation to El Ninño-Southern Oscillation and Southern Annular Mode variability. J. Geophys. Res. 113, C03S90 (2008). https://doi.org/10.1029/2007JC004269

Stukel, M. R., Coles, V. J., Brooks, M. T., and Hood, R. R.: Top-down, bottom-up and physical controls on diatom-diazotroph assemblage growth in the Amazon River plume, Biogeosciences, 11, 3259–3278, https://doi.org/10.5194/bg-11

Su Z, Zhang Z, Zhu Y and Zhou M (2022) Long-Term Warm–Cold Phase Shifts in the Gerlache Strait, Western Antarctic Peninsula. Front. Mar. Sci. 9:877043. https://doi.org/10.3389/fmars.2022.877043

Sweeney, C., Gloor, E., Jacobson, A. R., Key, R. M., McKinley, G., Sarmiento, J. L., & Wanninkhof, R. (2007). Constraining global air-sea gas exchange for CO_2 with recent bomb 14C measurements. *Global Biogeochemical Cycles*, 21, 2. https://doi.org/10.1029/2006GB002784

Takahashi, T. et al. The changing carbon cycle in the Southern Ocean. Oceanography 25, 26–37 (2012). https://doi.org/10.5670/oceanog.2012.71

Takahashi, T., Olafsson, J., Goddard, J. G., Chipman, D. W. & Sutherland, S. C. Seasonal variation of CO_2 and nutrients in the high-latitude surface oceans: a comparative study. Glob. Biogeochem. Cycles 7, 843–878 (1993). https://doi.org/10.1029/93GB02263

Takahashi, T., Sutherland, S. C., Chipman, D. W., Goddard, J. G., Ho, C., Newberger, T., et al. (2014). Climatological distributions of pH, pCO_2, total CO_2, alkalinity, and CaCO3 saturation in the global surface ocean, and temporal changes at selected locations. *Marine Chemistry*, 164, 95-125. https://doi.org/10.1016/j.marchem.2014.06.004

Takahashi, T., Sutherland, S. C., Sweeney, C., Poisson, A., Metzl, N., Tillbrook, B., Bates, N., Wanninkhof, R., Feely, R. A., Sabine, C., Olafsson, J., Nojiri Y. Global sea-air CO_2 flux based on climatological surface ocean pCO_2, and seasonal biological and temperature effects. *Deep Sea Research Part II: Topical Studies in Oceanography*, 49 (2002), 1601–1622. https://doi.org/10.1016/S0967-0645(02)00003-6

Takahashi, T., Sutherland, S.C., Wanninkhof, R., Sweeney, C., Feely, R.A., Chipman, D.W., de Baar, H.J.W. (2009). Climatological mean and decadal change in surface ocean pCO_2, and net sea–air CO_2 flux over the global oceans.

Deep Sea Research Part II: Topical Studies in Oceanography, 56, 554–577. https://doi.org/10.1016/j.dsr2.2008.12.009

Thompson, A. F. et al. Surface circulation at the tip of the Antarctic Peninsula from drifters. Journal Physics in Oceanographic, 39 (2009), pp. 3-26, https://doi.org/10.1175/2008JPO3995.1

Tovar-Sanchez, A. et al. (2007). Krill as a central node for iron cycling in the Southern Ocean. Geophys. Res. Lett. 34:L11601. https://doi.org/10.1029/2006GL029096

Troupin, C. et al. Generation of analysis and consistent error felds using the data interpolating variational analysis (Diva). Ocean Model. 52–53, 90–101 (2012). https://doi.org/10.1016/j.ocemod.2012.05.002

Turner, J. et al. Antarctic climate change and the environment: an update. Polar Rec. 50, 237–259 (2014). https://doi.org/10.1017/S0032247413000296

Turner, J., Guarino, M. V., Arnatt, J., Jena, B., Marshall, G. J., Phillips, T., et al. (2020). Recent decrease of summer sea ice in the Weddell Sea, Antarctica. Geophysical Research Letters, 47, e2020GL087127. https://doi.org/10.1029/2020GL087127

Tyaquiçã, P., Veleda, D., Lefèvre, N., Araujo, M., Noriega, C., Caniaux, G., Servain, J., & Silva, T. (2017). Amazon Plume Salinity Response to Ocean Teleconnections. *Frontier Marine Science*, 4, 250, https://doi.org/10.3389/fmars.2017.00250

Uppström, L. R. (1974). The boron/chlorinity ratio of deep-sea water from the Pacific Ocean. *Deep Sea Research and Oceanographic Abstracts*, 21, 161–162. https://doi.org/10.1016/0011-7471(74)90074-6

Utida, G., Cruz, F. W., Etourneau, J., Bouloubassi, I., Schefuß, E., Vuille, M., et al. (2019). Tropical South Atlantic influence on Northeastern Brazil precipitation and ITCZ displacement during the past 2,300 years. *Scientific Reports*, 9, 1, 1698. https://doi.org/10.1038/s41598-018-38003-6

Valerio, A.M., Kampel, M., Ward, N.D., Sawakuchi, H.O., Cunha, A.C., Richey, J.E. (2021). CO_2 partial pressure and fluxes in the Amazon River plume using in situ and remote sensing data. *Continental Shelf Research, 215*, 104348. https://doi.org/10.1016/j.csr.2021.104348

Van Caspel, M., Hellmer, H.H., Mata, M.M. On the ventilation of Bransfield Strait deep basins. Deep Sea Res. Part II Top. Stud. Oceanogr., 149 (2018), pp. 25-30. https://doi.org/10.1016/j.dsr2.2017.09.006

van Leeuwe, M. A., and others. 2020. Annual patterns in phytoplankton phenology in Antarctic coastal waters explained by environmental drivers. Limnol. Oceanogr. 65: 1651– 1668. https://doi.org/10.1002/lno.11477

Varona, H. L., Veleda, D., Silva, M., Cintra, M., & Araujo, M. (2019). Amazon River plume influence on Western Tropical Atlantic dynamic variability. *Dynamics*

of Atmospheres and Oceans, 85, 1– 15. https://doi.org/10.1016/j.dynatmoce.2018.10.002.

Venables, H. J. & Meredith, M. P. Feedbacks between ice cover, ocean stratifcation, and heat content in Ryder Bay, western Antarctic Peninsula. J. Geophys. Res. Oceans 119, 5323–5336 (2014). https://doi.org/10.1002/2013JC009669

Venables, H. J., Meredith, M. P. & Brearley, A. Modification of deep waters in Marguerite Bay, western Antarctic Peninsula, caused by topographic overflows. Deep Res. Part II Top. Stud. Oceanogr. 139, 9–17 (2017). https://doi.org/10.1016/j.dsr2.2016.09.005

Vera, C. S. & Osman, M. Activity of the southern annular mode during 2015–2016 El Niño event and its impact on southern hemisphere climate anomalies. Int. J. Climatol., 38 (2018), pp. e1288-e1295. https://doi.org/10.1002/joc.5419.

Wadham, J. L. et al. Ice sheets matter for the global carbon cycle. Nat. Commun. 10, 3567 (2019). https://doi.org/10.1038/s41467-019-11394-4

Waite, N. (2022). Palmer Station Antarctica LTER. Merged discrete water-column data from PAL LTER research cruises along the Western Antarctic Peninsula, from 1991 to 2020. ver 1. Environmental Data Initiative. https://doi.org/10.6073/pasta/65c43a4688eccf8ca7cc3a2d07a0cc78

Wang, B. et al. Meteoric water promotes phytoplankton carbon fixation and iron uptake off the eastern tip of the Antarctic Peninsula (eAP). Prog. Oceanogr. 185, 102347 (2020). https://doi.org/10.1016/j.pocean.2020.102347

Wang, X., Moffat, C., Dinniman, M.S., Klinck, J. M., Sutherland, D. A. & Aguiar-González, B. 2022. Variability and dynamics of along-shore exchange on the West Antarctic Peninsula (WAP) continental shelf. J Geophys Res Oceans 127: e2021JC017645. https://doi.org/10.1029/2021JC017645

Wanninkhof, R. (1992). Relationship between wind speed and gas exchange. *Journal of Geophysical Research: Oceans*, 97, 7373-7382. https://doi.org/10.1029/92JC00188

Wanninkhof, R. (2014). Relationship between wind speed and gas exchange over the ocean revisited. *Limnology and Oceanography Methods*, 12, 351–362. https://doi.org/10.4319/lom.2014.12.351

Wanninkhof, R. & McGillis, W. R. (1999). A cubic relationship between air-sea CO_2 exchange and wind speed. *Geophysical Research Letters*, 26, 1889-1892. https://doi.org/10.1029/1999GL900363

Wanninkhof, R., Barbero, L. Byrne, R., Cai, W.J., Zhang, H. Z., Baringer, M., & Langdon, C. (2015). Ocean acidification along the Gulf Coast and East Coast of the USA. *Continental Shelf Research,* 98, 54– 71. https://doi.org/10.1016/j.csr.2015.02.008

Ward, N. D., Keil, R. G., Medeiros, P. M., Brito, D. C., Cunha, A. C., Dittmar, T., et al. (2013). Degradation of terrestrially derived macromolecules in the Amazon River. *Nature Geoscience*, 6, 7, 530–533. https://doi.org/10.1038/ngeo181

Weiss, R. F. (1974). Carbon dioxide in water and seawater: the solubility of a non-ideal gas. *Marine Chemistry*, 2, 3, 203-215. https://doi.org/10.1016/0304-4203(74)90015-2

Weiss, R.F., & Price, B.A. (1980). Nitrous oxide solubility in water and seawater. *Marine Chemistry*, 8, 347–359. https://doi.org/10.1016/0304-4203(80)90024-9

Whitehouse, M. J., Atkinson, A. & Rees, A. P. Close coupling between ammonium uptake by phytoplankton and excretion by Antarctic krill, Euphausia superba. Deep Sea Res. Part Oceanogr. Res. Pap. 58, 725–732 (2011). https://doi.org/10.1016/j.dsr.2011.03.006

Williams, R. G. & Follows, M. J. Ocean dynamics and the carbon cycle: Principles and mechanisms (Cambridge University Press 2011).

Zeebe, R. and Wolf-Gladrow, D. (2001): CO_2 in Seawater: Equilibrium, Kinetics, Isotopes. *Elsevier Oceanography Book Series*, 65, 346. Amsterdam. ISBN: 0-444-50946-1 and 0-

Zeebe, R. E. History of seawater carbonate Chemistry, atmospheric CO_2 and ocean acidification. Annu. Rev. Earth Planet. Sci. 40, 141–165 (2012). https://doi.org/10.1146/annurev-earth-042711-105521

Zhou, M., Niiler, P. P., & Hu, J. H. (2002). Surface currents in the Bransfield and Gerlache straits, Antarctica. Deep-Sea Research Part I Ocean- ographic Research Papers, 49(2), 267–280. https://doi.org/10.1016/S0967-0637(01)00062-0

Zhou, M., Niiler, P. P., Zhu, Y., & Dorland, R. D. (2006). The western boundary current in the Bransfield Strait, Antarctica. Deep Sea Research Part I: Oceanographic Research Papers, 53(7), 1244–1252. https://doi.org/10.1016/j.dsr.2006.04.003.